FRICTION STIR PROCESSING FOR THE REVERSAL AND MITIGATION OF SENSITISATION AND INTERGRANULAR CORROSION IN ALUMINIUM ALLOY 5083-H321

By

GAVIN SIMON MEREDITH

A thesis submitted to
The University of Birmingham
for the degree of
DOCTOR OF PHILOSOPHY

The School of Metallurgy and Materials
College of Engineering and Physical Sciences
The University of Birmingham
April 2014

Abstract

AA5083-H321 is an aluminium alloy commonly used in ship hull superstructures as it has a corrosion resistance which affords an excellent degree of protection in chloride-rich marine environments. Corrosion performance can degrade in a process called sensitisation, due to the precipitation of a β-phase onto grain boundaries with exposure to elevated temperatures over decades of service. Friction Stir Processing (FSP) has been evaluated as a method for locally reversing the degraded microstructure and removing a susceptibility to Intergranular Corrosion (IGC) in immersed and atmospheric conditions.

Both the mechanical stirring and heat input to the plate by an FSP tool have been shown to remove the β-phase from grain boundaries which had been precipitated by a sensitisation heat treatment. Sensitisation was shown to cause intergranular corrosion of the alloy; however this susceptibility was removed after microstructural modification by FSP.

A re-sensitisation treatment of the previously sensitised and FSP'd region was seen to precipitate coarser and more discrete β-phase particles onto grain boundaries, which corroded at a faster rate than the once-sensitised material under electrochemical testing. This indicates that corrosion resistance degrades more quickly with subsequent sensitisation.

Acknowledgments

First and foremost I must share my appreciation for the time, effort and willingness that Dr Alison Davenport has shown me over my time in the Metallurgy and Materials Department and while under her supervision. The sheer breadth and depth of knowledge that she has to offer has undoubtedly helped me to progress as a scientist and researcher in the field of corrosion, while advice on a more practical level has allowed me to go forward and apply my skills with confidence.

My co-supervisors Dr Yu Lung Chiu and Dr Moataz Attallah have provided invaluable support and guidance from the first day of study until my last. I have received both the jump start that was necessary to get my project rolling as well as the last bit of energy that was needed to get me across the finishing line, while their individual technical expertise has no doubt made a positive impact upon the quality my work.

I would also like to thank the rest of the staff in the Metallurgy and Materials Department who are too numerous to list, but have made a contribution in some way towards furthering my research or have created an environment which has greatly enhanced the learning experience.

I have had the great privilege to work with many talented and dedicated students and researchers, especially in the Corrosion and Electrochemistry Group. Encouragement and interest in the work that we have done has made it very easy to stay on at the University and a joy to come in every day.

Lastly, and perhaps most importantly, this work is dedicated to my wife and family. Their patience, support and generosity have enabled me to be where I am today, and I am exceedingly grateful for all that they have given me.

This work was supported by the United States Office of Naval Research, Grant N00014-09-1-1034, with Dr Airan Perez as Project Monitor.

Table of Contents

List of Figures

List of Tables

List of Abbreviations

APR	**Advancement per Revolution**
BSE	**Back Scattered Electron**
CERT	**Constant Extension Rate Testing**
EDS	**Energy-dispersive X-ray Spectroscopy**
FSP	**Friction Stir Processing**
FSW	**Friction Stir Welding**
GTAW	**Gas Tungsten Arc Welding**
HAZ	**Heat Affected Zone**
IGC	**Intergranular Corrosion**
LT-ST	**Long Transverse-Short Transverse**
MIG	**Metal Inert Gas**
MPa	**Megapascal**
NAMLT	**Nitric Acid Mass-Loss Test**
OCP	**Open Circuit Potential**
RH	**Relative Humidity**
SCC	**Stress Corrosion Cracking**
SCE	**Saturated Calomel Electrode**
SEM	**Scanning Electron Microscope**
TEM	**Transmission Electron Microscope**
TIG	**Tungsten Inert Gas**
TMAZ	**Thermo-Mechanically Affected Zone**
ToW	**Time of Wetness**

Chapter 1 – Introduction

Aluminium alloys have found widespread use in applications requiring materials that have relatively high strength, yet are light compared to materials such as steels. In the case of cars and boats, this reduced weight leads to a desirable increase in efficiency.

The 5xxx series (Al-Mg) aluminium alloys have found favour in shipbuilding not only for those reasons already noted, but also for their ability to resist the corrosive salt water environment in which they operate. Such ships have expected service lives approaching half a century if care is taken in their fabrication and maintenance. While in service, some sections of the hull experience higher heat loads over the life of the boat, and so form a microstructure that is more susceptible to corrosion in the harsh marine environment, known as being sensitised.

The occurrence of Intergranular Corrosion (IGC) has been widely reported before, and is known to lead to Stress Corrosion Cracking (SCC) of Aluminium ship hulls. If intergranular corrosion is detected and it is not appropriate to perform a small, localised repair, large sections of the hull may need to be repair welded into place, at a cost to time, money and the service availability of the boat. Welding may not also be appropriate or feasible in some locations due to the influence of the weld itself on the rest of the superstructure and the relative difficulty of such operations outside of a boatyard.

A technique is therefore required which can repair the microstructural damage that occurs during 20+ years of sensitisation at elevated temperatures, without the need for large structural repairs, instead reverting the microstructure back to that in the hull plate when the boat first came into service.

It would also be of benefit if this technique showed signs of being able to slow down the microstructural changes which occur over time, to either prolong the initial service life of the hull, or to produce a repaired section which suffers corrosion at a rate not greater than seen during the initial life of the hull.

Friction Stir Processing (FSP) shows promise as a technique which can produce a microstructure which has favourable corrosion properties, yet the surface alteration nature of the process should not change the bulk mechanical properties of the hull plate away from the original design intent. This work will evaluate the efficacy of FSP in reversing the detrimental microstructural changes which occur in Al-Mg alloys through sensitisation which lead to IGC and SCC, and will investigate how this ‘repaired’ material suffers further sensitisation.

Chapter 2 – Literature review

2.1. Aluminium-Magnesium Alloys

2.1.1. Introduction to Al-Mg Alloys

The 5xxx series of aluminium alloys are a non-heat-treatable series which have found wide ranging uses in industry. They are favoured for their high strength, high toughness and excellent corrosion resistance, leading to their use as a construction material in ship hulls. Their strength is gained through cold working, dispersoid hardening and by retaining magnesium in solid solution, leading to yield strengths up to 300 MPa and tensile strengths approaching 500 MPa [1]. Cold working through deformation increases the dislocation content of the alloy more rapidly than annihilation by dynamic recovery, leading to the formation of dislocation tangles, while grain and sub grain structures are also changed. This leads to a decrease in mean free slip distance and therefore an increase in strength [2].

The effect of alloying elements in improving the properties of the alloy by solute strengthening will be discussed later, however the role of solute atoms in work hardening this series has been noted. Magnesium solute atoms are believed to have the effect of increasing the rate at which dislocations can multiply, slowing the rate of recovery and adding to the effectiveness of dislocations [3]. In addition to its good weldability, these properties have also led to the 5xxx series being used in structural bridge components, drinks cans and various components for cars.

The addition of magnesium to aluminium leads to an alloy with relatively good corrosion resistance due to the magnesium which stays in the solid solution, in addition to Al_3Mg_2 particles which are uniformly distributed throughout the matrix [4].

Precipitation of the β-phase is not usually a problem as this decomposition happens very slowly at service temperatures; however elevated temperatures and high levels of cold working can increase the rate, leading to precipitation of the β-phase onto high energy grain boundaries and dislocations. When precipitated at these sites, especially as a thin continuous band, they increase the susceptibility of the alloy to intergranular corrosion and Stress Corrosion Cracking (SCC) due to preferential attack at the grain boundaries.

2.1.2. Alloying elements

The 5xxx series of aluminium alloys gain their strength primarily by solute strengthening. High purity aluminium in an annealed state has a very low yield strength (7-11 MPa), which is too low for most engineering applications. For this reason additional alloying elements must be added in order to provide the necessary strengthening. Figure 1(b) shows how the addition of Mn and Cu are very effective at increasing the yield strength up to 0.5 % atomic weight; however these elements show limited usefulness as Mn precipitates out at these concentrations, while Cu forms constituent particles and grain boundary precipitates.

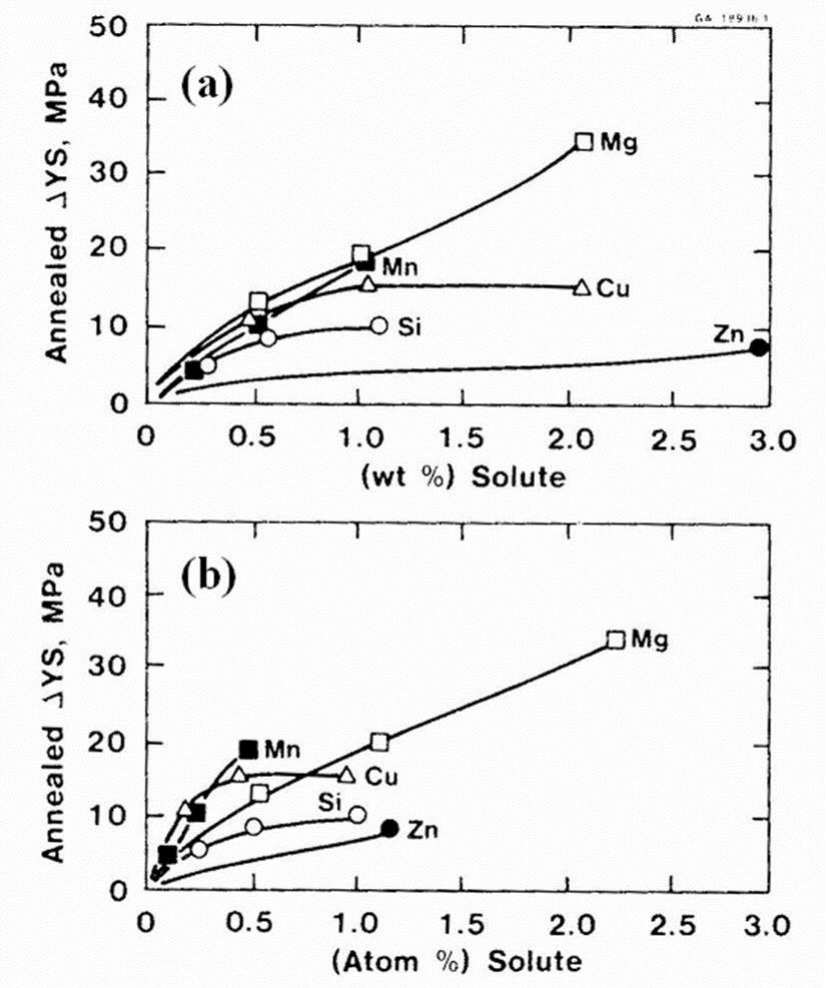

Figure 1 Graph of the effect of the addition of solute elements on the yield strength of aluminium (a) Weight % basis (b) Atomic % basis [2]

Figure 1 (a) shows how the addition of Mg on a weight % basis can lead to ever increasing yield strengths, due to its high solubility in aluminium. The effect of increasing the weight % of magnesium in aluminium is to increase the alloys strength, in terms of both the yield stress and ultimate tensile strength [2]. This solid solution strengthening is somewhat limited by other elements present; silicon reacts with magnesium on cooling to form an $Mg_{(x)}Si$ phase, which reduces the amount of magnesium retained in solid solution.

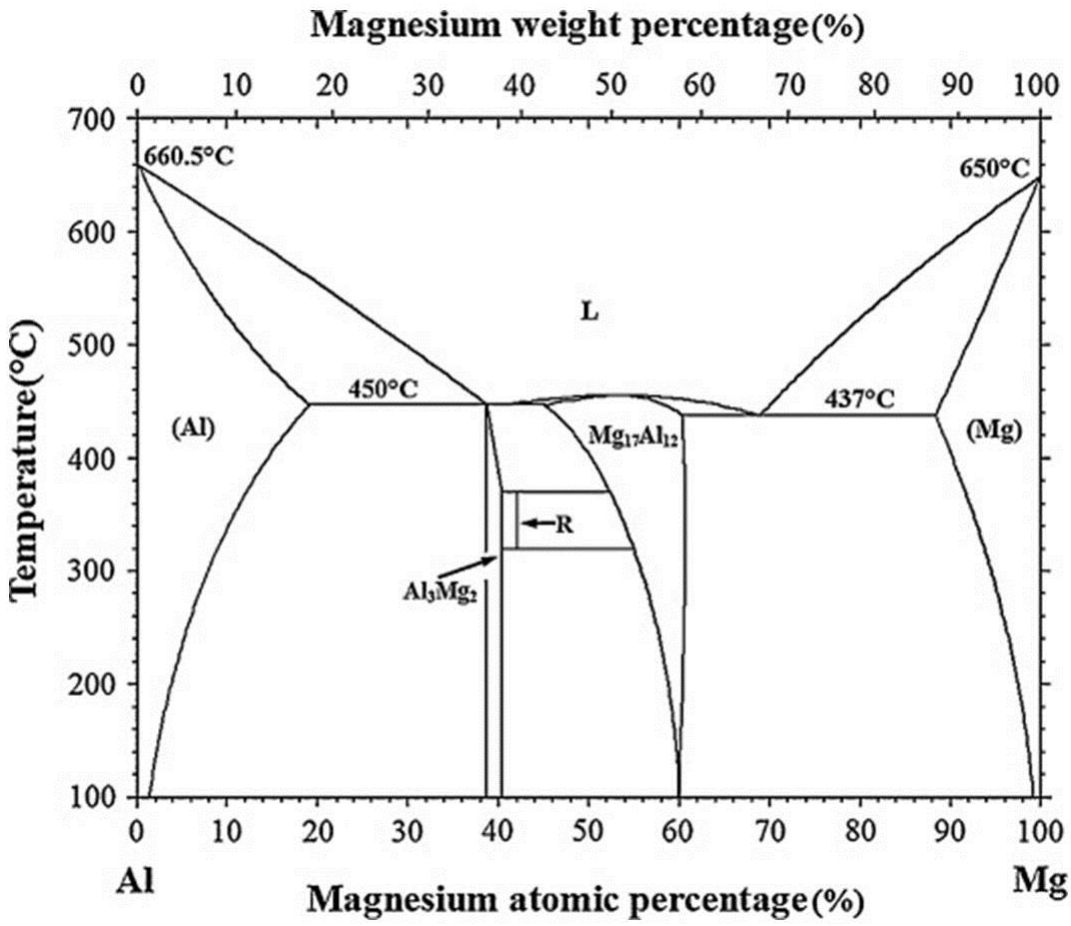

Figure 2 Aluminium-Magnesium binary equilibrium phase diagram. After [5]

In the 5xxx series of aluminium alloys, the amount of Mg added ranges from 0.5 to 12 wt. %, where the greater the addition, the greater the strength. This high percentage of Mg addition is possible as magnesium has a high solid solubility in aluminium (14.9 wt. % at 451 °C, Figure

2), however this is much reduced at room temperature, where solubility is only 1.7 wt. % [2]. When the solubility is reduced in such a way, the precipitation of a β-phase from the α-phase solid solution occurs. However it is this phase which acts to increase the corrosion susceptibility of the material, which is discussed later.

2.2. Sensitisation of Al-Mg Alloys

Sensitisation of an alloy refers to the microstructural changes which are brought about by precipitation of deleterious grain boundary phases which increase the susceptibility of a given alloy to intergranular corrosion. The method specific to Al-Mg alloys will be outlined here.

2.2.1. Segregation of magnesium to grain boundaries

Segregation of solute atoms in a material can lead to depletion or enrichment of magnesium atoms within an area, especially on or around grain boundaries.

The movement of impurity atoms towards grain boundaries is governed by one of two proposed mechanisms. The first of these is equilibrium segregation, formulated by Gibbs, where magnesium atoms are incoherent impurities which seek to have their bond energy reduced by migrating to regions of crystallographic misorientation, such as grain boundaries.

The second is non-equilibrium segregation, where grain centres and boundaries exhibit a vacancy concentration gradient [6]. When an alloy is subjected to a heat treatment where non-equilibrium conditions prevail, such as a quench, then the vacancy concentration will vary in different regions of the microstructure [7]. Grain boundaries were described here as good "vacancy sinks", where the concentration decreases on quenching, while vacancies in the grain centre have nowhere to go, thus is saturated with vacancies. It is along this vacancy gradient that vacancies move, taking with them impurity atoms, towards the grain boundaries and creating solute enrichment [7]. This excess vacancy driven segregation has been demonstrated in cold worked Al-Mg alloys [8, 9]. This system was described in early work by Perryman, who surmised that "magnesium-vacancy pairs are produced after cold working and it is likely that these will diffuse faster than magnesium atoms alone. When this pair reaches a

high angle grain boundary, the vacancy will be annihilated leaving an extra magnesium atom at the grain boundary" [10].

This segregation has been documented in aluminium alloys containing magnesium at heat treatment temperatures above 340 °C [11] . Segregation profiles have also been generated in Al-Mg alloys quenched from 450 °C [12], solution heat treated at 500 °C which show 100 nm wide regions of increased magnesium either side of the grain boundary [13], and samples aged for 10 hours at 175 °C [14].

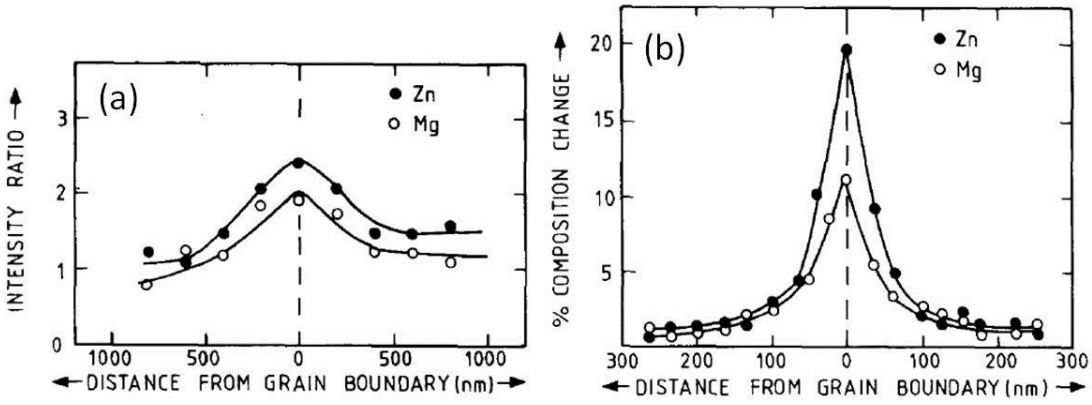

Figure 3 (a) EDS X-ray profiles across a grain boundary of an Al-Zn-Mg alloy showing Mg and Zn segregation profiles. (b) Thin-foil X-ray micro analysis profile across grain boundary in the same alloy system [15].

Magnesium segregation and enrichment has been documented at many areas in the Al-Mg systems; grain boundaries and triple points which are high energy sites with a large free volume [16], and in precipitate free zones and around the β-phase precipitate [17]. In the latter study, Yukawa et al. observed that the Mg levels between precipitates varied as a function of distance between the precipitates; the larger the spacing, the higher the Mg enrichment seen,

Figure 4. This magnesium segregation followed by β-phase precipitation has been linked to an increased susceptibility to IGC in an AA5182 alloy aged for 10 hours at 150 °C [18]

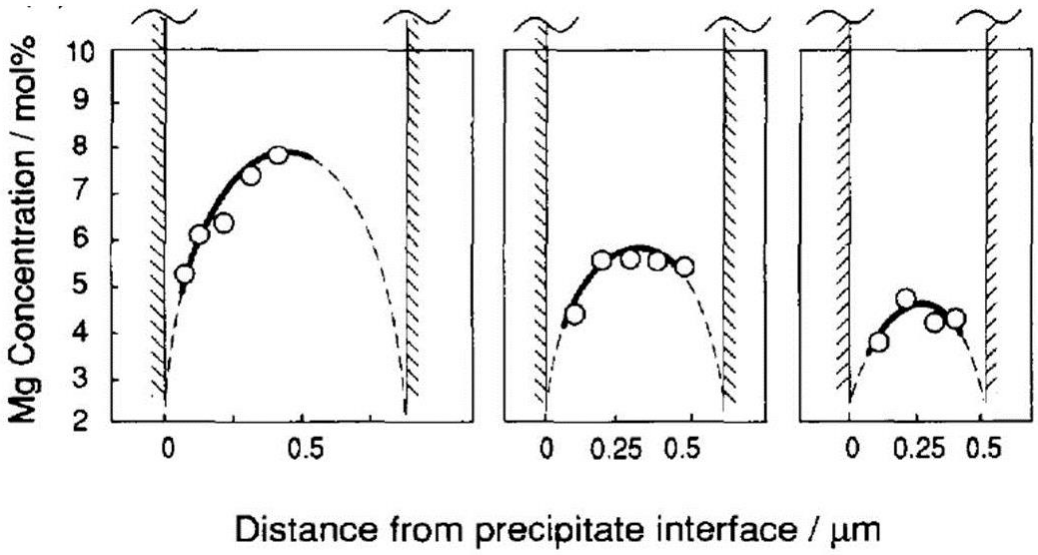

Figure 4 Mg concentration profiles within the interior matrix of Al-Mg binary alloy aged at 423 K for 2.6 Ms [17].

2.2.2. Precipitation of β-phase on grain boundaries

The precipitation sequence of the β-phase out of solid solution in Al-Mg alloys has been suggested as follows: solid solution (α_0) -> G.P. Zones (δ″) -> β″ -> β′ -> β [19-21]. The nucleation of the next precipitate should occur preferentially at the interphase boundaries of the first one. This will occur because of the greater importance of minimising the interfacial free energy [22]. It has however been seen that the appearance of each phase during the decomposition of the supersaturated solid solution does not directly contribute to the formation of the following phase of the precipitation sequence in a Al-12 wt.% Mg alloy [20].

2.2.2.1. β precipitation

There is disagreement in the literature of the past 40 years as to how the β′ then forms from the β″. Some studies have shown that the β′ particles nucleate on structural defects such as dislocations and vacancy voids/loops [21]. When the amount of these defects which facilitate the nucleation of β′ decreases, a direct formation of β (equilibrium phase) is observed. This is in contrast to later work by Starink and Zahra [23, 24] who discovered no evidence of nucleation of β′ precipitate on structural defects. While they did observe a great number of these vacancy-type defects (mostly dislocation loops), they concluded that β′ precipitation is an auto-catalytic process. Research by Itoh et al [25] and Eikum and Thomas [26] both concluded that dislocation loops play no role in the nucleation of β″, the former observing nucleation on tetrahedral shaped voids, while Gao believed the precipitation of β to be heterogeneous[27] .

The change into the stable incoherent β-phase (FCC structure) $Al_3 Mg_2$ [28] is the last of the phase changes to occur and appears only in the later stages of the ageing when the Mg

depletion of the matrix is nearly completed [29, 30]. Bournane noted that in the early stages of aging, the formation and growth of the coherent particles predominates, while the formation and coalescence of new phase particles occurs at prolonged stages of aging [19]. This kinetic precipitation and growth of the β-phase has been noted to be slow unless the material is moderately cold worked, owing to the phase having a large lattice parameter [9, 31].

The location and degree of this precipitation in AA5083 has been well documented recently. Goswami [32] and Choi [33] observed β-phase on grain boundaries as well as around Mn-rich particles in the matrix, reasoned to be due to the relatively low driving force for precipitation on these heterogeneous nucleation sites, Figure 5 and Figure 6. Discontinuous precipitates have been seen to grow at 200-220 °C [34, 35], while continuous precipitates were seen after aging at 160 and 270°C [34] and 182 °C [36]. The precipitates were seen to coarsen after an initial growth phase past 36 hours of aging at 100 °C [37]. β-phase has also been observed to nucleate and grow intragranularly in Al-Mg alloys [9, 38] While this site does not present a problem in terms of IGC and SCC, there is an idea that they could beneficially "scavenge" Mg before it reaches grain boundaries.

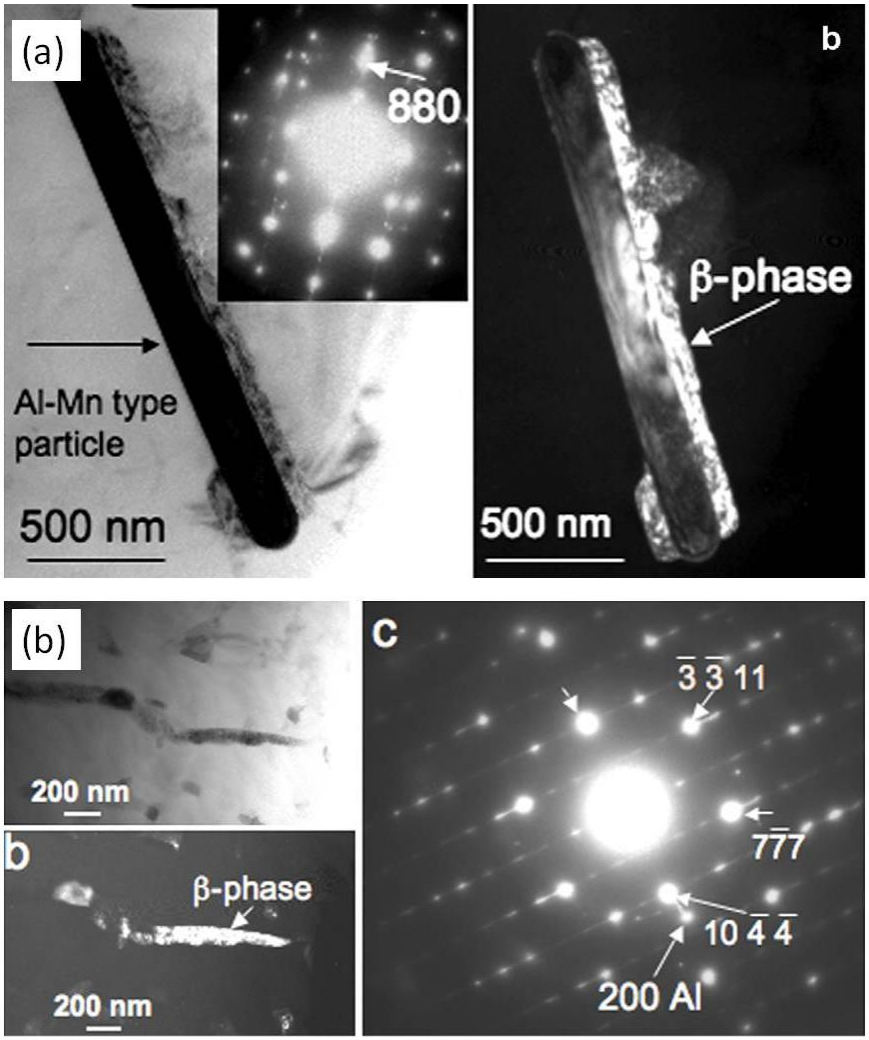

Figure 5 (a) TEM image of β-phase precipitate on an Al-Mn type particle. (b) TEM image of β-phase precipitate on a grain boundary [32].

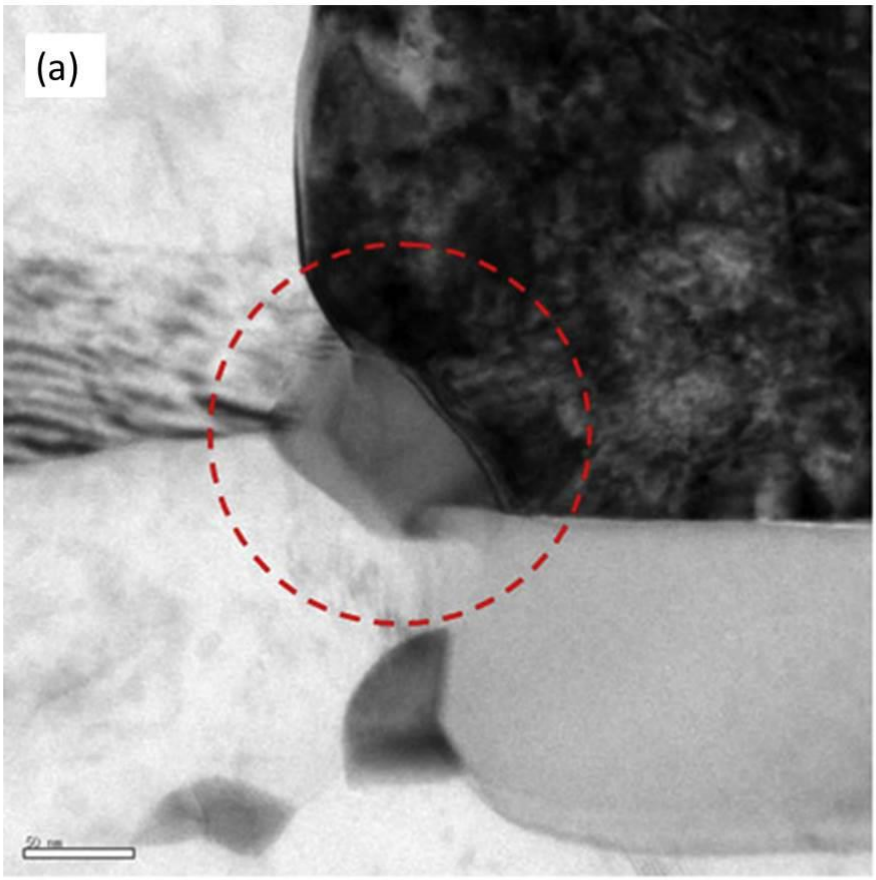

(b)

Element	Peak Area	Area Sigma	k factor	Abs Corrn.	Weight%	Weight% Sigma	Atomic%
Mg K	142	43	1.091	1.000	42.29	8.28	44.85
Al K	202	31	1.047	1.000	57.71	8.28	55.15
Totals					100.00		

Figure 6 (a) TEM image of β-phase precipitate at a grain boundary triple point, formed after sensitisation at 175 °C for 240 hours. (b) Table showing results of EDS analysis to show particle under consideration is Al_3Mg_2 [33].

2.2.3. Stabilisation

Stabilisation involves the precipitation of Mg out of solid solution to form coarse, randomly distributed Al_3Mg_2 precipitates. The aim is to reduce the total amount of Mg held in solid solution. This is thought to restrict the degree of sensitisation and precipitation possible at grain boundaries.

In the commercial production of stabilised alloys, two methods may be used; (i) the alloy can be heated up to 250°C for 4 hours or (ii) the alloy undergoes a controlled cooling of 5°C/minute following casting. IGC resistance comes about when there is a general precipitation of β-phase onto numerous lattice dislocations, as opposed to being on grain boundaries or in solid solution. The H3xx designation of H321 treated alloys indicates that it has undergone a formal stabilisation treatment and strain hardening to ¼ hardness.

2.2.3.1. Sensitisation to Stabilisation

A stabilising heat treatment is used in a wide variety of alloys in order to reduce their susceptibility to intergranular and stress corrosion by a favourable redistribution of solute atoms and precipitates. Work has been carried out recently to understand the transition between sensitisation and stabilisation that takes place when AA5083 is exposed to different temperatures over a range of times [39]. When the alloy is treated at temperatures between 100 and 200 °C for 10 to 100 hours, all of the samples show characteristics under phosphoric acid etching, the amount of charge passed during potentiostatic polarisation experiments and NAMLT values that are consistent with being in a sensitised condition, and susceptible to IGC. When the treatment temperature was increased to 250 °C for 10 and 100 hours, the

material showed a resistance to IGC, believed to be because β-phase had precipitated throughout the grains as coarse precipitates, rather than just on the grain boundaries.

The work by Winsley was noted to be consistent with much earlier work by both Sprowls and Brown, 1969 [9] and Dix et al., 1959 [40] who exposed a range of Al-Mg alloys with over 3.5 wt. % Mg to 205°C for 12 months. These samples were seen to be immune to intergranular corrosion, believed to be due to precipitates forming within the grain interiors and on grain boundaries as coarse non-continuous precipitates. Dix et al. also noted that when the same alloy was heated at temperatures between 37 and 150 °C all samples became susceptible to IGC.

Recent work has been undertaken to demonstrate how a stabilisation treatment can reverse the sensitisation that can occur in 5xxx alloys. Samples of AA5456 were sensitised for 24 hours at 150 °C then subjected to a range of stabilisation treatments between 75 and 340 °C for 10 and 30 minutes using a heating panel [41]. This study found that stabilisation temperatures of 240 – 280 °C applied for as little as 10 minutes were suitable for reversing the sensitisation without affecting the mechanical properties, Figure 7. This temperature range shows good agreement with the work by Winsley [39]. One limitation was that when exposed to the same sensitisation treatment as that applied in the beginning, the corrosion response of the sample was just as bad as the once sensitised state. This shows the technique to be useful as a reconditioning tool by giving the alloy another stabilisation treatment.

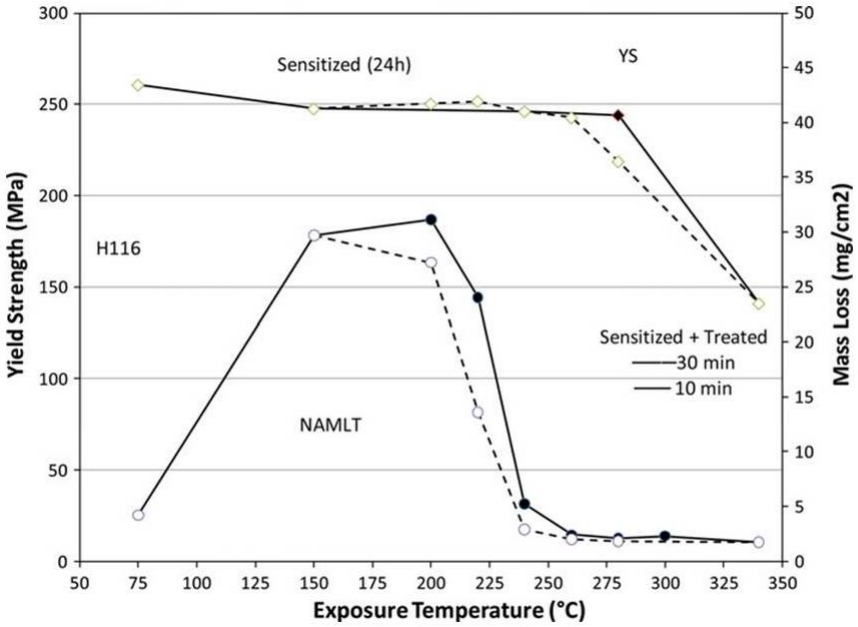

Figure 7 Yield strength and NAMLT results *vs*. exposure temperature in AA5456 [41].

2.3. Corrosion of Al-Mg Alloys

2.3.1. Corrosion of Aluminium in Aqueous environments

While pure aluminium is susceptible to corrosion in both acidic and alkaline aqueous environments, a passive oxide film easily forms, in so doing giving it excellent corrosion resistance.

When it is not protected by this oxide layer, it becomes highly soluble in extremes of pH and undergoes dissolution through the following anodic reactions:

Dissolution: $Al_{(s)} \rightarrow Al^{3+}_{(aq)} + 3e^-$

Hydrolysis: $Al^{3+}_{(aq)} + H_2O_{(l)} \rightarrow AlOH^{2+}_{(aq)} + H^+_{(aq)}$

Alkaline dissolution: $Al_{(s)} + 4OH^-_{(aq)} \rightarrow Al(OH)_4^-{}_{(aq)} + 3e^-$

The electrons generated during the anodic reactions are then consumed on the surface by the cathodic reduction of oxygen :

In acid environments: $O_{2(g)} + 4H^+_{(g)} + 4e^- \rightarrow H_2O_{(aq)}$

In neutral environments: $O_{2(g)} + 2H_2O_{(l)} + 4e^- \rightarrow 4OH^-_{(aq)}$

Or the generation of hydrogen gas:

In acid environments: $2H^+_{(g)} + 2e^- \rightarrow H_{2(g)}$

In neutral environments: $2H_2O_{(l)} + 2e^- \rightarrow 2OH^-_{(aq)} + H_{2(g)}$

As mentioned before, aluminium is easily oxidised so forms a thin, compact, and adherent oxide film on the surface that limits further corrosion by the following reaction:

Passivation: $2Al_{(s)} + 3H_2O_{(l)} \rightarrow Al_2O_{3(s)} + 6H^+_{(aq)} + 6e^-$

The passive film formed in air at ambient temperatures is approximately 5 nm thick. If formed at elevated temperatures or in the presence of water or water vapour, it will be thicker [1]. If the film becomes damaged, then it can re-form rapidly in most cases, and where it cannot do so corrosion can and will take place.

The oxide layer is able to limit corrosion as it is a good insulator [42] which acts to prevent electrons formed during oxidation from reaching the solution in which the corrosion is taking place. Since this is the site of the cathodic reduction of both oxygen and water, limiting the electron availability here and so the rate of these cathodic reactions will in turn slow the rate of oxidation in the anodic region.

The oxide layer is stable over the relatively neutral pH range 4-9, however it becomes soluble in both acidic and alkaline environments (amphoteric). The regions of passivity, immunity and corrosion are shown most clearly in the Pourbaix diagram for aluminium, Figure 8, which describes the thermodynamic stability of the oxide film in terms of potential and pH. The reactions which take place for the breakdown of the passive film in acidic and alkaline environments are as follows:

In acidic environments: $Al_2O_{3(s)} + 6H^+_{(aq)} \rightarrow 2Al^{3+}_{(aq)} + 3H_2O_{(l)}$

In alkaline environments: $Al_2O_{3(s)} + 2OH^-_{(aq)} \rightarrow AlO_2^-{}_{(aq)} + H_{2(g)}$

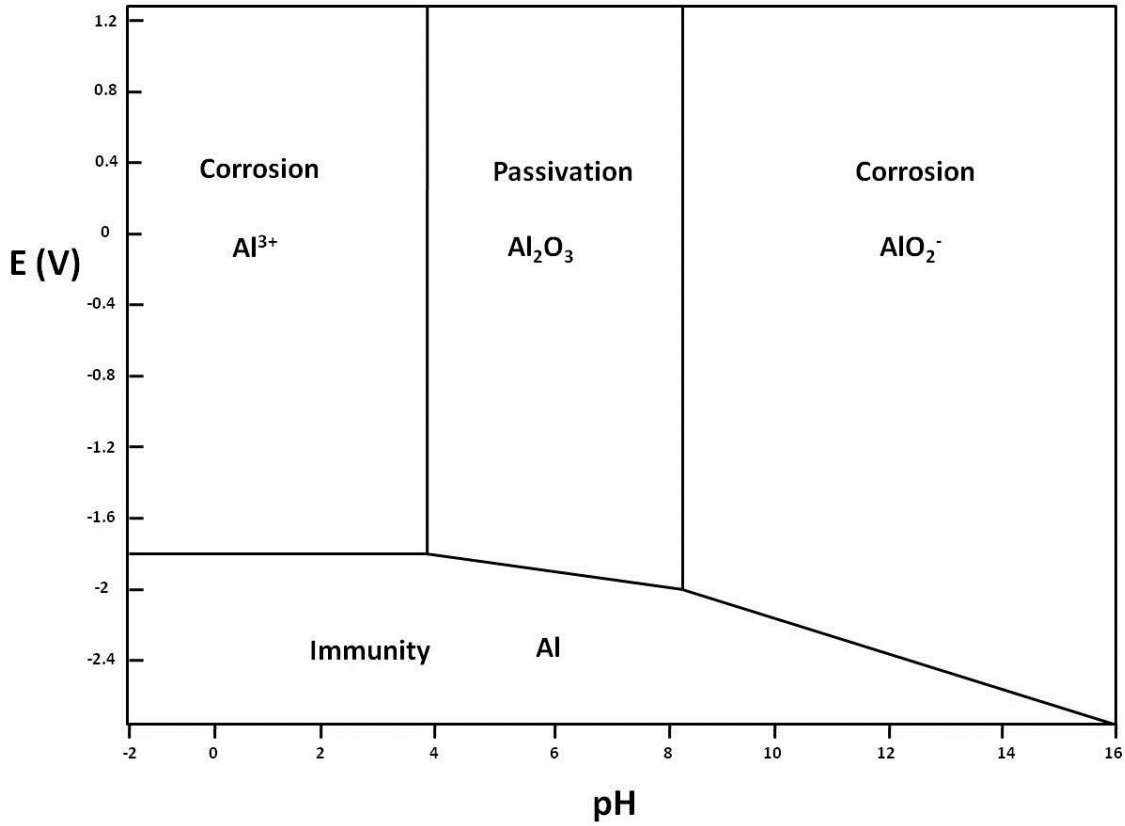

Figure 8 Pourbaix diagram for aluminium. After Pourbaix[42]

The oxide film is not homogeneous and contains regions where it is not as thick. Breakdown of the film at these points can lead to localised corrosion. With increasing alloy content and on heat-treatable alloys, the oxide film becomes more non-homogeneous.

The addition of alloying elements is necessary to produce an alloy with physical properties which exceed those offered by pure aluminium. This practice can in turn alter the resistance to corrosion that the alloy possesses, either enhancing its corrosion resistance or making it worse. Elements such as copper and manganese act to increase the corrosion potential of aluminium, while the addition of magnesium and zinc will reduce it. Figure 9 shows a graph by Hollingsworth and Hunsicker which demonstrates this variation.

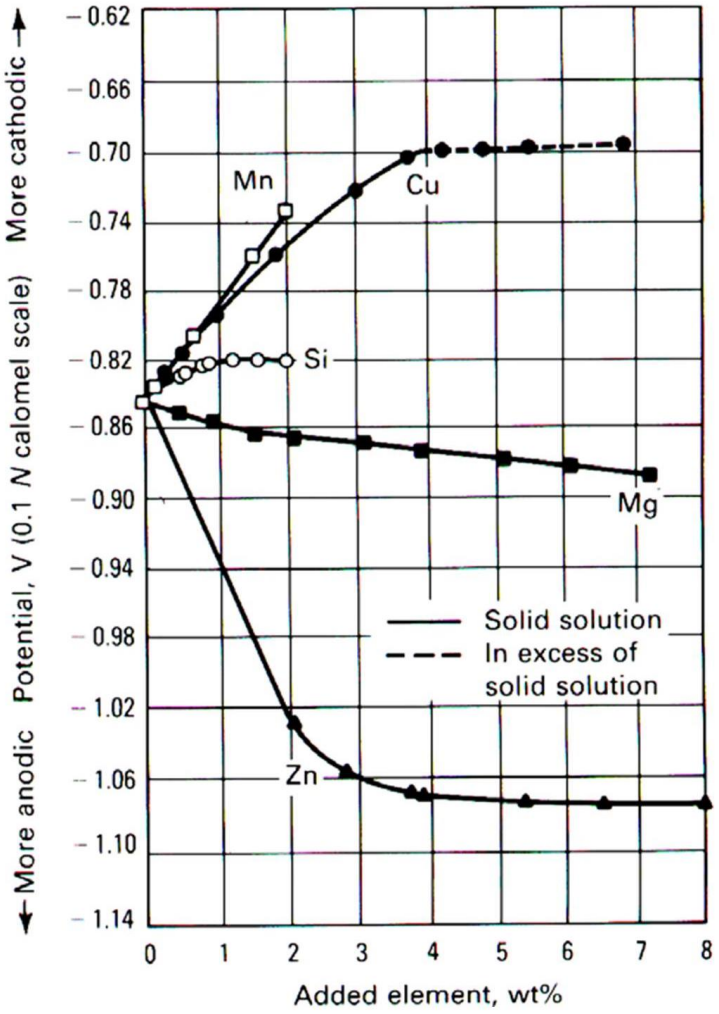

Figure 9 Graph showing the effect of additional alloying elements on the electrolyte-solution potential of aluminium. Potentials shown are for high purity binary alloys in a 1 M NaCl solution with 3 g/L H_2O_2 at 25 °C [43]

The solubility of these alloying metals in aluminium at equilibrium is very low, leading to the formation of secondary phases which can form as intermetallic particles. Given the electrochemical basis of the corrosion that takes place in most situations, the corrosion-potential relationship between the microstructural constituents (intermetallics and alloy matrix) will affect the corrosion behaviour seen in different alloys. The composition and distribution of the phases and solid solutions are the contributing factors in the type and severity of corrosion that will occur. It has been proposed that since the aluminium-rich solid

solution occupies the majority of the exposed area fraction, it is the composition of this which should determine the corrosion potential of the alloy [44].

These intermetallic particles are sites of particular concern for highly localised attack as they possess a thinner and more conductive oxide layer then the aluminium matrix, which acts to conduct electrons at a greater rate [45]. The manner in which these particles corrode is discussed later; however the different corrosion characteristics of each can be seen at a glance in a table generated by Birbilis and Buchheit, who measured the pitting and corrosion potential of many intermetallics common to aluminium, Table 1.

Table 1 Pitting potentials for intermetallic compounds common in aluminium alloys. results are average values incorporating the results of numerous tests [46].

		Pitting potential (mV_{SCE})		
Stoichiometry	Phase	0.01 M	0.1 M	0.6 M
Al_3Fe	β	442	106	−382
Al_2Cu	θ	−434	−544	−652
Al_3Zr	β	−223	−275	−346
Al_6Mn	-	−485	−755	−778
Al_3Ti	β	−232	−225	−646
$Al_{32}Zn_{49}$	T′	-	-	-
Mg_2Al_3	β	−818	−846	−959
$MgZn_2$	M, η	-	-	-
Mg_2Si	β	-	-	-
Al_7Cu_2Fe	-	−447	−448	−580
Mg (AlCu)	-	224	−2	-
Al_2CuMg	S	108	80	135
$Al_{20}Cu_2Mn_3$	-	−210	−428	−534
$Al_{12}Mn_3Si$	-	−563	−621	−712
Al (99.9999)	-	−545	−610	−696

2.3.2. Pitting corrosion of Al-Mg alloys

Pitting is a form of corrosive attack which occurs in a highly localised area. The process of pitting has been broken down into two stages; pit initiation and pit propagation.

Pits have been seen to initiate at many sites on the surface, including inclusions, second phase particles, solute segregated grain boundaries, flaws, mechanical damage and dislocations [47]. The presence of intermetallic particles within the alloy produce regions where the passive oxide film, which would otherwise protect the aluminium, is much thinner than that over the Al matrix.

The structural characteristics of the oxide also depend on electrolyte composition, potential and temperature. This thinner oxide layer can be breached and caused to fail by chloride ions in the environment, with three main mechanisms put forward to explain this failure; penetration of the Cl^- ions, adsorption of the ions, or the film breaking, shown diagrammatically in Figure 10. Reboul et al. summarised the next stages of pitting as oxygen reduction taking place in the cathodic area, and a breakdown of the oxide layer leading to oxidation of the bare aluminium [48].

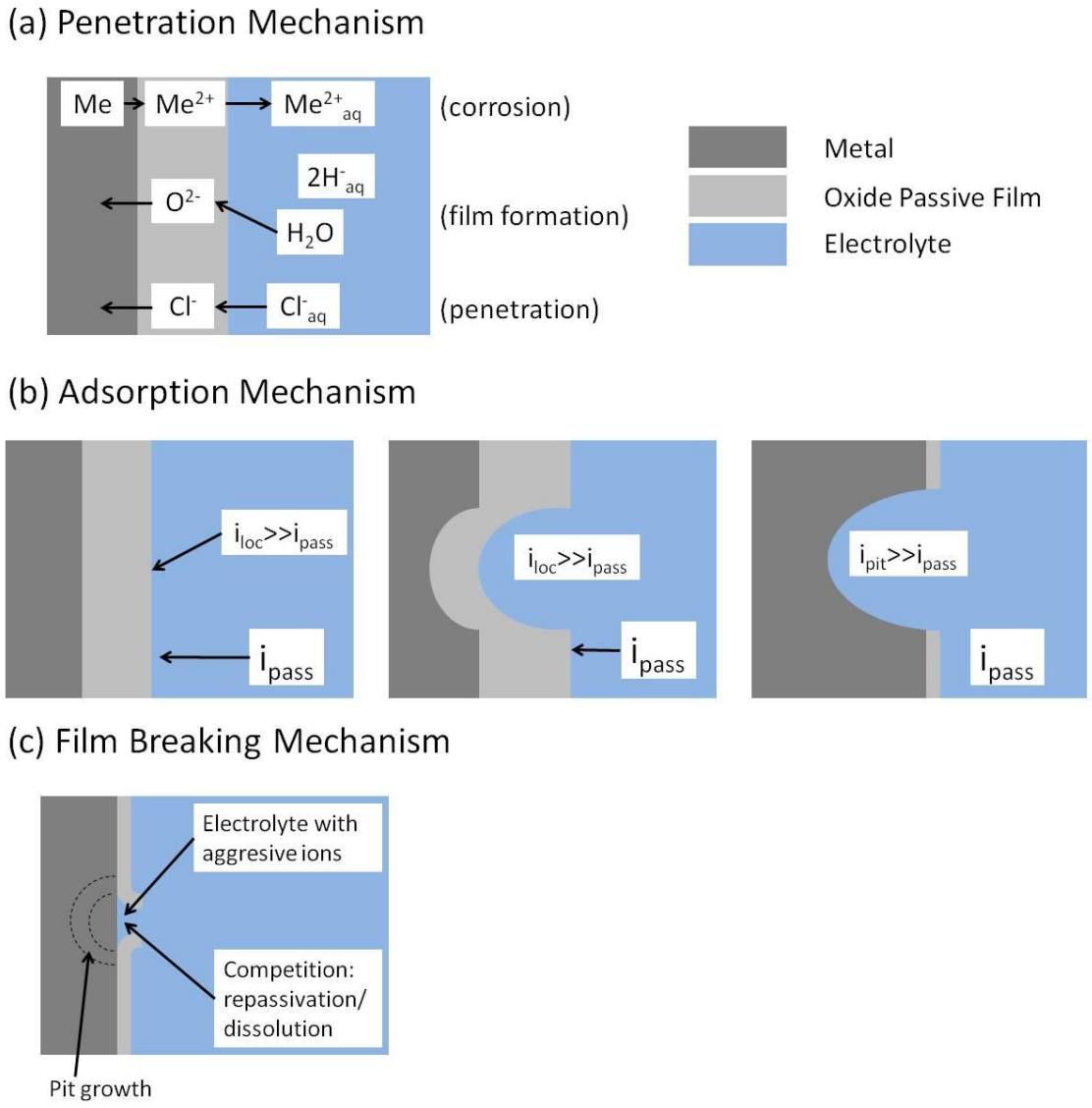

Figure 10 Schematic diagrams representing pit initiation by (a) penetration, (b) absorption and thinning, (c) film breaking. After [49].

Once this pitting has started, it has been shown to be autocatalytic in nature, where once a pit starts to grow, the conditions developed are such that further pit growth is promoted. Dissolution of Al followed by hydrolysis leads to the production of protons which act to locally lower the pH and maintain or increase the rate of dissolution. The acidity in the pitting region has been measured as low as pH 1-3 [50, 51]. More of the aggressive Cl^- ions are drawn into the pit by the protons, to further propagate the growth of the pit [52].

Measurements of pH have also been taken at AlFe intermetallic particles, where they were found to generate alkaline solutions due to the cathodic reactions taking place here [53]. These reactions produce hydroxide ions which dissolve aluminium, leading to ‘trenches’ of locally dissolved material around the intermetallic [54].

Pitting occurrence in AA5083 with respect to the intermetallic particles has been studied in great detail through the use of atomic force microscopy and scanning Kelvin probe force microscopy [55]. One family of intermetallics observed were iron-rich and noted to have a potential higher with respect to the matrix. They acted as cathodes and led to localised anodic polarisation due to a microgalvanic effect. An alkalinity has been observed around the particle due to the cathodic reduction taking place, which led to trenching of the surrounding alloy matrix. This observation has been seen in iron rich intermetallics in other alloys [56-61], Figure 11. Further attack led to a de-alloying of the particle. One interesting observation has been that the cathodic efficiency of the Fe-based intermetallics increases as the pH increases, meaning cathodic reduction reactions will drive up the efficiency of future reactions [61]. It was noted however that active growth of one pit prevented the initiation of nearby sites, until the first had become passivated.

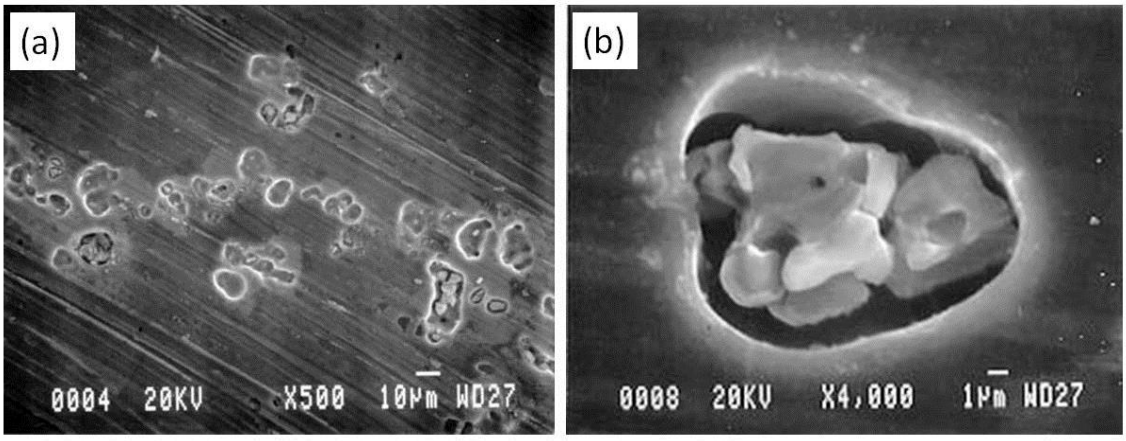

Figure 11 (a) and (b) SEM micrographs of an Fe-based particle and the corrosion grooving around it after immersion in a 3.5 % NaCl solution for 10 days [59].

The second family of intermetallic particles was identified as Mg_2Si, and had a potential lower relative to that of the matrix [55]. The particle is anodic to the matrix, and is corroded by selective leaching of Mg out of the particle, which has been observed to occur after several seconds in a corrosive solution [62]. Dissolution events follow, an observation also seen by Mizuno et al. [57], which is accompanied by a local increase in pH. Following the dissolution and de-alloying, hydroxide deposits formed at the base of the pit and acted to stop the propagation of the pit, while any attached remnants have been shown to become cathodic to the matrix [62].

2.3.3. IGC of Al-Mg alloys

Intergranular Corrosion (IGC) is a form of localised attack that selectively takes place at grain boundaries. In the presence of stresses in the material, IGC can develop into Stress Corrosion Cracking (SCC), which involves crack propagation by a mechanical stress as well as a corrosive environment. It is also referred to as intercrystalline corrosion because there is the selective corrosion of grain boundaries, while the grains or crystals themselves suffer little attack.

In general, IGC comes about when the grain boundaries are more anodically reactive than the grain interiors. This is usually because the composition of phases found on the grain boundary is different to that of the matrix, forming a localised galvanic couple. The bulk matrix between the grain boundaries is more cathodic and therefore is not affected. A slight variation exists in Al-Cu alloys, where Al_2Cu precipitates on the grain boundaries act cathodically to a Cu-depleted region just outside of it, which itself undergoes anodic dissolution [63]. In the case of 5xxx series alloys, the highly reactive grain boundary β-phase (Al_3Mg_2) acts anodically to the Al-Mg matrix when it is precipitated onto grain boundaries. This model was demonstrated in a simulated β and Al-matrix model by Ren, where bulk precipitates were melted and cast according to their chemical proportion, then mounted in an epoxy resin with an electrical connection [64]. As discussed already, the dissolution and subsequent precipitation of β-phase onto grain boundaries comes about through exposure to elevated temperatures for extended periods of time (sensitisation). However it is only once on the grain boundary that its anodic character becomes an influence.

2.3.3.1. Propagation of IGC

IGC propagates through a material by attacking the reactive grain boundary phase in preference to the matrix. Once the attack has initiated on the susceptible boundary at the surface, subsurface dissolution events take place, which become governed by the electrolyte composition and the material that is present. As penetration moves deeper into the material, the pH of the electrolyte within the crevice has been observed to drop [61], while a continuous path of β-phase is expected to give a higher penetration rate.

Many studies have looked into IGC of Al-Mg alloys and have concluded that the reactive β-phase is central in causing susceptibility to IGC and subsequently SCC in the 5xxx series [8, 14, 65-76]. What is not known however is the exact mechanism of IGC propagation along grain boundaries where the β-phase does not form a continuous path. One hypothesis is that the corrosion product built up at the leading edge of the fissure causes a ′wedging stress′ which extends the fissure by stress-assisted corrosion processes [77]. Another method may result from a change in the alloy chemistry close to the grain boundary through sensitisation and precipitation, leading to a change in the local corrosion properties. This has been reported for high Mg binary Al alloys [78], however no Mg depleted regions have been seen in the 5083 alloy [32]. The final hypothesis involves the dissolution of the precipitate changing the local chemistry at the fissure tip [39]. The β-phase dissolution would occur as the following reaction:

$$\mathbf{Al_3Mg_2 \rightarrow 3Al^{3+} + 2Mg^{2+} + 13e^-}$$

The metallic ions that are released into solution increase until a critical concentration is reached, at which point reduced water activity can impair repassivation and facilitate the propagation of the corrosion. Whichever hypothesis is closest to the true explanation, the

spreading has been confirmed recently to spread along a β-phase precipitate chain [79], Figure 12.

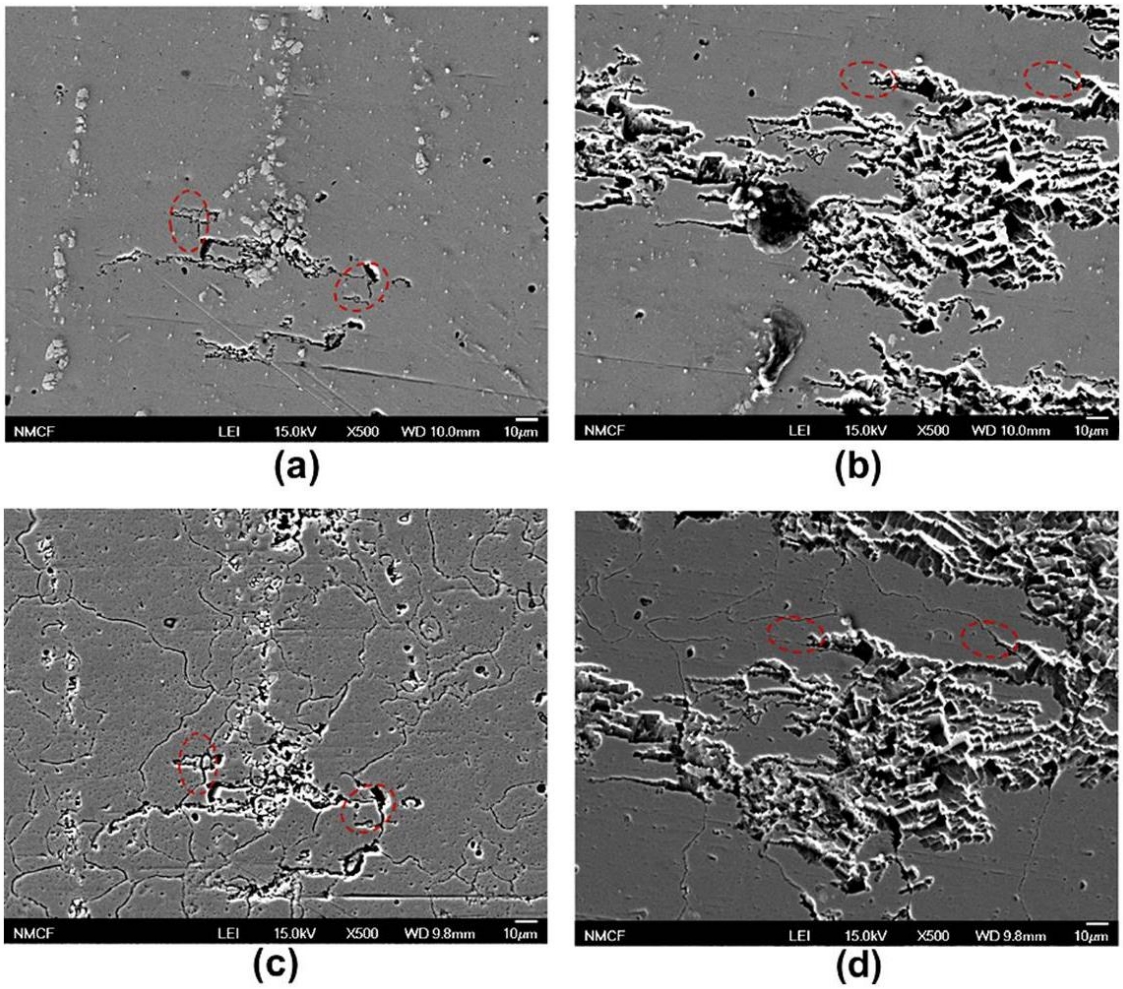

Figure 12 (a) and (b) SEM images of sensitised AA5083 (100 °C for 30 days) after 1 hr potentiostatic hold at -0.73 V_{SCE}. (c) and (d) SEM images of same area after etching in phosphoric acid to indicate remaining grain boundaries containing β-phase [79].

2.3.3.2. Characterisation of IGC

Very early work to characterise the sensitisation process and corrosion performance related to alloy composition found the open-circuit potential (OCP) of bulk β-phase to be very active (-1.15 V_{SCE}) [40]. Searles, Gouma and Buchheit [73] went further to establish that the

breakdown potential of β-phase was -0.94 V_{SCE}, which they observed to be considerably more negative than the pitting potential or OCP of AA5083.

As part of work on a generalised theory of stress corrosion of alloys, Mears et al.[80] demonstrated the importance of β-phase dissolution in the IGC of Al-Mg alloys. In a 1M NaCl + H_2O_2 solution, β-phase had a breakdown potential 0.2 V below that of the matrix, subsequently causing the rapid failure of a sensitised Al-10 % Mg sample by SCC when stressed. The conclusion of this body of work is that β-phase particles corrode preferentially to the matrix, which is in turn cathodically protected by the β-phase [68].

Several studies have investigated IGC susceptibility and its dependence on sensitisation parameters [71, 81, 82]. All came to the conclusion that susceptibility depends on sensitisation time and temperature. Davenport et al. saw Nitric Acid Mass-Loss Test (NAMLT) values in AA5182 increase with increasing ageing temperature and time Susceptibility became problematic at temperatures of 150 °C, and worsened with increasing exposure time. Similar results were observed in a separate study of AA5083 [82], where the material became sensitised after 20 hours at 150 °C. The same study showed that a higher Mg alloy (AA5456) showed a much higher corrosion rate through NAMLT values after exposure to comparable conditions. They concluded that the higher Mg concentration was the critical factor, and linked this to an increased β-phase occurrence, which showed up under a phosphoric acid etch.

Sensitisation of AA5083 between 125 and 325 °C has shown how the variation of temperatures can affect corrosion behaviour based on where the β-phase precipitates [83], Figure 13. Low temperature treatment led to β-phase precipitating onto grain boundaries and

showing low breakdown potentials, however higher heat treatments (275 °C and above) precipitated β-phase both on the grain boundaries and within the grain.

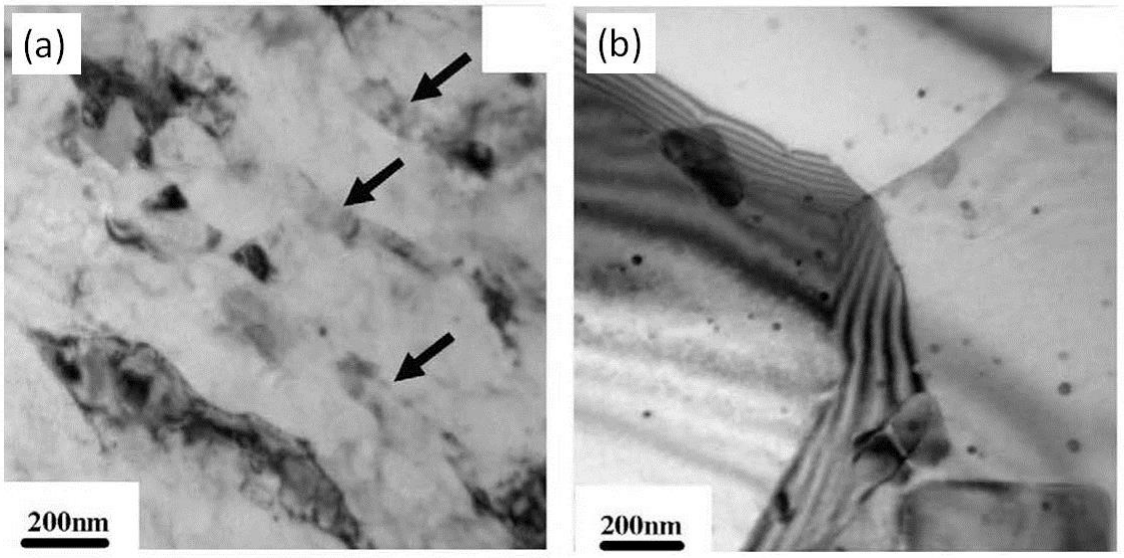

Figure 13 TEM images showing AA5083 following sensitisation for 2 hours at (a) 175 °C, with arrows indicating β-phase on grain boundaries, (b) 275 °C, where much less β-phase has precipitated [83].

The amount of β-phase that precipitates onto any given grain boundary has been found to be related to the misorientation of the grain boundary. Work by Yuan on AA5182 found boundaries that had a misorientation angle <20° were free from β-phase precipitates, while those with boundary angles >25° generally displayed either continuous or discontinuous precipitates, and on occasion no decoration [18]. The misorientation angle of the boundaries and the amount of β-phase which they contained showed very good agreement with corrosion tests that showed low angle boundaries to be resistant to IGC.

2.3.4. IGSCC of Al-Mg alloys

Stress corrosion cracking comes about by the action of an active environment combining with a mechanical tensile stress to open up a crack which can cause failure of a component. Normally such a crack or failure would not occur under one of these conditions on their own, however the combination leads to crack initiation and growth happening at a stress well below the expected yield stress. SCC has been described as delayed failure process, where the crack may initiate then propagate at very slow rates, until stresses in the remaining material exceed the fracture strength [84].

Three conditions have been identified that need to be fulfilled in order for stress corrosion cracking to occur; the alloy must have a microstructure that is susceptible to SCC, the environment must be damaging (e.g. NaCl solution) and the intensity of the stress must be sufficient [85, 86]. SCC in aluminium alloys primarily acts intergranularly, in the same manner as the β-phase or Mg-depleted region here acts as an anode in the system. A crack or crevice formed by IGC forms a stress concentrating region which can be sufficient to initiate SCC from.

2.3.4.1. Observations of β-phase / Heat treatment temperature and time on SCC behaviour

A great deal of work has been carried out to date involved with understanding the relationship between the precipitation of β-phase and stress corrosion cracking in Al-Mg alloys [9, 14, 27, 66, 68, 73, 81, 86-92]. The trend of all results shows greater degrees of grain boundary precipitation to exhibit worse SCC behaviour (accelerated SCC growth).

Searles [73] conducted constant extension rate tests (CERT) on AA5083, where a degradation in ductility was seen as higher heat treatments were applied. The heat treatments precipitated increasing amounts of β-phase onto grain boundaries, up to the point at which a continuous grain boundary film had formed and the worst deterioration had occurred, shown in Figure 14. The ductility was observed to have recovered after a further thermal exposure as the continuous precipitate film had disintegrated. Similarly, exposure to temperatures above 180°C were also seen to eliminate the corrosion susceptibility due to coarsening of the precipitates and the continuous grain boundary pattern in tests by Summerson and Sprowls [93]. Jones observed that as the crack advanced onto β-phase particles, they were converted into Al_2O_3 particles, which the crack either traversed or moved around [94], visualised in Figure 15.

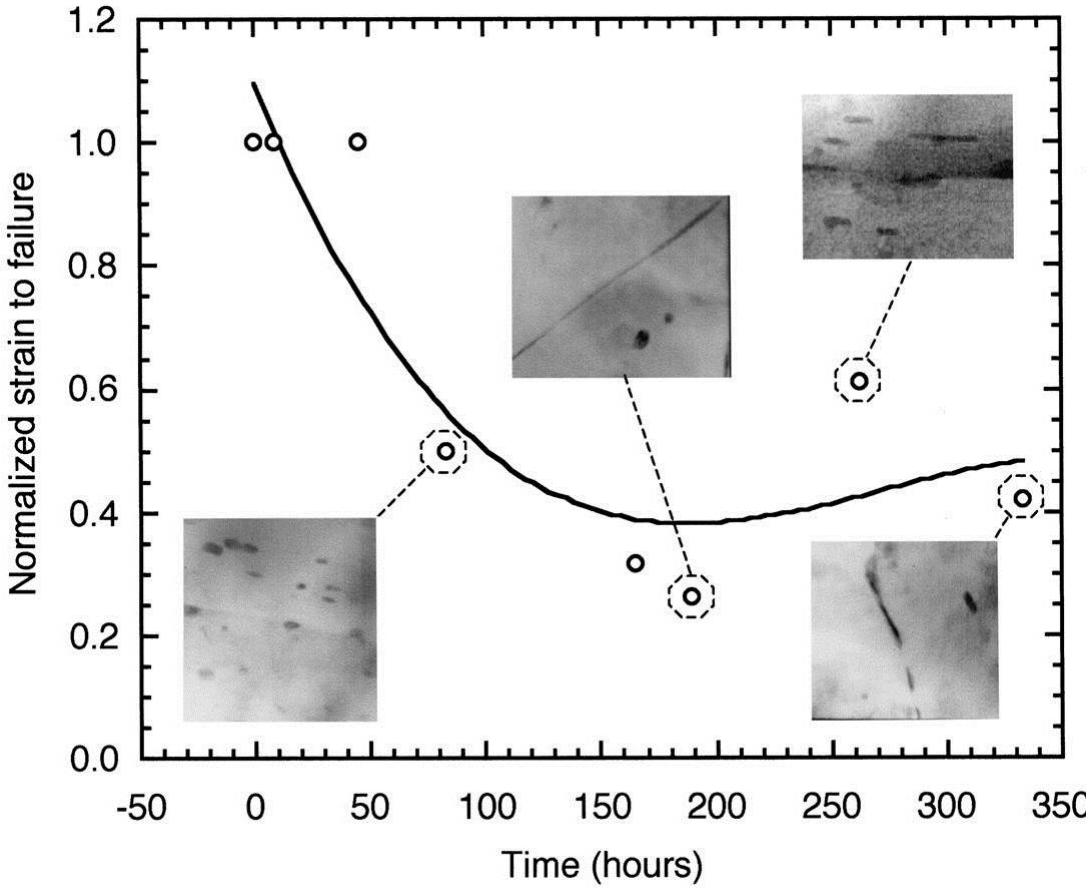

Figure 14 Normalised strain to failure vs. sensitisation time for an AA5083 sensitised at 150 °C then subjected to constant extension rate testing. Inserts are TEM micrographs showing the degree of β-phase precipitation at various stages of heat treatment [73].

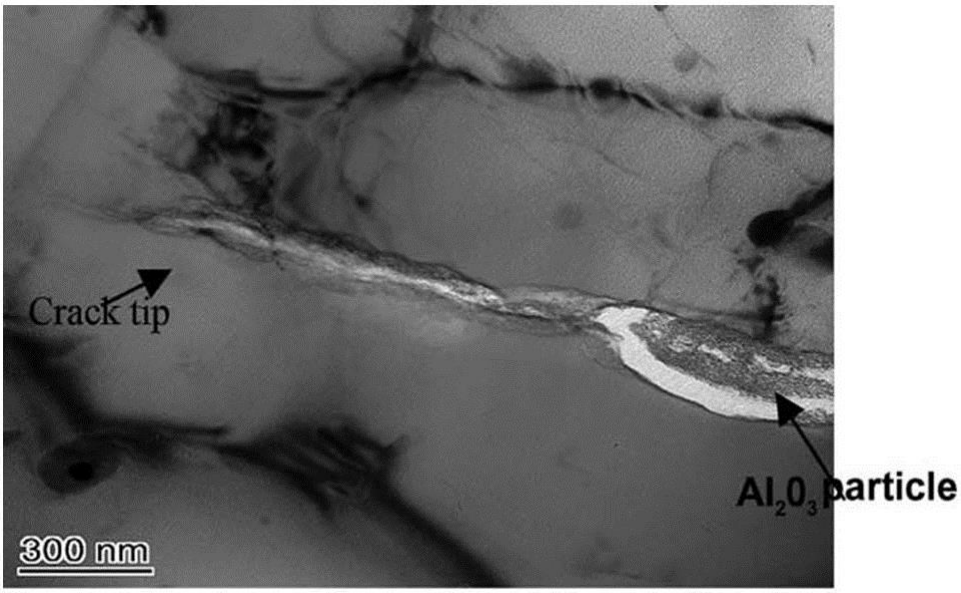

Figure 15 Intergranular oxide particles along intergranular crack [94].

2.3.4.2. Hydrogen induced cracking

Scamans and Rehal made an early observation in the corrosion of Al-Mg alloys that bubbles formed on the grain boundaries and dislocations after exposure to water vapour, inferring the existence of hydrogen from the reaction between alumina and H_2O [95]:

$$Al_2O_3 + 3\ H_2O = 2\ Al(OH)_3$$

An initial understanding of the dominant role that hydrogen embrittlement has in the SCC of AA5083 was brought about by Pickens et al. [72]. Arsenic was added to a NaCl solution to ensure that any atomic hydrogen did not combine into H_2, the result of which was a halving in the time to failure of stressed specimens. Since hydrogen gas was not evolving, more atomic hydrogen was available to diffuse into the metal. Gruhl also noted that hydrogen embrittlement of the seams of β-phase was causative to SCC in the 5xxx series [96]. The dissolution of H into an Al-8% Mg alloy was observed by Ohnishi and Higashi [97] who then

saw a decrease in mean dimple size on the fracture surface, which was believed to be caused by hydrogen nucleating microvoids.

2.3.5. Atmospheric corrosion

Atmospheric corrosion differs from immersed corrosion in that there is a limited electrolyte volume, either by the presence of a droplet or a thin film of solution. Atmospheric corrosion is strongly influenced by temperature, relative humidity and chloride concentration [98]. Temperature can vary on daily or seasonal cycles, while relative humidity can vary based on similar time frames or geographic locations, with warm marine environments and arid deserts providing contrasting locations. Chloride concentration is a simplified example of many environmental pollutants which can impact of corrosion behaviour when part of a solution in contact with the component in question.

Two approaches towards assessing atmospheric corrosion have been commonly reported in literature. In-situ experiments which often compare the effect of varying environmental conditions are useful in noticing trends in corrosion behaviour on a macro scale. Conversely, micro scale droplet studies are able to probe into the dynamics and kinetics of corrosion beneath the solution surface and identify anodic and cathodic areas in relation to the droplet and the atmosphere outside of it.

2.3.5.1. In-situ testing

The conditions for field tests are completely subjective and are beyond experimental control, so sites are chosen for their varying atmospheric exposure conditions. Having analysed field tested samples, the chloride ion concentration and time which the metal surface spent wetted were observed to be the most significant factors in the corrosive process [99, 100]. This

introduces the concept of time of wetness (ToW) where corrosion processes may only occur in the presence of a solution, as opposed to a dry state. In the studies by Hernandez et al. [99] and Syed [100], both observed the chloride content to have a linear effect on both pit density and pit depth, Figure 16, however this was related to salt spray from the sea which was measured infrequently and only gives a broad indication as to the effect of chloride on corrosion. These results are however backed up by controlled laboratory based experiments where pit density and depth were seen to increase with greater chloride deposition rates [101].

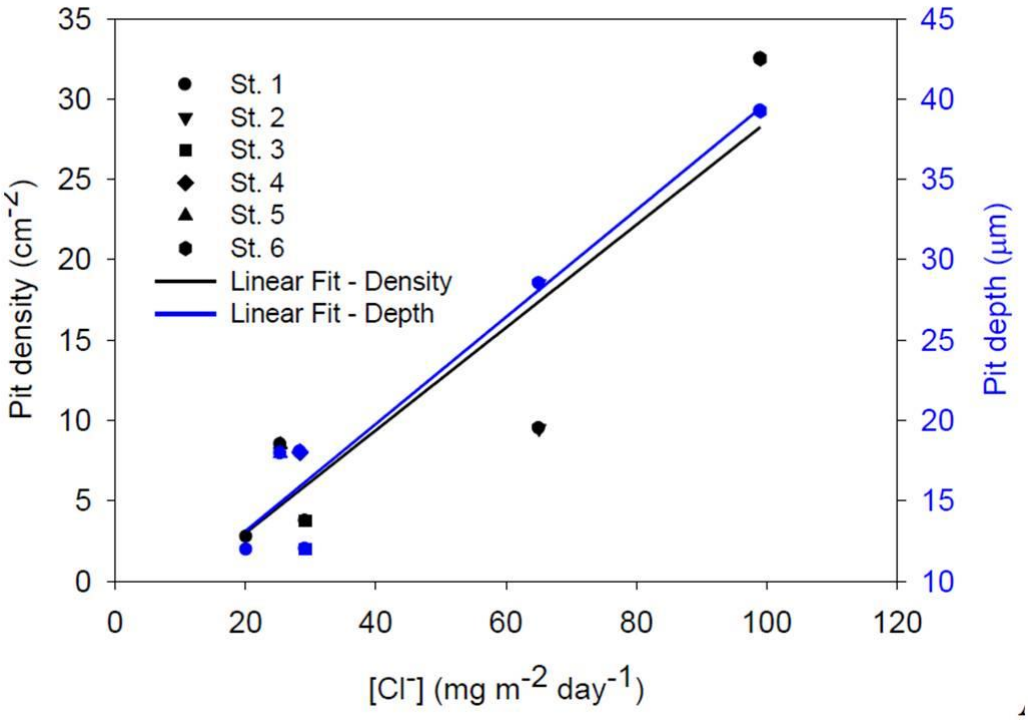

Figure 16 Graph showing the increase in pitting depth and density on a an Al 99.5 % plate with increasing chloride content [99].

2.3.5.2. Lab-based testing

Lab-based droplet tests have provided greater insights into the fundamentals of atmospheric corrosion, allowing single variables to be altered in a controlled manner.

Blucher et al. were able to understand the specific influence of some specific sulphates and chlorides on the corrosion of aluminium [102]. Sodium chloride was found to be the most corrosive salt as sodium ions supported the development of a higher pH in cathodic areas, which resulted in alkaline dissolution of the passive film and rapid general corrosion. Conversely, magnesium ions could not support the high pH values in cathodic areas, a concept linked to the relatively slow rate of corrosion by $MgCl_2$ containing seawater. The combination of chlorides in addition to a solution with a relatively high pH has been shown to produce rapid atmospheric corrosion in aluminium [103].

The use of a scanning Kelvin probe by Chen et al. confirmed the formation of the anodic areas in the centre of droplets, where a potential minimum was measured [104], Figure 17. This is consistent with observation of regions of low pH which formed immediately after testing had started in a droplet study by King et al. on AA2024 [105], Figure 18. The potential maximum seen at the perimeter of droplets has been seen frequently by many authors and has been linked with the cathodic reduction taking place due to the close proximity of oxygen in the atmosphere and the metal surface. This is an example of a differential aeration corrosion cell. The greater cathodic reduction rates occurring through water layers of lesser thickness have also been reported elsewhere [106, 107], Figure 19, the study by Cheng et al. concluding that the oxygen reduction current being inversely proportional to the electrolyte layer thickness, for layers of 100-200µm.

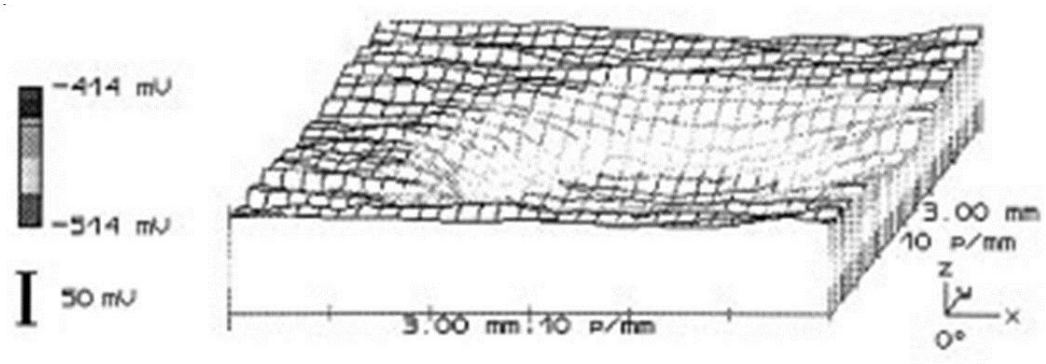

Figure 17 Potential distributions for AA2024 covered by a droplet of 0.5 M NaCl, where a potential minimum exists in the middle [104].

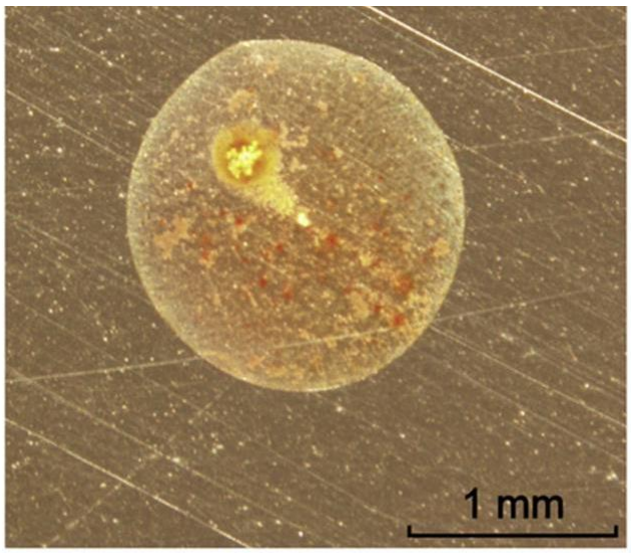

Figure 18 Optical image of a seawater droplet with added pH indicator on a sample of AA2024 after 10 minutes exposure. Acidic regions are signified by the red or orange colours [105].

Li et al. observed an increase in pitting incidence as they increased the Relative Humidity (RH) in their tests from 33 to 75% RH [108], findings in agreement with those mentioned previously and linked to increased oxygen solubility. However, this study noted that as the droplet grows and the oxygen solubility increases, the chloride concentration within that droplet will decrease. This study noted larger and more numerous pits were present at lower chloride concentrations in bigger droplets, a finding consistent with pitting observed in

stainless steels, which showed that smaller and fewer pits were present under smaller droplets [109]. These studies indicate that the solubility of oxygen and therefore the rate of cathodic reactions to be critical in the advancement of corrosion processes.

Critical to the volume of the droplet produced is the chloride deposition density that is introduced to the material surface. For a given chloride deposition density, the height and volume of a droplet will increase with increasing RH. The concentration of the solution will decrease as its water activity increases to match the RH.

2.3.5.3. Micro-droplet formation

An interesting phenomenon observed during droplet experiments is that of micro-droplet formation outside of the main droplet [106, 108, 110]. This was noted by Li et al. following the observation of a filiform like attack under micro-droplets, outside of the main droplet area. They summarised this attack as being initiated by metastable pitting at the edge of the initial droplet, which then attracted and adsorbed water from the environment to equilibrate with the concentrated solution formed by dissolution.

The work of Tsuru et al. established that the edge of the primary droplet was the cathodic area and maintained a high pH by oxygen reduction, as were the micro droplets, indicating the same set of reactions taking place [106]. This was confirmed by Zhang et al. who saw no micro-droplets forming when the oxygen in the atmosphere was replaced with nitrogen, hence stopping the cathodic reduction of oxygen [110]. Tsuru also observed that the micro-droplets contained mainly sodium ions, when an initial solution of NaCl was used. They reasoned that the formation of OH- ions in the micro-droplets attracted Na+ ions, and forced water

absorption to balance the water activity. This result was not seen when using an $MgCl_2$ solution, owing to the production of solid $Mg(OH)_2$ precipitates [102].

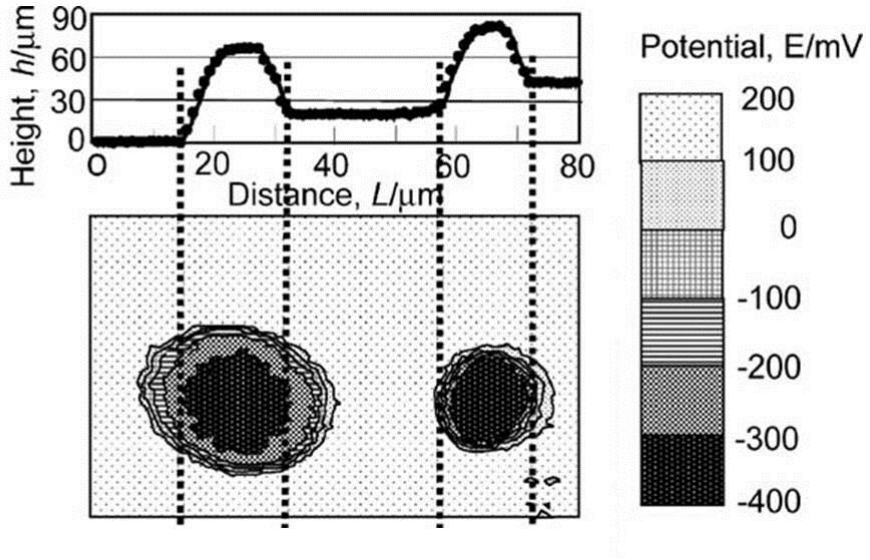

Figure 19 Potential distribution maps and height profiles of 0.5 M NaCl droplet on carbon steel in 80 % RH, where a potential maximum exists around the edges [106].

Zhang concluded that a corrosion current established by the potential difference between the central anodic region and the peripheral cathodic region was the driving force for micro droplet formation, meaning micro-droplets will only form in electropositive areas. Tsuru had previously stated that the anodic area forms early and maintains its size, while the cathodic area expands with time, suggesting water being supplied from the parent droplet and air into the micro-droplet [106].

2.4. Friction Stir Processing of Al-Mg alloys

2.4.1. Friction Stir Welding and Friction Stir Processing

Friction stir welding (FSW) is a relatively new joining process, invented in the early 1990′s at The Welding Institute. It is unique in that it is a solid-state joining technique where the melting of materials is unnecessary. It also offers the advantage of no filler material being used; no extra cover gas is required, while being relatively energy efficient.

FSW relies upon a rotating tool passing along the interface between two plates, which causes local softening and mixing. The tool is non-consumable and entails a pin and shoulder section. The pin is submerged below the top layer of the plates to be joined, and mixes material through the thickness. The shoulder section sits on top of the plates as the weld is made and contributes heat to the softening of the material. Frictional heat is the primary source of heat input to the system, raising the temperature of the material to a point at which it softens, up to 400-500°C [111, 112]. The rotation of the submerged pin section then introduces deformation and moves material from the front of the pins travelling direction and deposits it in its wake. The process leaves an asymmetric weld due to the rotation of the tool piece within the material. The sides of the weld are known as the advancing and retreating sides due to the tool piece either rotating into the material as it advances, or moving material backwards on the other side. The process is represented in Figure 20. The relative volume flow alters with both the advancing and rotation speeds, while the total stir zone is primarily a function of the advancing speed [113].

Rodrigues has demonstrated that high traverse rates can be used to FSW AA5083 while achieving a defect free weld [114].

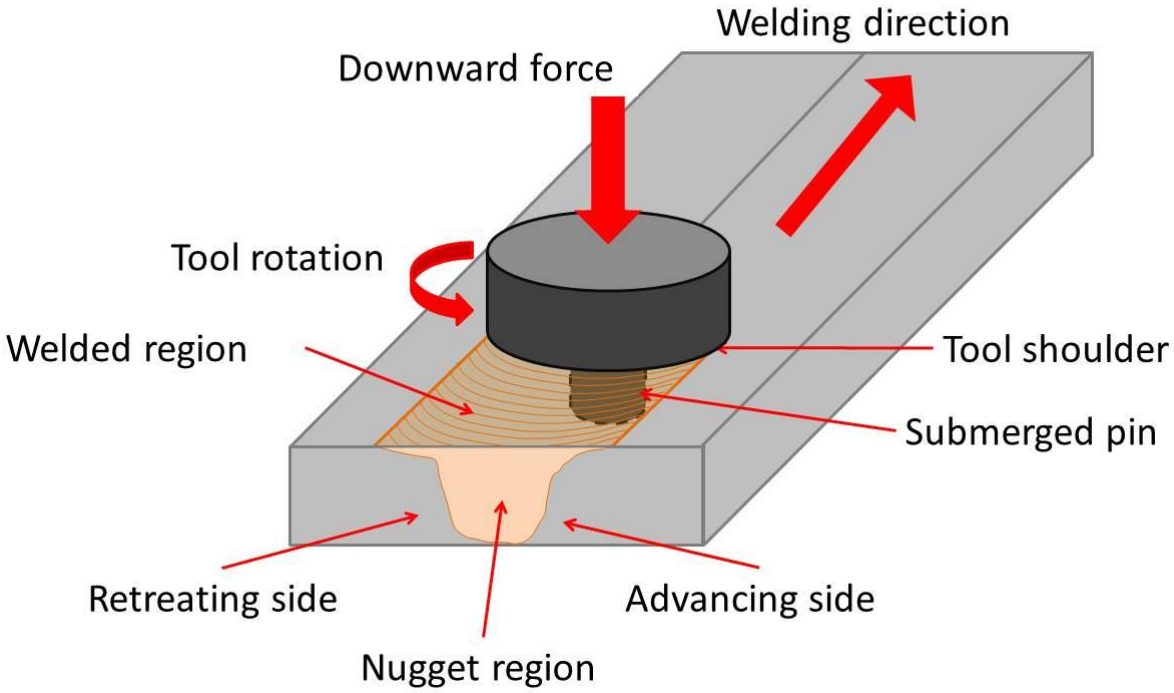

Figure 20 Diagram of the Friction Stir Welding technique

Friction stir welding has seen prominent use in the joining of 2xxx and 7xxx Al-alloys in the aerospace industry as conventional hot welding techniques have led to cracking during joining [111]. This technique also shows promise in the joining of dissimilar metals such as aluminium, magnesium and Steel [115-117].

2.4.1.1. Nugget region

In the nugget region the FSW tool piece mixes and heats the two plates, in order to create a join with a homogenised microstructure. In this region there is intense plastic deformation and frictional heating which results in the formation of a recrystallised fine grained microstructure, also known as the dynamically recrystallised zone [118, 119]. The mechanism

responsible for the dynamic recrystallisation has been described as dislocation glide assisted subgrain rotation [120]. Grain subdivision has also been observed in the weld material just ahead of the FSW tool where there temperatures are not particularly high [121]. This process results in grain sizes between 1-10 µm [112, 119].The shape of the nugget zone is dictated primarily by the shape of the tool pin, but is also influenced by the processing parameters, and the temperature of the workpiece [111]. The wider upper surface is a result of extreme deformation and frictional heat caused by contact with the tool shoulder [33]. The dynamic recrystallisation that takes place in the nugget region results in fine, equiaxed grains [118, 122-128], where the parameters, tool geometry, temperature and vertical pressure influence the size of the recrystallised grains.

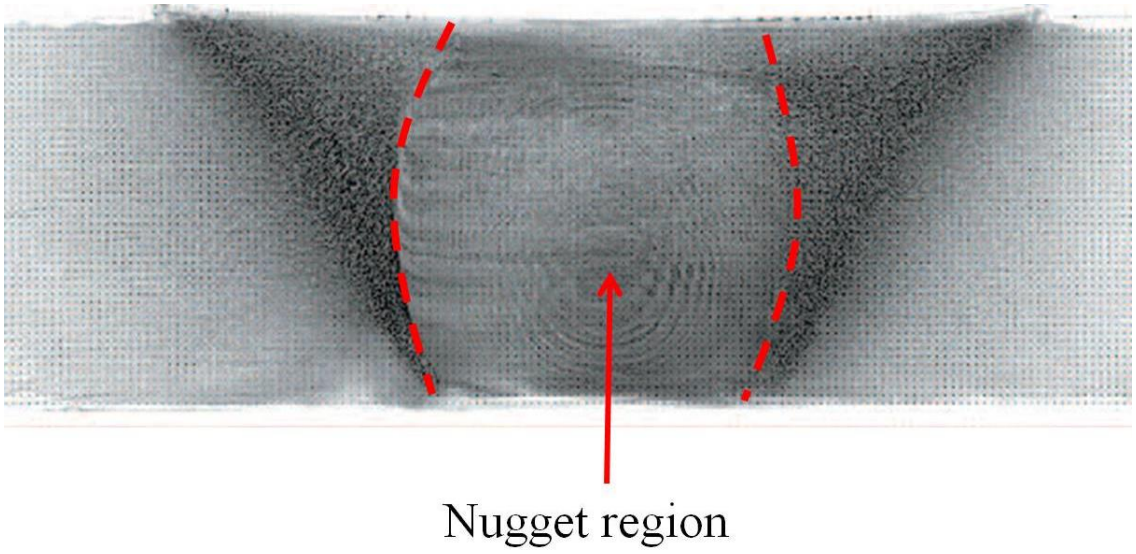

Figure 21 Cross section of a Friction Stir Weld of AA2519 after etching with Kellers reagent to highlight the central nugget region [129].

2.4.1.2. TMAZ

Between the weld nugget and the parent material lies a transition region called the thermo-mechanically affected zone (TMAZ), The TMAZ is subjected to both heating and

deformation, however it does not undergo recrystallisation as there is insufficient deformation strain. It has however been seen that the TMAZ usually contains many sub-boundaries [130].

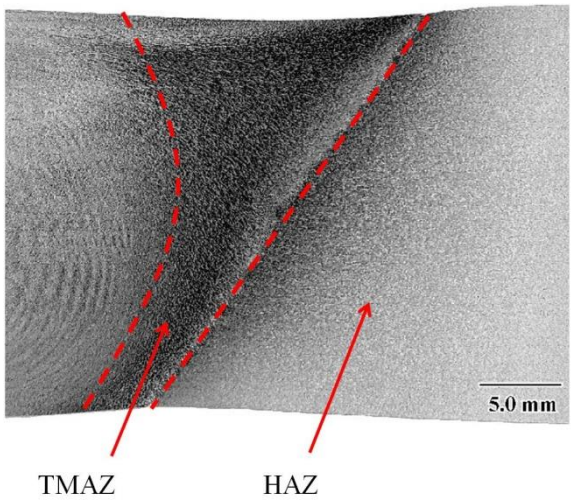

Figure 22 Cross section of a Friction Stir Weld of AA2519 after etching with Kellers reagent to highlight TMAZ and HAZ

2.4.1.3. HAZ

The heat - affected zone (HAZ) sits outside of the influence of the plastic deformation from the weld tool, but does experience a thermal load. The grain structure is not affected by this heating, however it has been shown to coarsen precipitates within the microstructure [131, 132]. The microstructural changes have been observed to gradually lessen with distance away from the weld nugget and the heating zone [133].

2.4.2. FSP

FSP differs from FSW in that it is not a joining technique; instead its primary use has come in the modification of surfaces for a wide variety of uses. FSP was developed by Mishra et al. [134], in order to produce microstructural modification of the surface layer which was shown to induce high strain rate superplasticity and achieve very fine grain sizes in cast commercial alloys. In AA1xxx and high purity Al alloys, FSP has the ability to produce very small grains (under 2 μm) which have been shown to exhibit better a hardness and tensile strength in the alloy [135-138]. A FSP tool differs from a FSW tool in that it is primarily concerned with altering the surface layer, therefore it is not necessary to have a long pin to extending into the material, although this can be used for stabilisation. The technique instead relies on the tool shoulder as its primary method of frictional heating and mixing, and is applied to only one piece of material rather than joining two, represented in Figure 23. This has progressed into being able to process large areas using multiple passes [139], with attention paid to the orientation of the overlaps showing an overlap of the advancing side creating a layer with the most uniform thickness [140].

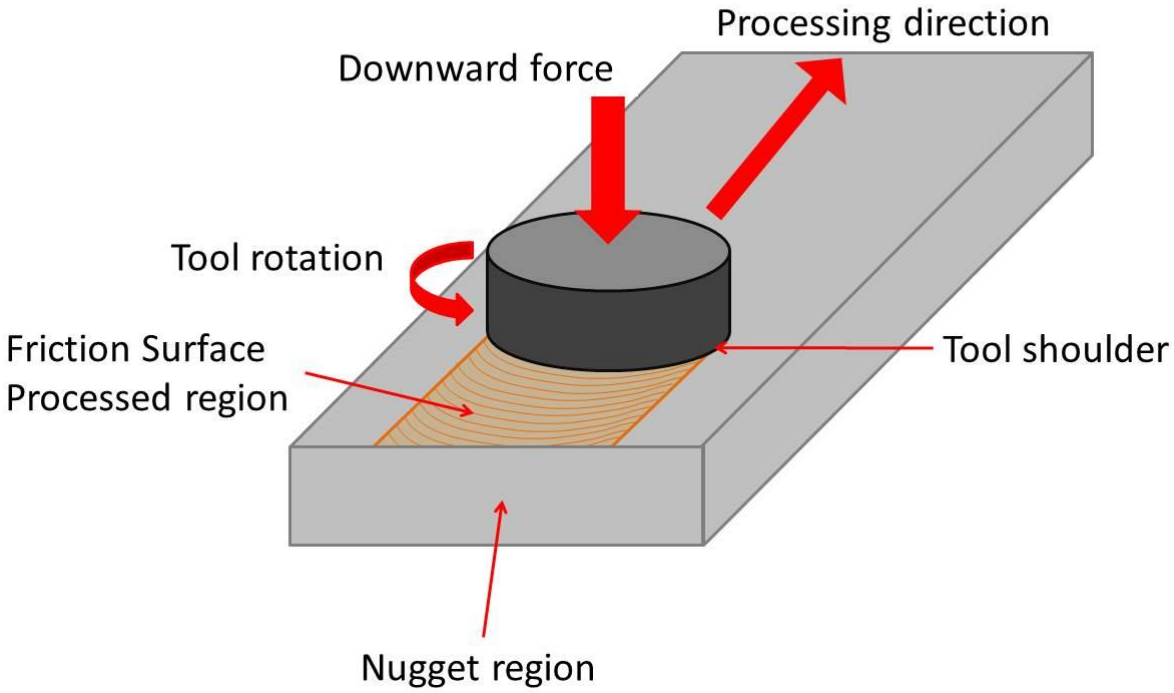

Figure 23 Diagram of the Friction Stir Processing technique

Since its invention, FSP has been used to produce a refined microstructure [111, 120, 139, 141-143], homogenise the microstructure [127, 141, 144, 145], produce composite surface coatings [146, 147] and produce a surface with better hardness and wear resistance [141]. Many of these microstructural and mechanical properties can be controlled by optimizing the tool design and the parameters used [148], for example the thickness of the modified layer has been shown to increase with an increasing rotation speed [146], Figure 24.

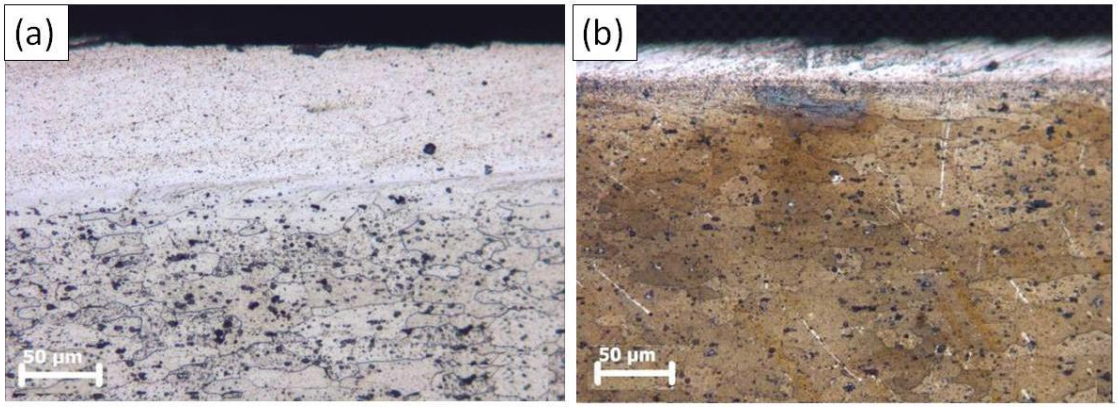

Figure 24 Cross sections of FSP′d AA1050 showing the small distance under the surface which has been microstructurally altered. (a) 100 µm depth with 15 mm/s tool travel speed, (b) 30 µm depth with 30 mm/s tool travel speed [146].

2.4.3. FSW of Al-Mg alloys

Conventional MIG welding has been used in the joining of Al-Mg alloys for many years, however temperatures in the HAZ were shown to reach up to 500 °C for short periods of time and cause local softening [149]. With the advent of FSW, welds in the 5xxx series have been shown to have more homogenous microstructures, including HAZ regions which are harder than other welding methods [150]. Friction stir welding has frequently been used in the joining of Al-Mg alloys, as it is an alloy used primarily in marine systems where joining of large plates is necessary. Research has therefore been necessary in characterising the microstructure.

Some of the earliest work on the 5xxx series was conducted by Jin [151], who saw that weld zones in AA5182 were homogenous, with a dynamically recrystallized fine grain microstructure, results consistent with the fundamentals of FSW, and which have been observed since by others in AA5083 [127, 152, 153]. Peel described the cause of the recrystallization as the thermal excursion of the unstable base material resulting in a zone of equiaxed grains around the weld line [153]. It was also seen that this width of the recrystallized zone could be narrowed by increasing the traverse speed of the FSW tool, as it would reduce the heat input to a particular part of the material.

Mechanical properties of welds of the AA5xxx series, including hardness of the resulting microstructure, have been studied in order to characterise the change brought about in the weld nugget. Early work on AA5083 by Sato found that the hardness of the weld region cannot be explained by the resultant grain size (Hall-Petch relationship). Instead it is likely to depend on small particle distribution, which was seen to be homogenous, as was the hardness throughout the weld [127]. In other research where a high density of small particles was

observed, Svensson concluded that these formed little basis for strengthening, instead the hardness profile depends on the dislocation density [154].

This thinking contrasts with recent studies which found that hardness within the nugget region increased as the grain size was reduced, resulting from a decreased friction heat flow [152, 155]. There also exist differences in observation of strengthening or softening in the stir zone of AA5xxx welds, Peel [153] and Gan [156] have seen the former and where Jin [151] the latter. Gan reasoned the softening to be from the recovery of cold work at the temperatures experienced during FSW. The full details of the processing parameters were not reported by the authors so cannot be assessed as determining factors. If this is the determining factor in the resultant hardness, a variation exists within the AA5xx series as to the minimum grain size which is achievable. Morishige et al. observed the minimum grain size to decrease with increasing the Mg content of the alloy, as this lowered the stacking fault energy within the alloy.

Studies into the methods of heat input to Al-Mg FSWs have been conducted, with consistent findings that increasing rotation speed of the FSW tool, decreasing the speed with which it traverses the weld and increasing the tool shoulder diameter will all lead to a higher heat input [116, 157]. This higher heat input leads to smaller grains formed upon recrystallisation [158], Figure 25, where a reduction in average size down to 1 μm has been shown to give optimum mechanical properties as a result of FSP [155]. A similar finding of better properties resulting from greater microstructural refinement has been shown in studies of Mn additions to AA5083 [159].

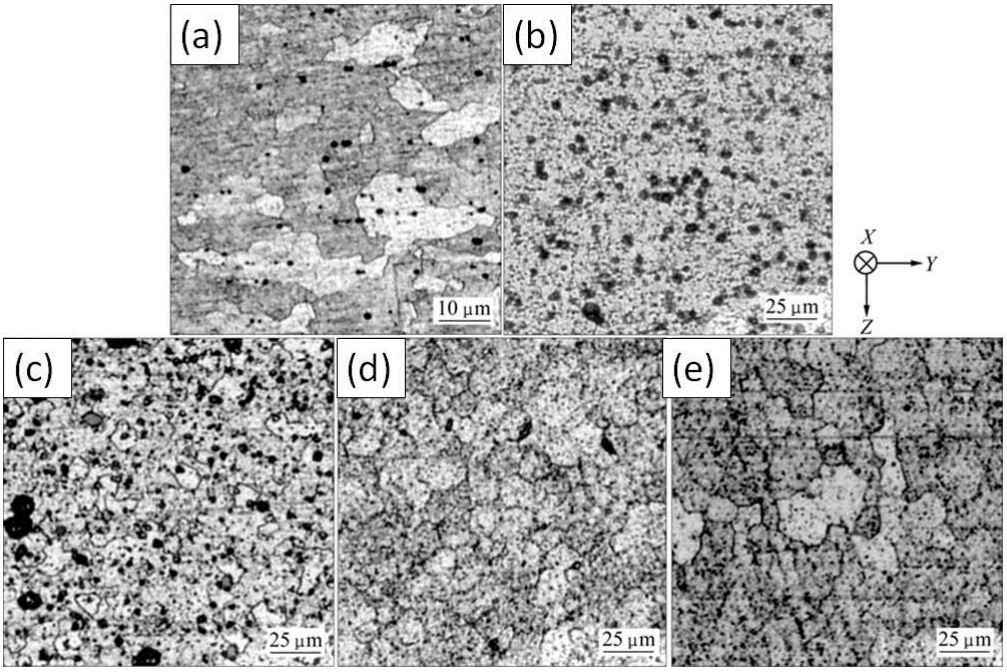

Figure 25 Optical micrographs of the cross sections of (a) AA5052 base metal. Central regions of FSWs with a rotational speed of (b)500, (c) 1000, (d) 2000, (e) 3000 r/min [158].

Outside of the weld nugget, strengthening in the TMAZ has been observed by Attallah [160]. In this region, the strengthening was seen to be controlled primarily by grain boundary strengthening and dislocation-particle strengthening (Orowan). Investigation of the properties within the HAZ outside of this remains poorly studied, with one investigation failing to notice that such a region even existed [161], while others have seen such a region across many Al-Mg alloys [162].

Most recently, FSP has been applied to Al-Mg alloys, with the intention of creating an alloy with preferential mechanical properties. A microstructure of ultrafine equiaxed grains has been produced in the friction stir processing of AA5083, where attention was also paid to the effect of altering processing parameters[163]. Lower rotation speeds were seen to produce a higher hardness, as a result of a smaller average grain size and higher average misorientation

angle, Figure 26. FSP was also shown to give the material much greater super-plasticity. The effect of varying alloy compositions has been shown to vary the minimum grain size achievable in Al-Mg alloys through FSP. The use of AA5083, which has a higher Mg wt. % than AA5052, reduced the minimum grain size achieved, owing to lower stacking fault energy [164].

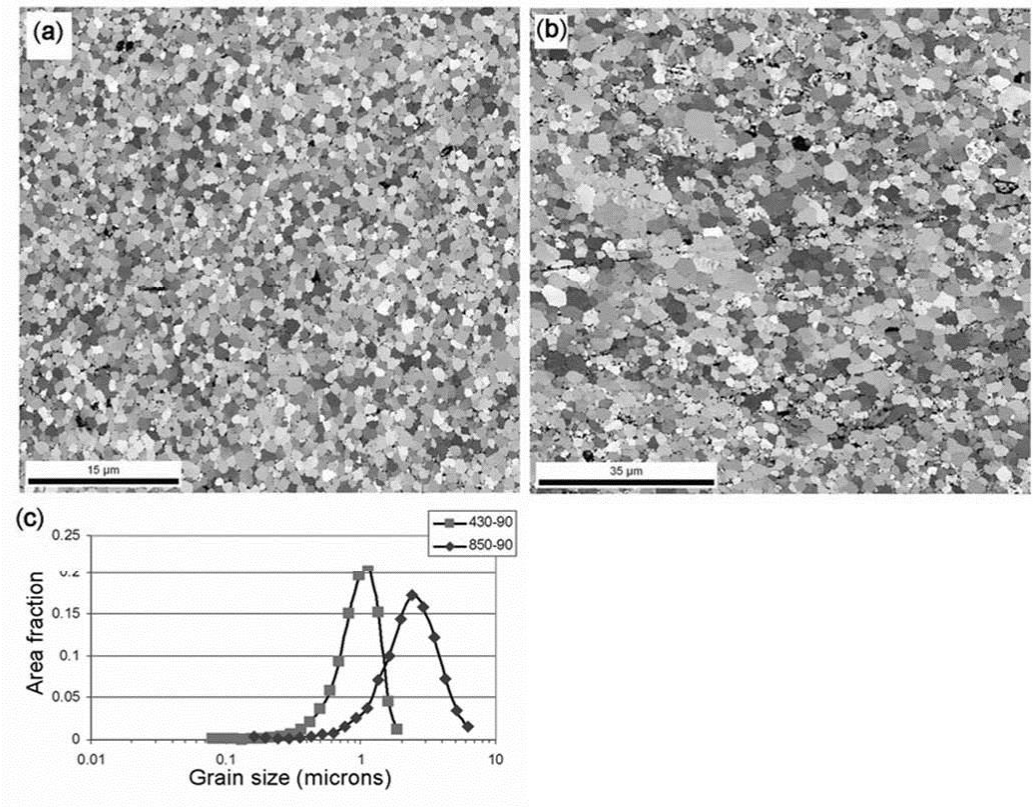

Figure 26 Misorientation maps for AA5083 FSP′d with (a) 430 r/min and 90 mm/min (b) 850 r/min and 90 mm/min. (c) shows the area fractions of the grain sizes achieved [163].

2.4.4. Microstructural development during thermal and thermomechanical processes

The effect of both thermal and thermomechanical treatments on the properties of Al-Mg alloys has been well studied with good agreement as to the outcome of each. Fundamental to this was the work of Conserva and Leoni in the 1970's who took an interest in the processing stages of Al-Mg alloys and the effect of varying the minor alloying elements [165]. They had noted that while the presence of dislocations stimulates the decomposition of the solid solution at temperatures slightly above ambient, the dislocations also make a heterogenisation treatment which precipitates the β-phase to the interior of the grains much easier.

Initial findings showed that a sensitisation treatment of 150°C for 16 hours led to a greater degree of β-phase precipitation onto the grain boundaries than an identical alloy which had undergone mechanical rolling prior to sensitisation [165]. This effect was reasoned to come from the favourable distribution of dislocations from the mechanical treatment which led to the β-phase precipitating in a discontinuous globular form around the grain interior rather than on the grain boundaries. This led to the conclusions that hot rolling, followed by cold rolling, then a heat treatment at 225 °C led to a microstructure which was less susceptible to stress corrosion.

More recently, Tan and Allen have looked at the effect of thermomechanical treatments on the corrosion of AA5083, using cold rolling and an annealing treatment, followed by a sensitisation of 100 °C for 500 hours [166]. A much greater fraction of high angle grain boundaries were observed after the mechanical treatment, Figure 27, which have been observed elsewhere to harbour a greater number of discontinuous or continuous precipitates after sensitisation [18]. This however was not the case as the dislocations introduced by thermomechanical processing led to the β-phase growing in a discontinuous fashion, but not

on planes which were parallel to the grain boundaries. They then concluded that this decreased volume fraction of β-phase on the grain boundaries should be sufficient to reduce the corrosion susceptibility of the alloy to IGC.

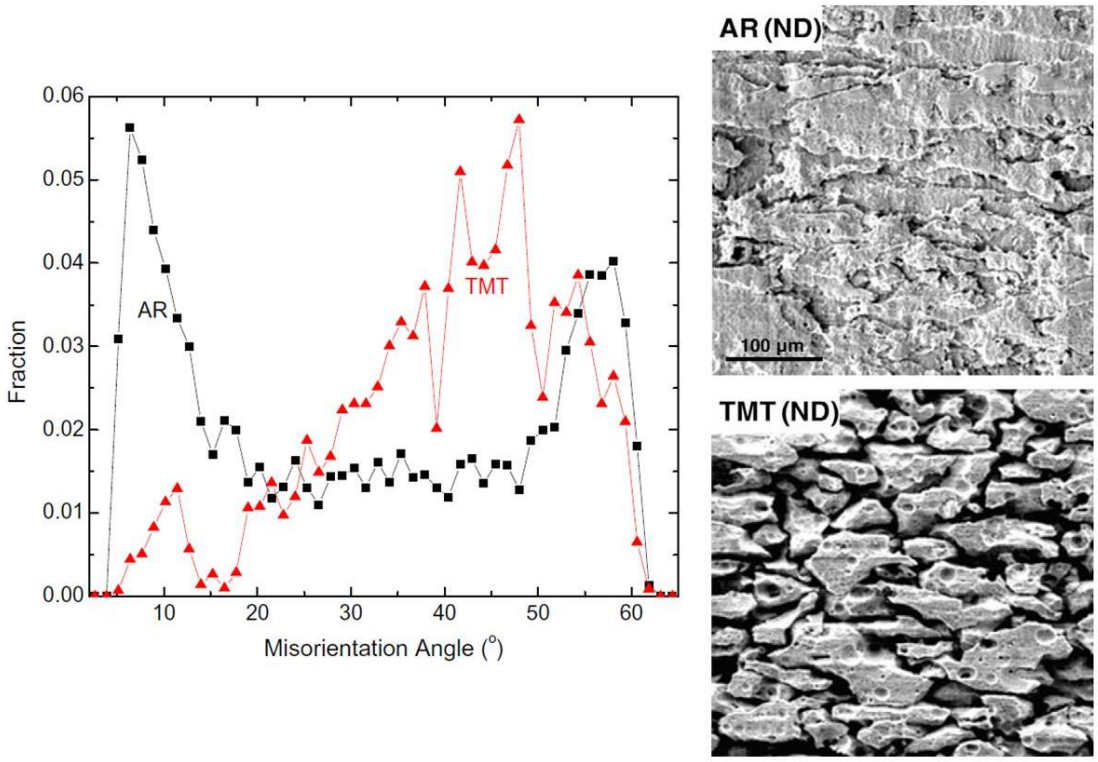

Figure 27 Graph showing the fraction of grain boundaries as a function of misorientation angles of the as received (AR) and thermo-mechanically treated (TMT) samples. Surface morphologies of the two conditions after NAMLT testing is also shown [166].

A comprehensive study into the effects of heat treatments on the corrosion behaviour of AA5083 has been conducted by Winsley [39]. Sensitisation heat treatments of 100-200 °C for at least 10 hours were shown to precipitate the β-phase onto the grain boundary, which increased the susceptibility to intergranular corrosion, Figure 28. Altering the initial heat treatments to which a sample is exposed before sensitisation was also shown to greatly vary the corrosion susceptibility. Solution heat treating samples at 400-500 °C followed by

quenching was believed to increase the amount of magnesium in super saturated solid solution, therefore creating a non-equilibrium single phase condition where little β-phase exists. This was seen to have limitations in that initial heat treatments of over 1 hour put even more magnesium into solid solution, leading to the possibility of greater grain boundary segregation and precipitation of magnesium.

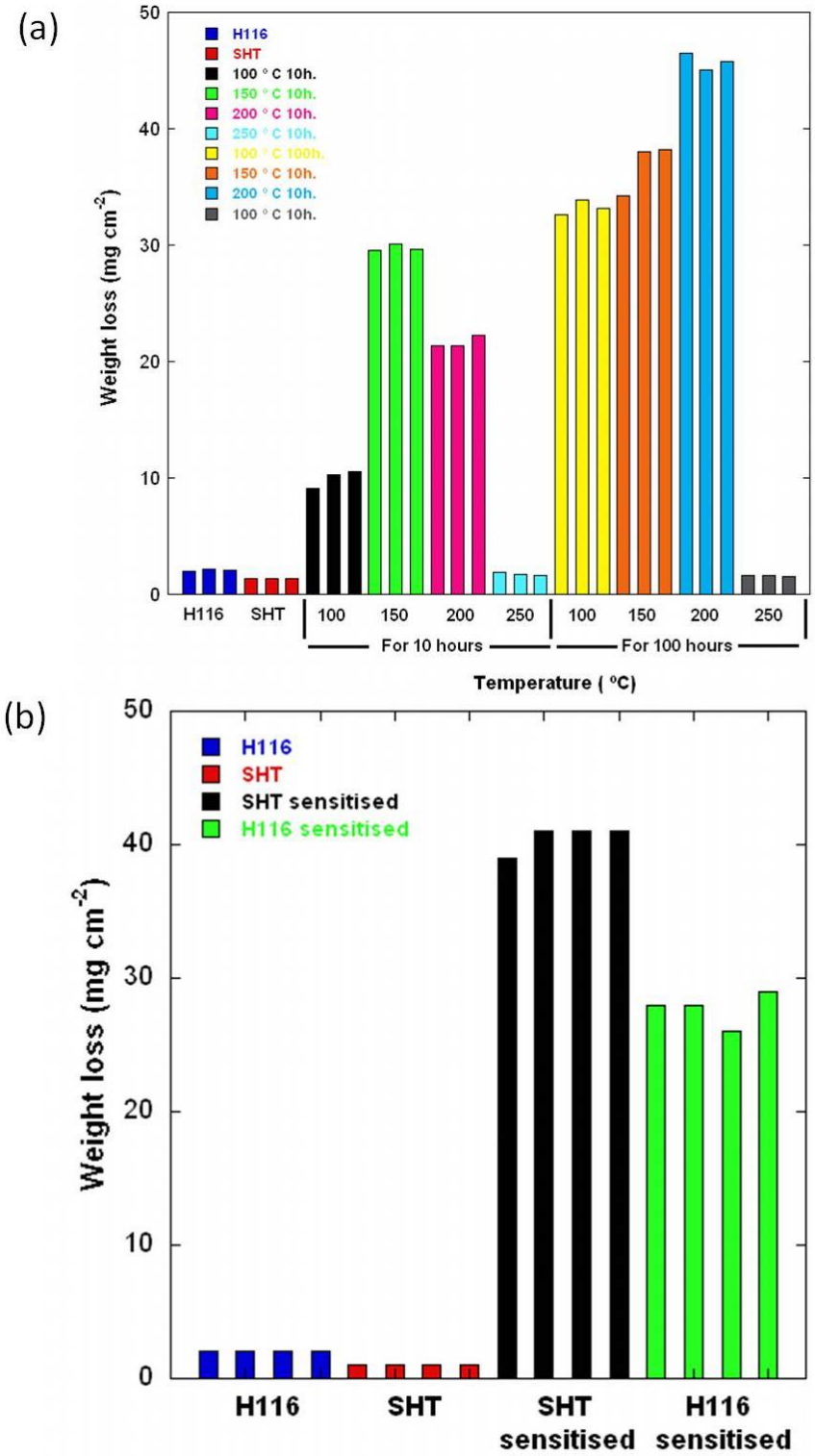

Figure 28 (a) Graph demonstrating NAMLT values as a function of sensitisation treatment temperatures and durations. (b) Graph of NAMLT values where a solution heat treatment followed by sensitisation shows higher values than sensitisation alone [39].

2.4.5. Corrosion of FSW and FSP regions

Much research exists surrounding the corrosion response of aluminium alloys after friction stir welding, and while the 2xxx series has been the focus of much of it, the principals of mechanical and heat influence on altering the microstructure and the corrosion response remain.

Friction Stir Welding and Processing of the 2xxx series alloys has shown that a significant improvement in corrosion resistance can been gained. Microstructural refinement, uniformity and homogeneity have been brought about in 2xxx alloys resulting in increased corrosion resistance [167], while the reduction and redistribution of second phase particles has been shown to increase corrosion resistance, while also giving better mechanical properties [168].

In a comparative study of TIG welding and FSW, the unaffected parent material showed a pitting tendency, while both the HAZ and nugget material showed more noble behaviour under electrochemical testing [169]. Xu et al. went further with electrochemical testing to show that a weld nugget in AA2199 had a much higher open circuit potential, while the E_{corr} and E_{pit} were also higher after processing [170].

This is not however the full story as several authors have reported seeing poor corrosion behaviour of FSW regions in both 2xxx [171, 172] and 7xxx [173] aluminium alloys. This poor corrosion behaviour has been related to the fine grain structure in the nugget region being prone to IGC, and the TMAZ experiencing a coarsening of precipitates on the grain boundaries which show poor corrosion resistance. Paglia and Bucheit did however suggest that this poor corrosion behaviour could be mitigated by a post weld heat treatment [173].

2.4.6. Corrosion of Al-Mg Friction stir welds

The corrosion of welded AA5083 has been investigated for some time, with mixed observations regarding the efficacy of MIG welding, [174, 175], hence the use of FSW has been investigated as to beneficial corrosion properties which may arise.

Consistent findings in terms of corrosive attack have been observed in the resulting microstructures after AA5xxx series alloys have been friction stir welded. Frankel and Xia were one of the earliest to observe that pits only formed in the HAZ region of a AA5454 weld, whereas the FSW weld region showed much greater pitting resistance than the base material or HAZ, where a much higher pitting potential was also observed in the nugget region [176]. The tendency for less pitting in the weld region was also seen by Zucchi et al. in AA5083, where the higher pitting potential and lower cathodic current were again observed [177]. Microstructural investigation by Winsley [39] attributed the increased pitting resistance and higher breakdown potentials to a decrease in the number of coarse, reactive Mg_2Si constituent particles in the FSW nugget region of AA5083, due to the mechanical mixing and stirring experienced in this region.

Intergranular corrosion susceptibility by means of β-phase precipitation remains the biggest threat to the structural integrity of the AA5xxx series while in service in marine environments. Fonda et al. were able to observe the incidence and formation of β-phase in the different weld regions after FSW of 5456, as well as using a droplet cell to take electrochemical measurements. [178]. Phosphoric acid etching revealed there to be no β-phase precipitation in the TMAZ or HAZ, while most of the β-phase appeared to have precipitated in the weld nugget. The FSW nugget showed the worst corrosion susceptibility; lower breakdown potentials and higher anodic activity was recorded in this area compared to the base, HAZ and TMAZ, as a result of there being the most nano scale β-phase precipitates dispersed

throughout the matrix in this region, Figure 29. The greatest β-phase precipitation was seen in the lower part of the weld nugget where the most extensive fragmentation of Al_6Mn precipitates was seen, reasoned to be nucleation points for the β-phase alongside dislocations.

A reduction in corrosion susceptibly of sensitised AA5083 by FSW has been shown by Choi, who concluded that the temperature experienced in the nugget region must have been above 450 °C in order to dissolve the β-phase back into the Al matrix [33]. This was confirmed by observing a removal of β-phase in the microstructure after FSW and an improvement in the IGC performance by NAMLT tests.

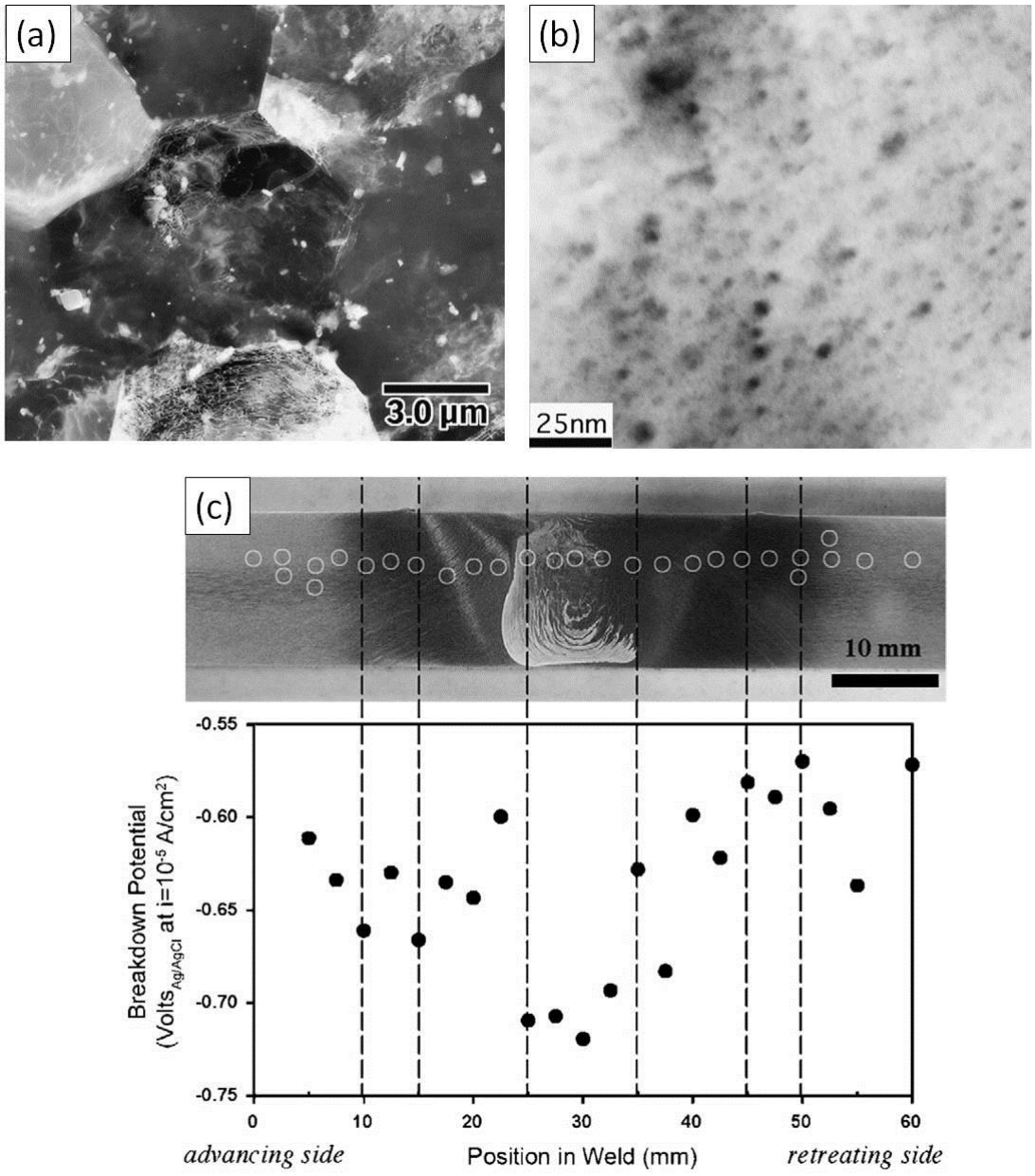

Figure 29 (a) TEM micrograph of the refined grain structure in the FSW nugget of an Al 5456 plate. (b) Brightfield TEM micrograph showing the nano-scale β-phase deposits. (c) Macrograh of weld cross section with graph relating breakdown potentials to location in the weld [178].

A further sensitisation treatment applied to a FSW of AA5083 was not seen to decrease pitting resistance, while a FSW nugget region that has been re-sensitised showed better IGC resistance than sensitised parent material [39]. The sensitisation treatment was however seen

to bring about the worst IGC behaviour in the HAZ outside the nugget, although the means and mechanism were not discussed.

SCC susceptibility has mainly been studied with reference to the performance of FSW against other welding techniques. Both MIG [177] and GTAW [176] welding techniques were shown to have inferior SCC resistance to FSW welds to the extent that no SCC was observed in either of the FSW welds.

2.5. Processing parameters

The variation of the processing parameters used has been shown to affect the corrosion behaviour of FSW and FSP regions, however only with reference to the AA2xxx series.

Corrosion resistance has been shown to increase with an increased tool rotation speed and travel speed [179], but conversely, it has been shown that increasing the rotation and traverse tool speeds results in less mechanical stirring and less dissolution of secondary particles which make the material susceptible to corrosion, because the tool is in a given region for a shorter period of time [170].

It would appear that a compromise of fast rotation speed with shorter traverse speeds would enable maximum heat and mechanical stirring to be imparted into the weld region to gain the greatest corrosion resistance. To this end, further investigation by Surekha [180] showed that multiple FSP passes increase the corrosion resistance with each pass, by increasing the dissolution of $CuAl_2$ particles in 2xxx alloys.

2.6. Literature Summary

It has been shown that the Al-Mg series of alloys have a mixture of high strength, high toughness and excellent corrosion resistance through the use of solute strengthening and choice of alloying elements. In addition to these properties, a good weldability makes these alloys an excellent choice of material for use in the construction of ship hulls. The addition of magnesium as an alloying element produces improved properties, however the limit of solid solubility is greatly reduced at room temperature; 1.7 wt. %. These insoluble elements existing within the matrix can lead to the formation of the β-phase precipitate, which can lead to an increased susceptibly to corrosion called sensitisation.

A process of stabilisation has been developed where the formation of the β-phase is done in a controlled way in order to reduce the amount of magnesium held in solid solution. This is believed to restrict the ability of the material to sensitise by forming coarse randomly distributed β-phase which is not available for further precipitation onto areas such as grain boundaries. The difference between sensitisation and stabilisation has been established as subjecting the material to temperatures above or below 250 °C, which are favourable and detrimental respectively. More recently it has been shown that a stabilisation heat treatment can reverse the sensitisation that has occurred in Al-Mg alloys.

The oxide film on aluminium alloys is not homogenous and contains weak points usually around precipitates such as the β-phase in Al-Mg alloys. The β-phase is more electrochemically active than the bulk of the alloy and is a site for the initiation of intergranular corrosion which can propagate over the surface and into the alloy along the susceptible grain boundary. IGC in the presence of an applied stress in service can lead to Intergranular Stress Corrosion Cracking which is detrimental and dangerous in that it can cause large structures to fail rapidly.

Atmospheric corrosion is of particular interest as its occurrence has been seen to vary with temperature, humidity, oxygen solubility and environmental pollutants within a droplet, such as chlorides. Studies have shown chloride concentration to increase the frequency with which corrosion is seen, believed to be due to its ability to support a higher pH in cathodic areas which results in alkaline dissolution of the passive film. Distinct separation of the anodic and cathodic regions by location under a droplet has been seen, linked to the relative ease of oxygen access at the edge of a droplet.

Friction Stir Processing is derived from Friction Stir Welding, where microstructural modification is being applied to the top surface of the material. Both processes create a nugget region where the mixing and heating takes place, and a Heat Affected Zone outside of it which has only been locally heated.

FSW has successfully been applied to Al-Mg alloys where a homogenous and dynamically recrystallised microstructure has been formed. When FSP has been applied to Al-Mg alloys to create preferential mechanical properties, ultrafine equiaxed grains were produced as a surface layer, while alteration of the processing parameters such as tool rotation and advance speed could produce a varied microstructure.

Friction Stir Welding and Processing show a good ability to improve the corrosion resistance of many aluminium alloys by microstructural refinement. Friction stir welding of Al-Mg alloys has shown improved corrosion properties over those produced by TIG-welding in that there was a lower tendency for pitting corrosion. The IGC susceptibility in the nugget region of FSW′d Al-Mg alloys after ageing has also seen to be better than in the parent material. Sensitisation of the weld HAZ region has however been seen to bring about worse IGC behaviour.

2.7. Aims of Project

This thesis will aim to understand the microstructural changes which occur through sensitisation and FSP processes in Al-Mg alloys, and the effect which this has on the corrosion resistance of the alloy. This aims to be analogous to ship hull plate experiencing sensitisation while in service, then being exposed to atmospheric and immersion corrosion conditions. The application of FSP will be investigated to ascertain whether it can reverse the microstructural changes brought about by sensitisation, and how this microstructure fares against further sensitisation, with a view to mitigate IGC susceptibly. Variation in microstructure will be compared to the corrosion behaviour observed under laboratory tests.

Chapter 3 – Experimental method

3.1. Material

3.1.1. AA5083 plates under investigation

The AA5083 was supplied in 12.7 mm thick plates which measured 36 x 20 cm. Plates were supplied in the H321 temper, or with one of two sensitisation heat treatments. Some samples were subsequently treated with friction surface processing (FSP). Both the heat treatments and processing were carried out at the Department of Mechanical Engineering in the University of South Carolina.

3.1.2. Friction surface processing parameters

The initial testing of FSP on sensitised material was conducted with a full thickness FSP tool made from tungsten, with a pin that submerged 12.6 mm into the plate (Chapter 4). Here, one plate was left in the H321 temper and the other was sensitised at 150 °C for 100 hours before processing. Four processing passes were made, 2 in each plate, Table 2 indicates the parameters used for each.

Table 2 Processing parameters used in full thickness processing of AA5083-H321 and sensitised plates

5083-H321			
Base Metal			
Weld Number	Centimetres /Minute	RPM	Peak tool temperature (°C)
3156	5.1	80	404
3164	15.3	240	518

5083-H321			
Sensitised (100 hours @ 150 °C)			
Weld Number	Centimetres /Minute	RPM	Peak tool temperature (°C)
3157	5.1	80	404
3163	15.3	240	514

Subsequent tests were carried out using superficial friction surface processing to give a shallower processed layer (Chapter 5). These samples were sensitised at 100 °C for 14 days. Processing was carried out with an FSP tool which had only a 0.5 mm deep pin to locate the tool in the work piece. The tool was rotated at 2000 rpm, and travelled at 15.3 cm/minute over a distance of 33 centimetres, with an applied force of 4545 kg. This processing was repeated in 8 parallel passes with an overlap of 25 % of the previous pass.

3.2. Sample preparation

3.2.1. Mounting and polishing

Several methods of mounting samples were used depending on the method of testing or inspection. Observations of heat input to the sample are noted as the precipitation under investigation is heat sensitive and may be influenced by the preparation methods.

Samples which were inspected in an SEM were hot mounted in conductive Bakelite, where a hot mounting press melted grains of Bakelite around the sample for 7 minutes at 175 °C.

Where light microscopy was used, and for general purpose mounting of samples for testing, the cold mounting Vari-set 20 powder/liquid system by MetPrep was used. The hardening reaction was exothermic and reached 50 °C for 5 minutes, after which the sample could be extracted from the mould. This was not judged to present an issue with regards to precipitation due to the low time and temperature.

When support for the specimen edges was required for inspection of the cross section, the Tri-Hard cold mounting system by MetPrep was used. This system is designed to give minimal shrinkage of the mounting media, and no heat change was observed during the reaction.

Once mounted, samples were ground using SiC grinding papers on a grinding wheel, moving from grit size P120 to P400, while a non-aqueous lubricant was applied. At this point, the samples were rinsed with de-ionised water and were dried thoroughly in hot air to remove all of the water.

Polishing of the samples progressed from 3 µm DiaDuo suspension on a MD-Plus polishing cloth, then 1 µm DiaDuo on a MD-Nap polishing cloth, finishing with 0.04 µm OP-S on a MD-Chem cloth for a mirror finish. Following polishing, the samples were cleaned again in

de-ionised water and an ultrasonic bath, dried thoroughly under hot air, then stored in a desiccator.

In order to inspect the surface of samples that had undergone corrosion under immersion and atmospheric conditions, corrosion product was removed by a light polish using 0.04 µm OP-S on a MD-Chem cloth for 10 seconds.

3.2.2. TEM sample preparation

TEM sample preparation took two different approaches depending on the condition of the samples with regard to sensitisation. For the samples where no β-phase was expected on the grain boundaries, 3 mm diameter discs were sectioned from samples by cutting 300 µm thick slices from the sample then using a punch to create the disc. This disc was then ground down to 150 µm thickness using a specially designed holder, grinding paper and a non-aqueous lubricant.

These discs were then electro-polished using a Struers Tenupol-3 twin jet electropolishing machine. A 5 % perchloric acid solution was made up using methanol as the balance, to be used as the polishing solution, while liquid nitrogen was added to keep the temperature between -20 and -30 °C. A voltage of 20 V was applied as the solution was jetted onto the disc until breakthrough of the sample had been achieved. This point of breakthrough was used as the area of inspection.

For samples where β-phase was present on the grain boundaries, it was found to dissolve out during electropolishing. Instead, samples were extracted using a Focused Ion Beam/SEM. The ion beam was used to mill out a 20 µm x 10 µm x 100 nm slice from the sample surface, then mounted onto a 3 mm inspection disc, which was ready for inspection in a TEM.

3.2.3. Etching in Kellers reagent and Phosphoric acid

Metallographic etching in Keller's reagent was used to observe macro scale features in the samples. The etch consisted of 1 % hydrofluoric acid, 2 % Nitric acid and 3% Hydrochloric acid, with the balance being de-ionised water. Samples were immersed in the etchant for 20-30 seconds, or until the microstructural changes became evident, then were cleaned in de-ionised water and methanol. These microstructural changes were viewed using a light microscope or a digital camera with a macro lens attached.

Phosphoric acid etching was used to show those grain boundaries that are susceptible to intergranular corrosion. A 10 % solution of phosphoric acid was made with de-ionised water, then heated to 60 °C in a water bath. Samples were immersed for 30 seconds then immediately washed in de-ionised water; care was taken to carry out a consistent etching treatment across all samples so that the extent of attack could be compared.

3.3. Microscopy

3.3.1. Light microscopy

A Leica microscope with a 5 MP camera and image capture software was used to capture optical micrographs.

3.3.2. SEM microscopy

Several SEM's were used for the inspection of samples; a JEOL 6060 and 7000, and a Philips XL-30, where an acceleration voltage of 21 kV was used for secondary electron imaging and 14 kV for EDS detection. An Oxford Instruments EDS detector and INCA software were used for gathering and analysis of data.

3.3.3. TEM microscopy

The thin foil sections created by electropolishing or FIB milling were analysed using JEOL 1200 and 2100 Transmission Electron microscopes and a Philips Technai F20 FEG TEM. The JEOL 1200 operated at 100 kV, while the 2100 and F20 operated at 200 kV and had an Oxford INCA EDS system attached.

3.3.4. EDS of cross section and particles

Two methods of chemical composition sampling were used on the JEOL 6060 SEM for different purposes. Point sampling was used to try and isolate X-rays from individual intermetallic particles to avoid background readings, whereas large areas (100 x 100 μm) were sampled in order to generate the cross-sectional composition

3.4. Hardness measurements

Hardness measurements were made with an Indentec macro hardness machine, where a 5kg load was applied and measurements taken on the Vickers hardness scale.

3.5. Corrosion testing

3.5.1. Immersion testing

Samples for immersion testing were cut from the plate, and in the case of the full thickness FSP (Chapter 4), the cross section of the plate was ground and polished to a mirror finish using the specification outlined above. For the surface FSP samples (Chapter 5 and 6), 1mm of the plate top surface was removed in order to remove the small nugget region, then the top surface ground and polished as outlined previously. Each sample received a final rinse in de-ionised water in an ultrasonic bath before being dried in hot air 24 hours before immersion. Those sides which were not under investigation were covered in Microshield stopping-off lacquer prior to immersion. Immersion was carried out in naturally aerated solution of 1 M NaCl at room temperature (22 ±1 °C) for varying time periods.

3.5.2. Atmospheric corrosion under droplets

Samples for atmospheric droplet testing were sectioned from the plate, with either the cross section (Chapter 4) or top surface (Chapter 5 and 6) prepared for exposure by mounting and polishing as outlined above. A solution of saturated KCl containing crystals was prepared to maintain the RH at 87 %. 6 droplets of 1 M NaCl measuring 0.5 µl each were placed onto the surface of the samples with a Eppendorf Research plus pipette, then sealed in a container with the KCl solution in a container in the bottom. The sample was left at room temperature (25 ± 1°C) for 6 weeks. Each of the droplets was imaged immediately for baseline measurements of droplet size, then again after testing had ended.

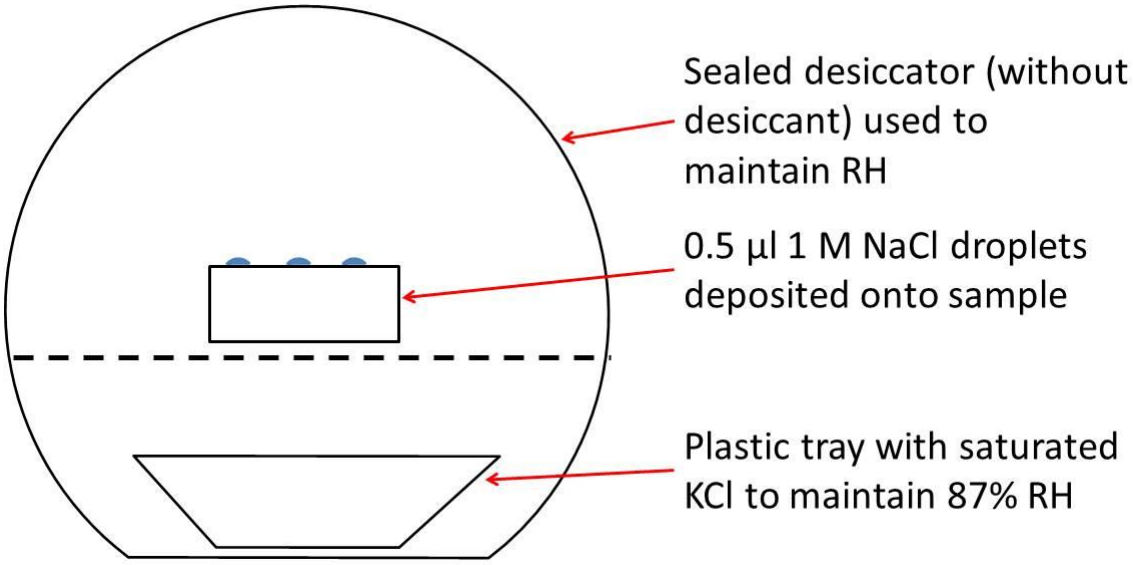

Figure 30 Diagram of the apparatus used to expose a sample to an atmospheric droplet of solution in fixed humidity conditions

3.5.3. Confocal microscopy

Confocal microscopy was used to accurately image and measure the corrosion morphology after immersion and atmospheric corrosion. The Olympus LSM confocal microscope and software uses a laser to scan across the surface of the sample and determine the topography by measuring the intensity of reflected light at different heights. The software used to control the microscope compiles the data into a 3D representation of the scan data, from which depth and volume of attack can be measured

3.5.4. Electrochemical techniques used

An ACM Instruments Gill AC potentiostat was used to make all the electrochemical measurements in this study, while a naturally aerated solution of 0.1 M NaCl acidified to pH 2.75 with HCl was used throughout. Samples were mounted and polished to a mirror finish as

outlined previously 24 hours prior to testing. The cross section was studied for the full thickness FSP in chapter 4, while the top surface was tested for chapter 5 and 6.

All of the electrochemical testing was conducted on a macro scale with a "flat cell" electrochemical cell, Figure 31. This cell pressed the sample against an O-ring to create a seal for the solution within the cell and to define the area to which the solution was exposed, in this case, 0.2075 cm^2. The cell consisted of three electrodes; the sample acted as the working electrode, a Pt coil acted as the counter electrode and a calomel electrode was used as the reference electrode. Before each test, the reference electrode was compared to a calibrated reference electrode to ensure its accuracy. In all cases, the difference between the two was less than 4 mV.

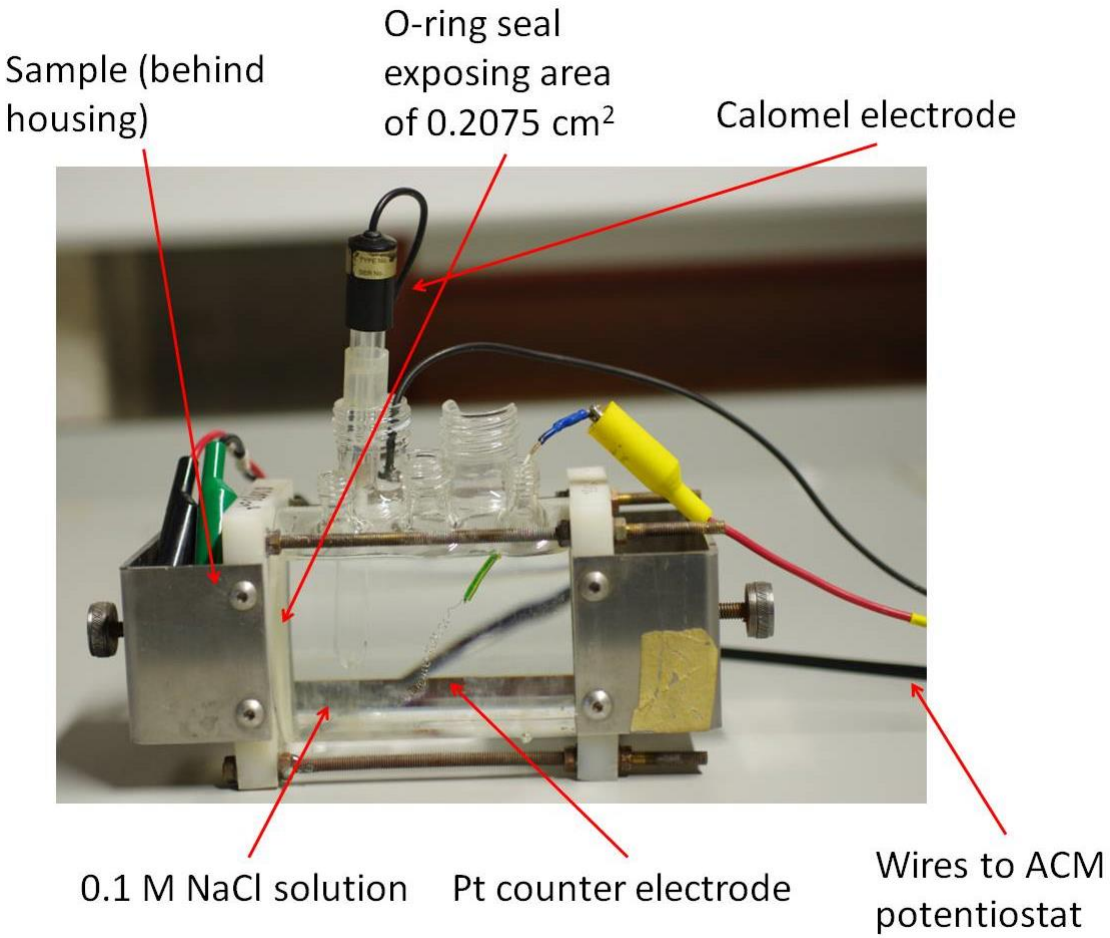

Figure 31 Electrochemical flat cell used for electrochemical measurements

Two types of measurements were taken using the flat cell and potentiostat. Potentiodynamic measurements were taken first to establish pitting, breakdown and open circuit potentials for each sample. The open circuit potential (OCP) was measured for 5 minutes prior to anodic polarisation, which was started just below the OCP and swept at 1 mV/s.

Following this, potentiostatic measurements were taken in order to study the intergranular susceptibility of the samples. A potential of -710 mV(SCE) was chosen as it was just below the corrosion potential of AA5083-H321 determined form the polarisation curves.

3.6. Synchrotron investigation of IGC susceptibility

Synchrotron micro-tomography was carried out on the TOMCAT tomography beamline at the Swiss Light Source. The X-ray energy of 21.9 keV was selected using a double multi-layer monochromator

Test sample pins were CNC machined from the various plate conditions, so that their length ran along the rolling direction of the plate. This was followed by turning down to the final required diameter with a lathe. The centre point of each of the pins was 2mm from either the top or bottom surface of the plate. Each pin had a 3 mm diameter base to fit into the sample holder provided at the beamline, and a 1 mm diameter head which was the area of focus. The total height of the pins produced was 17 mm. After machining, each of the samples was immersed in concentrated nitric acid in order to passivate the sides of the sample. Immediately prior to testing, the top of the 1 mm end of the pin was ground away using 4000 grit paper and degreased with ethanol.

Onto this surface, a 0.2 µl droplet of 5 M $MgCl_2$ was deposited with a Hamilton 7000 series HPLC syringe, to create a droplet with a chloride deposition density of 9 mg/cm^2. The RH within the cell was maintained at 59 % by soaking a piece of filter paper with saturated NaBr and placing it in the cell above the sample. A schematic diagram of this set-up is shown in Figure 32.

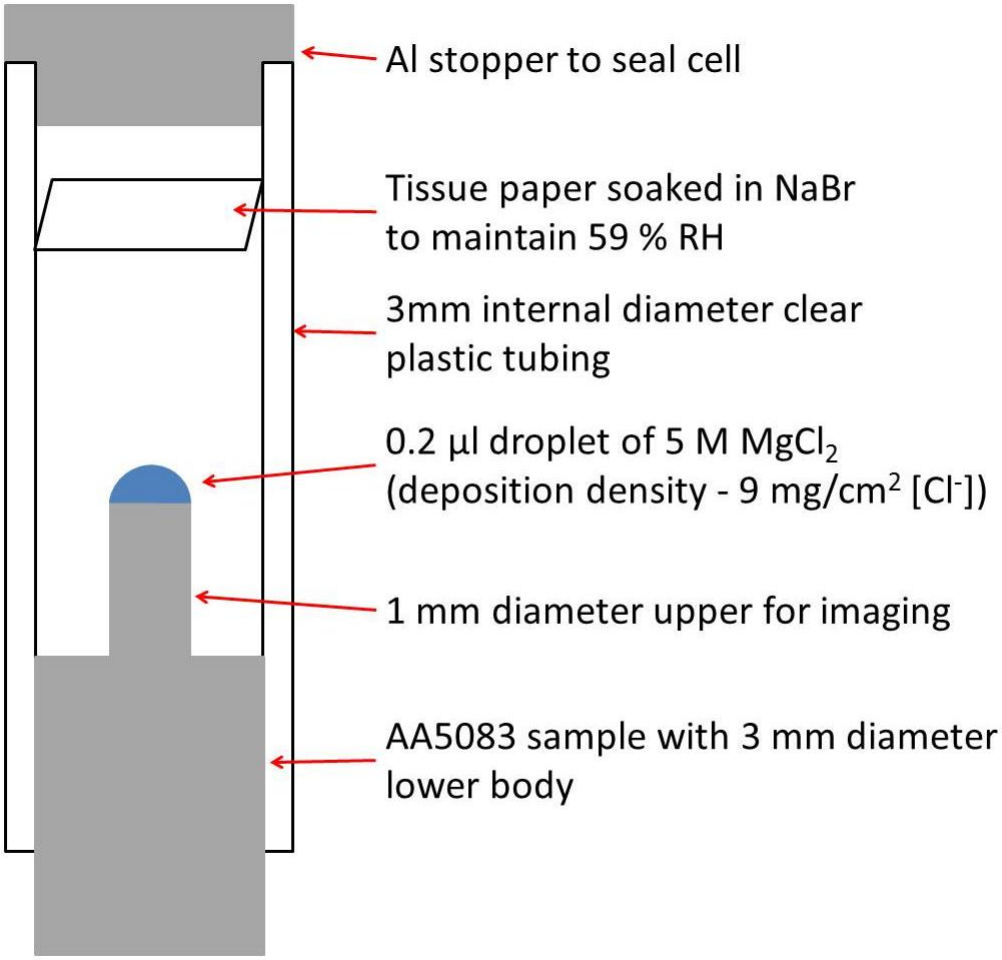

Figure 32 Diagram of the apparatus used to expose samples to atmospheric droplets on the synchrotron tomography beamline.

Detection of signal was achieved by converting the x-rays into the visible light spectrum with a 20 µm LuAg scintillator, where the resultant image was magnified at 10x and captured on a PCO 2000, PCO AG camera. The 2048x2048 image captured had an effective pixel size of 0.74 µm. 1200 individual projections of the sample were captured as it rotated through 180°, where an exposure time of 150 ms led to the scan time totalling 12 minutes per sample. Projection data was tomographically reconstructed using a gridding method [181]. The tomographic slices that are produced from the reconstruction were then inspected using FIJI image analysis software to determine sites of corrosive attack by observing structural defects

in all three dimensions, Figure 33. It was at this point that the size and depth of the attack could be quantified using the width of the 1mm sample to set the scale.

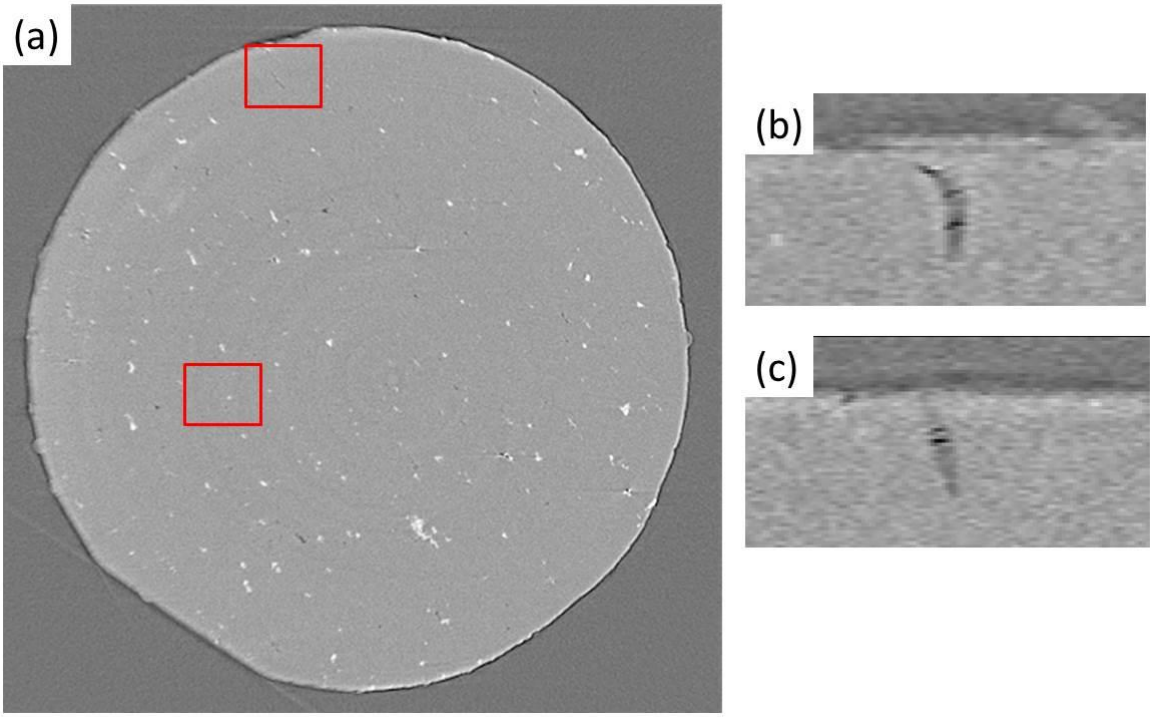

Figure 33 (a) Screen capture of FIJI software being used to identify sites of IGC (red squares) in reconstructed tomographic slices of the 1mm diameter test specimen looking down the Z axis. (b) and (c) are images of two sites of IGC observed in the x axis.

Once identified, the tomographic slices of interest containing sites of IGC were imported into Avizo visualisation software. With this software, the space left by the IGC was selected in each slice, so that when the layers were recombined, a 3D construction of the IGC path in the material was produced. This site could then be visualised in the context of the sample surface by adding a 3D model of the entire sample. This process is outlined in Figure 34 (a) to (d).

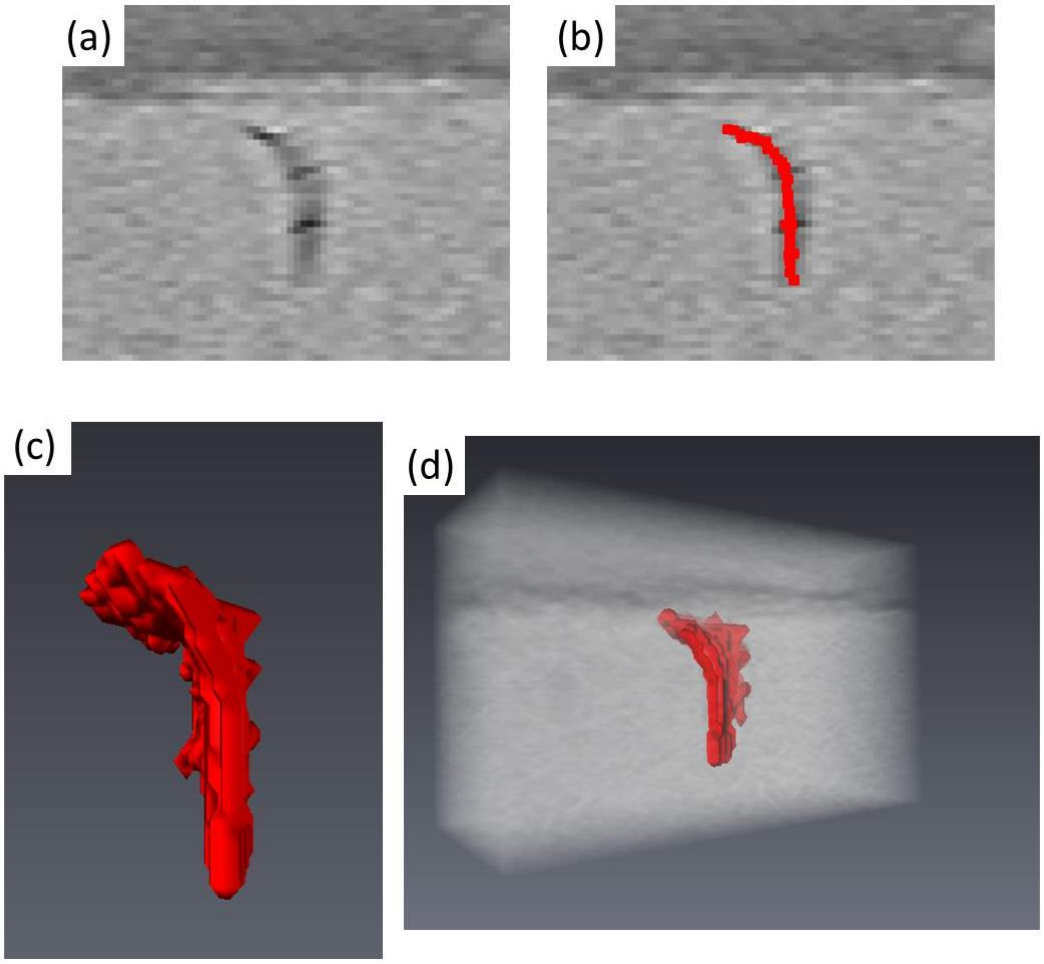

Figure 34 (a) Image of the IGC observed in the z axis of tomographic reconstructions (b) z axis image imported to Avizo visualisation software and the IGC site selected (c) 3D composition of IGC site formed by summation of areas selected in multiple slices (d) IGC site visualised at the surface of the sample.

Chapter 4 – Effect of friction stir processing on the microstructure and corrosion behaviour of AA5083-H321 and AA5083-Sensitised

Friction stir processing (FSP) has been proposed as a method for corrosion mitigation in AA5083 plates with respect to intergranular corrosion susceptibility, which is a consequence of sensitisation. In order to study the effects of FSP, one plate of 5083-H321 has been processed with full thickness processing passes with two different sets of parameters, as outlined in Chapter 3. These same two processing passes were applied to a plate of sensitised AA5083 in order to determine the effect of processing on the microstructure and corrosion response of the plate.

The effect of varying the processing parameters has been highlighted in friction stir welds where the corrosion characteristics can vary with processing parameters [179]. The full thickness processing used in this work was carried out with the same tool that creates friction stir welds. The microstructural and corrosion changes brought about by the processing will be compared with an H321 base plate and another sensitised but not processed plate.

4.1. Microstructural Characterisation of AA5083-H321

4.1.1. Optical observations of processed plate

Figure 35 shows a plate of AA5083-H321 which has been Friction Stir Processed (FSP). In Figure 35 (a) and Figure 36 (a), it can be seen that processing has produced a weld channel 2.9 cm in width, equal to the shoulder width of the tool used in processing. The thermal and mechanical effects of the 1.2 cm length probe can be seen on the bottom of the 1.27 cm thick plates in Figure 35 (b) and Figure 36 (b), where a light pattern of discolouration indicates where the tip of the tool has produced a small amount of local mixing. In the same region, the heat from the process has created a heat-affected zone (HAZ) roughly equal in width to that of the tool shoulder, Figure 35 (d)

Figure 35 (c) shows the region where the tool piece was extracted from the sample after finishing the processing. This gives an idea of the volume taken up by the pin of the tool, and its size relative to the tool shoulder width. Next to the extraction zone, the surface finish produced by the advancing and rotating movement of the tool shoulder can be seen. The striations are deposits of material left behind the tool as it moves forward. The appearance and spacing of the marks are identical in the low and high power welds as both have the same tool advancement per revolution (APR).

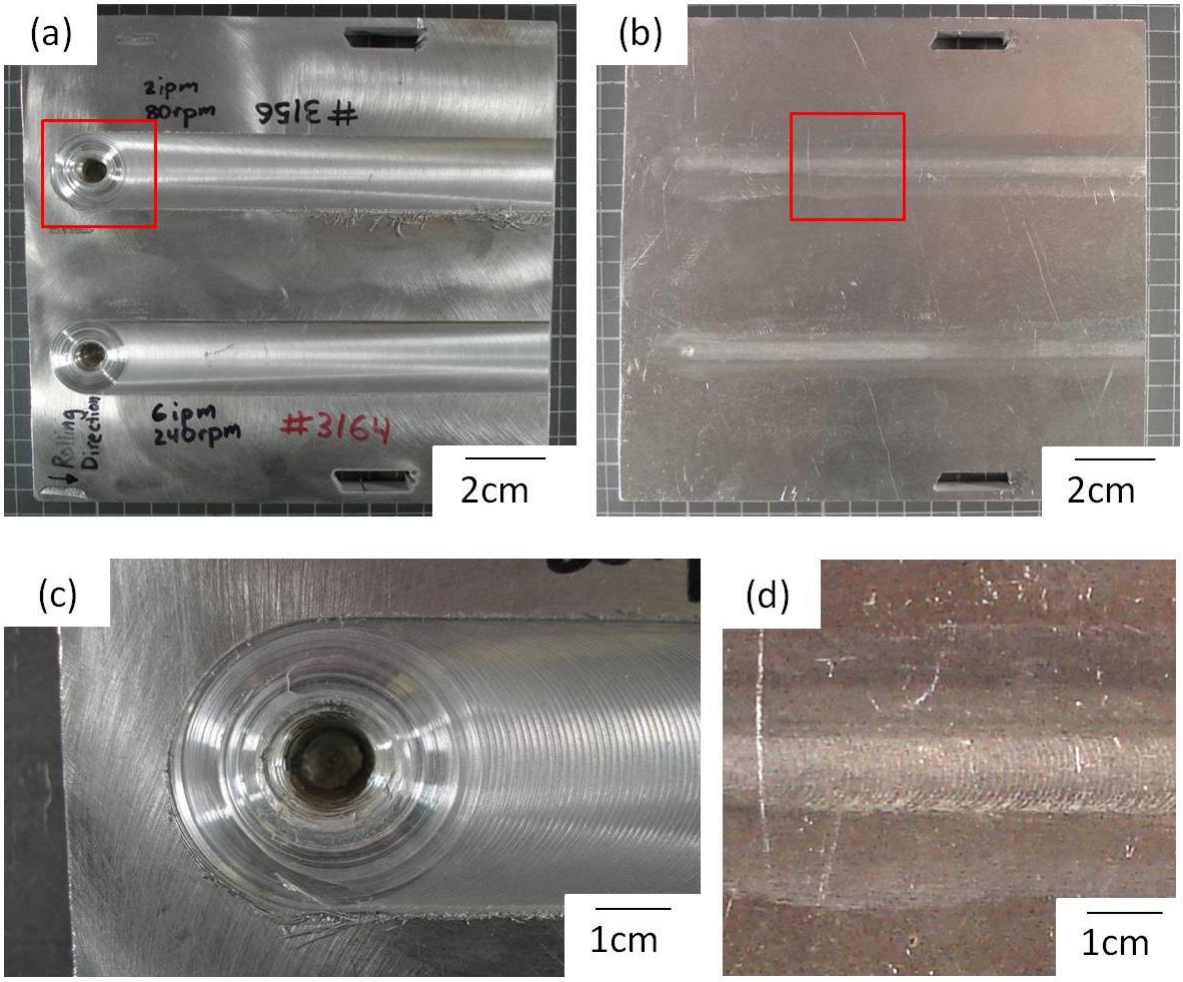

Figure 35 Macroscopic view of the processed AA5083-H321 plate showing (a) top view of the parallel passes made with different processing conditions, (b) bottom view of the same plate where the processing has reached the bottom, (c) magnified view of the tool extraction site from the low-power weld, (d) magnified view of the underside of the plate where the tool pin has deformed the surface slightly.

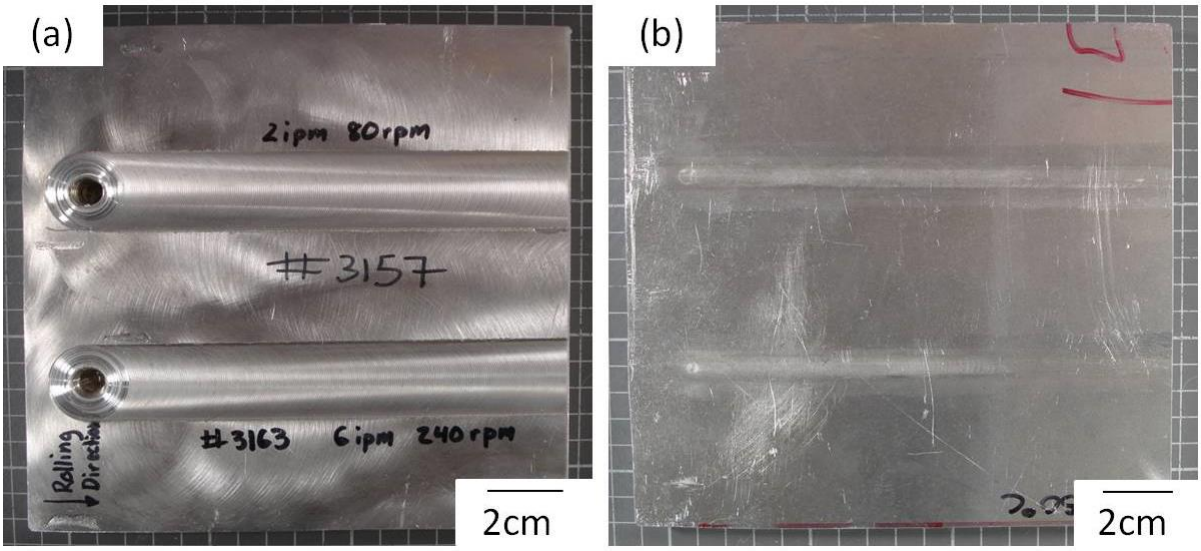

Figure 36 Macroscopic view of the sensitised plate showing (a) top view of the parallel passes made with different processing conditions, (b) bottom view of the same plate where the processing has reached the bottom.

4.1.2. Through thickness variation in Mg content

It has previously been reported that a significant compositional variation can exist through the thickness of AA5083 plate, away from the expected 4.0-4.9 Mg wt.% [39]. In order to determine the extent to which the same phenomenon has occurred within plate used in the present study, EDS area scans of 100 x 500 μm were sampled every 100 μm through the thickness of H321 parent plate. The results in Figure 37 display the Mg wt % recorded at 125 intervals starting at the top surface and finishing at the bottom surface. No significant variations in the composition of other elements such as Si, Fe and Zn were observed.

It is apparent that Mg levels up to 5 mm from either the top or bottom surfaces are entirely within expected values, measuring between 4 and 4.65 wt.%. However there is a 3 mm band at the midline of the plate where the magnesium content drops below 4 wt.%, reaching as low as 3.5 wt.%. This is low compared with the rest of the plate and the average Mg level which is expected of 4.0-4.9 wt. % for AA5083 (Table 3).

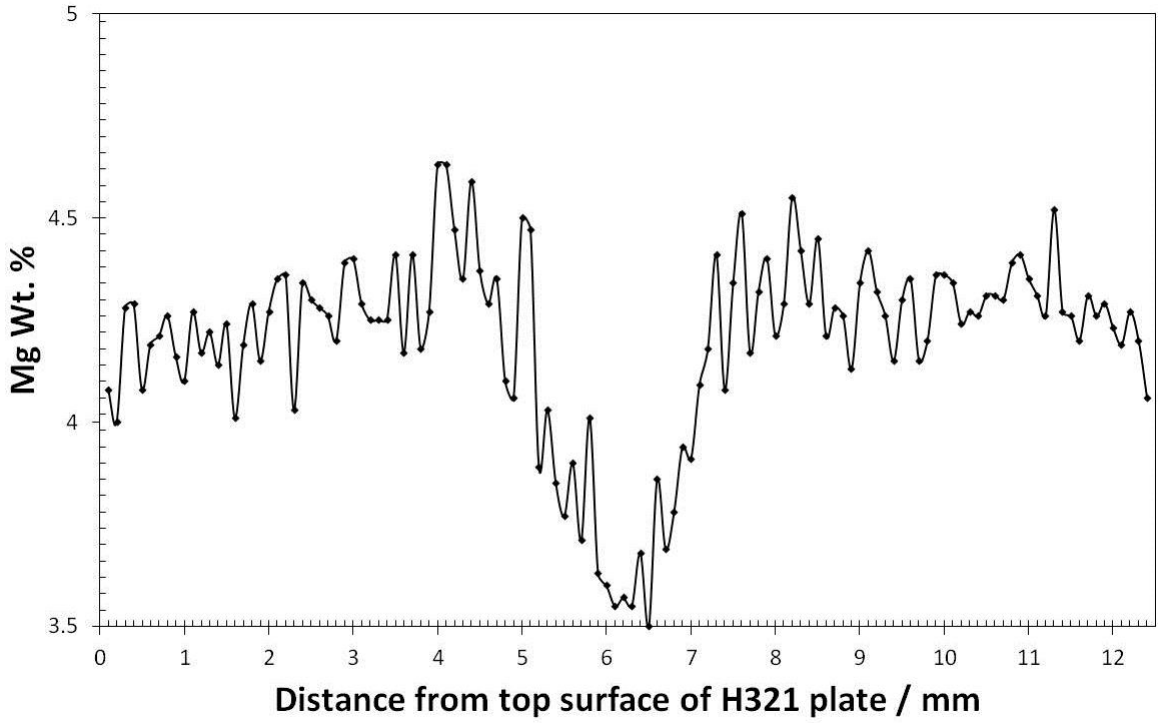

Figure 37 Graph illustrating the through-thickness magnesium variation from EDS area scans through the depth of AA5083-H321 plate. Each point is the average wt.% of an area 100 µm (vertical) by 500 µm (horizontal) centred with the position shown in the x-axis of the graph.

Table 3 Typical composition of AA5083-H321 [182].

	Al	Mg	Si	Fe	Cu	Mn	Cr	Zn	Ti
wt. %	bal	4.0-4.9	0.4	0.4	0.1	0.4-1.0	0.05-0.25	0.25	0.15

4.1.3. Observations of microstructure and intermetallic particles in AA5083 plate

Figure 38 illustrates the distribution of coarse intermetallic phases through the matrix when seen through the ST-LT direction. Two distinct types of particles are present, shown clearly in Figure 38 (b) and (d) as light and dark particles relative to the matrix. Both figures also indicate, as expected, there is no obvious difference which exists between the distributions of these particles in the H321 temper and the sensitised condition. Figure 39 shows an example of each type of constituent particle from the H321 and sensitised plate, imaged using back scattered electrons (BSE).

The results of EDS analysis, shown in Table 4 and Table 5, identify the lighter particles observed in the matrix as being enriched with Fe, Mn and Si or Fe and Mn. These have been identified elsewhere as either Al(MnFeCrSi) or Al_6(Mn,Fe) [55].

Table 6 shows the darker phases to be composed of mostly Mg and Si, so are likely to be Mg_2Si intermetallics. Figure 40 shows a plot of Mg (wt%) vs. Si(wt%) in the intermetallic particles. The broken line connects the ratio in the matrix with the ratio expected for stoichiometric Mg_2Si, to take into account the signal that would be generated if the EDX signal came from a mixture of particle and matrix. However, the measured composition of the particles shows a considerably lower Mg/Si ratio than that predicted by the broken line, suggesting that the Mg composition is much lower than is to be expected from Mg_2Si.

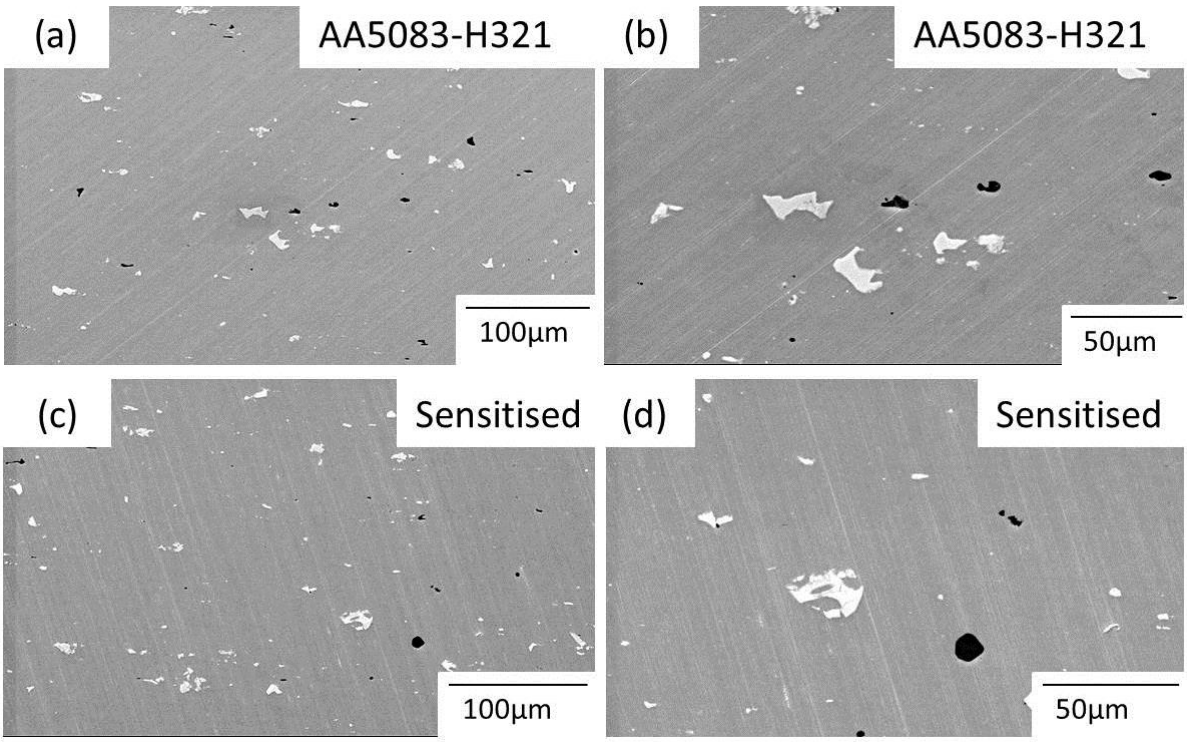

Figure 38 Back-scattered electron images of AA5083 plate after polishing, showing the distribution of intermetallic particles in the Long Transverse -Short Transverse (LT-ST) plane of (a) and (b) H321 plate, (c) and (d) sensitised plate (100 hours @ 150 °C).

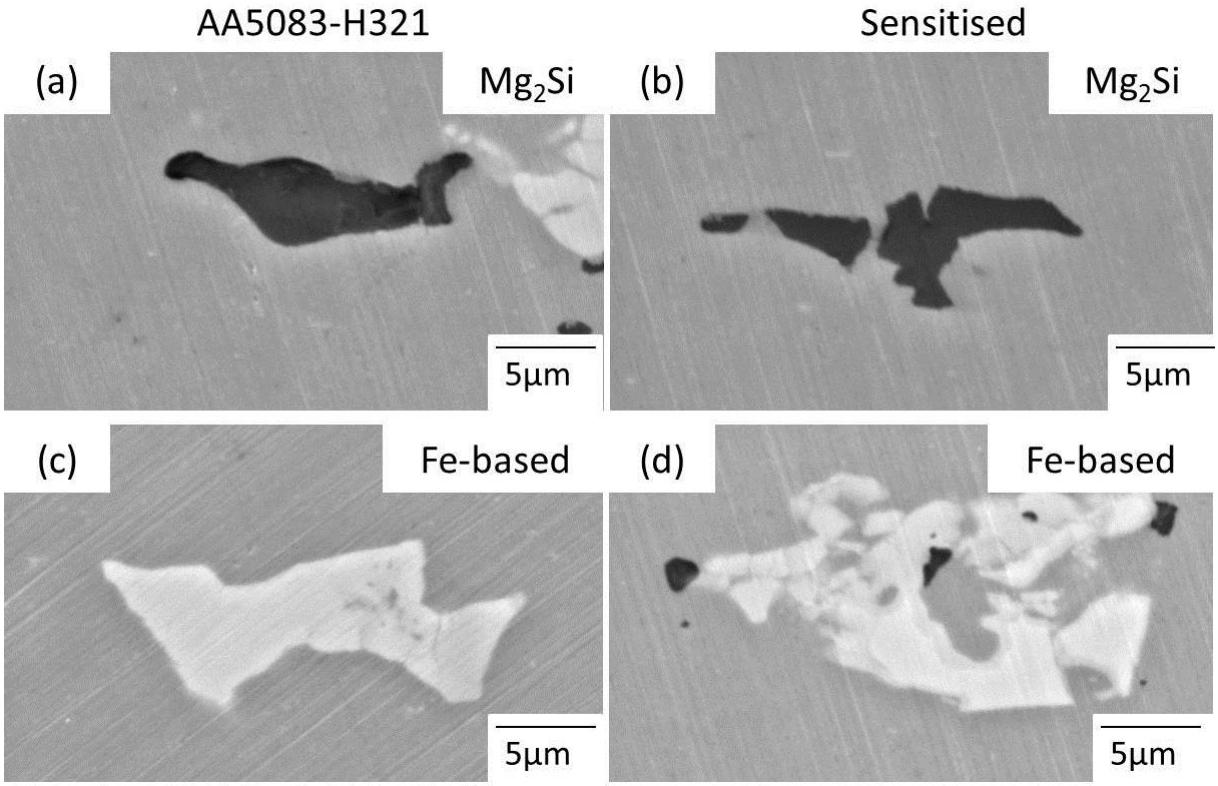

Figure 39 Details of intermetallic particles from the ST-LT plane: (a) BSE $Mg_{(2)}Si$ in AA5083-H321 plate; (b) BSE $Mg_{(2)}Si$ in AA5083-sensitised plate; (c) BSE Fe-based intermetallic particle in AA5083-H321 plate; (d) BSE Fe-based intermetallic particle in AA5083-sensitised plate.

Table 4 Summary of EDS analysis from the white phases in the AA5083-H321 base plate LT-ST section which contain silicon. Acceleration voltage is 13 kV.

	Wt. % of Element in spectrum								
Element	1	2	3	4	5	6	7	8	Average
Aluminium	61.5	61.7	61.1	61.0	61.1	61.3	61.6	60.9	61.3 ± 0.3
Silicon	3.9	3.7	3.8	3.9	3.9	3.5	3.6	3.9	3.8 ± 0.2
Manganese	13.9	13.8	13.7	13.6	14.1	14.1	14.9	15.7	14.2 ± 0.7
Iron	20.7	20.3	20.2	20.5	20.0	20.1	19.9	18.2	20.0 ± 0.8
Chromium		0.7	1.2	1.1	1.1	1.0		1.2	1.0 ± 0.2

Table 5 Summary of EDS analysis from the white phases in the AA5083-H321 base plate LT-ST section which do not contain silicon. Acceleration voltage 13 kV.

	Wt. % of Element in spectrum								
Element	1	2	3	4	5	6	7	8	Average
Aluminium	70.5	69.6	69.2	71.6	69.7	69.8	69.5	70.6	70.0 ± 0.8
Manganese	11.9	11.1	12.6	11.3	12.7	10.6	13.1	9.4	11.6 ± 1.3
Iron	17.1	18.8	17.9	16.7	17.6	19.6	17.4	20.1	18.1 ± 1.2
Chromium	0.6	0.5	0.3	0.5					0.5 ± 0.1

Table 6 Summary of EDS analysis from the black phases in the AA5083-H321 base plate LT-ST section. Acceleration voltage 13 kV.

	Wt. % of Element in spectrum								
Element	1	2	3	4	5	6	7	8	Average
Magnesium	40.8	45.2	42.3	42.1	47.1	40.2	34.6	45.0	42.2 ± 3.9
Aluminium	5.2	3.8	4.5	2.9	1.5	4.9	0.9	3.9	3.4 ± 1.6
Silicon	54.1	41.0	53.2	55.0	51.4	54.9	64.5	51.2	53.2 ± 6.4

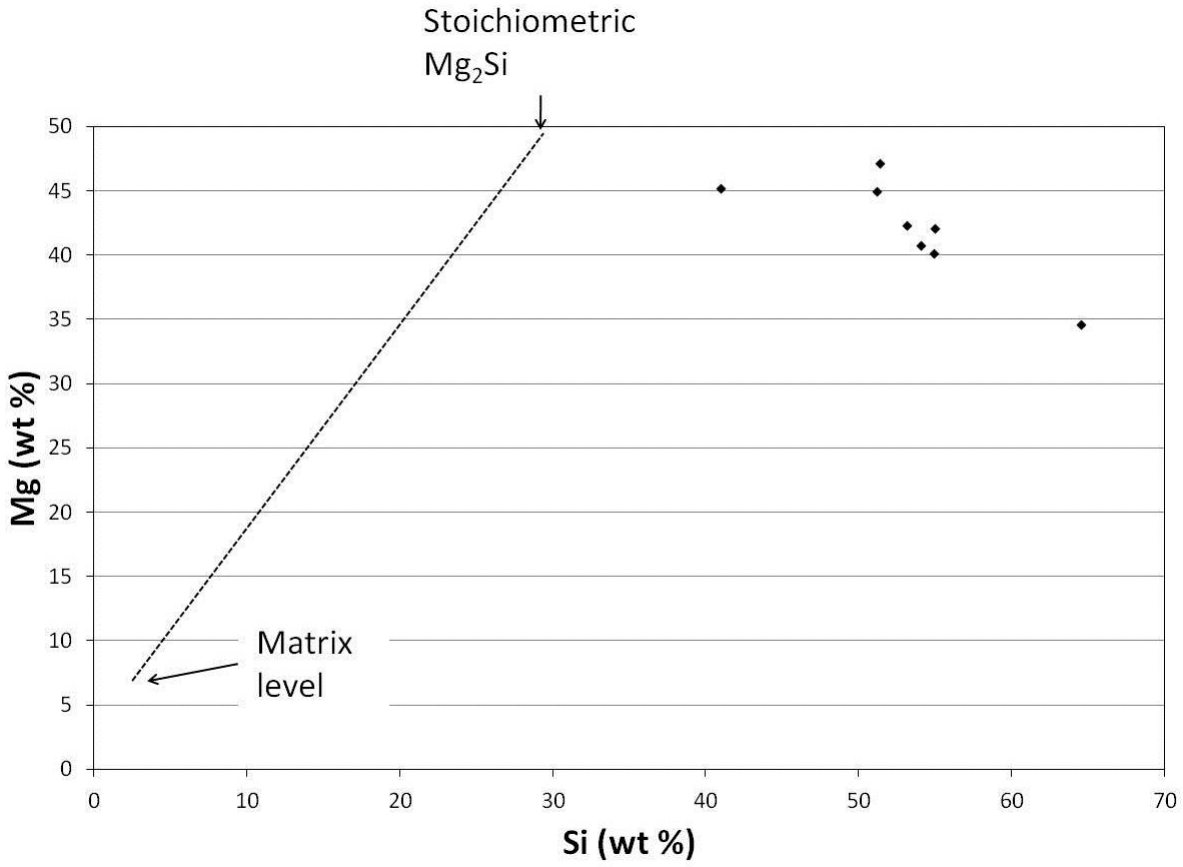

Figure 40 EDS spectra from darker particles identified as containing Mg and Si, plotted against the expected stoichiometric composition of Mg_2Si. Sample polished with 0.04 µm colloidal silica.

4.2. Effect of processing on microstructure

4.2.1. Optical observations of FSP nugget region

Figure 41 shows the appearance of the welds in the ST-LT direction (plate cross section), looking at the profile of the weld after etching in Keller's Reagent. In the low power welds (a) and (b), light and dark bands are evident on the advancing (right) side of the weld nugget. Since the same pattern is not visible in either of the high power processed regions, the phenomenon seems to be attributed to the speed at which the tool is rotating rather than the tool advancement per revolution, which is constant across both processing powers.

A dark band can be seen at the midline of both welds through the sensitised plate (b) and (d). This coincides with the band of low Mg wt.% seen in Figure 37, and demonstrates that the different compositions found within AA5083 etch differently.

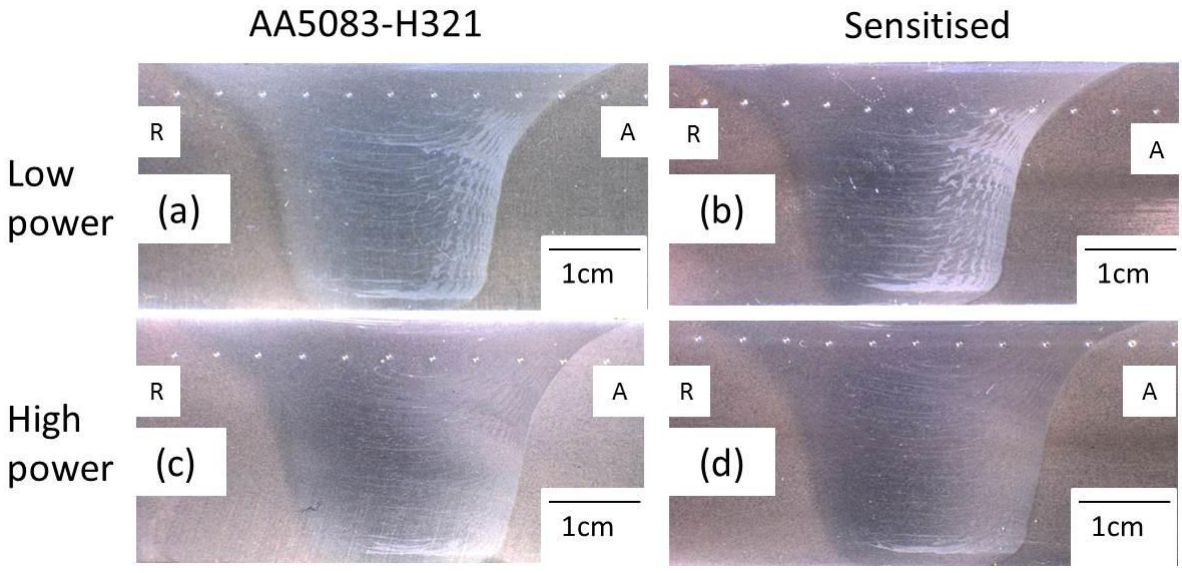

Figure 41 Macroscopic picture of cross sections of processed regions etched in Keller's reagent (a) low power weld in AA5083-H321 plate (b) low power weld in sensitised plate (c) high power weld in AA5083-H321 plate (d) high power weld in sensitised plate.

The appearance of the intermetallic particles in the weld nugget after processing is shown in Figure 42. The rotating action of the tool has broken up the small intermetallic particles as it advances into many more, even smaller particles, and has deposited these in a more homogeneous fashion than those in Figure 39. It can be seen that the particles are much smaller in shape, greater in number and more regular in appearance.

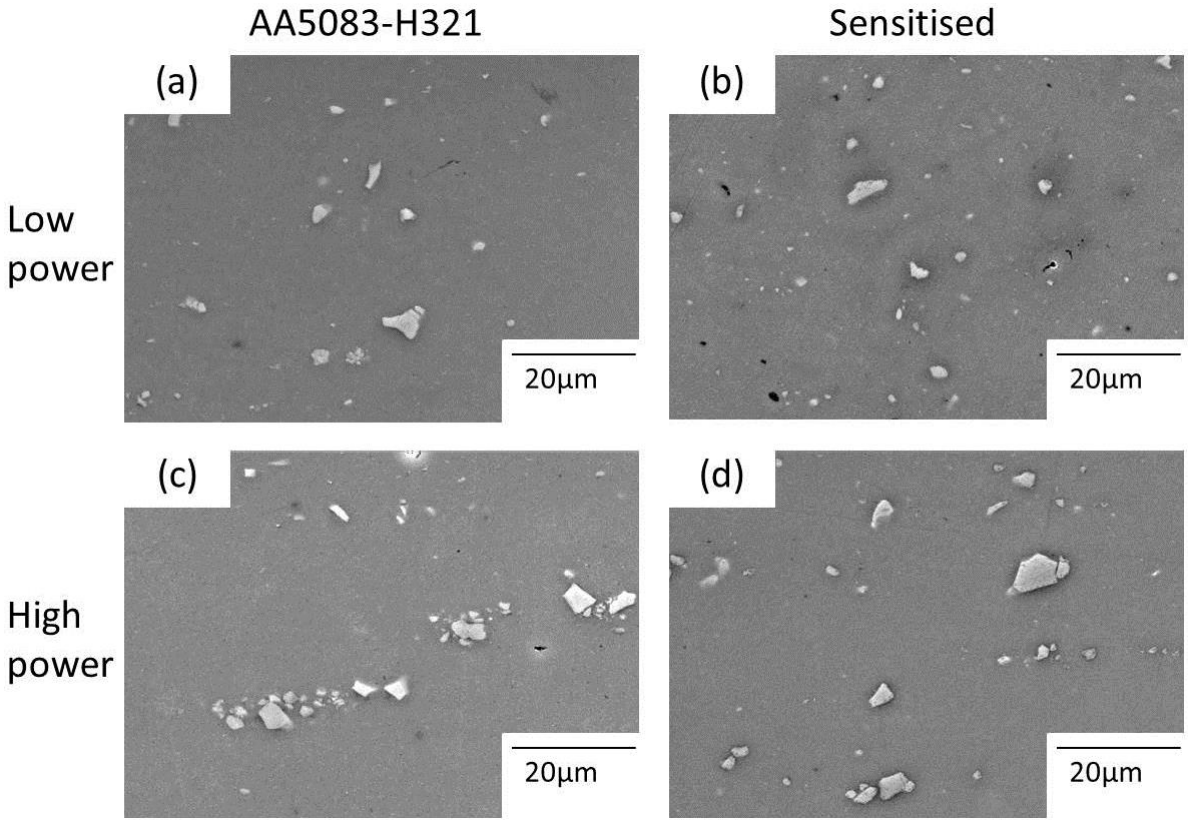

Figure 42 SEM images of intermetallics in the weld nugget after processing (a) BSE of low power weld on AA5083-H321 plate; (b) BSE of low power weld on AA5083-sensitised plate; (c) BSE of high power weld on AA5083-H321 plate; (d) BSE of high power weld on AA5083-sensitised plate.

4.2.2. Hardness

Figure 43 demonstrates the difference in hardness measured on the ST-LT face seen between the AA5083-H321 and sensitised plate. The hardness is consistently seen to be higher in the H321 plate, where the average is 96 Hv, compared with the sensitised plate, which has an average value of 87 Hv.

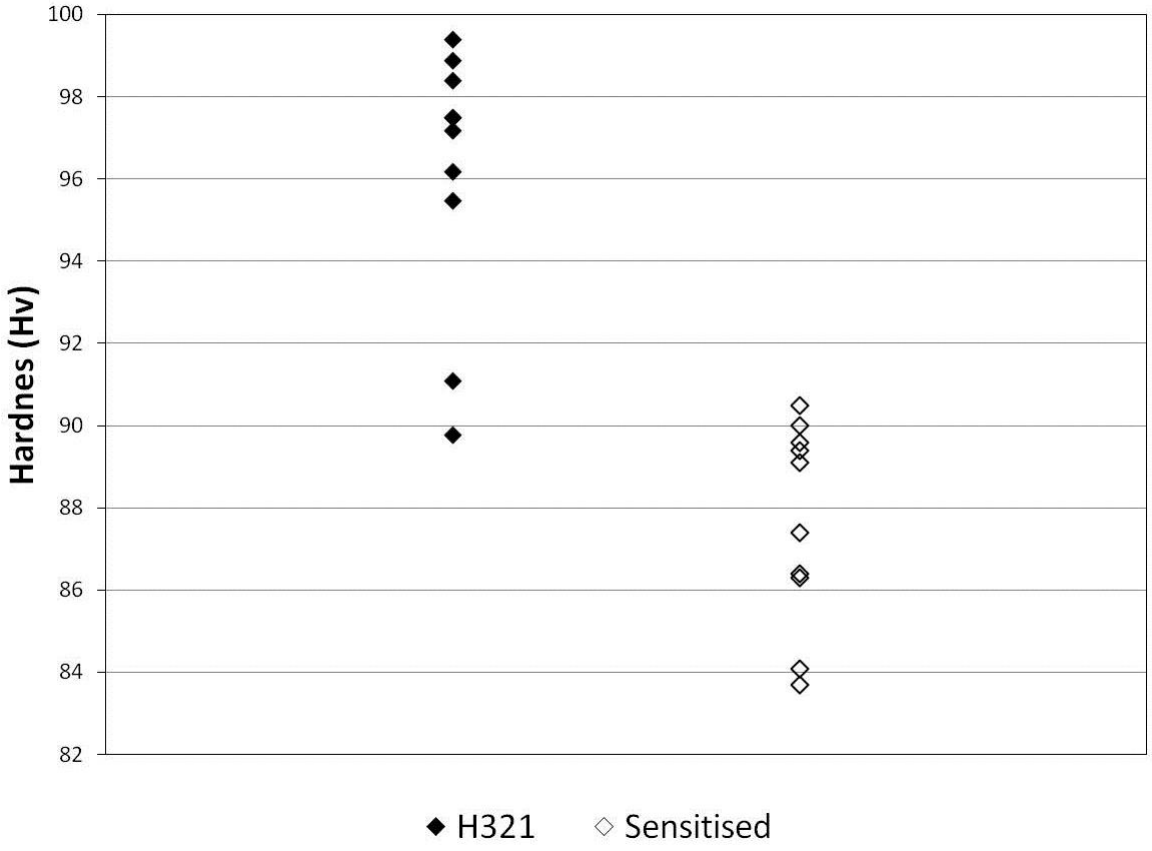

Figure 43 The hardness of AA5083 (a) H321 and (b) sensitised plate measured in the cross section of the plate, 2 mm from the top edge, using an Indentec Vickers hardness testing machine with a load of 5 kg.

Figure 44 shows the hardness variability seen after high and low power processing in the H321 and sensitised plate. The advancing side of the weld is denoted by the letter “A” as opposed to the retreating side, “R”. All welds show lower hardness values in the HAZ, closer to the weld centreline. Each hardness profile reaches a lowest value of 79-84 Hv 5 mm from the centreline on the advancing side where the HAZ/TMAZ interface occurs. At this point, the hardness profile of the low power welds rises sharply and returns to values close to those seen in the sensitised plate (91 Hv). The high power welds, in contrast, have relatively low hardness values (82 Hv) that are consistent through the processed area. On the advancing side of the weld (right side of Figure 44) the hardness is seen to return to levels seen in the H321 plate (~97 Hv).

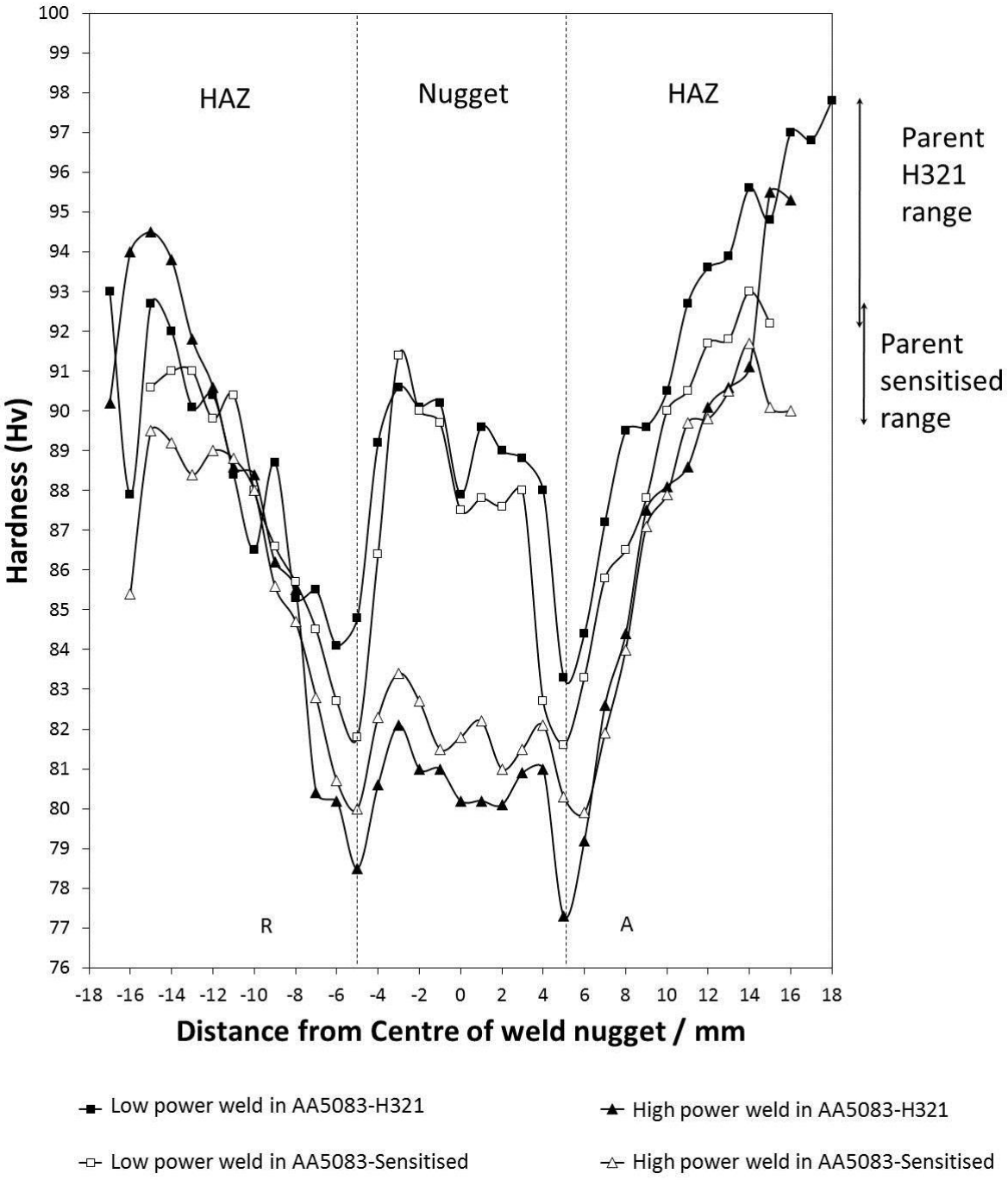

Figure 44 Graph showing hardness across all four welds, measured 2 mm below the surface of the plate using an Indentec Vickers hardness testing machine with a load of 5 kg. "R" and "A" refer to the retreating and advancing sides of the weld, respectively.

4.2.3. Effect of processing on sensitised microstructure

An indication of the amount of β-phase located on grain boundaries before and after processing and sensitisation can be gathered from the degree to which samples etch in 60 °C phosphoric acid, which selectively attacks β-phase [183]. Figure 45 (a) shows the microstructure of the H321 plate after etching, revealing no grain boundary attack, implying that β-phase has not segregated to the grain boundaries as the exposed surface has only been etched around intermetallic particles. After sensitisation, in Figure 45 (b), all of the grain boundaries have been selectively etched, providing evidence that they contain β-phase that has segregated there during sensitisation.

To study the effect of sensitisation on processed regions, the same etch was used on the 4 FSP'd areas, either in the H321 or sensitised plate. Figure 45 (c) and (e) show no sign of grain boundary attack, indicating that the action of the FSP on H321 plate does not put significant amounts of β-phase onto the new grain boundaries formed after processing.

Figure 45 (d) and (f) show that the thermomechanical effects of processing dissolve β-phase from the sensitised boundaries and produce a microstructure in which the β-phase does not form on grain boundaries that was present in the sensitised condition. However a small amount of discontinuous attack still exists, showing a similar state to that of the weld nuggets in the H321 plate.

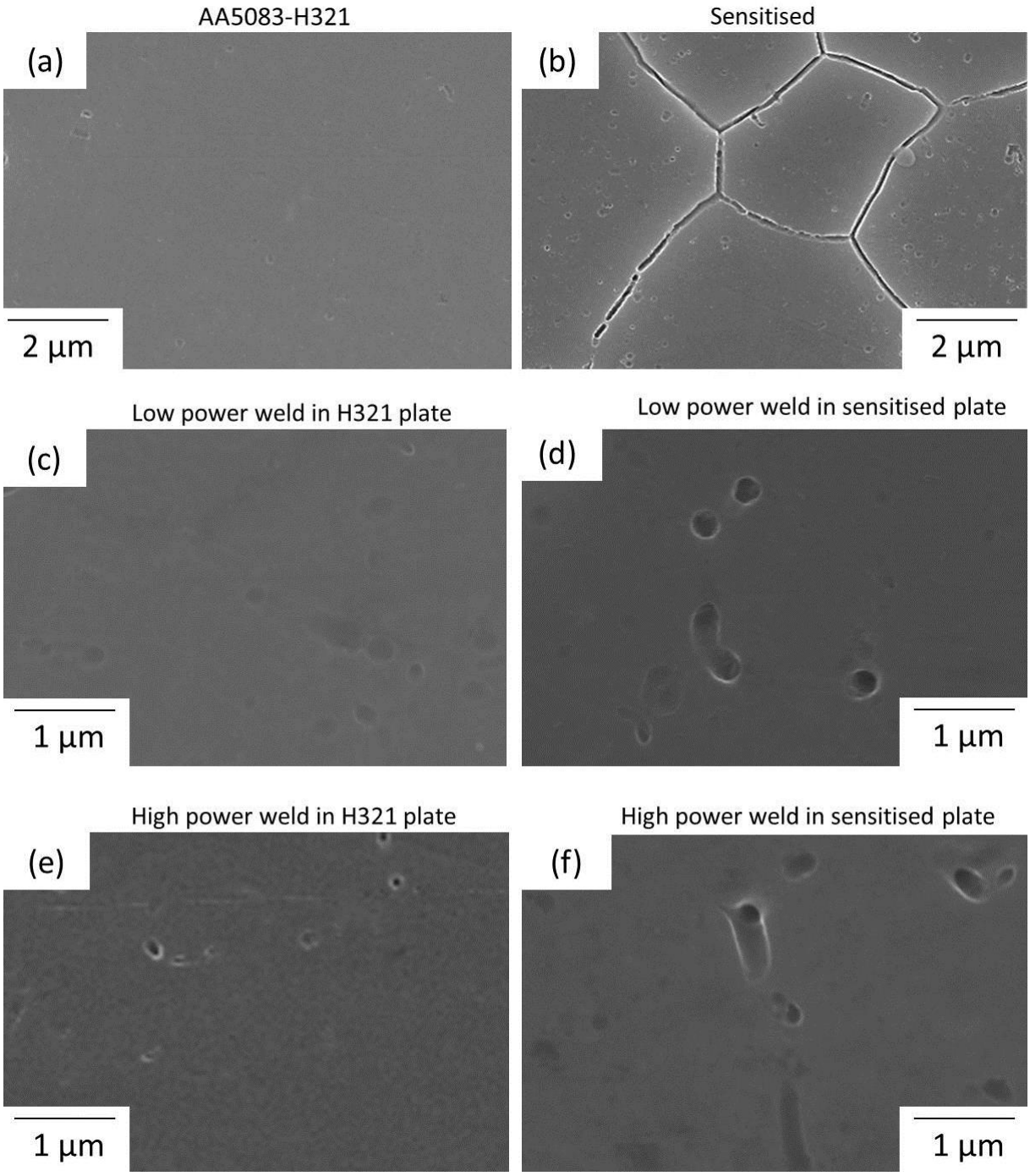

Figure 45 SEM micrographs taken of the cross section after etching samples in phosphoric acid at 60°C for 90 seconds: (a) AA5083-H321 parent plate; (b) AA5083-sensitised parent plate; (c) low power weld nugget in AA5083-H321 plate; (d) low power weld nugget in sensitised plate; (e) high power weld nugget in AA5083-H321 plate; (f) high power weld nugget in sensitised plate.

4.2.4. TEM investigation into fine-scale microstructure

The use of TEM is considered to be particularly important as it is only by direct imaging that the occurrence of the β-phase can be properly visualised. To this effect, TEM micrographs have been taken of the various conditions under investigation in order to assess the presence of the β-phase.

Figure 46 (a) and (b) show two typical grain boundaries observed in the AA5083 H321 plate. Both grain boundaries are clean and clear of any precipitates; this was observed for 50+ other grain boundaries in this condition. Figure 47 shows a composite TEM micrograph of a grain boundary in the sensitised plate. The grain boundary is decorated with precipitates up to 50 nm in thickness and regions of continuous and discontinuous precipitation. Sub grain boundaries are also visible in this condition, Figure 48, where the low temperature, long time heating (100 h at 150 °C) has led to some recovery of structure and the formation of low angle sub grain boundaries. The low angle nature of these boundaries was confirmed by observing the slight variation in diffraction pattern in the TEM as the boundary was crossed with the beam.

EDS point sampling was conducted on the matrix of the sample and on the grain boundary to determine the elements present in each place, Figure 49 (a) and (b). In the matrix, the magnesium content was measured at 4.5 wt. % with the rest aluminium. In the surveyed grain boundary area the magnesium content was much higher, at 13.5 wt. % with the rest aluminium. While not reaching the stoichiometric levels expected for Al_3Mg_2, which was believed to be due partly to a drift in the TEM beam during measurements, an increase in magnesium content is observed as is to be expected with segregation and precipitation.

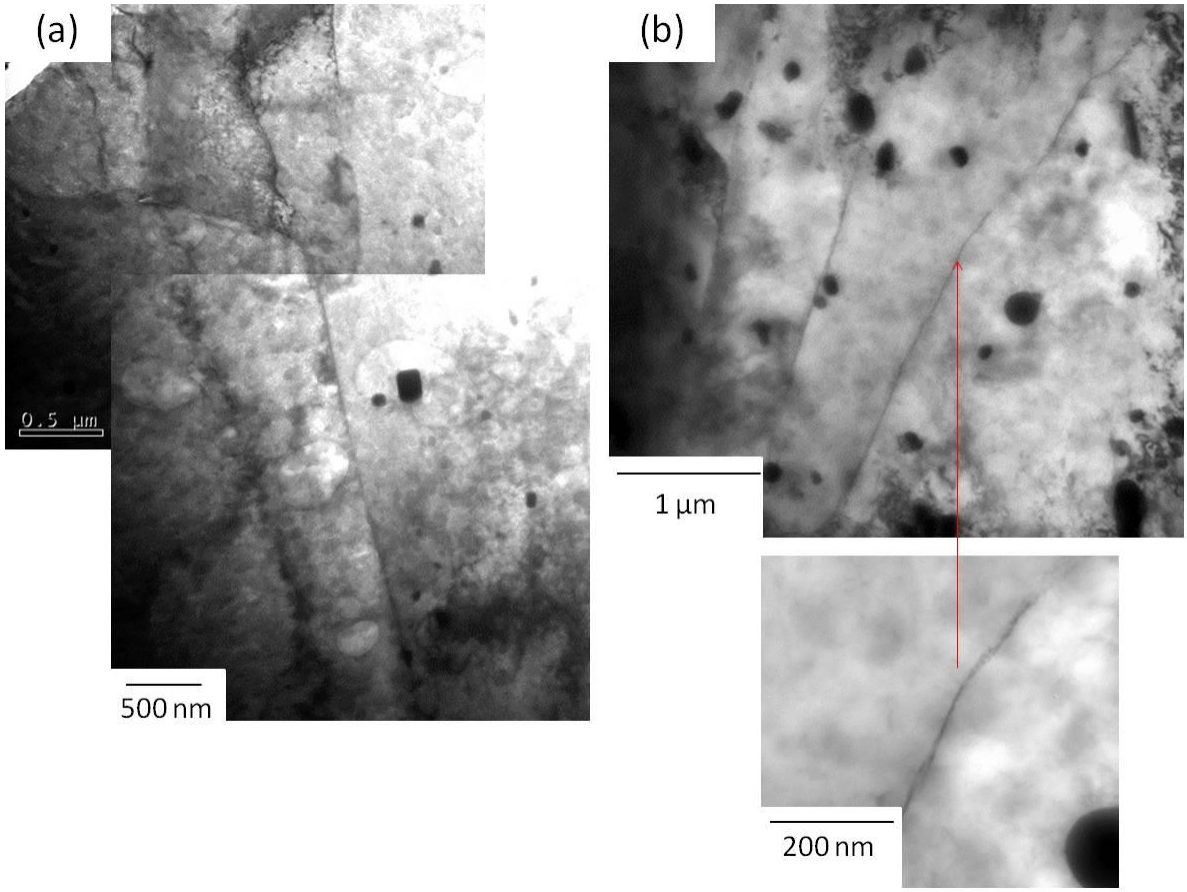

Figure 46 (a) and (b) TEM micrographs from the AA5083-H321 base metal.

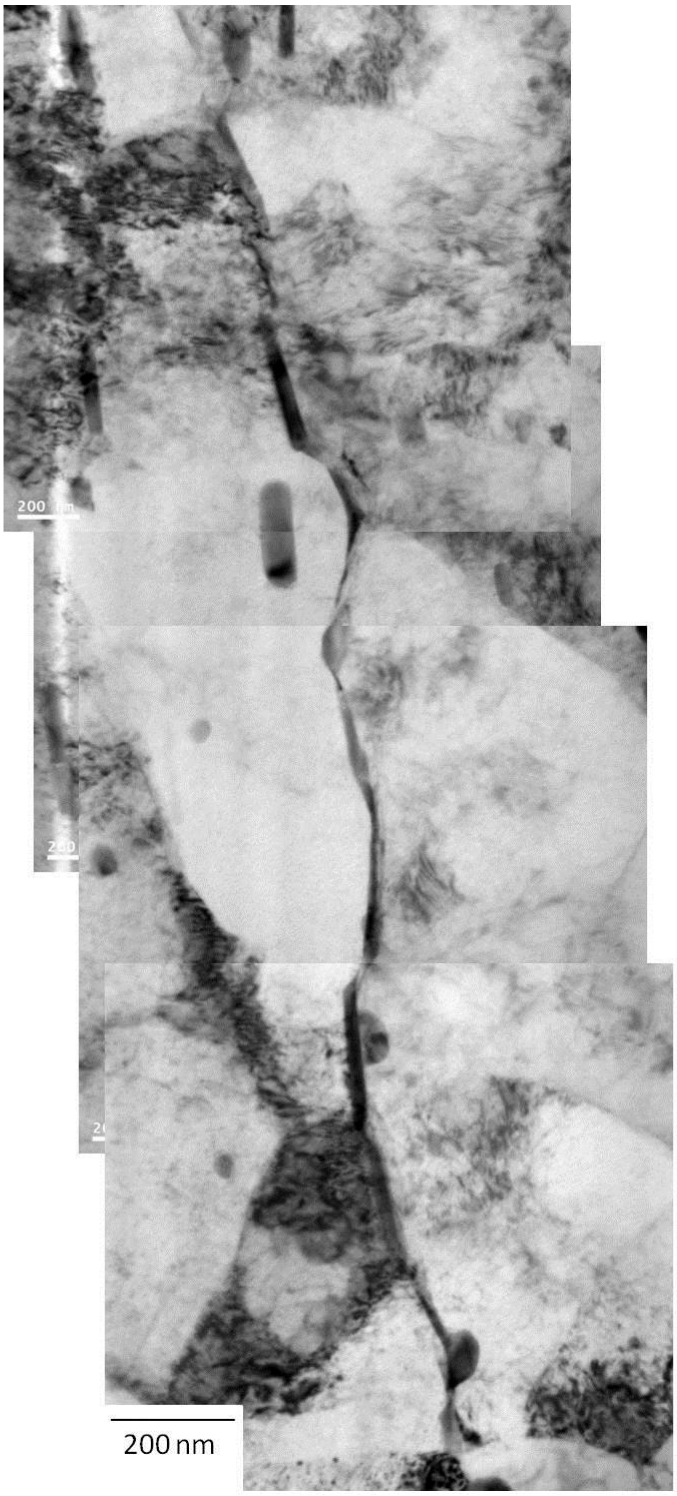

Figure 47 Composite TEM micrograph of a grain boundary from AA5083-H321 sample sensitised at 150 °C for 100 hours, showing precipitates on a grain boundary

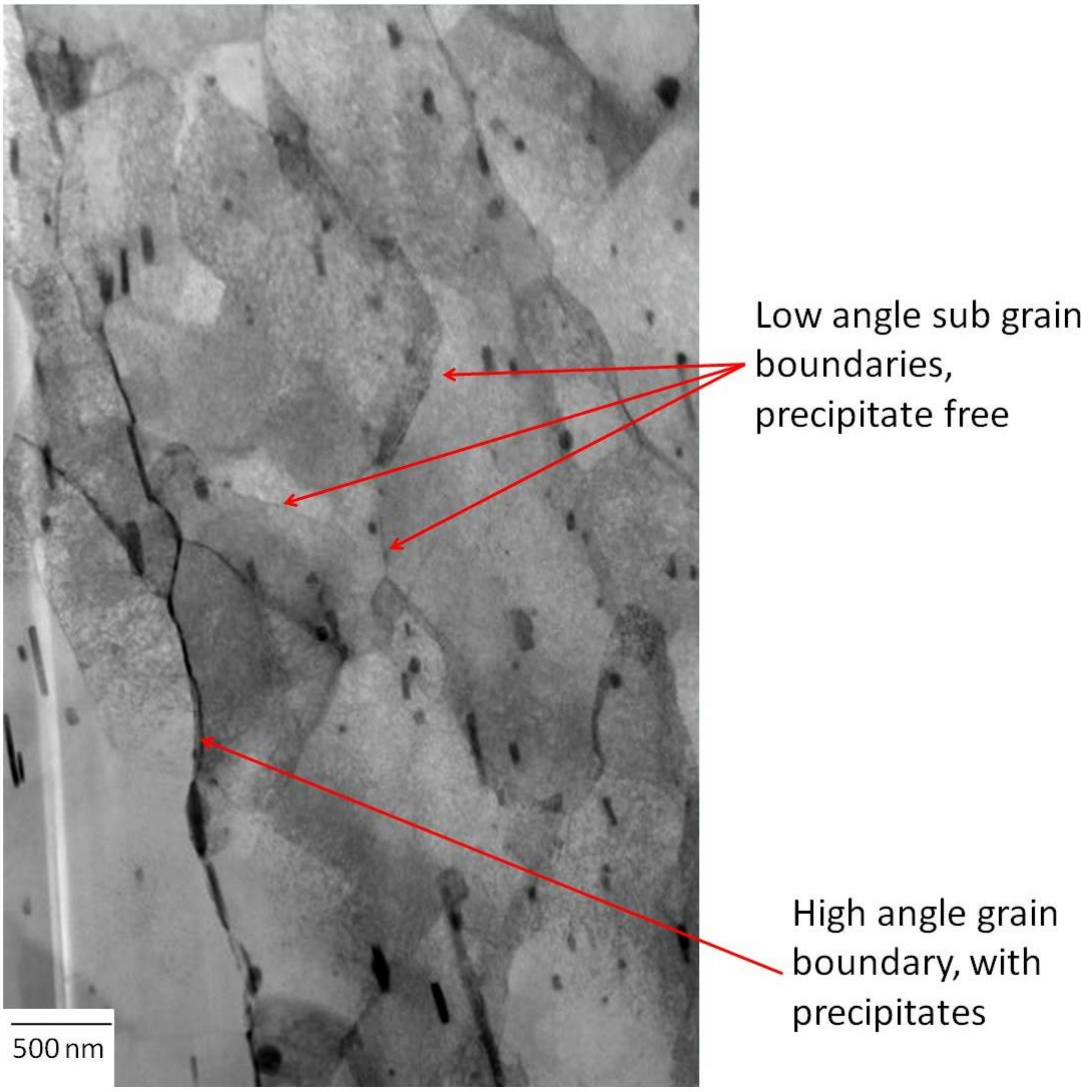

Figure 48 TEM micrograph of the AA5083-sensitised plate where high and low angle sub-grain boundaries are highlighted.

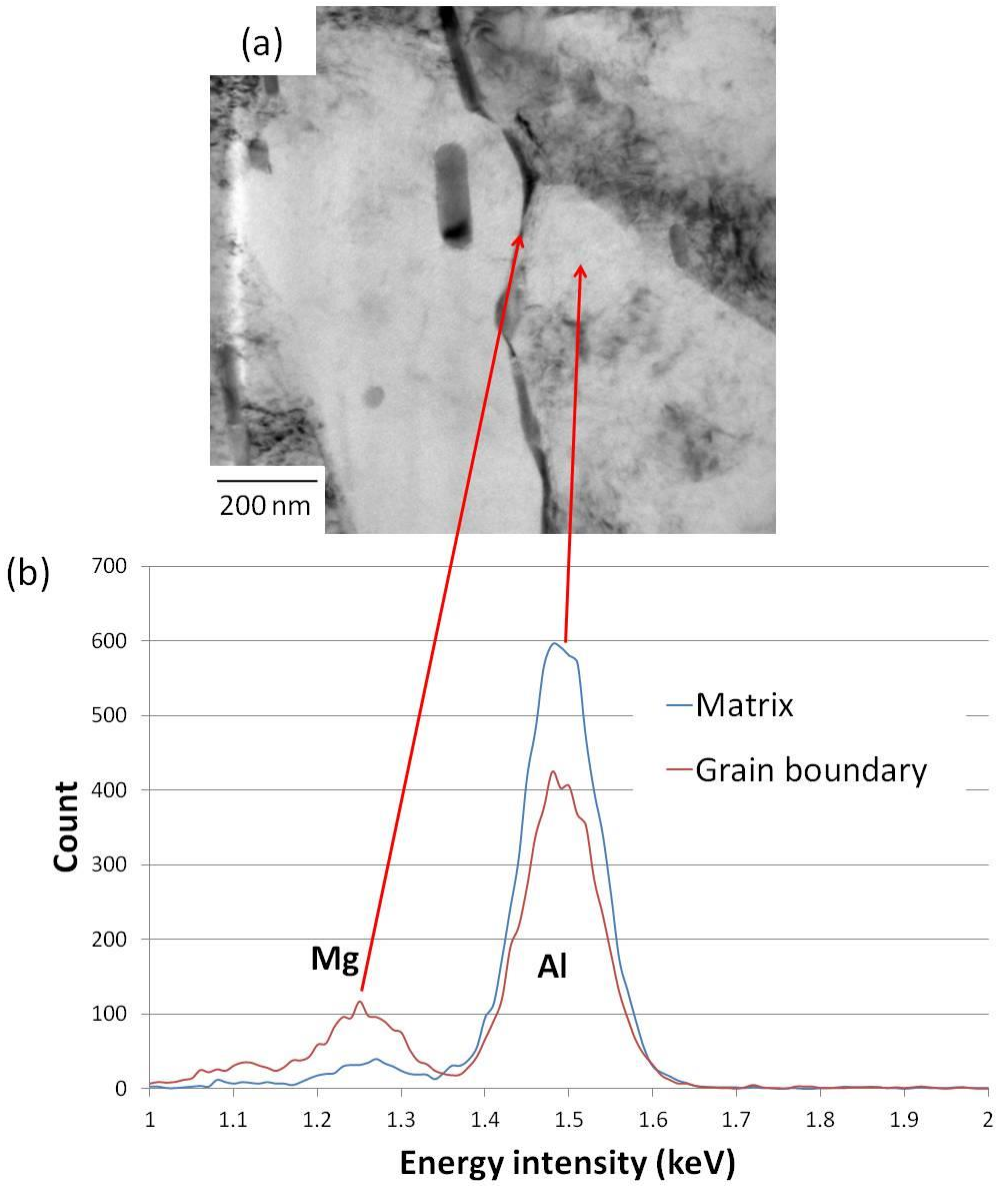

Figure 49 (a) TEM micrograph from the sensitised sample, (b) Graph displaying EDS data from the matrix region and from a grain boundary phase.

To further ascertain the distribution of precipitates, EDS mapping was carried out with a Scanning TEM equipped with an EDS detector. The area of inspection is shown in Figure 50 (a) where the high angle grain boundary seen in Figure 47 runs horizontally, and two low angle sub grain boundaries branch off to the top and bottom of the frame. The high angle grain boundary was identified by observing a marked change in diffraction pattern produced

between two grains, while the sub grains did not show such a change as they are only slightly disorientated from other parts of the grain.

The EDS map of most interest is that of the magnesium, Figure 50 (d), which shows two areas of enrichment on the high angle grain boundary, as discrete precipitates. Interestingly, these locations are also the points of intersections of the main and sub grain boundaries, with no observable enrichment in the area between the two. This area has been highlighted, as has a corresponding region of aluminium depletion, Figure 50(c).

Also present in this scan are several rod shaped Mn-rich particles, around which there are no regions of Mg enrichment, Figure 50 (e). As Gallium was used in the focused ion-beam milling of the sample, it is also present in the EDS scan, Figure 50 (f) where it is seen to lie primarily along the high angle grain boundary.

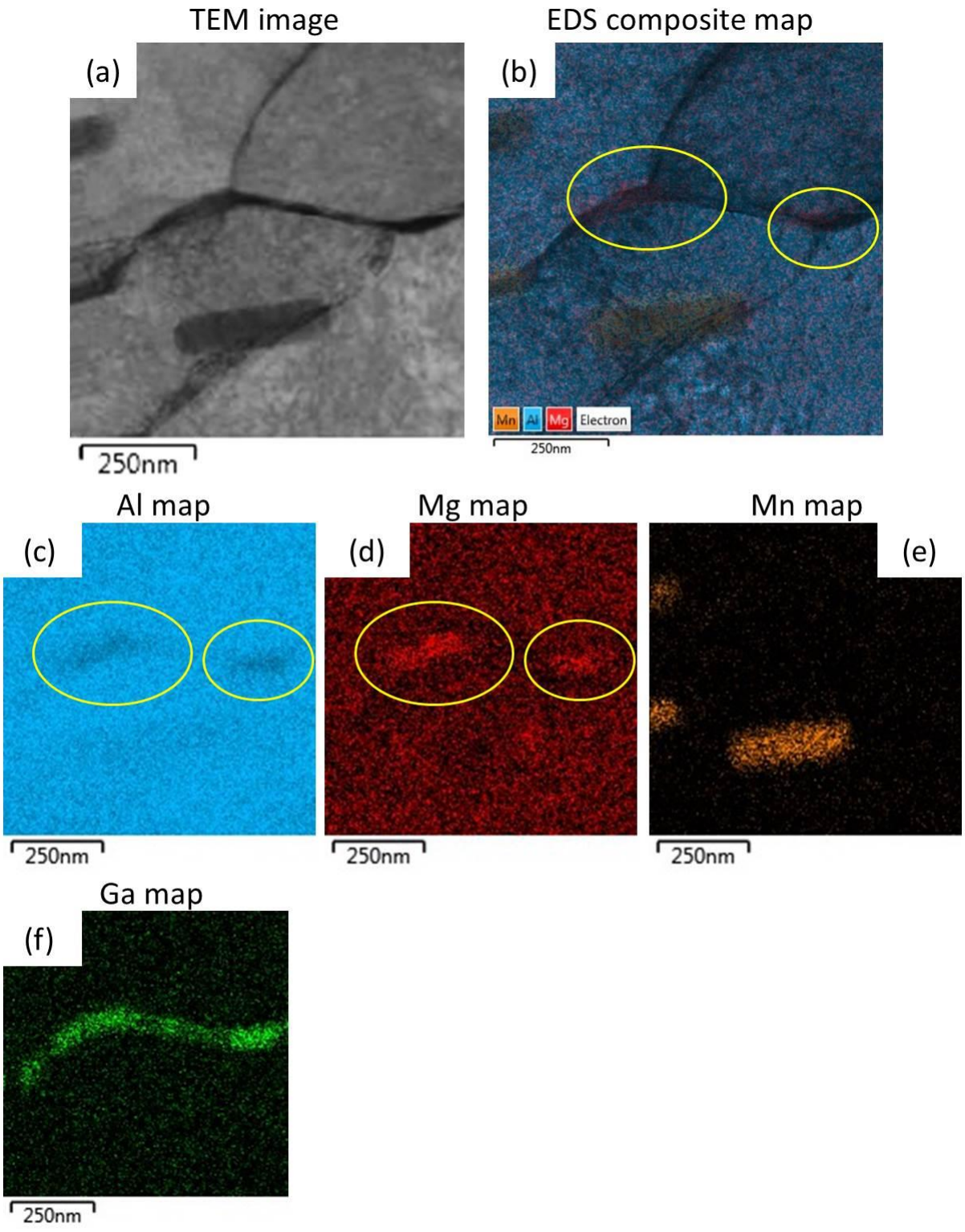

Figure 50 (a) TEM micrograph of grain boundary from AA5083-H321 sample sensitised for 100 hours at 150°C (b) EDS composite map of Al, Mg and Mn constructed using Oxford INCA software in area of inspection, (c)-(f) EDS maps of individual elements from area of inspection in (a). Yellow rings represent comparative areas in composite, aluminium and magnesium maps.

Once the through thickness FSP had been performed, similar TEM micrographs were taken from the nugget and HAZ regions of the high and low power welds. Figure 51 (a) and (c) show the weld nuggets from the low and high power welds, where the grain boundaries once again are free from any precipitates. It is also evident from these micrographs that the grain structure has been refined to the point where grains are a few μm across.

Figure 51 (b) and (d) show equivalent TEM micrographs from the HAZ regions outside of the welds in the sensitised plate. In this region no grain boundary β-phase precipitates were observed in over 50 grain boundaries observed, of which those in Figure 51 are representative.

When comparing the micrographs in Figure 51, fine recystallised grains can be seen in the nugget region, while the grains in the HAZ are much larger, as they are in the base material.

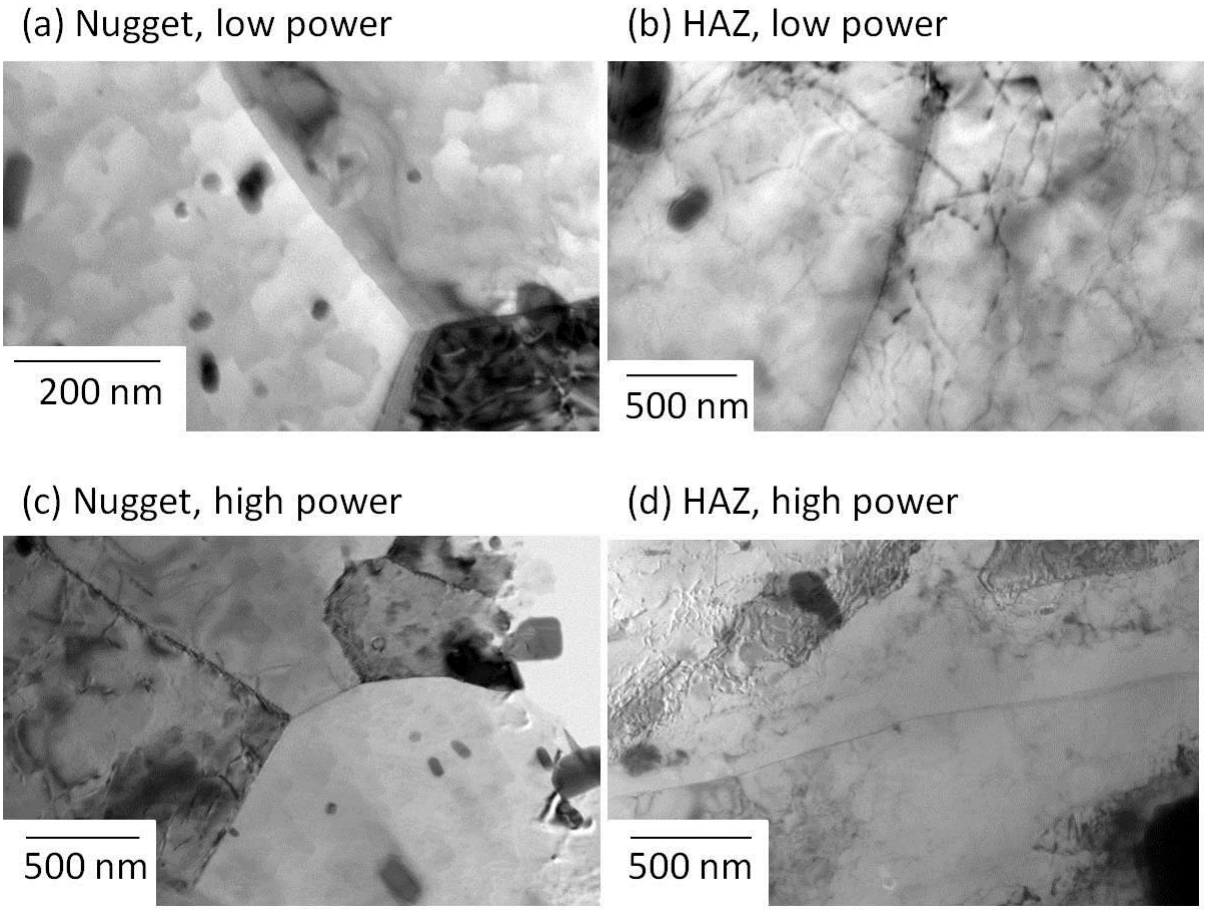

Figure 51 TEM micrographs showing the microstructure of (a) the nugget region of the low powered weld in the AA5083-sensitised plate, (b) the HAZ outside of the low powered weld in the AA5083-sensitised plate (c) the nugget region of the high powered weld in the AA5083-sensitised plate, (d) the HAZ outside of the high powered weld in the AA5083-sensitised plate.

4.3. Corrosion testing

4.3.1. Immersion testing of parent material

Sections of the parent plate and cross sections of processed regions were immersed in 1 M NaCl for 10 days in order to observe the corrosion behaviour that occurred. Figure 52 (a) and (b) show a macroscopic picture of the H321 and sensitised parent sections after having the corrosion product removed. Figure 52 (c) and (e) show the H321 plate to have sites of anodic attack and attack of the matrix around the periphery of Fe-based intermetallic particles, known as cathodic grooving. Most of the sensitised sample displays similar behaviour except for the two large regions of IGC shown in (d) and magnified in (f). In the macroscopic picture of the sensitised sample, a large region that is free from smaller anodic attack can be seen around the IGC cracks.

Figure 53 displays the site of IGC in Figure 52 (b) after etching in Keller's reagent. The grain boundaries in the sensitised material have been made more apparent and the morphology of the intergranular attack can clearly be correlated to the grain size of the material.The only region that has been attacked in the sensitised parent region are the grain boundaries, while no sites of cathodic grooving around intermetallic particles can be seen.

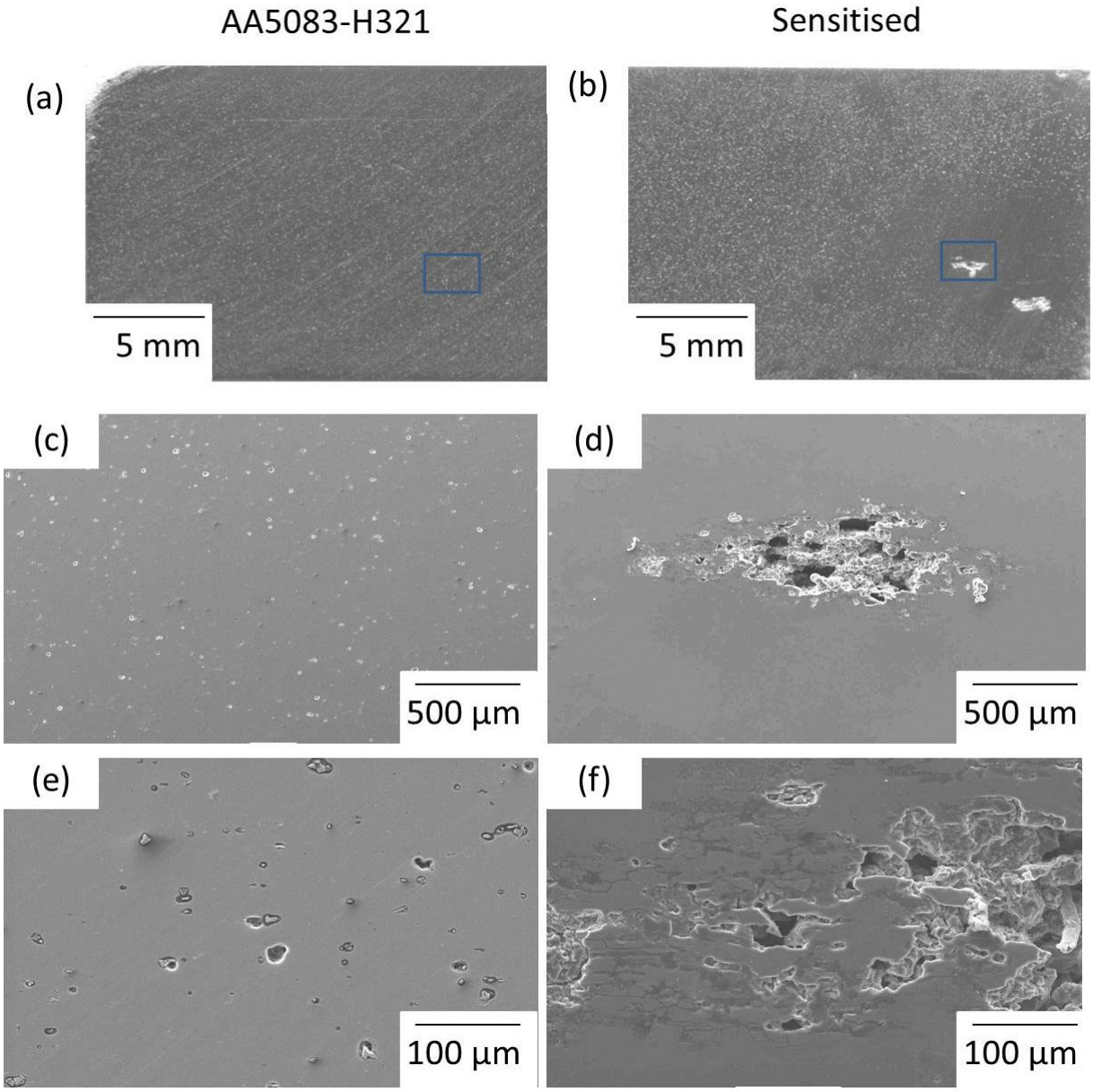

Figure 52 Macroscopic images from (a) AA5083-H321 and (b) AA5083-sensitised samples; showing (c) and (e) evenly distributed localised attack including cathodic grooving on the AA5083-H321 sample; (d) and (f) a large site of IGC on the AA5083-sensitised sample.

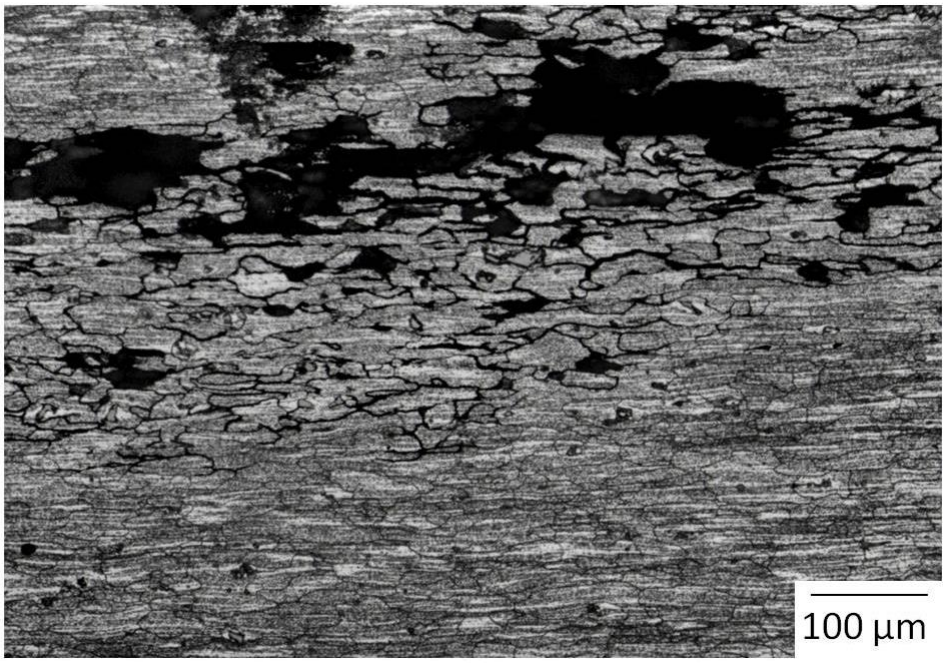

Figure 53 Optical micrograph of a site of IGC in the parent region of a AA5083-sensitised plate after immersion in 1M NaCl for 10 days, then etching in Keller's reagent.

4.3.2. Inspection of the cross section of immersed parent material

Sections of the sensitised parent material were cut to inspect the cross section of the corrosion attack that had occurred on the top surface during immersion in NaCl solution.

Figure 54 shows a vertical section of the sensitised plate in which sites of cathodic grooving around Fe-based particles can be observed. Some grooves completely surround the particles. These sites were not frequently observed, but this is to be expected as they are small in size and are unlikely to be cut through when the plate was sectioned.

The main anodic attack observed was intergranular; typical morphology is shown in Figure 55 (a). For the period of exposure, attack depth ranged from 120-150 μm, and was consistent across all plate regions.

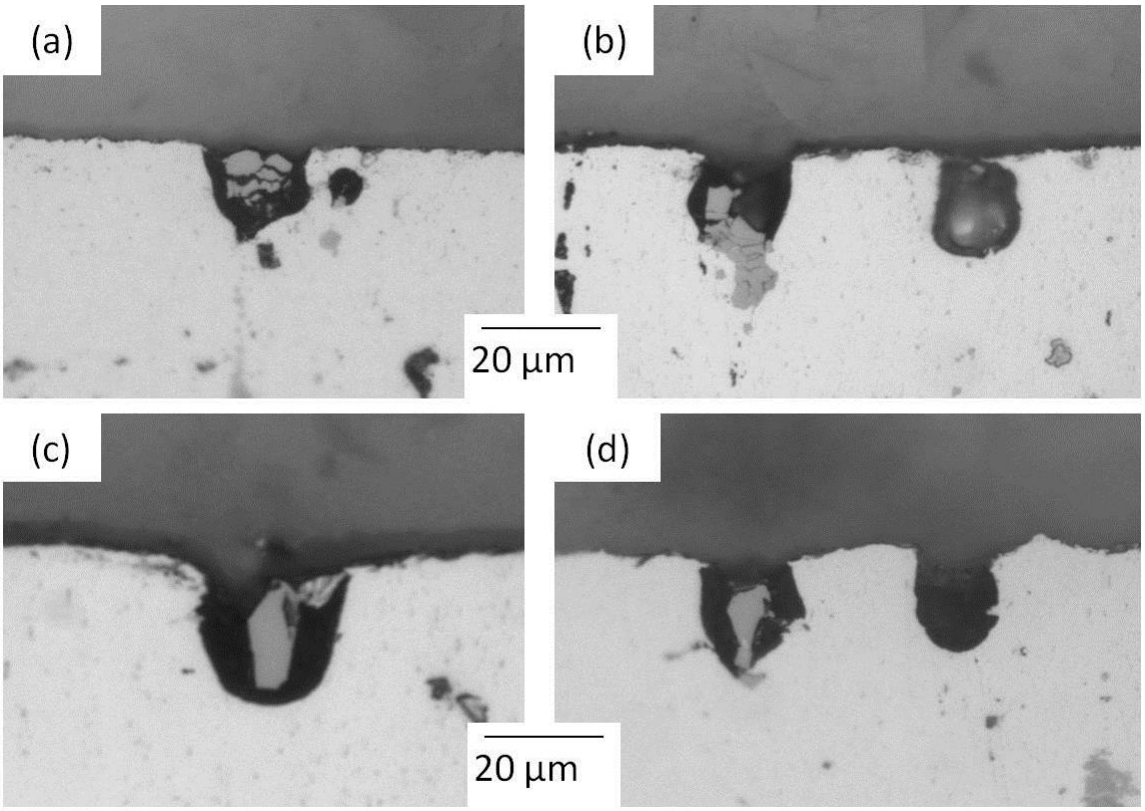

Figure 54 Optical micrographs from the cross section of the AA5083-sensitised parent plate after immersion in 1M NaCl for 10 days showing corrosive attack around the Fe-based particles. This attack is the same cathodic grooving observed from above in Figure 52.

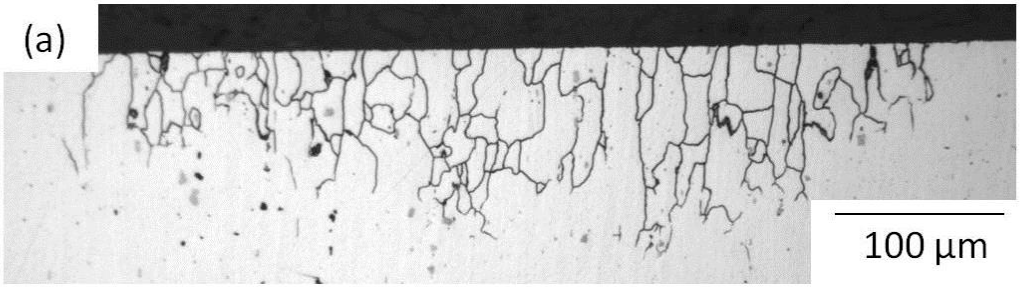

Figure 55 Optical Micrographs from the cross section of AA5083-sensitised parent section after immersion in 1M NaCl for 10 days showing (a) typical intergranular attack up to 100 µm below the surface, which comprised the majority of the attack seen.

4.3.3. Immersion testing of processed material

Corroded cross sections from the H321 and sensitised plates which have been processed are displayed in

Figure 56, where the corrosion product has been left in place. In general, more corrosion product has been deposited on the HAZ and parent material regions than in the nugget of the processed area, especially in the sensitised samples (b) and (d). The lesser degree of corrosion product in the nugget regions indicates that the thermomechanical effects of the processing alter the microstructure sufficiently to reduce its susceptibility to corrosion.

The two sensitised samples (b) and (d), show large deposits of corrosion product in the parent regions furthest from the processed region. This indicates that the most corrosion has taken place in this region, as opposed to the nugget and HAZ created by processing. The base H321 samples show no such deposits, merely low levels of corrosion product across the whole sample.

In the sensitised samples, (b) and (d), less corrosion product can be seen at the midline of the plate, where a lower wt. % of magnesium has previously been observed. This correlation may show regions of lower magnesium content to be less susceptible to corrosive attack.

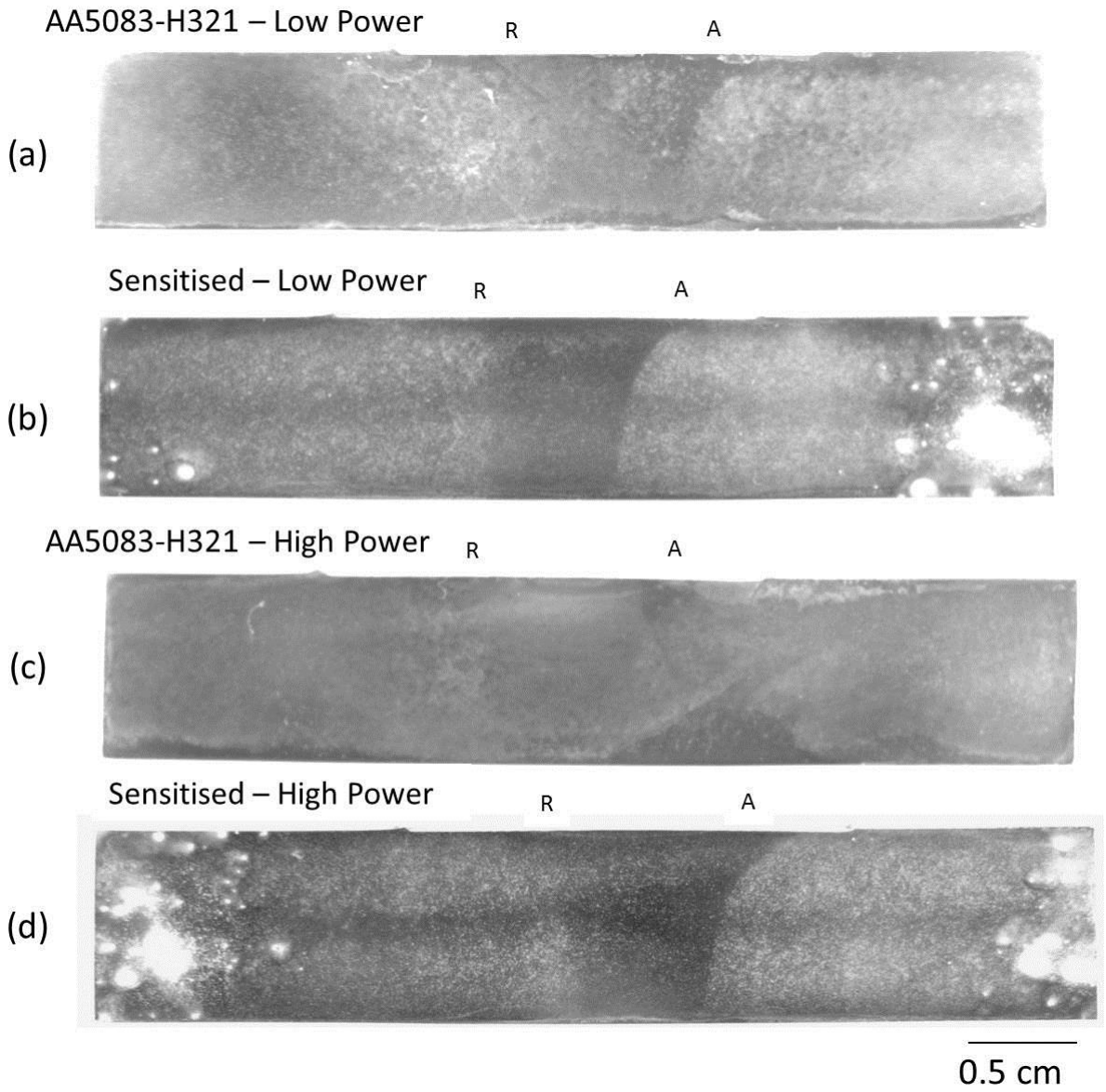

Figure 56 Macroscopic images of the cross sections of processed regions (a) low power processing through AA5083-H321 plate; (b) low power processing through AA5083-sensitised plate; (c) high power processing through AA5083-sensitised plate; (d) high power processing through AA5083-sensitised plate after immersion in 1 M NaCl for 10 days. 'A' and 'R' above each sample denote which side of the nugget was at the advancing and retreating side of the tool piece respectively.

SEM micrographs of the corroded surfaces from the processed H321 and processed sensitised material after the corrosion product has been removed are shown in Figure 57 and Figure 58. While none of the images show clear differences between the high and low power processing through either plates, none of the FSP nugget regions displayed any IGC, leading to the conclusion that FSP has mitigated the risk of IGC, even in a previously sensitised sample.

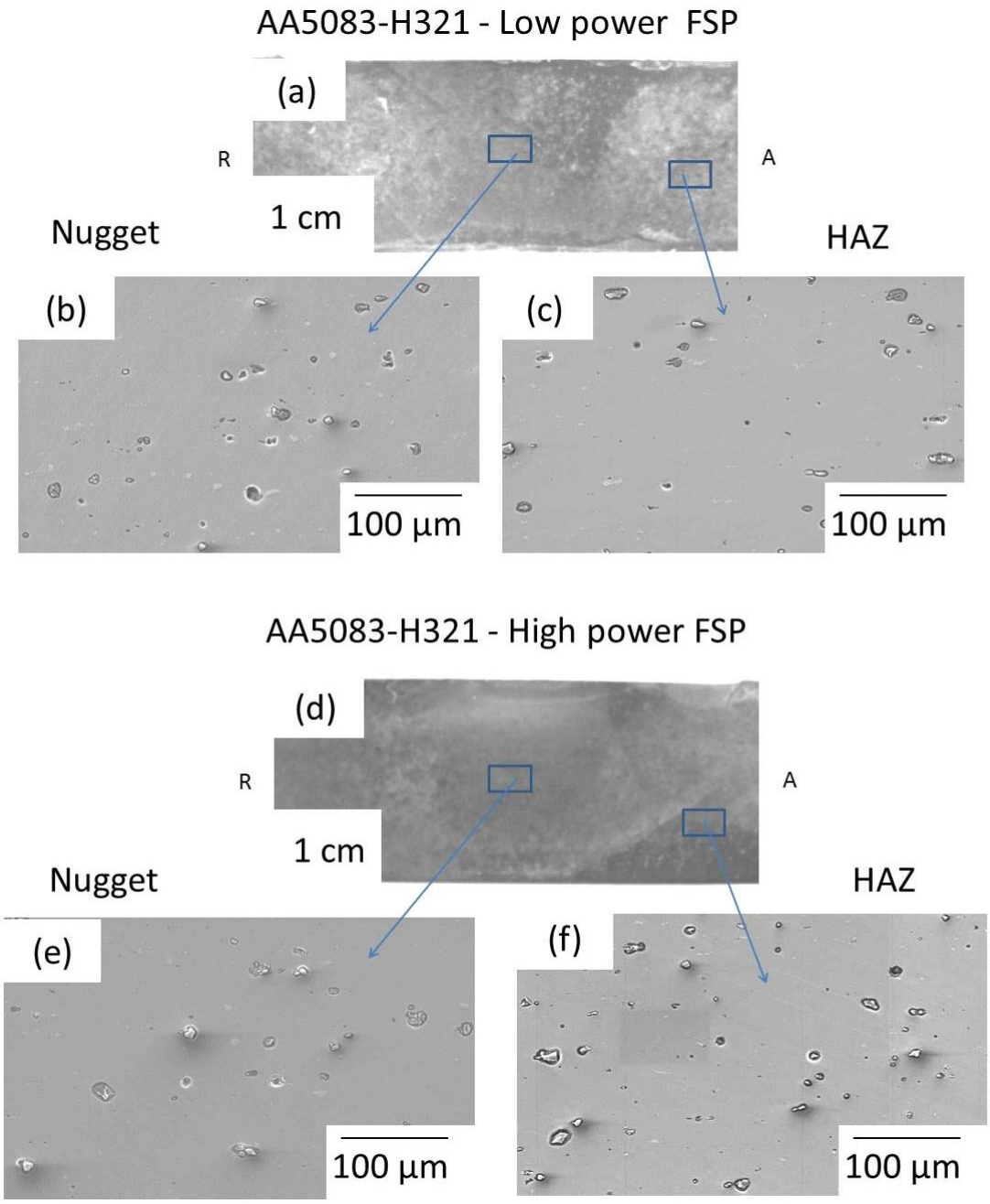

Figure 57 (a) and (d) Macroscopic images of the processed regions in the AA5083-H321 plate after immersion in 1 M NaCl for 10 days. (b) (c) (e) and (f) SEM images of the cross section after immersion with the corrosion product removed

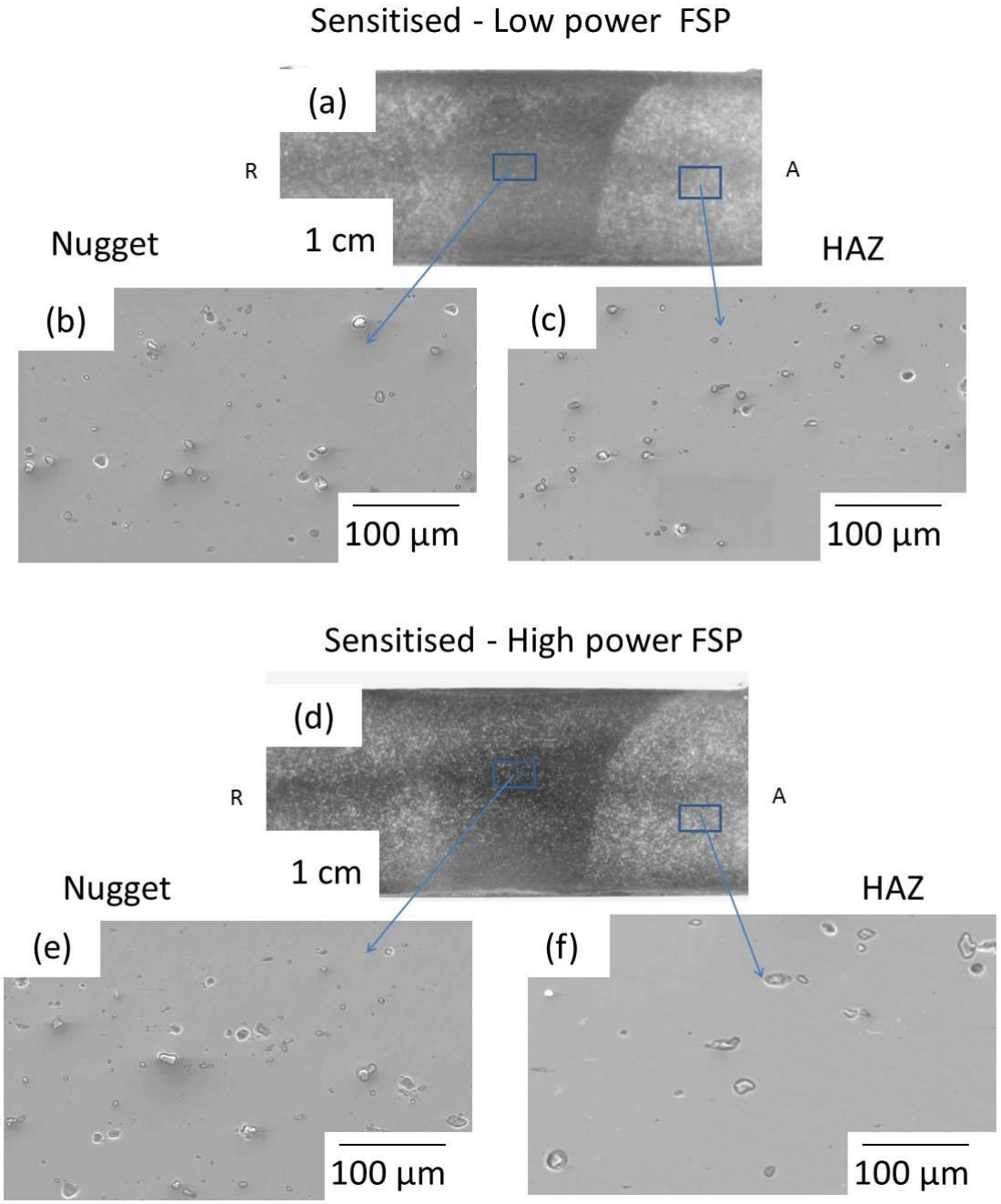

Figure 58 (a) and (d) Macroscopic images of the processed regions in the AA5083-sensitised plate after immersion in 1 M NaCl for 10 days. (b) (c) (e) and (f) SEM images of the cross section after immersion with the corrosion product removed.

In Figure 59 the corrosive attack of the intermetallic particles can be seen more clearly. In the lower site a Fe-based particle can be seen, which has acted as a cathode and caused anodic dissolution of the aluminium surrounding it, otherwise known as cathodic grooving. The site

above it may also be a site of cathodic grooving where the particle has subsequently fallen out, or may be the site of anodic dissolution of an $Mg_{(x)}Si$ particle. It can also be seen that particle surrounding these sites have suffered no corrosive attack, a proposed explanation being that the active development of one pit leads to anodic polarization of the surrounding region shifting it to a passive zone [55].

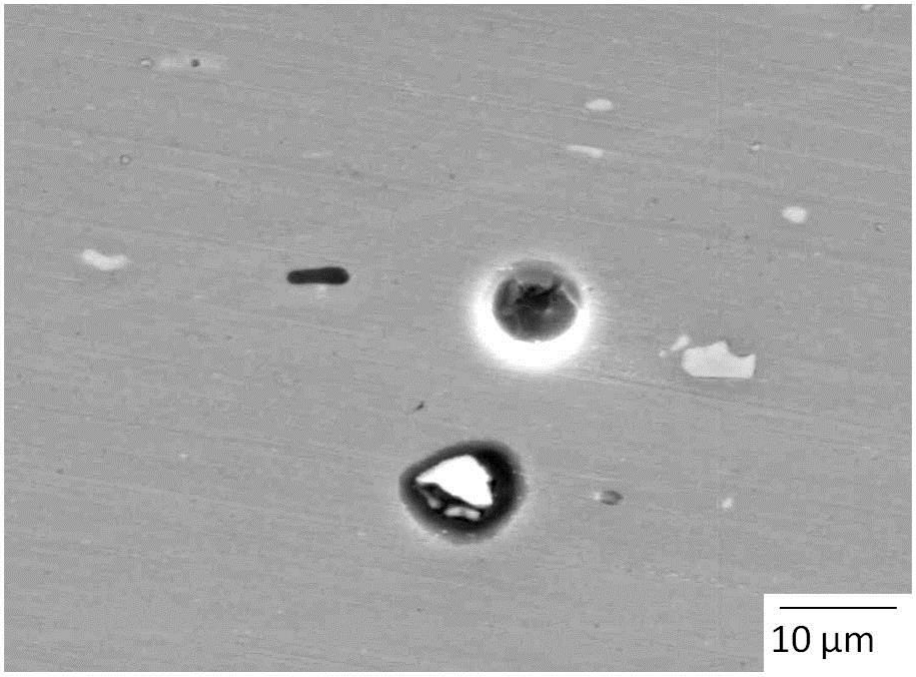

Figure 59 SEM micrograph highlighting the two types of localised corrosion that occur around intermetallic particles. 'Cathodic grooving' around a white Fe-based particle can be seen below another site of either cathodic grooving or anodic dissolution of another particle.

An optical micrograph of the processed nugget region and the HAZ after immersion followed by etching in Keller's reagent are shown in Figure 60 (a) and (b). In both images the processed region is on the left and is darker and striated.The dark spots that can be seen throughout the regions are sites of attack of intermetallic particles. These are largest in the HAZ of the sensitised plate, while in the adjacent nugget region, the sites are far more

numerous and homogeneous, but are much smaller. This is in good accordance with the observations that intermetallic phases are smaller and more numerous in the processed regions. In the H321 plate (a), the sites of attack in the HAZ are less frequent than the equivalent area of the sensitised plate, while the processed region of the H321 plate shows the least pitting attack. This would appear to show that the processed region of a sensitised plate is more susceptible to attack around intermetallic particles than an equivalent region in a AA5083-H321 plate.

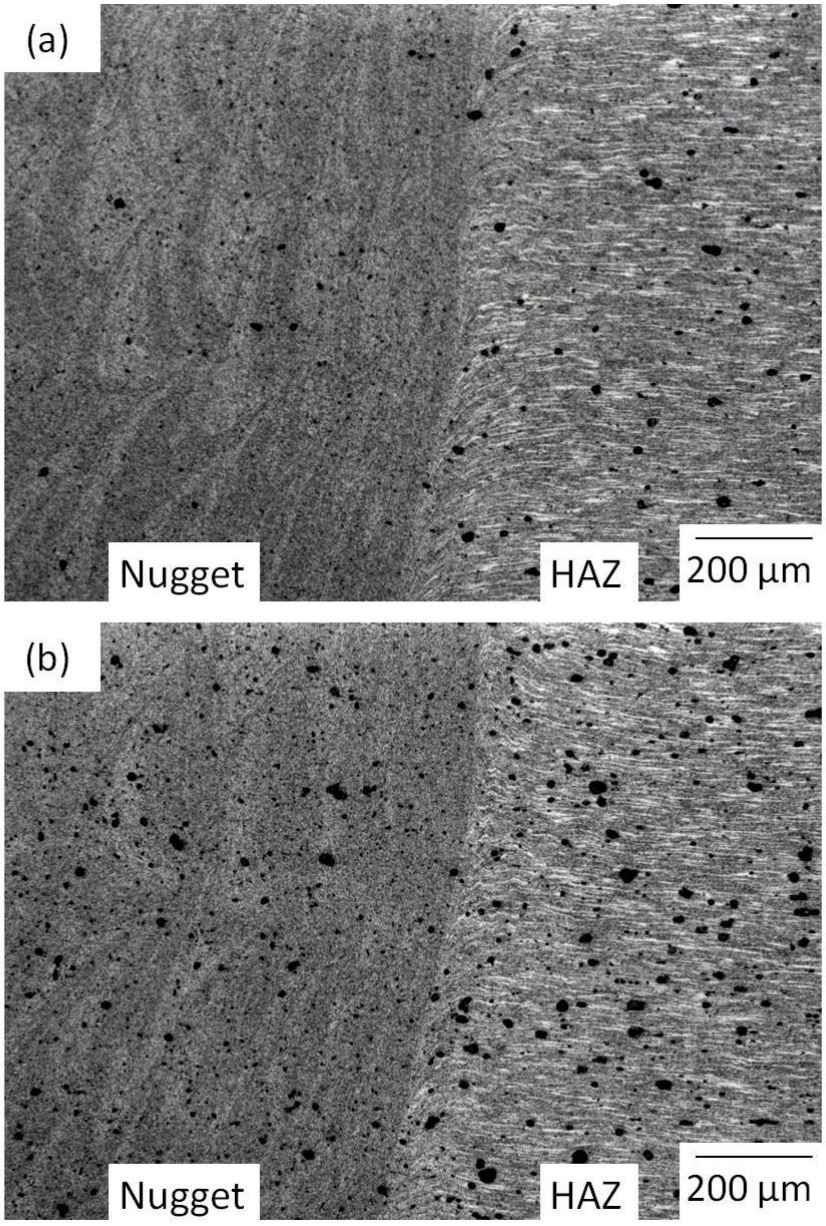

Figure 60 Optical micrographs from (a) low power weld through AA5083-H321 plate (b) low power weld through sensitised plate after immersion in 1 M NaCl for 10 days, then etching in Keller's reagent for 30 seconds each.

4.3.4. Electrochemical testing

Potentiodynamic sweeps were first conducted on the base and sensitised sample in order to understand the effect of the sensitisation upon the electrochemical behaviour on the alloy. This test was carried out using a flat cell set up and a potentiostat as described in Chapter 3. The open circuit potential (OCP) was monitored for 30 minutes, then the sweep was started 100 mV below the OCP, and stopped once the breakdown potential of 0.1 mA/cm^2 had been passed.

In Figure 61, the base alloy shows a rapid increase in the current density (breakdown potential) at -580 mV $_{(SCE)}$. The sensitised samples show a much lower potential at which the breakdown current density is reached at -680 mV $_{(SCE)}$.

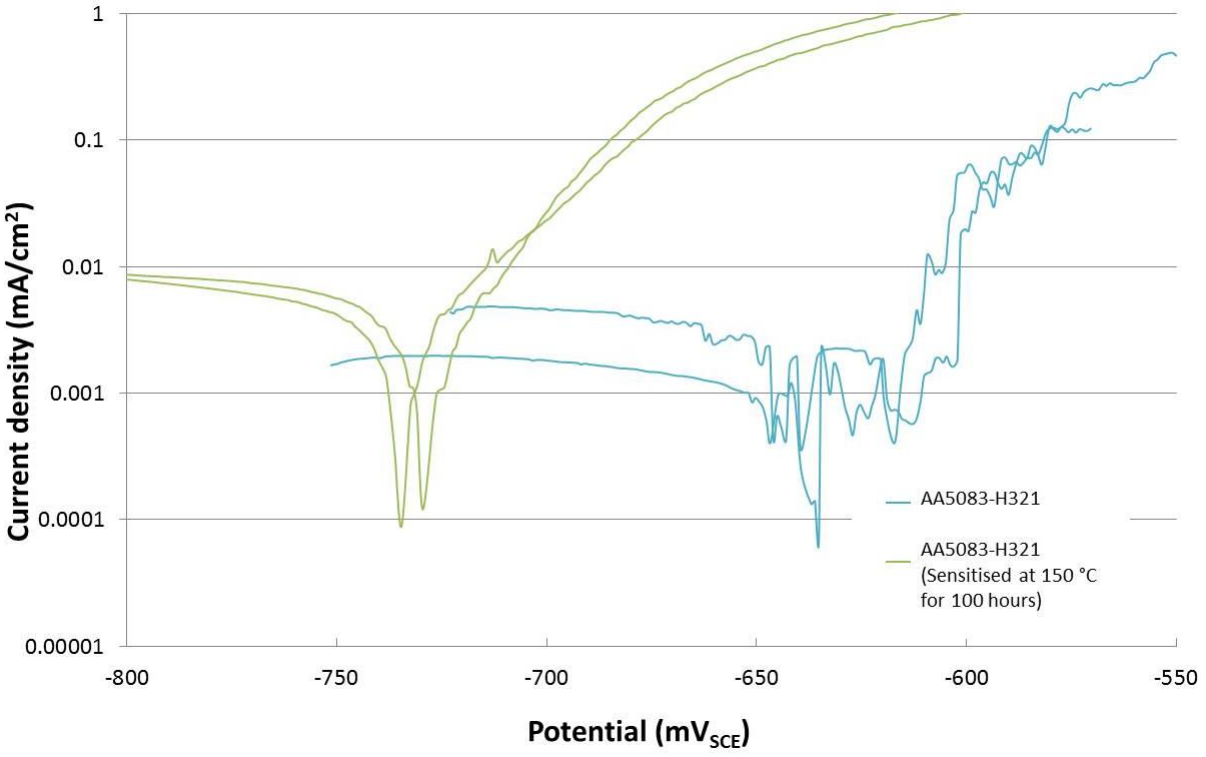

Figure 61 Potentiodynamic sweeps conducted on the AA5083-H321 and AA5083-sensitised samples in 0.1 M NaCl.

Figure 62 shows the potentiodynamic sweeps of the H321 and sensitised samples in addition to the nugget and HAZ regions from the two processed areas. All of the nugget and HAZ regions show a breakdown potential much higher than the sensitised samples, although there is a great deal of scatter and there is no correlation between the high and low power processing nugget regions and the HAZ outside of them. This data shows the breakdown potential of a sensitised plate that has been processed to have returned to the level of the AA5083-H321 material. Inspection of the corroded samples showed only small degrees of attack around intermetallic particles in the FSP nugget and HAZ samples after the potentiodynamic sweeps.

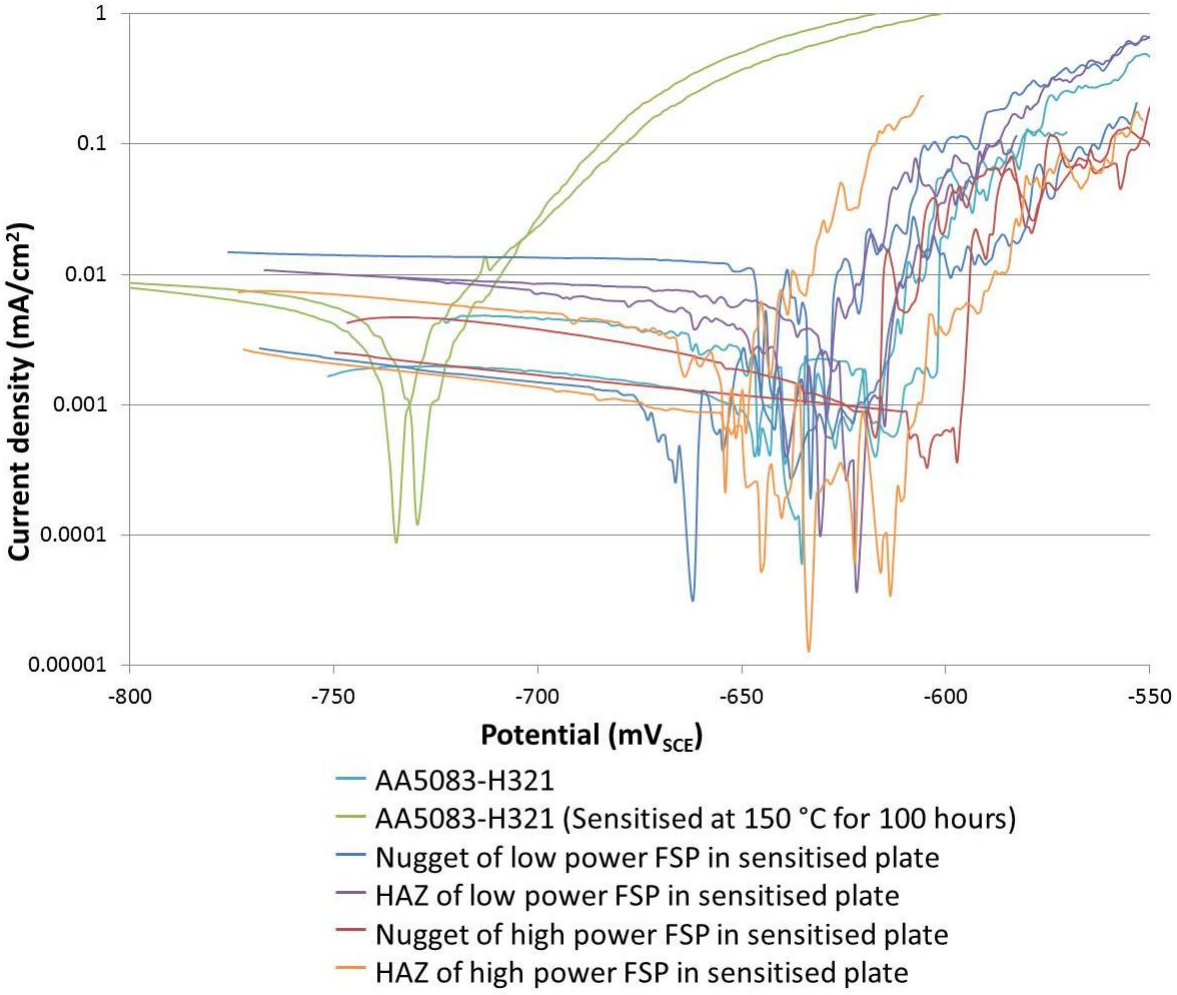

Figure 62 Potentiodynamic sweeps conducted on the as AA5083-H321, AA5083-sensitised, nugget and HAZ regions of the high and low power processing samples in 0.1 M NaCl. Measured against a saturated calomel electrode.

4.4. Discussion

4.4.1. Compositional variations

A clear reduction in the Mg composition exists between the top and middle of the plate. Figure 37 shows the composition dropping from 4.5 to 3.5 wt.% over the 6 mm from the top to middle of the plate. This has been noted as a common phenomenon of macrosegregation which can come about as a result of the direct chill method of casting [184].

It has frequently been reported that Al-Mg alloys require a minimum of 3-4 wt.% Mg in order to be susceptible to corrosion [1, 9, 14, 68, 75]. The solid solubility level of Mg in Al is 3-3.5 wt.%; alloys with values below this do not have sufficient Mg to segregate to grain boundaries and precipitate onto them. This precipitation kinetics in the Al-Mg system was investigated by Gaber, with one conclusion that the lower the concentration of Mg within the alloy, the higher the driving force required for precipitation [185]. Although the material requires a greater energy input to achieve precipitation in the midline, it can still occur.

The current observations indicate that both the top surface and the midline have sufficient magnesium (>3 wt. %) and will be susceptible to sensitisation, so if material were to be moved from the middle to the top of the plate by the action of the FSP, it will still be sensitised and susceptible to IGC if the thermomechanical effects do not “repair” the material.

4.4.2. Intermetallic particles observed

Of the three different populations of intermetallic particles that have been observed, two are aluminium-based and iron-rich, while the third comprises magnesium and silicon (Table 4, Table 5, and Table 6, respectively). These have been identified in many other studies as Al-(Fe,Mn,Cr,Si), Al_6(Fe,Mn) and Mg_2Si [39, 55, 71, 166]. Since the composition of the Mg-

based particles does not match closely to the known stoichiometry of Mg_2Si, shown in Figure 40, it is not possible to classify the particle in the plate as such, so the use of $Mg_{(x)}Si$ is more appropriate. The composition of the Mg-rich phase observed in this study was also significantly different to those seen elsewhere [39, 55], where Winsley attributed the lower levels of Mg to removal during sample preparation.

These particles are known to have different corrosion potentials relative to the matrix, leading to different methods of localised corrosion. The $Mg_{(x)}Si$ particles are known to be anodic to the matrix, highly reactive and have a corrosion potential much lower than the matrix, measured to be -1.5 V(SCE) in 0.1M NaCl [46]. In contrast, the Fe-based particles are cathodic to the matrix, and have a more noble corrosion potential relative to the Al matrix. While the highly reactive $Mg_{(x)}Si$ particles dissolve readily to form a cavity, Figure 59, the Fe-based particles act as cathodes and cause the Al matrix surrounding them to dissolve preferentially, Figure 54.

4.4.3. Processing parameter variations on macrostructure

The processed region that FSP has produced can be seen in Figure 41. The use of different processing parameters appears to vary the resulting microstructure; the high power processing has left a homogenous FSP nugget whereas the low power processing shows a banded microstructure deep within the nugget. Since both routes have the same tool advancement per rotation, the increased speed or rotation must be the cause of the difference. Rodrigues observed that welds with higher tool rotation speeds which achieve higher temperatures will also have a larger grain size [186]. The temperature in the high power weld may have been

sufficient to allow recrystallisation and hence a homogenous microstructure, with large grains growing as the temperature dropped more slowly

The phenomenon of interest has been referred to as “friction heat flow”, several studies confirming that the tool advancement speed is the determining factor in the amount of material flow possible [113, 152, 170]; increasing the speed leads to less material flow and stirring.

While the majority of the FSP nugget shows a varied microstructure between processing conditions, the top 2 mm below the surface appear to be the most homogenous. The region at the top is heated not only by the submerged pin, but also by the tool shoulder so will be the area which experiences the highest temperatures. The edge of the tool shoulder, which is also the widest part, will experience the highest tangential velocity, imparting the highest shear forces and moving the material the most. This area just below the surface will therefore be of greatest interest for providing the best conditions for protection of material or recovery from a sensitised condition.

4.4.4. Hardness variations with sensitisation and processing

Sensitisation has been shown to reduce the hardness in the parent material from 97 to 91 Hv after 100 hours at 150°C, Figure 43. This is in good agreement with work by Oguocha who saw the same initial values and drop in hardness in AA5083-H116 after the same sensitisation conditions [71], while a drop from 113 to 94 Hv was noted in a AA5456-H116 alloy [89]. Under the same conditions for the same temper alloy, Winsley did not see a change in hardness after sensitisation, the value remaining at a much lower 85 Hv [39]. Where change has occurred, it has been attributed partly to a reduction in the density of dislocations, which

occurs during recrystallisation of the cold worked microstructure as new grains were formed. In addition to this, the precipitation of the Mg-rich phase and segregation of Mg atoms at grain boundaries have been noted to altering the hardness values. As Mg atoms are drawn away from the α-matrix, the concentration of solute Mg atoms drops and the remaining Mg atoms become ineffective obstacles to the movement of dislocations [71].

The hardness profiles through processed regions that have different processing parameters show that the low power processed areas retain their hardness in the nugget region, while the same region created by high power parameters is 10 Hv softer, Figure 44. This observed relationship differs from that seen by others in FSP'd 5083, in that lower power processing (lower rotation and travelling speeds) has been shown to produce the lowest nugget hardness [155]. It should be noted that the rotation speed in the present study were much lower than those used by Cui, 80 rpm as opposed to 400, showing that the trend observed may not continue into the parameters of the current study. Despite the grain size refinement that takes place during FSP, hardness has been shown to be dependent on particle distribution rather than grain size [127].

The reduction in hardness in the HAZ as the measurements approach the FSP nugget can only be attributed to particle distribution and a decrease in dislocation density, as grain size is largely unchanged outside the thermomechanically affected zone. The thermal effects seen in this region are similar to those seen by Sato, who noted that thermal cycles during FSW can cause coarsening and dissolution of strengthening precipitates [187]. While slight differences in the distribution of $Mg_{(x)}Si$ and Fe-based particles have been observed, it is the $Al_6(Fe,Mn)$ particles which are more important in strengthening AA5083 [162]. The distribution of these particles has not been quantified and therefore may be considered, among other conditions, as being worth taking note of during future TEM work.

4.4.5. TEM observations in sensitised and processed material

The TEM micrographs in Figure 46 show the grain boundaries in the H321 temper plate to be free from grain boundary precipitates or other features. This is to be expected as the H321 temper is designed to stabilise the alloy, and is an observation consistent with previous studies [18, 39]. After sensitisation at 150°C for 100 hours, inspection of the grain boundaries reveals that a high degree of precipitation has occurred on the grain boundaries. Figure 47 shows one such grain boundary, where decoration by precipitates up to 50 nm in width can be seen over a distance of 3 μm. This observation matches with that of Searles et al. who similarly sensitised AA5083 at 150°C, then observed the β-phase precipitation with a TEM [73]. Sensitisation for 82.5 hours produced discreet precipitation of β-phase particles, while extending the sensitisation time to 189 hours was seen to produce a continuous film of β precipitates.

The composition of the grain boundary precipitates was examined by EDS, in comparison to the matrix outside of it. Figure 49 shows the grain boundary region to have more magnesium and less aluminium, which is to be expected after the sensitisation heat treatment to promote segregation of Mg and subsequent precipitation of the β-phase. Again, the work of Searles et al. showed a similar increase in Mg levels by segregation along the sensitised grain boundary [73].

EDS maps shown in Figure 50 show there to be a concentration of magnesium at two points along the high angle grain boundary, with a corresponding Al depletion at the same two points. Both of these sites are at the incident points between the high angle grain boundaries and low angle sub grain boundaries which were formed during recovery from long term heat treatment. These sites would be the highest energy sites along the grain boundary, where it would be easiest for the Mg to segregate to, as opposed to the region between these sites

which would have a slightly lower free energy. Segregation has then led to the formation of precipitates at these high energy sites. EDS mapping also shows there to be rod-like Mn particles in the matrix, which do not show any signs of magnesium enrichment around them, indicating that they are not the preferential sites for segregation and precipitation.

Following the through thickness FSP, TEM micrographs were obtained from the nugget and HAZ regions of the low and high power passes. In both nugget regions, no grain boundary precipitates can be seen while a large degree of grain refinement producing grains 1-2 μm in size was observed Figure 51 (a) and (c). Inspection of the HAZ region also revealed the grain boundaries to be free from segregation and precipitates after processing, yet none of the grain refinement seen in the nugget as there was no mechanical deformation and much less heat imparted, Figure 51 (b) and (d). The observations of no grain boundary β-phase after sensitisation then processing has also been reported before in the nugget and HAZ regions of FSW'd 5083by Winsley [39].

4.4.6. Effect of processing on sensitised microstructure

While the intermetallic particles show signs of localised corrosion through anodic dissolution or cathodic grooving, these forms of corrosion are not the greatest risk to systems formed of Al-Mg alloys that undergo sensitisation. Instead it is the precipitation of the β-phase onto grain boundaries. The effect of this can be seen in Figure 45 (b) where phosphoric acid has selectively etched out the grain boundaries that have been sensitised, compared to the H321 sample which in Figure 45 (a) where the grain boundaries contain no β-phase and have not been attacked by the etch. In figures (c) and (e), the FSP nugget in the H321 base plate shows little β-phase after processing. While high temperatures were achieved in this region

(300-400°C); they were well above the solvus of β-phase and were not maintained for long enough to allow precipitation.

The effect of processing on the sensitised plate is shown in Figure 45 (d) and (f), where the selective grain boundary etch seen in the sensitised plate (b) is no longer present. This would suggest that a combination of the mechanical mixing action of the FSP bit and the high heat generated by the frictional heating are sufficient to re-dissolve the β-phase and leave a microstructure that no longer has a reactive phase on grain boundaries.

Analogous studies have only been carried out very recently with regards to removing the β-phase from sensitised grain boundaries. Kramer et al. have shown the application of local heating to previously sensitised material reverses the susceptibility of the material to IGC [41]. By heating the material to 260°C for 10 minutes with electric heater strips, the β-phase was re-distributed so as not to be on the grain boundaries and the material was seen to have been stabilised. It was noted that temperatures above this were above the solid solubility limit for the β-phase, so would only put it back into solution, rather than re-distributing it in a more helpful manner. This is the case in the nugget region.

4.4.7. Corrosion behaviour of sensitised and FSP'd material

The corrosion activity in the H321 plate after immersion in a NaCl solution is limited to cathodic grooving around Fe-based intermetallic particles, which shows an even morphology over the whole area of the sample, Figure 52 (a), (c) and (e). The sensitised test piece corroded under the same conditions shows sites of IGC, Figure 52 (b).

After processing the H321 sample, the cathodic grooving is still observed (Figure 57), but there are fewer sites observed and they are smaller in size, Figure 60 (a). Following FSP of

the sensitised sample, the IGC seen in the base sensitised plate no longer occurs. The only corrosive attack is pitting, in a similar fashion to the processed H321 sample, however the subsequent pits are more numerous and larger in size, Figure 60 (b).

4.4.8. Electrochemical investigation

The results of potentiodynamic sweeps on the 5083-H321 plotted next to those of the 5083-Sensitised are shown in Figure 61. The sensitised sample shows a much lower corrosion potential and breakdown potential resulting from the sensitisation heat treatment and the precipitation of the β-phase which has occurred. This finding is consistent with the phosphoric acid etching, which showed the sensitised sample to be more susceptible to IGC, and the immersion corrosion which brought about IGC in only the sensitised sample.

The drop in breakdown potential at 0.1 mA/cm^2 from -580 mV in the AA5083-H321 sample to -680 mV is of a similar scale to that seen elsewhere. A drop from -580 to -680 mV was also seen by Winsley in an 5083-H116 alloy [39], and from -660 to -740 mV in an AA5456 alloy[89], where the base alloys were compared to sensitisation at 150 °C for 100 hours, the same as this study. This drop in breakdown potential has also been seen with a sensitisation treatment of 500 °C for 1 hour where Chang recorded values of -653 and -740 mV for a AA5083-H321 and sensitised sample respectively [188].

Both studies attributed the difference in polarisation behaviours to the presence of the highly anodic β-phase which precipitated out during sensitisation, leading to its selective dissolution.

Potentiodynamic sweeps conducted after processing had been carried out on the sensitised plate show that the breakdown potential in the HAZ and nugget regions returns towards values seen within the base material. The breakdown potentials measured at 0.1 mA/cm^2

range from -550 to -600 mV and are significantly lower than those in the sensitised material. Given that the drop in breakdown potential is attributable to the precipitation of β-phase onto grain boundaries, the converse is likely to be true after processing has removed it.

4.5. Conclusions

Preliminary investigation into the effect of friction stir processing on AA5083-H321 and sensitised plates has shown that:

- When AA5083 undergoes sensitisation, β-phase is precipitated onto the grain boundaries, in turn leading to an increased susceptibility to intergranular corrosion, owing to the anodic nature of the β-phase relative to the matrix.
- Full thickness Friction Stir Processing removes the β-phase from grain boundaries in both the nugget and HAZ regions. This improves the materials resistance to IGC.
- Two types of intermetallic particles have been observed in the microstructure; the first are Fe-based and act cathodically to the matrix leading to grooving around the particle, while the other is Mg_xSi and undergoes dissolution as it is anodic to the matrix. Both sets of particles become fragmented in the FSP nugget region.
- A through thickness variation in the Mg concentration of the plate under investigation has been noted; however it does not appear to have an effect on sensitisation or corrosion behaviour.

Chapter 5 - The effect of heat imparted by Friction Stir Processing on the microstructure and corrosion behaviour of sensitised AA5083

In Chapter 4, it was concluded that the susceptibility of sensitised AA5083 to intergranular corrosion was mitigated after full-thickness Friction Stir Processing. This finding was true of both the nugget region and the adjacent HAZ, which had only been subjected to thermal effects, but no mechanical stirring.

The natural progression of this technique with respect to in-service repair and prevention of corrosion is to apply the protective effects while changing the bulk microstructure as little as possible. The alloy has been chosen for its specific properties, and employing a full thickness FSP over very large areas will undoubtedly change the bulk mechanical properties to an unknown degree. Instead it would be useful to apply these changes to only the outermost surface, that which is exposed to the corrosive environments, while also protecting to a small depth under the surface to protect this region if the plate were to be damaged.

The use of a Friction Surface Processing tool satisfies both of these requirements in that it will microstructurally modify the top surface by the action of the tool shoulder, while the heat should penetrate into the material and either provide a protective or repair function to sensitised microstructures.

This chapter will focus on the microstructural and corrosion characterisation of the AA5083-H321 plate, a sensitised plate where different sensitisation parameters to Chapter 4 have been used, and a sensitised plate with surface processing applied. Details of the sensitisation and processing are provided in Chapter 3.

As the outer thermomechanically affected layer is very thin, has a rough texture and is discontinuous in coverage, it is difficult to accurately perform a complete set of tests, so the HAZ under the surface, which forms a much thicker and more readily testable layer, was examined.

5.1. Microstructural characterisation of material under investigation

5.1.1. Optical observations of processed plate

Figure 63 (a) shows a sensitised plate (14 days at 100°C) which has received overlapping surface FSP. Figure 63 (b) and (c) show magnified views of the modified surface including the degree of overlap, and the surface finish left in the wake of the rotating tool. All of the material which can be seen from the top has undergone both thermal and mechanical processing.

The cross section in Figure 64 (a) shows the sensitised plate following etching in Kellers reagent. The plate shows a uniform appearance, except for the darker band at the midline, which was identified as a region of decreased Mg content in the previous chapter. The effect of processing on the cross section can clearly be seen in Figure 64 (b). The dark discontinuous bands at the top of the sample are the nugget region created by the small submerged pin of the FSP tool. The curved band beneath this is the heat-affected zone and has been formed from the heat input from the friction of the tool shoulder on the top of the plate.

For the corrosion tests carried out from this point onwards, a layer containing the nugget regions was removed so that a continuous layer of HAZ surface was available for testing.

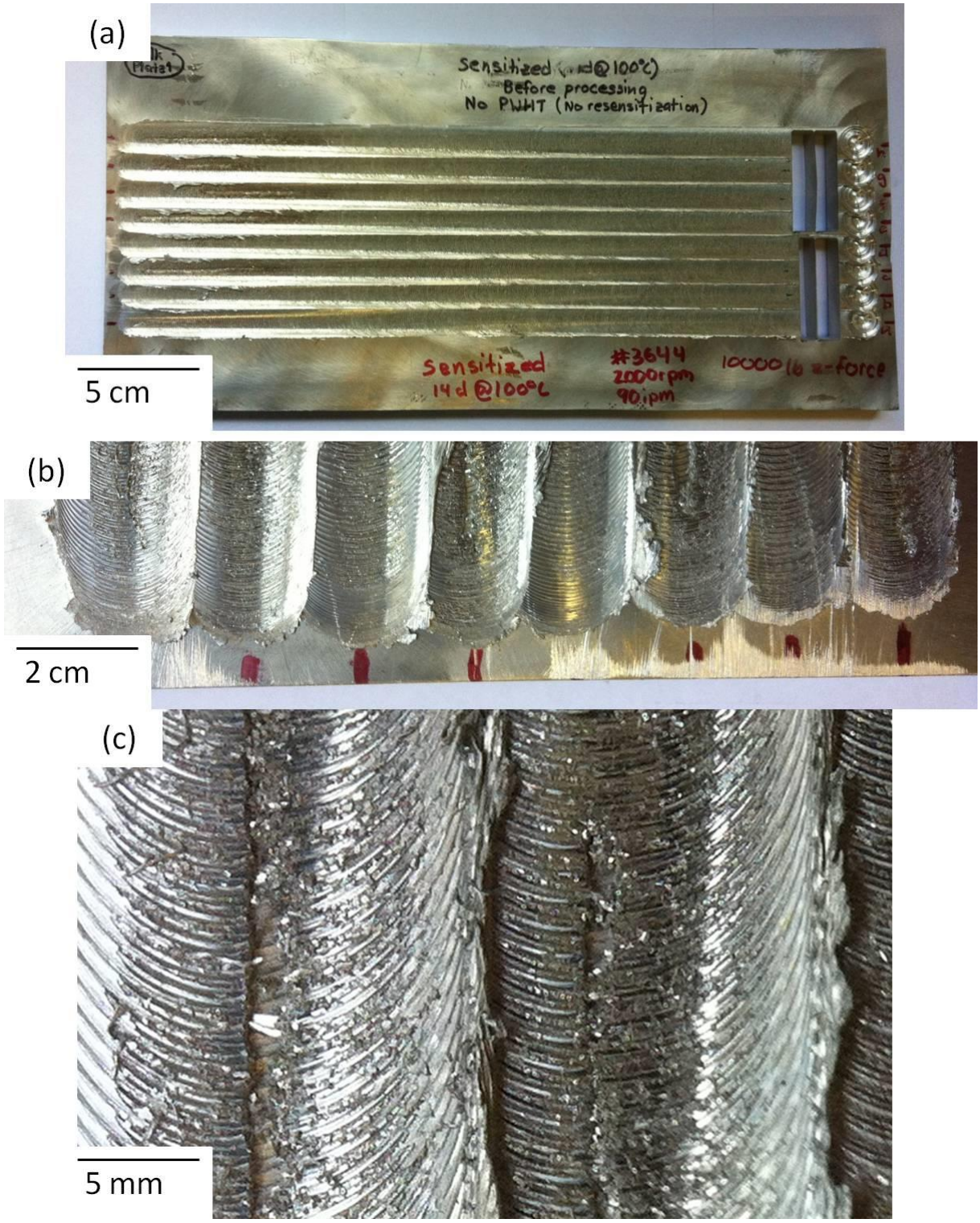

Figure 63 (a) Macro view of the AA5083-sensitised then processed plate, with FSP extending over the length of the plate. (b) Close up view of the FSP passes showing the degree of overlap. (c) Two FSP tracks showing the curved track left in the wake of the FSP tool as it rotates and advances.

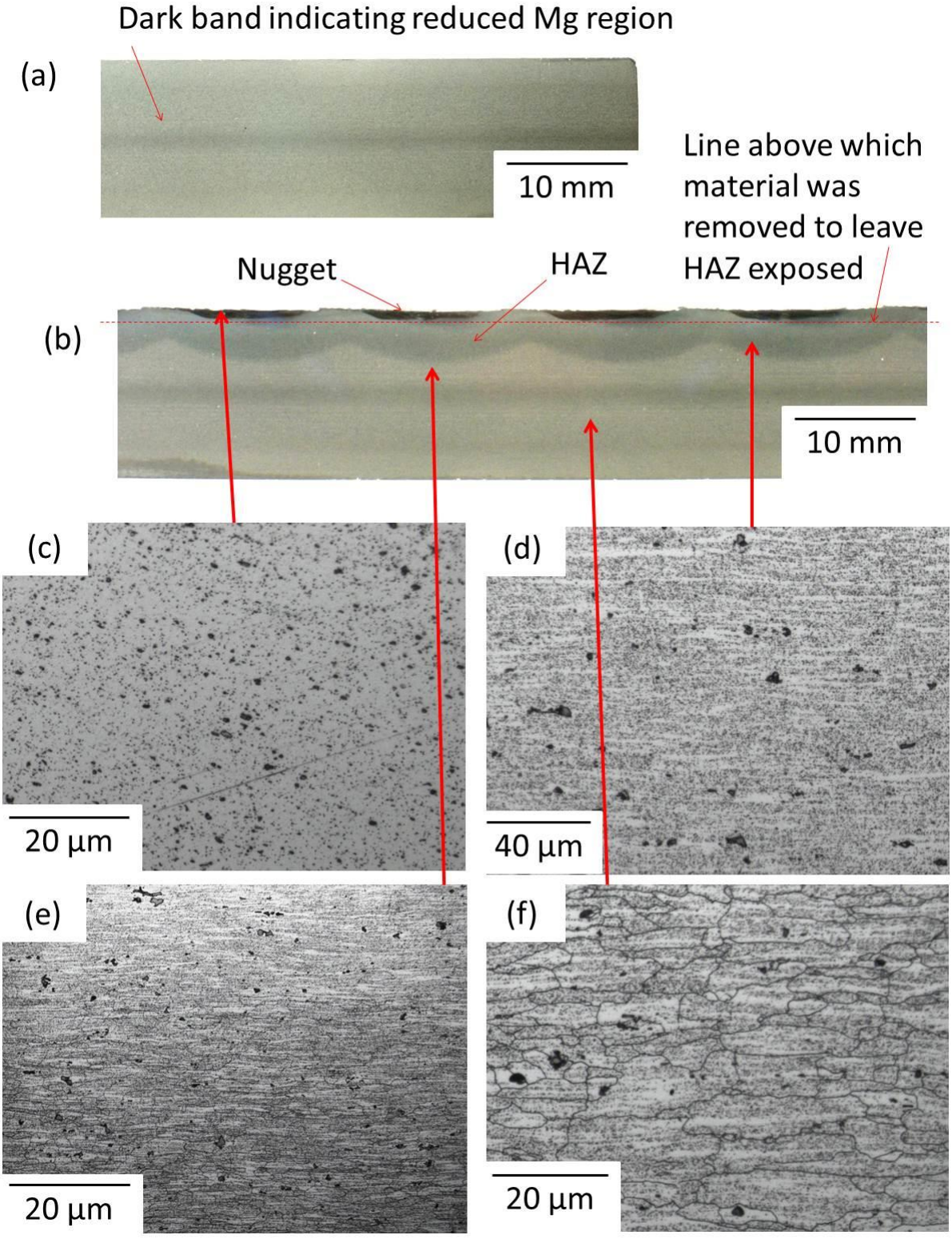

Figure 64 (a) Cross section of the AA5083-sensitised sample after etching in Kellers reagent. (b) Cross section of the sensitised then processed plate, with the nugget and HAZ at the top of the plate. (c), (d), (e) and (f) are magnified optical images of the nugget, HAZ, HAZ/base transition and sensitised base in the cross section after etching in Kellers.

5.1.2. Observations of microstructure and intermetallic particles

SEM inspection of the cross section of the plates has been carried out, with observations of the AA5083-H321 plate being shown in Figure 65(a) and (b) to provide a baseline for comparison. This material contains coarse, randomly distributed intermetallic particles, in the range of 5-20 μm. The microstructure of the sensitised plate (2 weeks at 100°C) is shown in Figure 65(c) and (d), where it was observed that the size and distribution of the particles showed no difference from those in the AA5083-H321 plate.

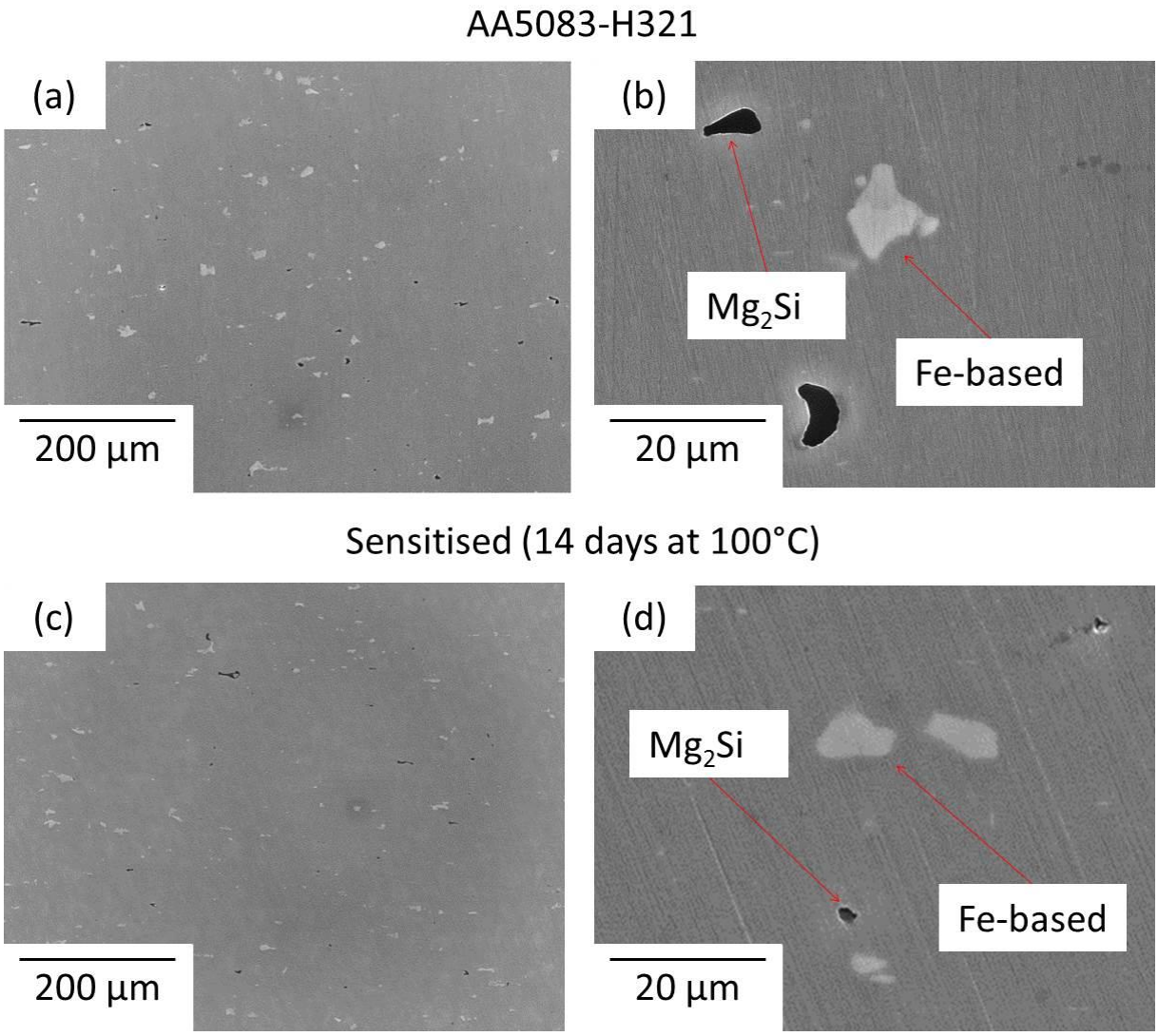

Figure 65 SEM of the microstructure in the: (a) and (b) AA5083-H321, (c) and (d) AA5083-sensitised plate (14 days at 100°C), showing both Fe-based and Mg_2Si particles.

The effect of sensitisation then processing on the microstructure can be seen in the two distinct regions of the nugget and HAZ mentioned earlier. In the nugget, Figure 66 (a) and (b), the coarse particles have become much smaller, and have been much more homogenously distributed. This is primarily due to the mechanical stirring action of the pin of the FSP tool. The HAZ however shows no signs of microstructural alteration, as seen when comparing

Figure 66 (c) and (d) to Figure 65 (c) and (d). This can be explained by considering the history of this region as having undergone two heat treatments, the first at low temperature for a long time, the second produced by the heat from the processing and being of a much higher temperature but for only a few seconds. Neither of these events was sufficient to affect the larger scale intermetallics visible by SEM.

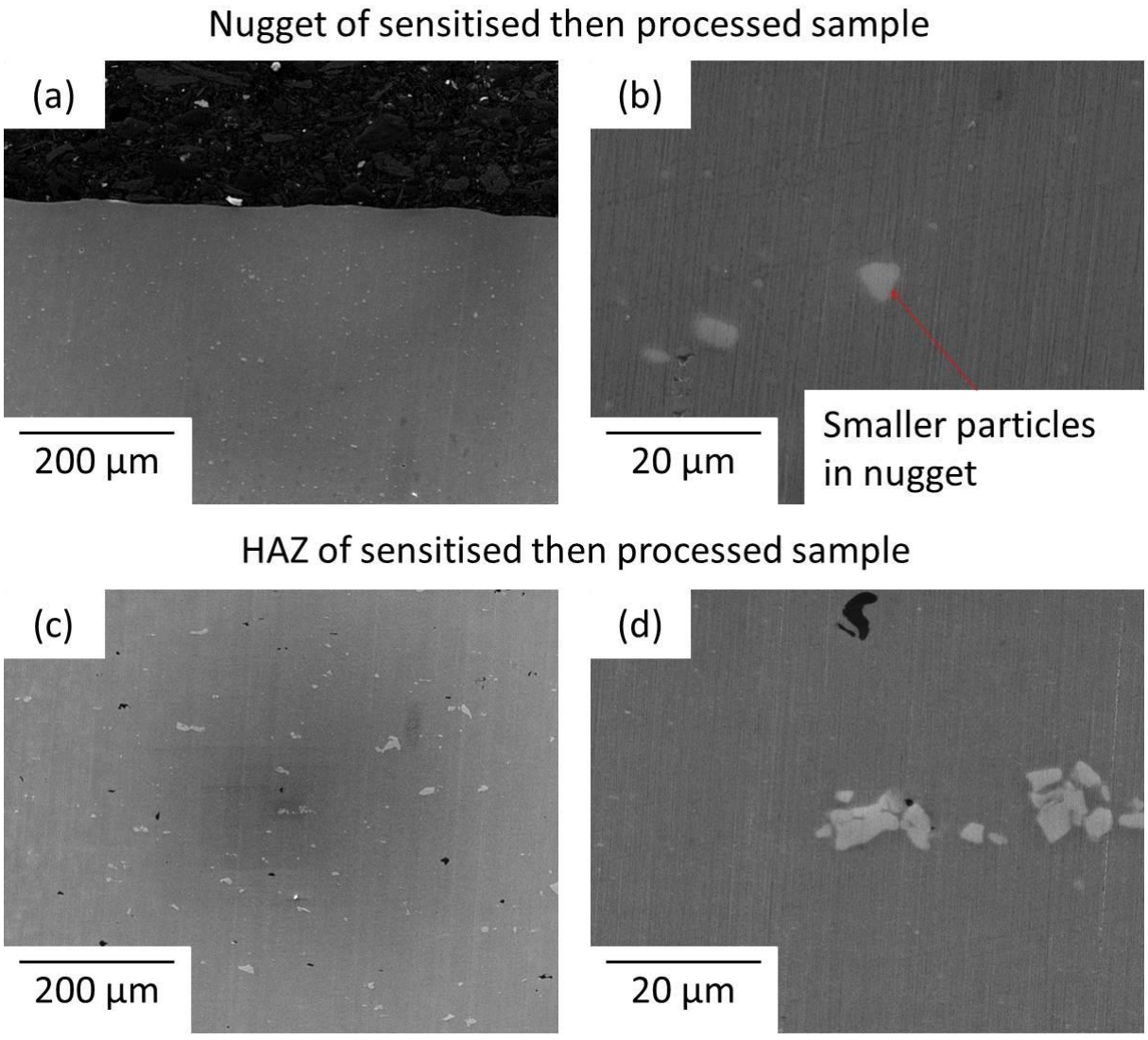

Figure 66 (a) and (b) SEM of the microstructure in the Nugget of the sensitised then processed sample. (c) and (d) SEM of the microstructure in the HAZ of the sensitsed then processed sample.

5.1.3. TEM observations of grain boundaries

Figure 67 (a) and (b) are representative TEM images taken in the AA5083-H321 material. Of the 100+ grain boundaries surveyed, none contained observable grain boundary precipitates, and it can be reasonably surmised that the AA5083-H321 was free of grain boundary β-phase.

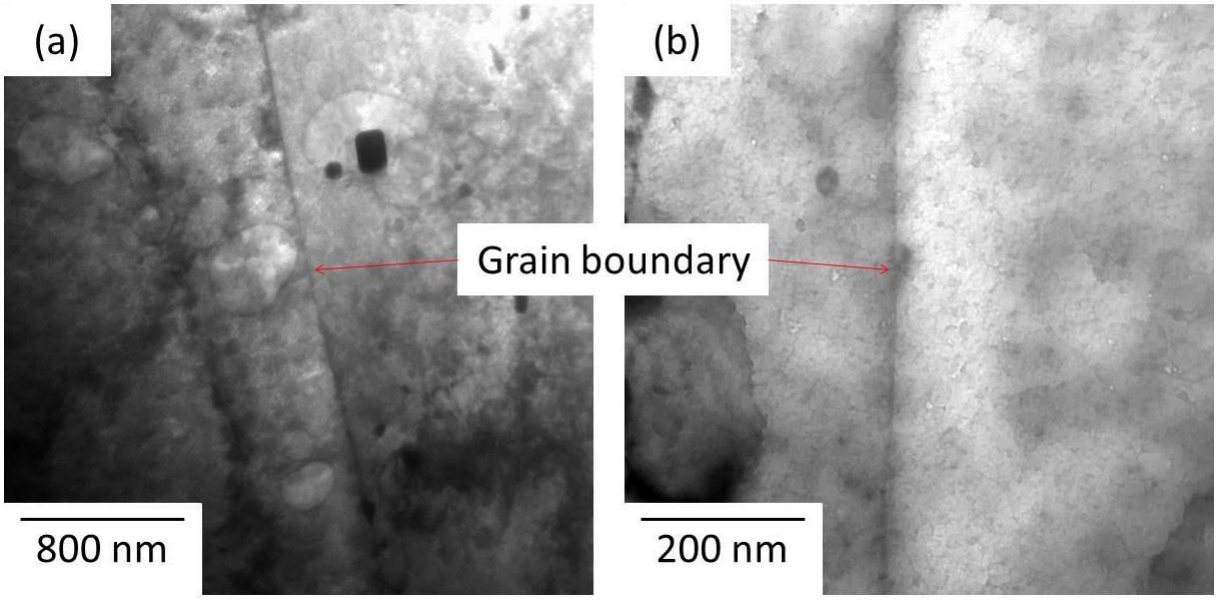

Figure 67 TEM micrographs from the AA5083-H321 plate showing clean grain boundaries free from β-phase.

Upon inspection of the sensitised sample, many sites of discrete precipitate formation were noticed, most easily seen on grain boundaries, Figure 68 (a) and (b). This precipitates were all very small, no more than 100 nm in thickness and no more than 500 nm in length.

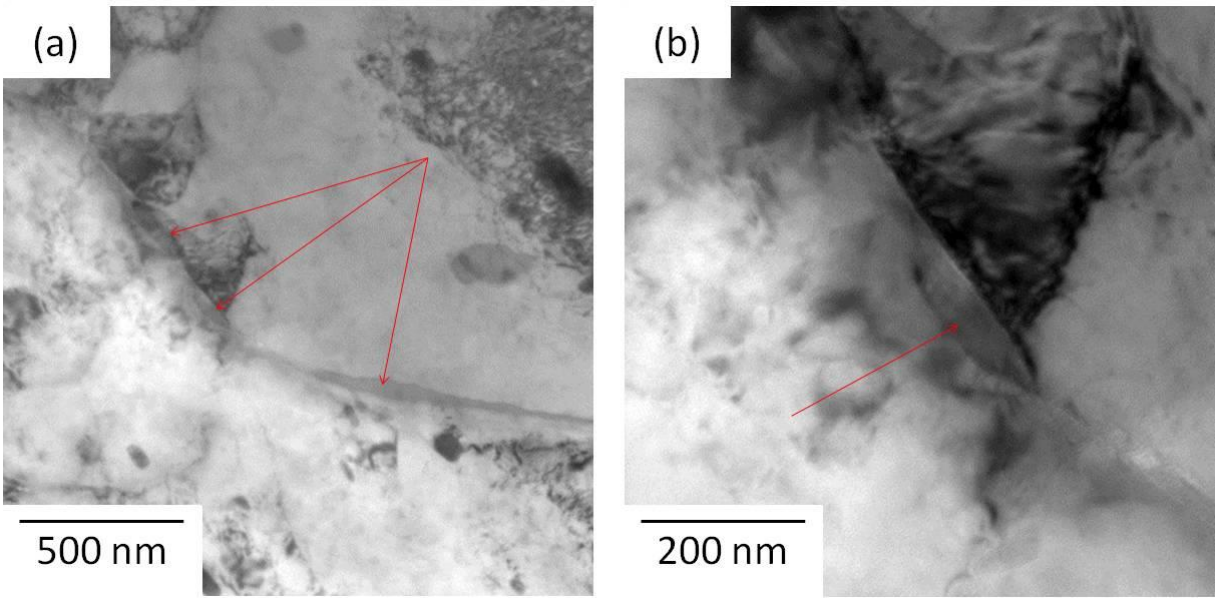

Figure 68 TEM micrographs from the AA5083-sensitised plate where arrows indicate the presence of a grain boundary precipitate.

Inspection of the HAZ region from the sensitised then processed region revealed that no grain boundary precipitates were present in over 100 grain boundaries that were surveyed. Representative grain boundaries are shown in Figure 69 (a), (b) and (c).

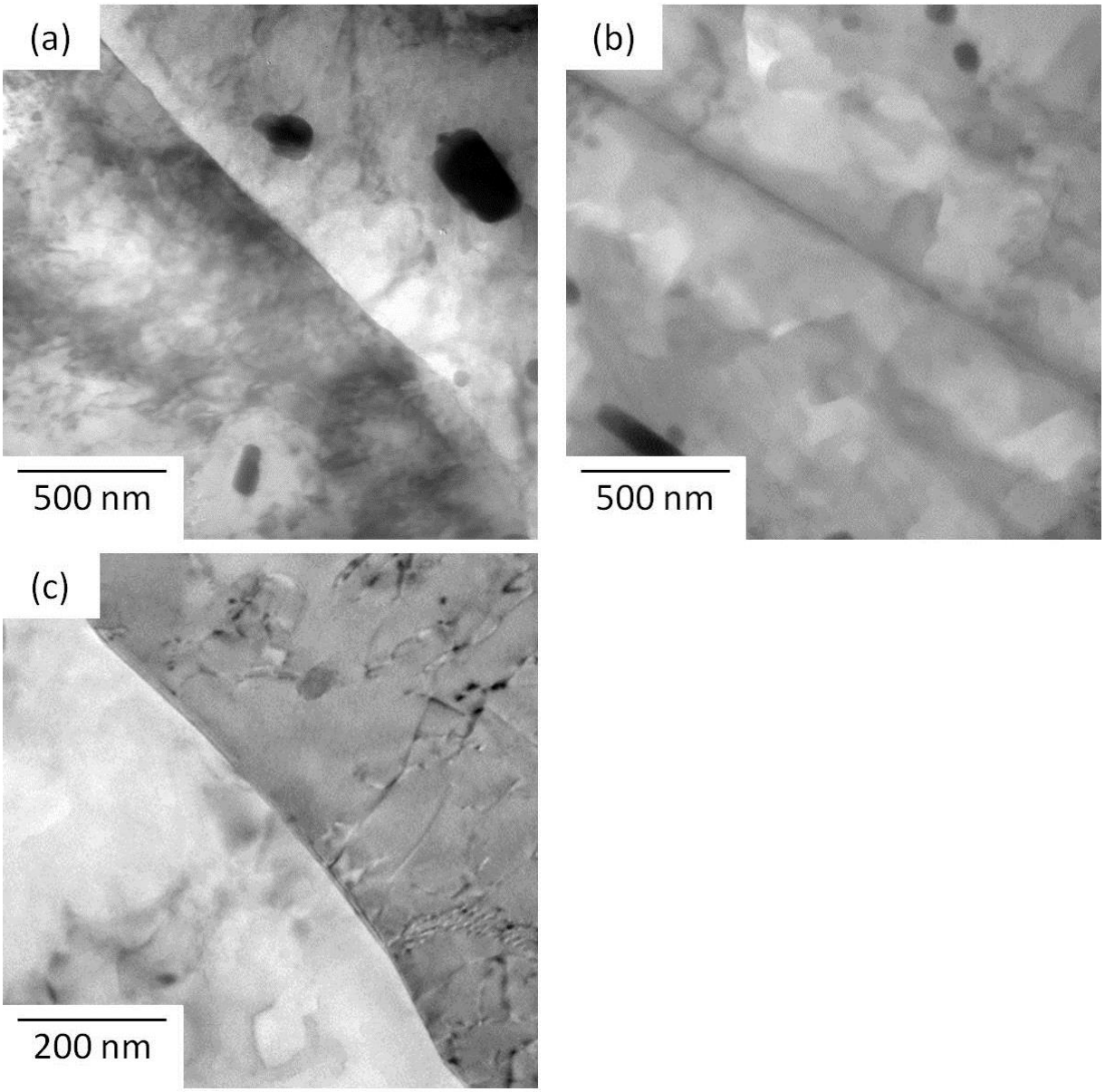

Figure 69 TEM micrographs from the sensitised then processed plate showing clean grain boundaries free from β-phase.

5.1.4. Phosphoric acid etching to indicate degree of β-phase present on grain boundaries

Etching with 60 °C phosphoric acid has been shown to preferentially attack any β-phase present in the alloy, and can give a visual indication of how susceptible to IGC an alloy is.

When the AA5083-H321sample is polished, etched and observed under an SEM, very little attack is seen, Figure 70 (a) and (d). Very small, discreet sites have been removed but are not indicative of any amount of grain boundary precipitates being present.

In contrast, when the sensitised sample is etched, Figure 70 (b) and (e), an extensive network of susceptible grain boundaries is revealed. The attack or removal of β-phase is continuous and along every grain boundary where precipitates were shown to exist under TEM. This indicates while the sensitisation heat treatment was not sufficient to affect the large intermetallics, is has been able to promote segregation and precipitation on the grain boundaries.

When the HAZ of the sensitised then processed sample was etched under the same conditions, the resulting surface showed no continuous grain boundary etching, and only small, discreet attack sites, Figure 70 (c) and (f). This result is comparable with that of the AA5083-H321 sample, Figure 70 (d), and indicates that the heat from processing that creates the HAZ is sufficient to remove the susceptibility to IGC that the sensitisation brought about. There is, however, enough attack to able to make out the outlines of grains.

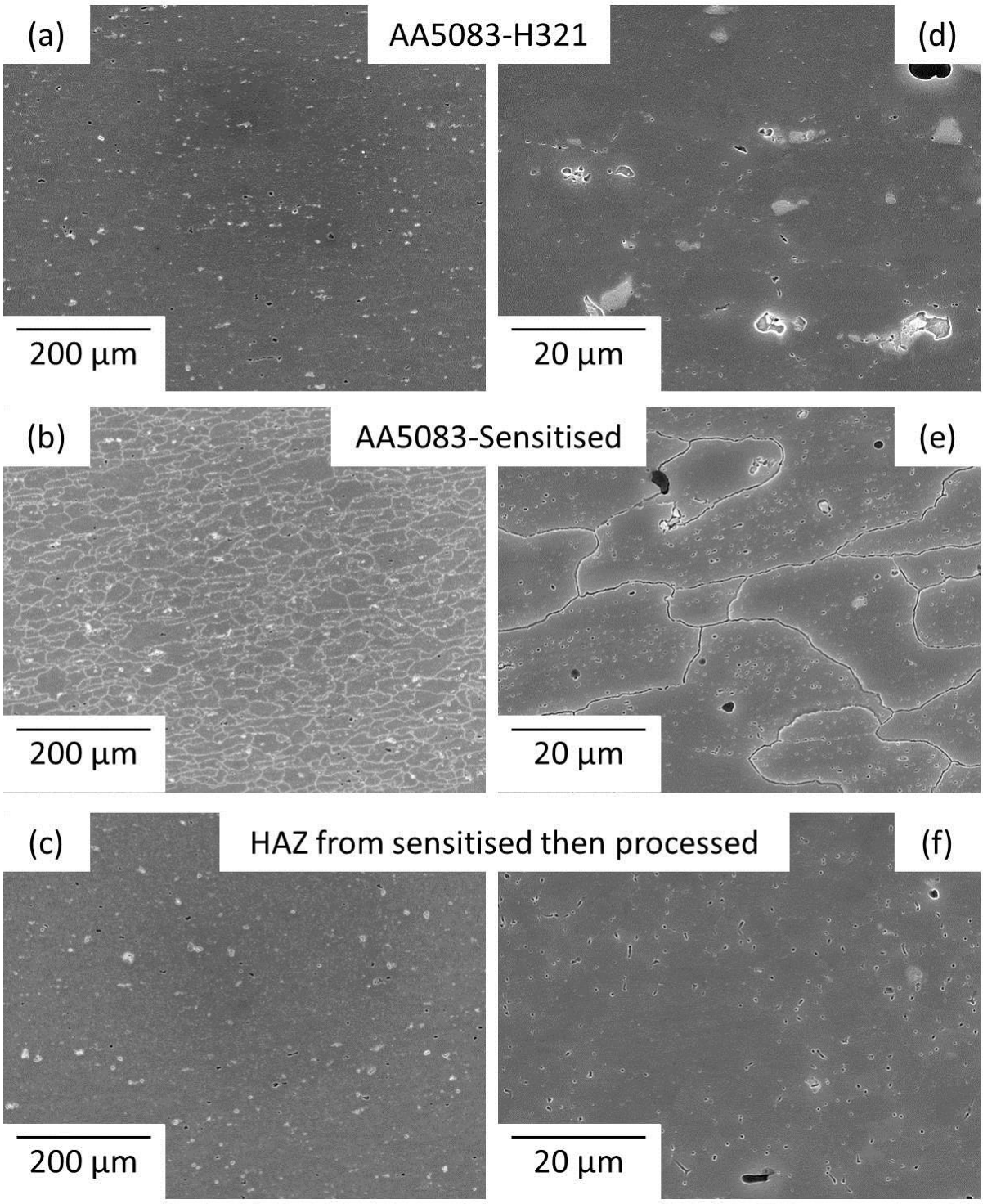

Figure 70 (a) (b) and (C) SEM images of the as AA5083-H321, AA5083-sensitised, and processed samples respectively plate after etching in phosphoric acid to reveal the degree of β-phase precipitation (10% solution at 60°C for 30 seconds). (d) (e) and (f) are magnified views of the same samples

5.2. Corrosion testing

5.2.1. Immersion testing

In order to observe the corrosion behaviour of the various conditions in this study, the sample was immersed in a corrosive solution and the morphology of the corrosion which takes place was observed. To do this, the top surface of the plate was mechanically removed to create a level surface, which included removing the nugget region which was made up of the FSP track seen in Figure 63 (c). Samples were polished in accordance with the methods outlined earlier, then immersed for 6 weeks after which optical and SEM analysis were carried out.

Figure 71(a) (b) and (c) show micrographs of the corroded surfaces and the corrosion product left on the surface. The AA5083-H321 sample shows little corrosion product over the majority of the surface but does show several small sites where the corrosion product has built up. The sensitised sample shows a large degree of corrosion product over the whole of the surface implying that corrosion has taken place across the whole surface to a greater extent, and several sites where a large degree of corrosion product has built up. The sensitised then processed sample shows a good degree of corrosion product spread across the whole surface, however differs from the previous conditions in that no large sites of corrosion product can be seen.

Figure 71 (d) (e) and (f) are micrographs of the immersed samples after the corrosion product has been removed. The AA5083-H321 sample shows no signs of large scale corrosive attack, while in the sensitised sample a large site of attack is clearly visible. The sensitised then processed sample shows no large scale corrosive attack, much like the AA5083-H321 sample.

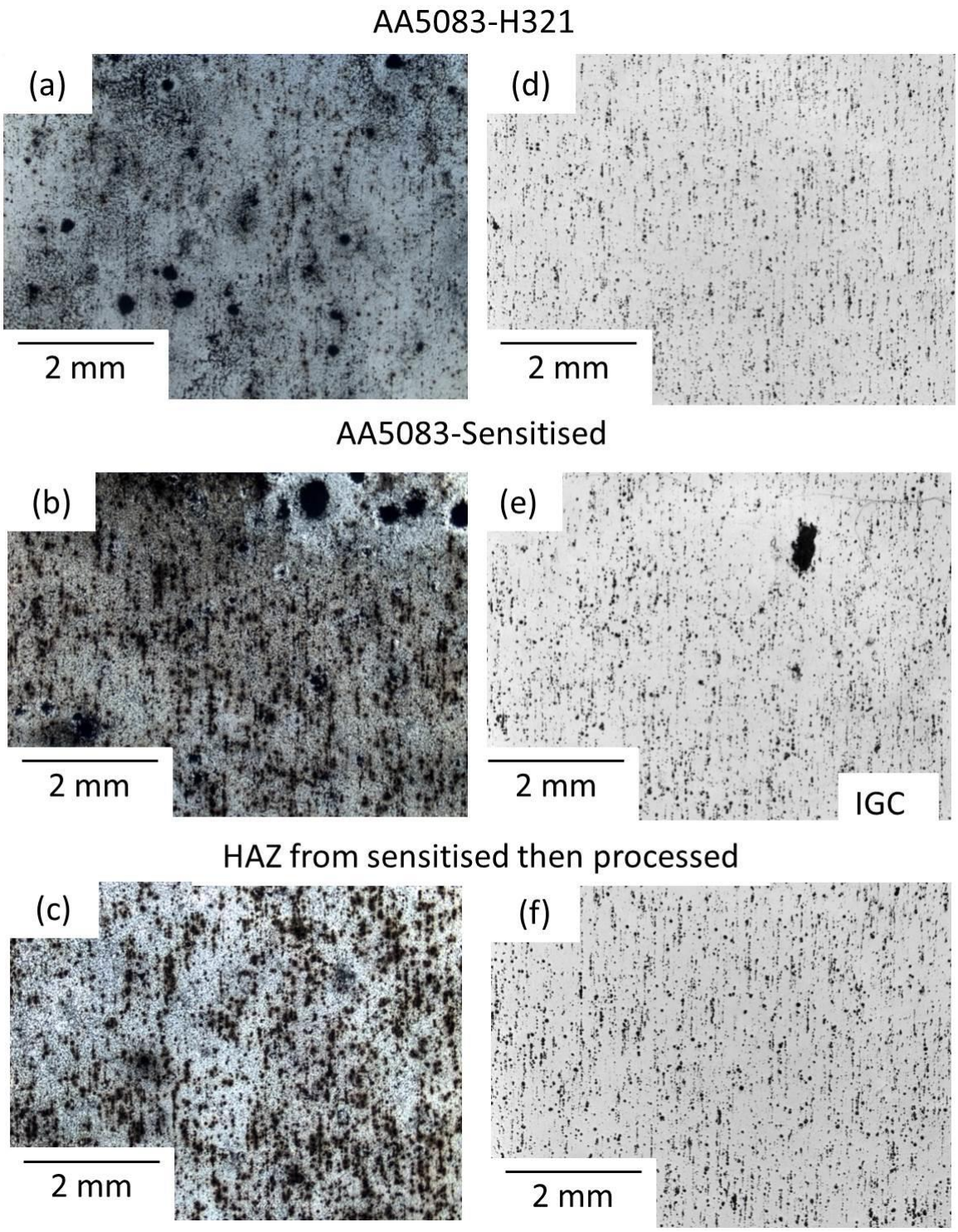

Figure 71 (a) (b) and (c) Optical images from the AA5083-H321, AA5083-sensitised and sensitised then processed samples respectively after immersion in 1M NaCl for 6 weeks. (d) (e) and (f) Optical images of same AA5083-H321, AA5083-sensitised and sensitised then processed surfaces respectively after corrosion product has been removed.

Figure 72 (a) (b) and (c) show detailed micrographs of the immersed samples where the corrosion product has been removed. The size of the grain fall-out from the sensitised sample can clearly be seen, when compared to the AA5083-H321 and AA5083-sensitised then processed samples which show no severe corrosion. Figure 72 (d) (e) and (f) show the corrosion in greater detail. In contrast, the sensitised then processed samples show only cathodic grooving around the Fe-based intermetallic particles, supporting the hypothesis that the processing can remove the susceptibility to IGC that sensitisation can bring about.

Figure 73 shows micrographs of the immersed samples after the corrosion product has been removed and the surface etched with phosphoric acid to reveal the underlying grain structure and highlight those which are susceptible. The corrosion of the AA5083-H321 sample does not follow any of the grain boundaries which the etch has exposed, showing the corrosion not to be intergranular in nature. The edge of the large site of grain fall out in the sensitised sample is detailed in Figure 73 (b), where the IGC propagation outwards from the centre of the site follows the susceptible grain boundaries which have been exposed. The processed sample shows neither susceptible grain boundaries, nor any form of intergranular corrosion, confirming that this material is not sensitised.

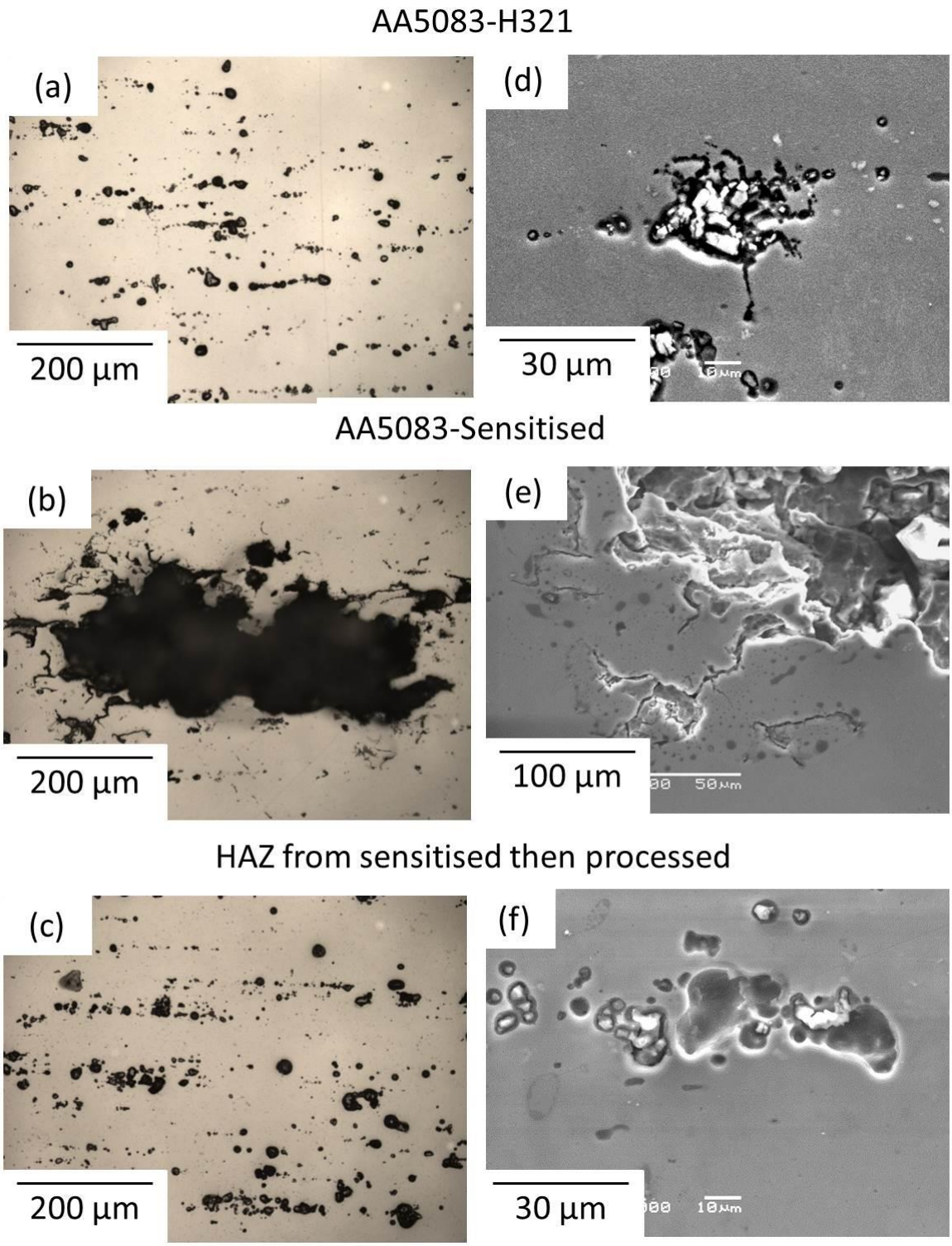

Figure 72 (a) (b) and (c) Optical images from the AA5083-H321, AA5083-sensitised and sensitised then processed samples, respectively, showing a close up of the corrosion on the surface. (d) (e) and (f) SEM images of same AA5083-H321, AA5083-sensitised and sensitised then processed surfaces respectively showing closer detail of the corrosion that has taken place.

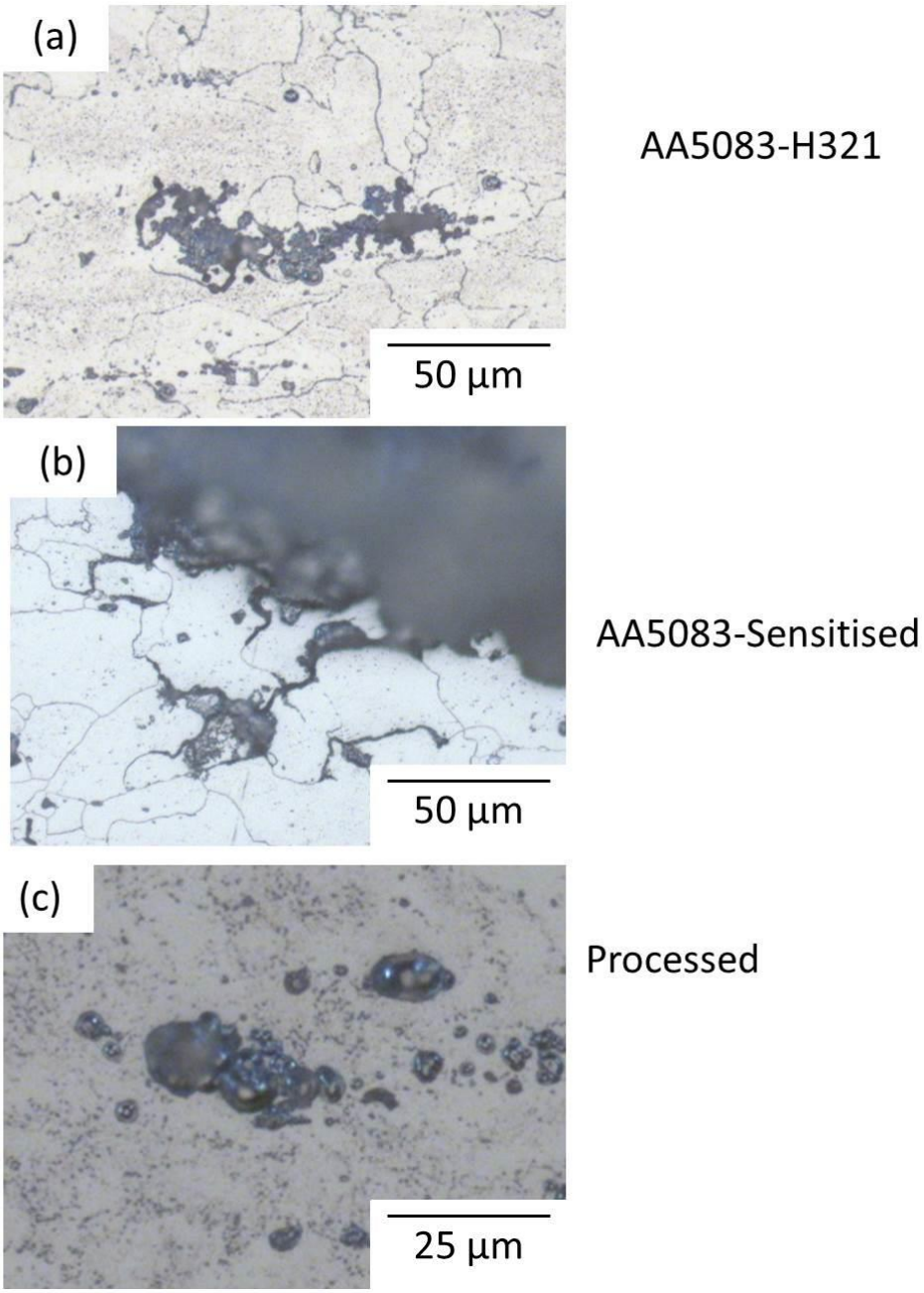

Figure 73 (a), (b) and (c) Optical micrographs of the AA5083-H321, AA5083-sensitised and sensitised then processed samples after immersion in 1 M NaCl for 6 weeks, with the corrosion product removed, then etched in phosphoric acid to reveal the susceptible grain boundaries.

5.2.2. Confocal Laser Scanning Microscopy (CLSM) of immersion samples

Figure 74 shows a 3D model generated by CLSM of the surface of the AA5083-H321 sample after immersion in 1 M NaCl for 6 weeks. The samples have been lightly polished with 0.04 µm colloidal silica for 2-3 seconds to remove any corrosion product around the corrosion sites. The model shows a completely flat and featureless surface which has been unaffected by corrosion. The cathodic grooving around intermetallic particles is also limited to the extent where it is less than 1 µm beneath the surface, and not visible on this model.

The model generated from the sensitised sample which was immersed shows that a great deal of severe corrosion has taken place, Figure 75. A large area of grain fall-out can be seen, over an area 700 µm in length, 300 µm in width (estimated at 200,000 μm^2). This is by far the largest area of corrosive attack seen in any condition, and is the only site of IGC on the sensitised sample which had been immersed.

Figure 76 shows the model generated from the CLSM of the sensitised then processed sample which was immersed under the same conditions as before. The model shows a very flat surface which has been unaffected by IGC, two small areas of cathodic grooving around intermetallic particles can be seen, however they have not penetrated more than 1 µm into the sample. This shows significant improvement in corrosion behaviour over the sensitised sample Figure 75.

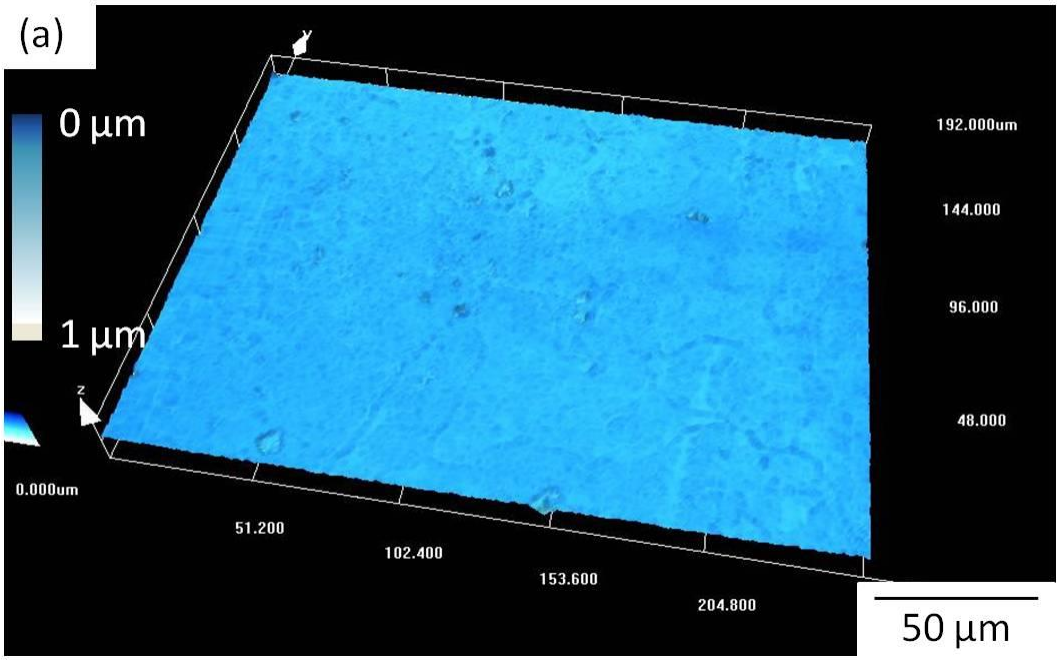

Figure 74 3D texture representation using data from CLSM of the AA5083-H321 sample which was corroded by immersion in 1 M NaCl for 6 weeks, after corrosion product has been removed.

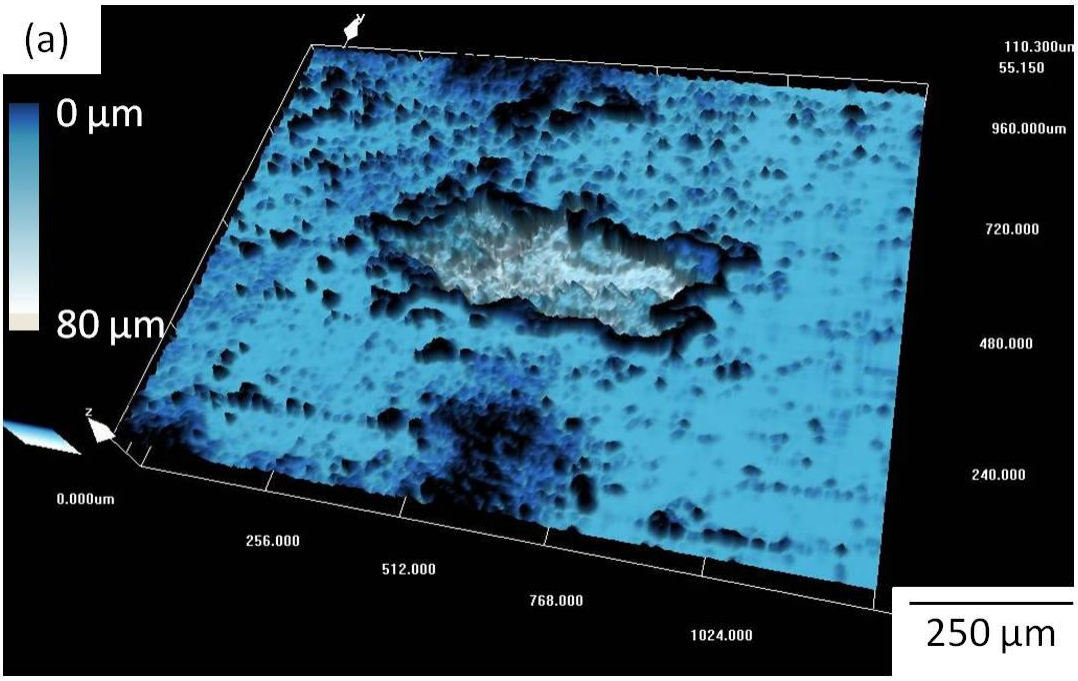

Figure 75 3D texture representation using data from CLSM of the AA5083-sensitised sample which was corroded by immersion in 1 M NaCl for 6 weeks after corrosion product has been removed.

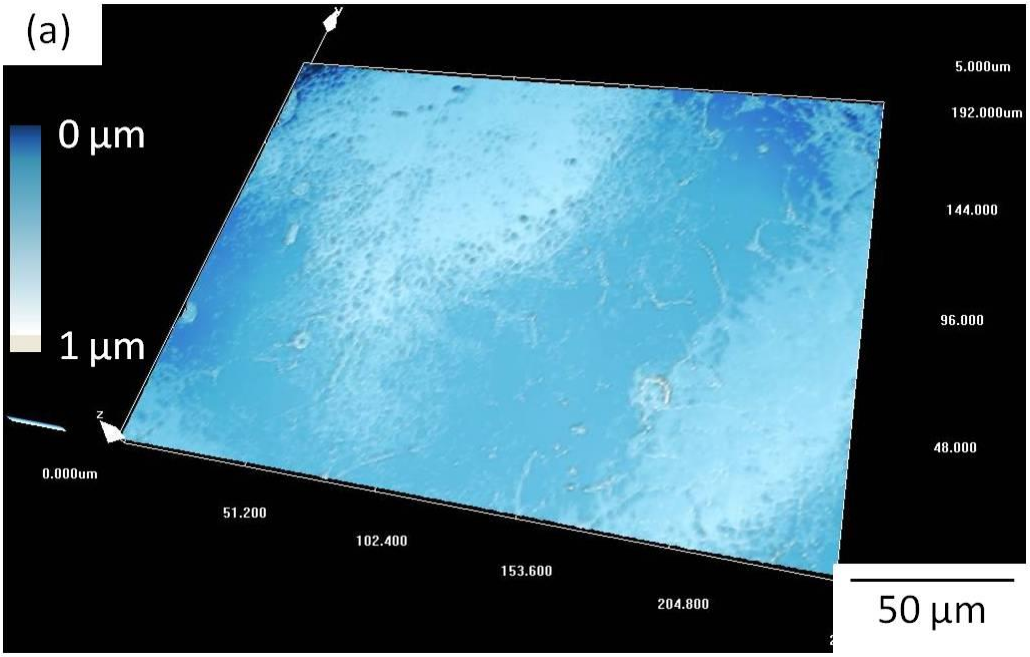

Figure 76 3D texture representation using data from CLSM of the sensitised then processed sample which was corroded by immersion in 1 M NaCl for 6 weeks after corrosion product has been removed.

5.2.3. Atmospheric corrosion

Atmospheric corrosion studies were carried out, in which 12 droplets of solution were placed onto the surface of samples from each condition under investigation.

When droplets of NaCl were placed onto the polished top surface of an AA5083-H321 sample and left in an RH of 85% for 6 weeks, little corrosion appears to have taken place, as is evident from two small sites of localised corrosion product in Figure 77 (a). After the same period of time, droplets placed on the sensitised sample (b), have left a large covering of corrosion product on the whole of the surface as well as several large sites of dense product, initially indicating that more dissolution and corrosion may have taken place. In contrast, the droplets placed on the sensitised then processed sample show no build-up of corrosion product at any point under the surface (c). Drying the droplets reveals the sensitised sample in Figure 77 (e) to have a layer of corrosion product on the surface, while the AA5083-H321 and processed samples show small deposits of localised corrosion product, (d) and (f).

In all samples, it is evident that a degree of corrosion has taken place outside of the identified droplet. This is reasoned to have occurred due to the presence of a thin film of moisture on the sample surface under which corrosion can take place.

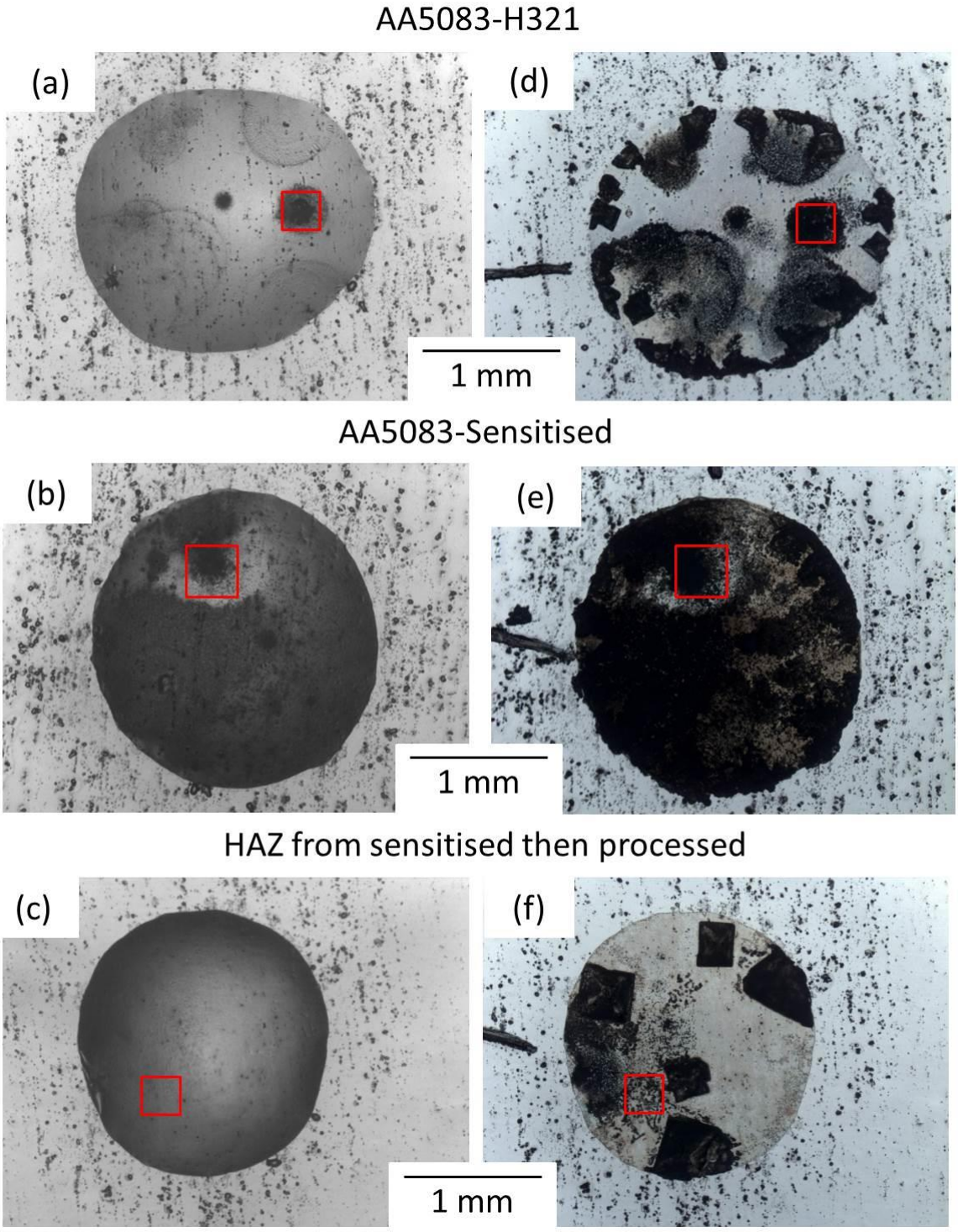

Figure 77 (a) (b) and (c) Optical images of atmospheric droplets on the surface of the AA5083-H321, AA5083-sensitised and sensitised then processed samples respectively after 6 weeks. (Chloride deposition density of 1.3 mg / cm^2, deposited on polished surface and left in 85% RH). (d) (e) and (f) Optical images of the droplet area after being removed from the humid environment and allowed to dry, leaving behind NaCl crystals and corrosion product on the surface. The red box shows the location of Figure 78 SEM images.

The extent of the corrosion on the surface is visible in the AA5083-H321 and sensitised samples once the corrosion product has been removed in Figure 78 (a) and (b). The major sites of corrosion have been highlighted, as has the original shape of the droplet. In the processed sample, no large sites of corrosion can be seen on the surface, Figure 78 (c). SEM micrographs of the areas highlighted are shown in Figure 78 (d) (e) and (f). Both the AA5083-H321 and sensitised samples exhibit intergranular corrosion. The sensitised sample shows a much larger area of corrosion, around 250 μm in size as opposed to 60 μm in the AA5083-H321 sample resulting from more grain boundaries having been attacked. The IGC sites inspected under SEM are the only such sites seen under each droplet. In contrast, the sensitised then processed sample shows no signs of IGC, with only minor cathodic grooving around intermetallic particles, Figure 78 (b). This lack of attack was noted in all 12 droplets applied to the sensitised then processed sample, giving strong evidence that the processing has eliminated the risk of IGC.

Figure 79 shows the 2nd out of 12 repeats for each droplet this experiment, once again showing the AA5083-H321 and sensitised samples having IGC, while the sensitised then processed sample shows no signs of IGC.

Each of the samples was then etched in phosphoric acid in an attempt to confirm that any attack observed was occurring on susceptible gain boundaries. Figure 80 (a) and (b) show the anodic attack sites in the AA5083-H321 and sensitised samples to be situated amongst etched grain boundaries, which had previously contained β-phase. The lack of IGC in the processed sample couples with the observation of un-etched grain boundaries, which contain no β-phase (c). The grain boundaries in this condition are not anodic to the matrix; therefore corrosion will not initiate here preferentially or propagate.

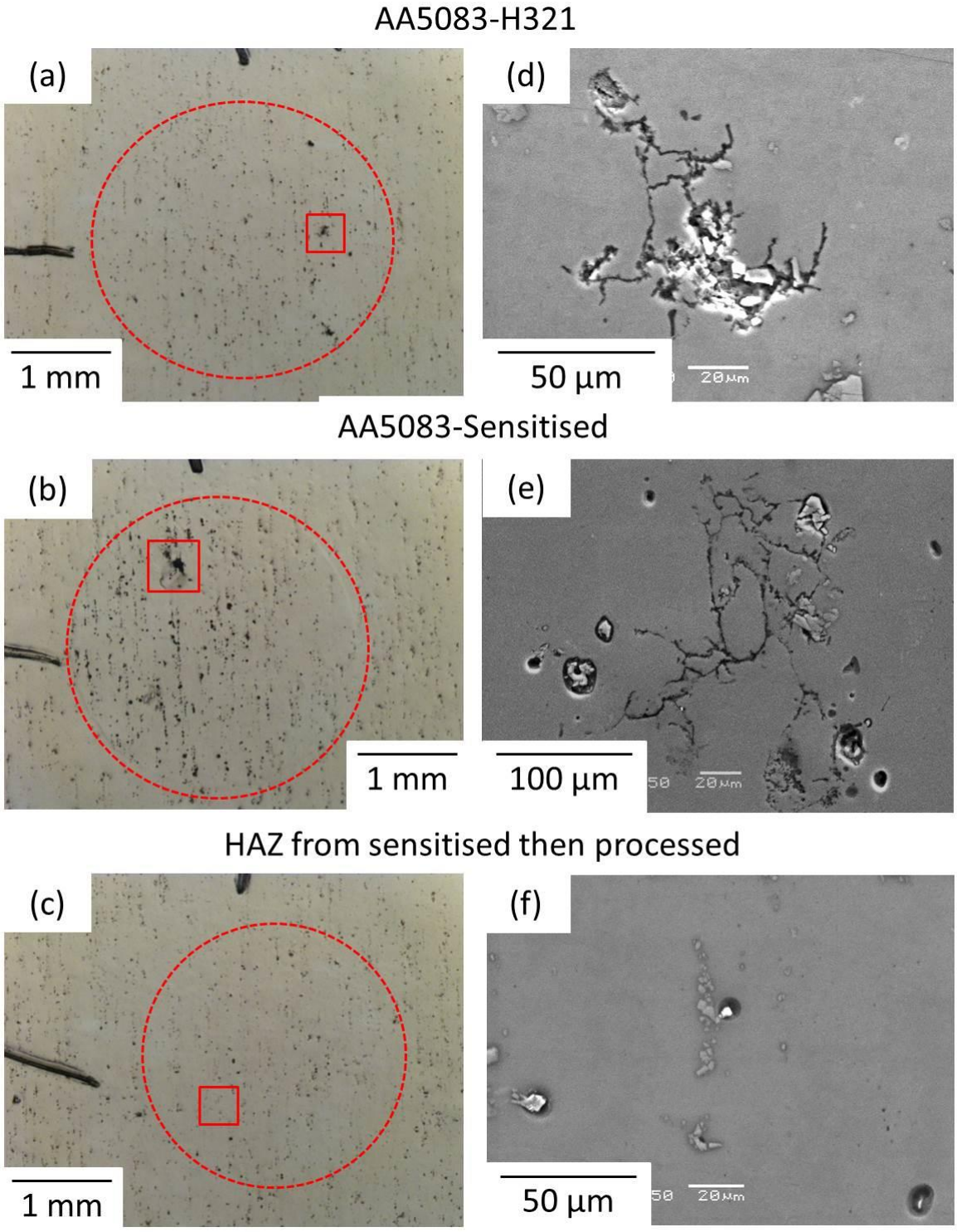

Figure 78 (a) (b) and (c) Optical images of the droplet area after the salt and corrosion product have been removed on the AA5083-H321, AA5083-sensitised and sensitised then processed samples respectively. The red boxes show the locations of the SEM images in (d) (e) and (f) which are micrographs of the corrosion on the surface of the samples.

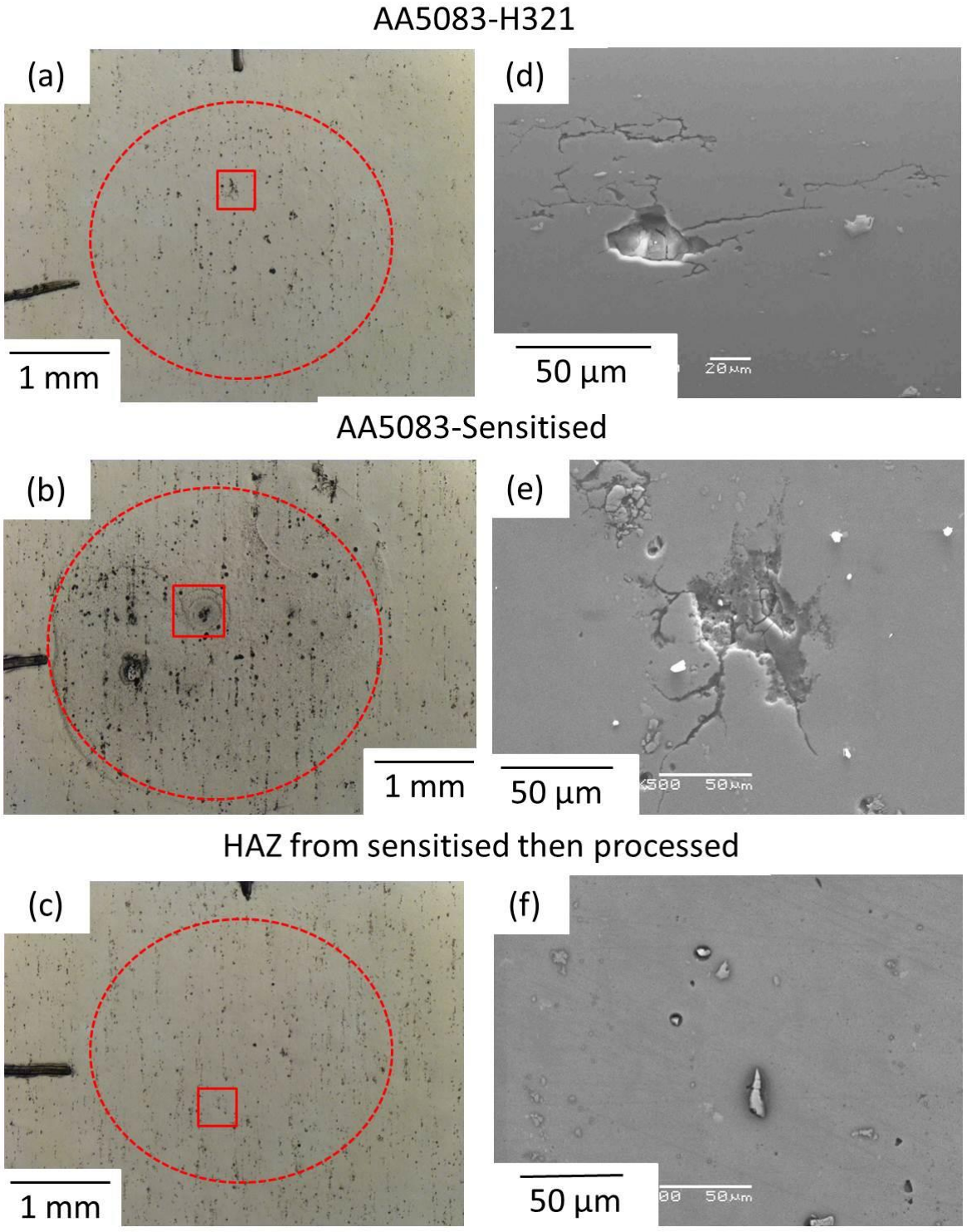

Figure 79 Repeat set of droplets from each condition, shown previously in Figure 78. (a) (b) and (c) Optical images of the droplet area after the salt and corrosion product have been removed on the AA5083-H321, AA5083-sensitised and sensitised then processed samples respectively. The red boxes show the locations of the SEM images in (d) (e) and (f) which are micrographs of the corrosion on the surface of the samples.

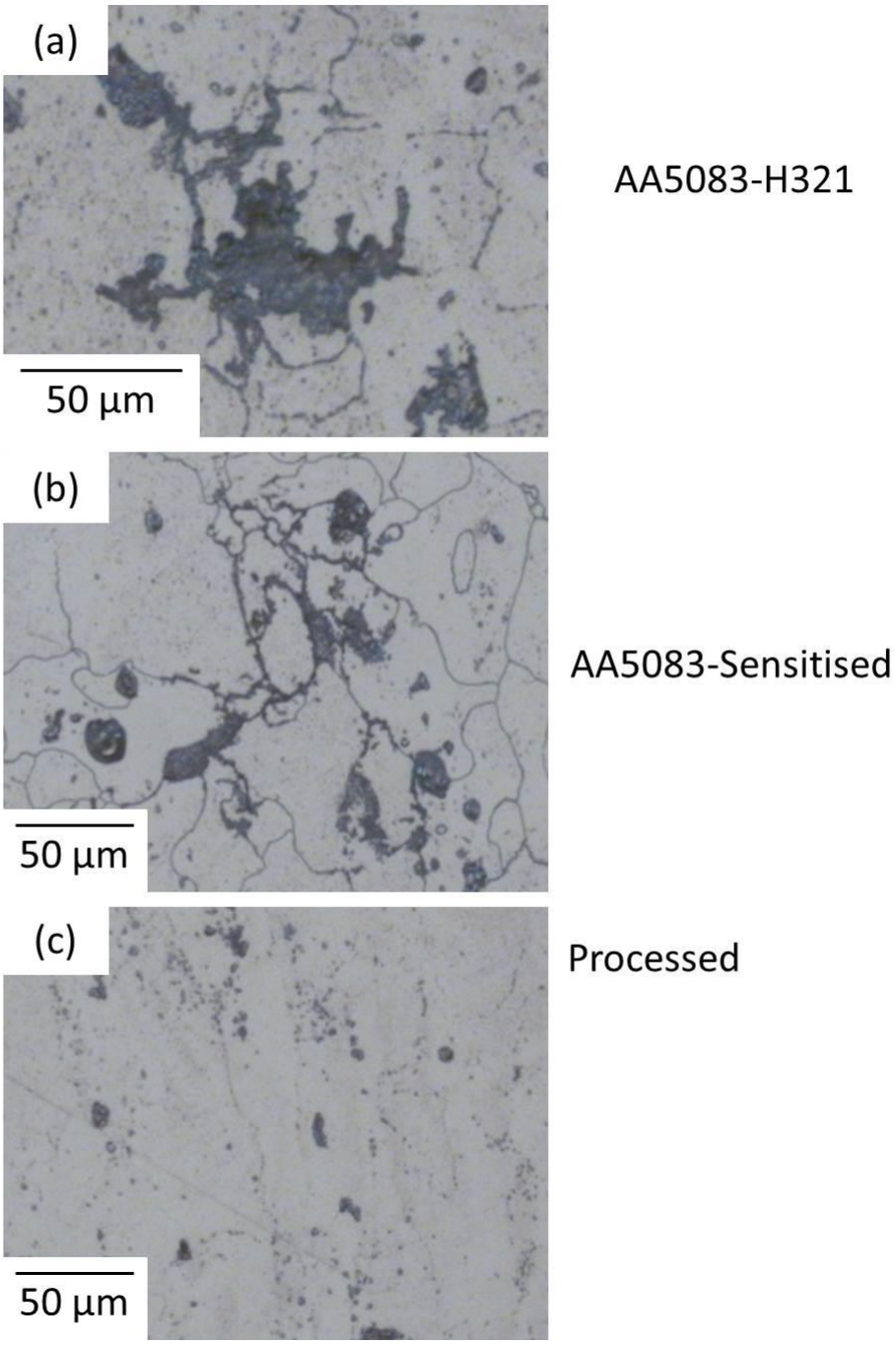

Figure 80 (a) (b) and (c) Optical micrographs showing the corrosion sites in Figure 78 after etching in phosphoric acid to reveal the sensitised grain structure if present, from the AA5083-H321, AA5083-sensitised and sensitised then processed samples

5.2.4. Confocal Laser Scanning Microscopy (CLSM) of atmospheric corrosion samples

Figure 81 (a) and (b) show a micrograph and 3D model of the area of IGC observed in the AA5083-H321 sample which has been corroded under an atmospheric droplet, using (CLSM), again after the corrosion product has been lightly polished off. This model shows the depth of corrosion that has taken place to be 5µm, most likely resulting from a small piece of a grain which has fallen out. Figure 81 (a) also shows the presence of several intermetallic particles on or next to the corroded area.

Use of the CLSM to generate a 3D model of the corrosive attack under the droplet on the sensitised sample is shown in Figure 82. The large scale of the attack is shown in this model, while also showing the lack of depth, only 3 µm, likely due to there being no grain fall-out. Comparison of the large circular areas in Figure 82(b) with those in Figure 82(a) reveals them to be sites of cathodic grooving around intermetallic particles.

This lack of IGC underneath the droplet on the processed sample is shown very clearly in the CLSM 3D model, Figure 83 (b), where corrosive attack is limited to cathodic grooving around intermetallic particles to a depth of less than 1µm. No network of grain boundary attack is present, nor has de-alloying of the intermetallic particle taken place.

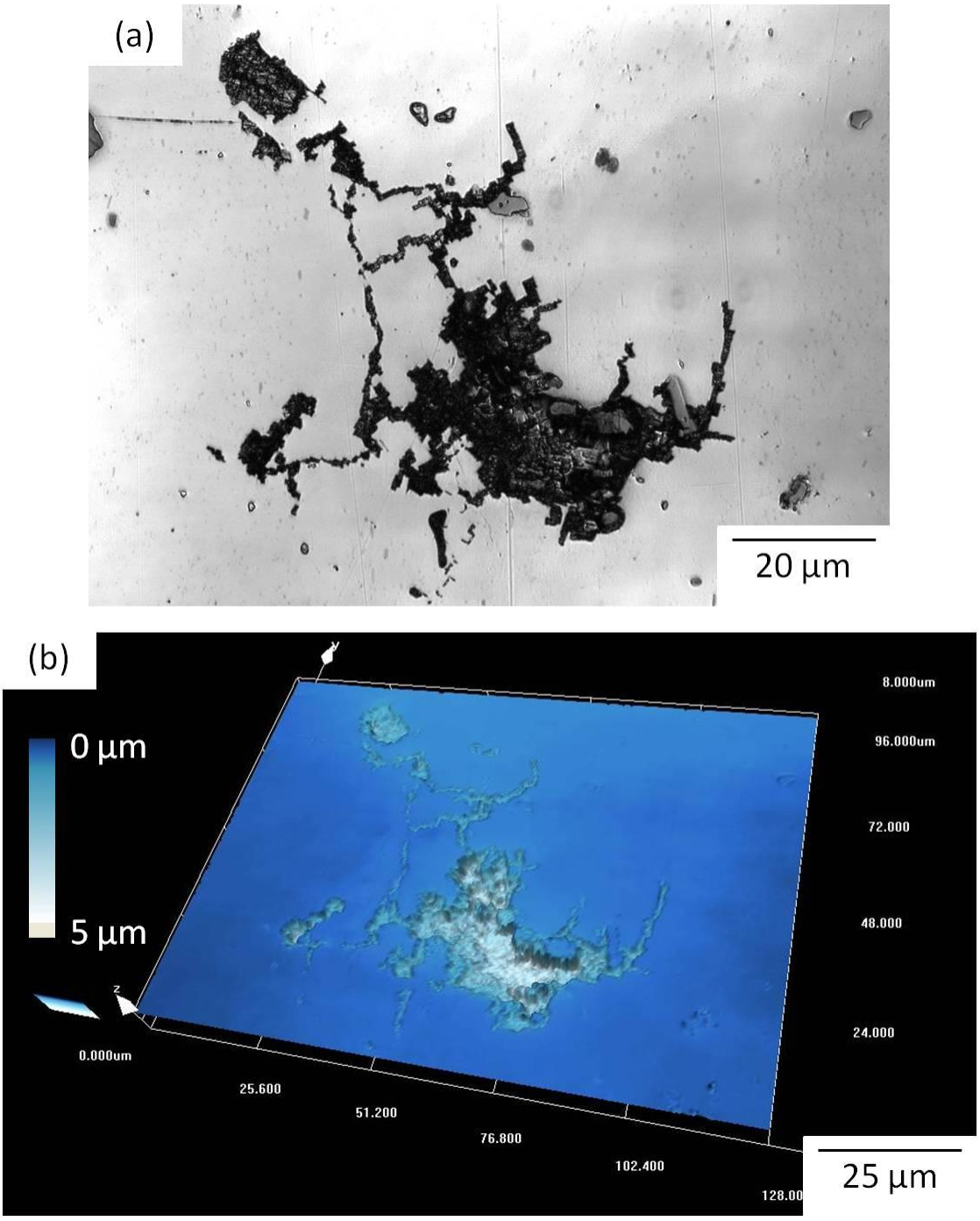

Figure 81 (a) Light microscopy image taken with the CLSM (b) 3D texture representation of same area, taken using data from CLSM, both from the AA5083-H321 sample which was corroded by an atmospheric droplet after corrosion product has been removed.

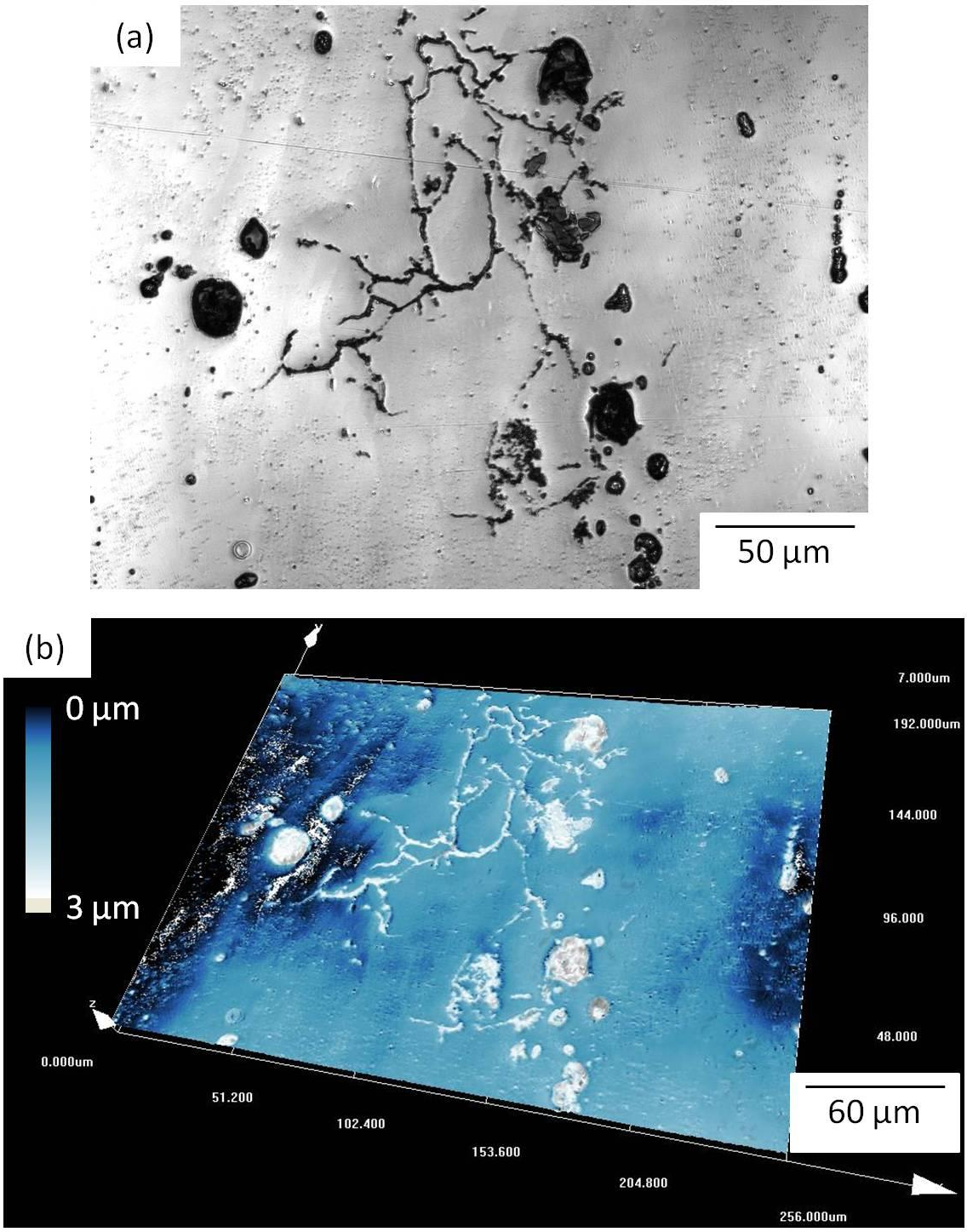

Figure 82 (a) Light microscopy image taken with the CLSM (b) 3D texture representation of same area, taken using data from CLSM, both from the AA5083-sensitised sample which was corroded by an atmospheric droplet after corrosion product has been removed.

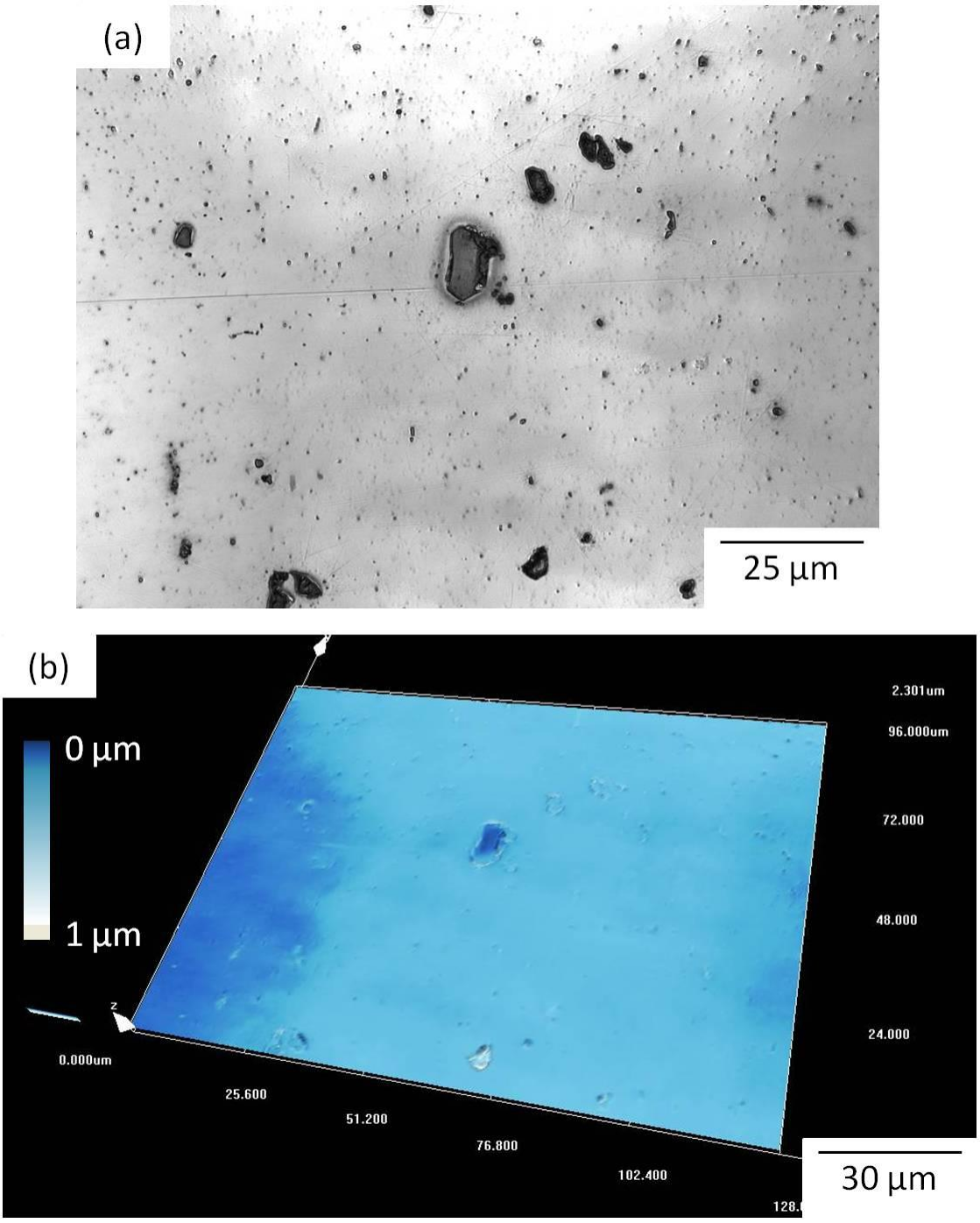

Figure 83 (a) Light microscopy image taken with the CLSM (b) 3D texture representation of same area, taken using data from CLSM, both from the sensitised then processed sample which was corroded by an atmospheric droplet after corrosion product has been removed.

5.3. Electrochemistry

Figure 84 shows a graph of the potentiodynamic sweeps conducted on the AA5083-H321, sensitised, and processed samples. The results indicate that there is very little difference in the breakdown potential measured at a current density of 0.1 mA/cm^2; all of the results being between -680 and -670 mV with the sensitised sample being the lowest, the AA5083-H321 highest, and the processed sample falling between the two. This indicates that there is very little difference between the samples in terms of the breakdown potential in a potentiodynamic sweep, so a further test is required to differentiate between them.

Figure 85 shows the resulting current density for samples polarised at -710 $mV_{(SCE)}$ for 1 hour. The sensitised sample shows a much higher current density over the course of the test, while the sensitised then processed sample shows a much lower current density, on par with the unsensitised sample.

Figure 86 shows the surface of each of the samples after polarisation, where the AA5083-H321 and processed samples show no signs of intergranular attack, while the sensitised sample shows a network of attacked grain boundaries.

Figure 87 shows the resulting current density for samples polarised at -710 $mV_{(SCE)}$ for 24 hours. Here the current density for both the AA5083-H321 and processed samples remain very low and are the same after 24 hours. In contrast, the sensitised sample immediately show a much higher current density which was more than an order of magnitude greater than the other conditions after 24 hours.

Figure 88 shows the surface of the samples after the experiment shown in Figure 87. The AA5083-H321 sample shows very small signs of attack, with discontinuous intergranular character whereas the sensitised sample shows substantial amounts of intergranular attack.

The sensitised then processed sample shows the least attack, with little or no sign of intergranular attack, indicating the effectiveness of the process in returning the sample to an AA5083-H321 state.

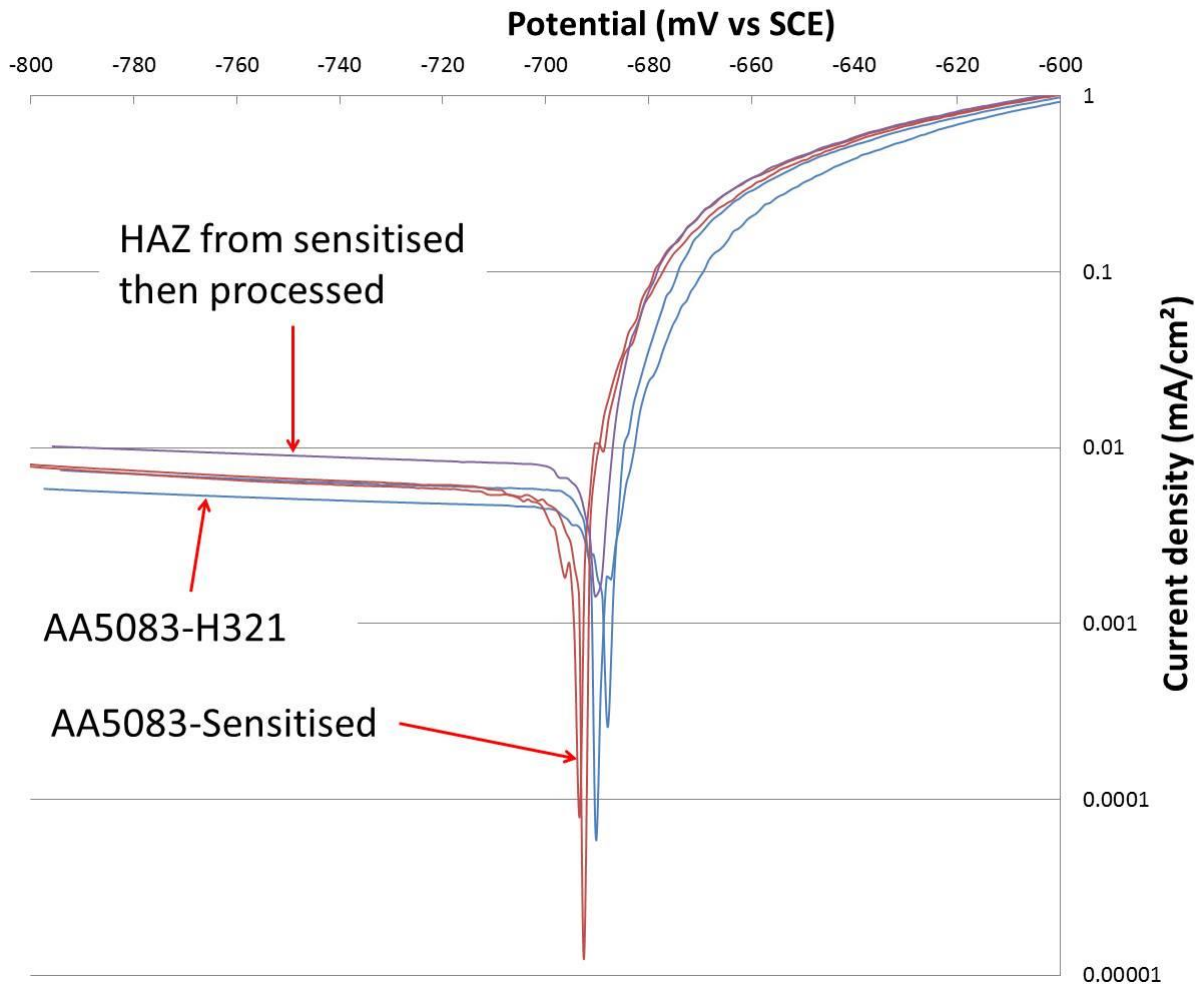

Figure 84 Potentiodynamic sweeps conducted on the AA5083-H321, AA5083-sensitised and sensitised then processed samples in naturally aerated 0.1 M NaCl at a sweep rate of 1 mV/s.

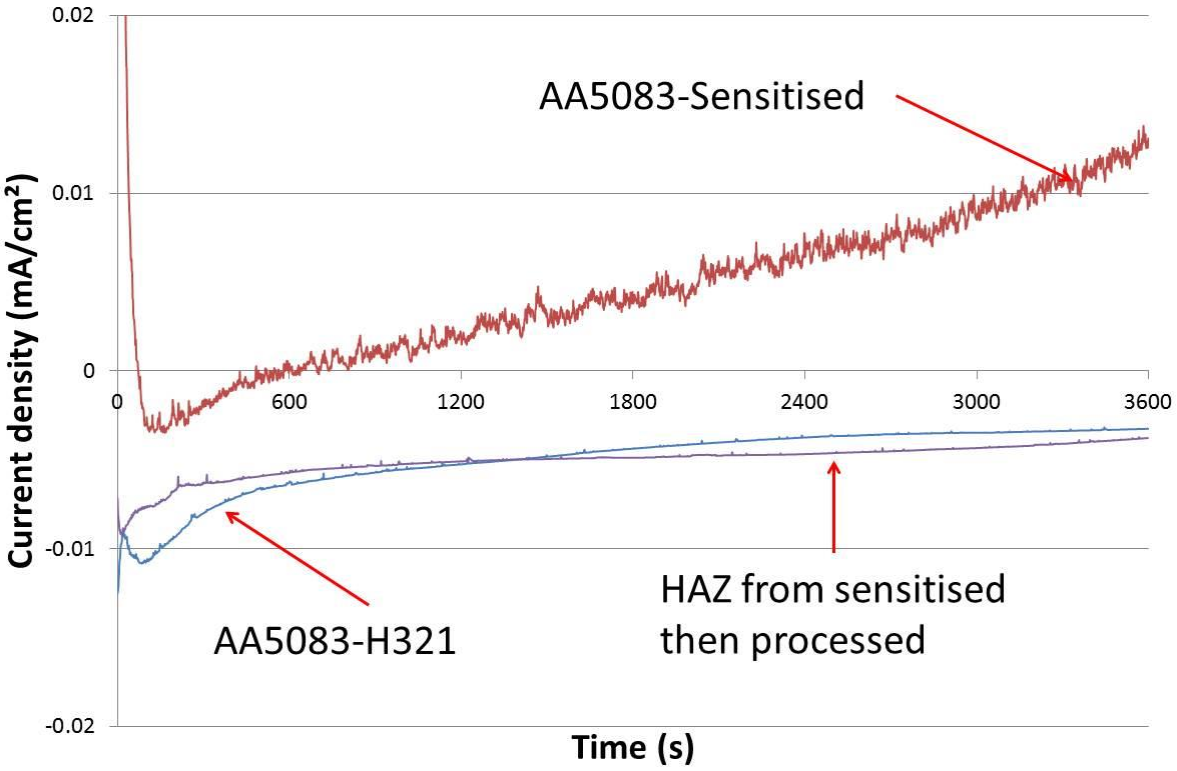

Figure 85 Potentiostatic polarisation at -710 $mV_{(SCE)}$ for 1 hour conducted on the AA5083-H321, AA5083-sensitised and sensitised then processed samples in 0.1 M NaCl, acidified to pH 2.75 at a sweep rate of 1 mV/s.

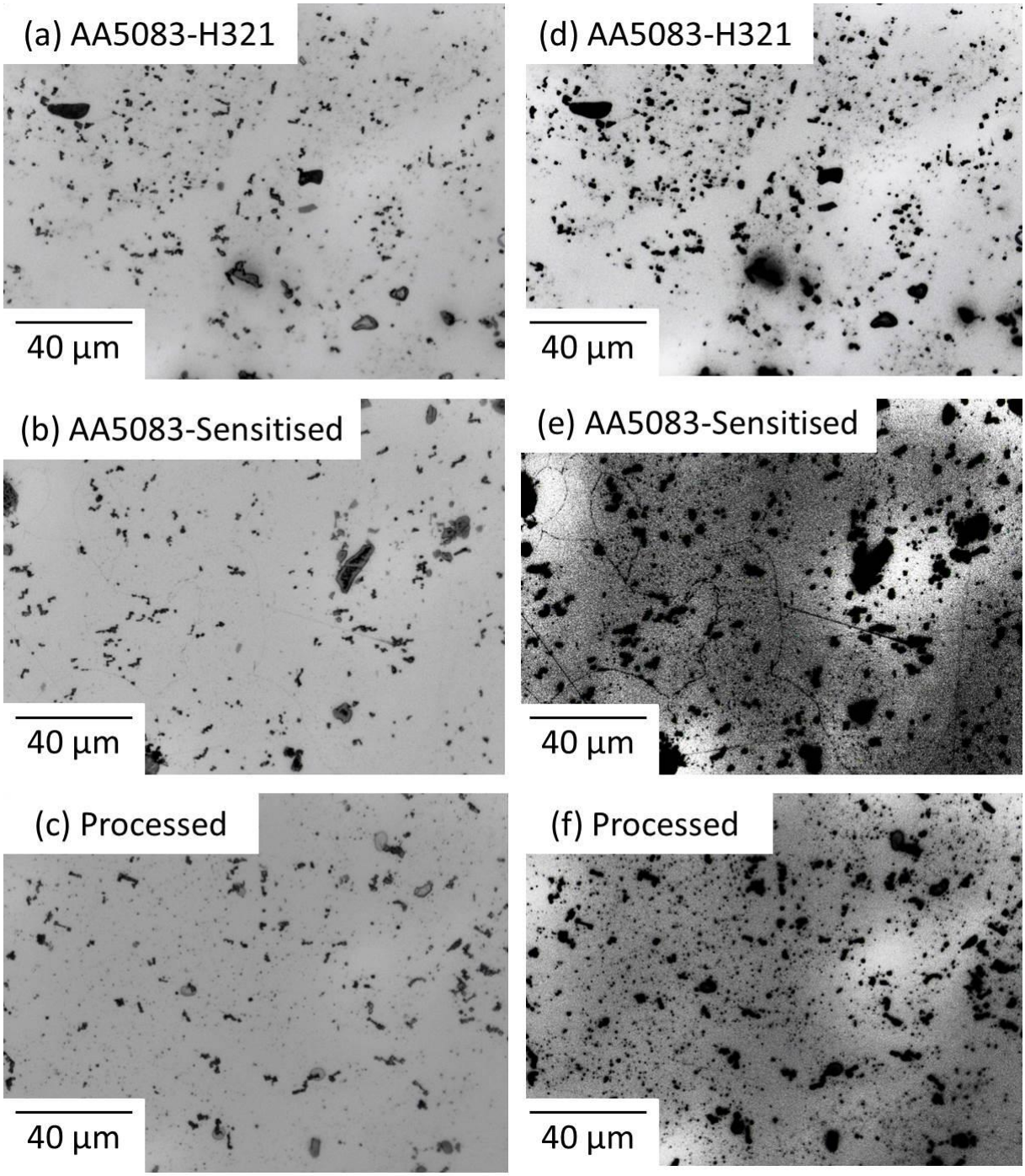

Figure 86 (a) (c) and (e) Optical micrographs of the surface of the AA5083-H321, AA5083-sensitised and sensitised then processed samples after potentiostatic polarisation at -710 mV for 1 hour in 0.1 M NaCl, shown in Figure 85. (b) (d) and (f) show the same images after image processing to highlight the intergranular attack in the sensitised sample, but lack of any IGC in the AA5083-H321 and processed samples.

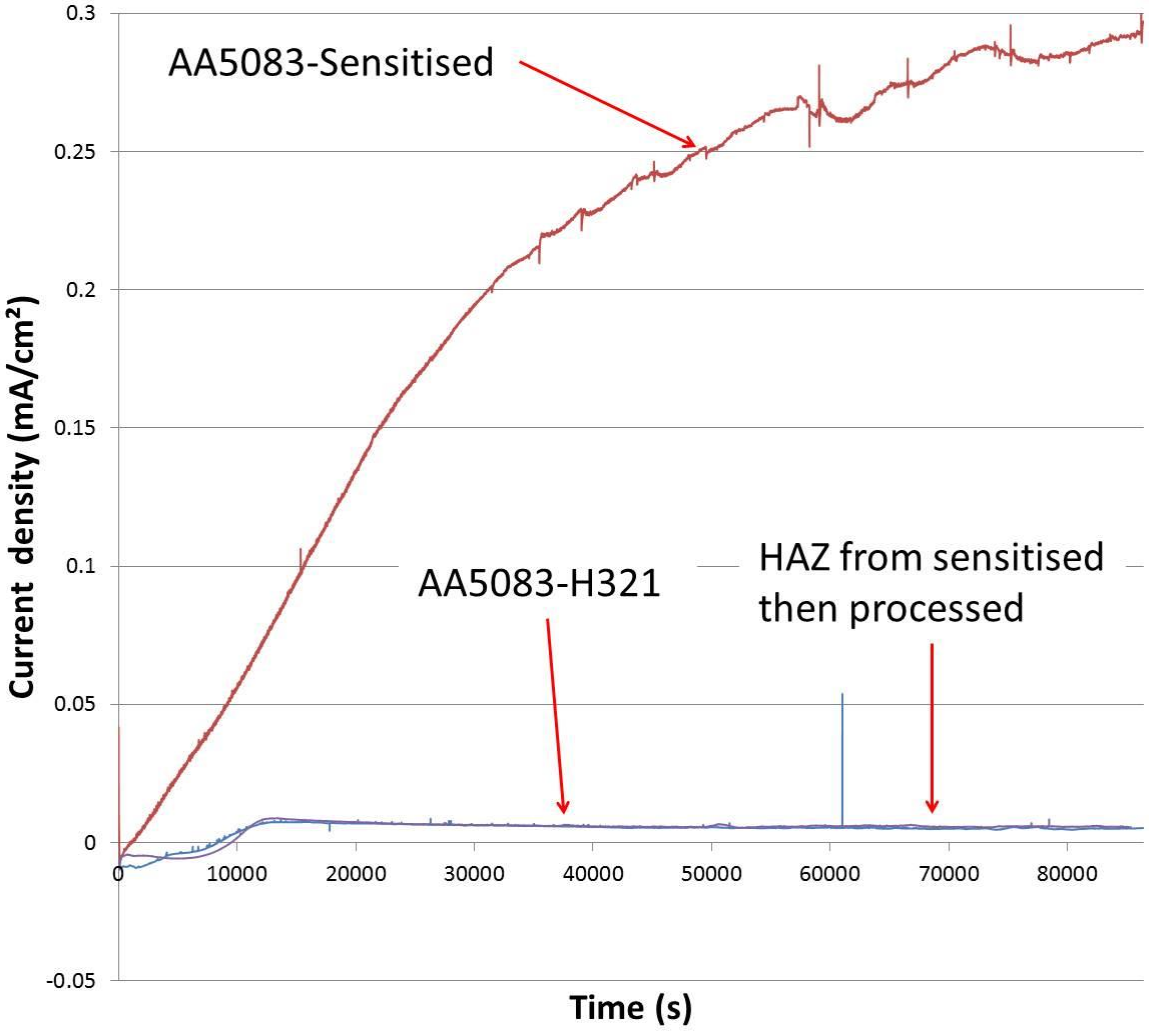

Figure 87 Potentiostatic hold at -710 mV for 24 hours conducted on the AA5083-H321, AA5083-sensitised and sensitised then processed samples in 0.1 M NaCl, acidified to pH 2.75 at a sweep rate of 1 mV/s.

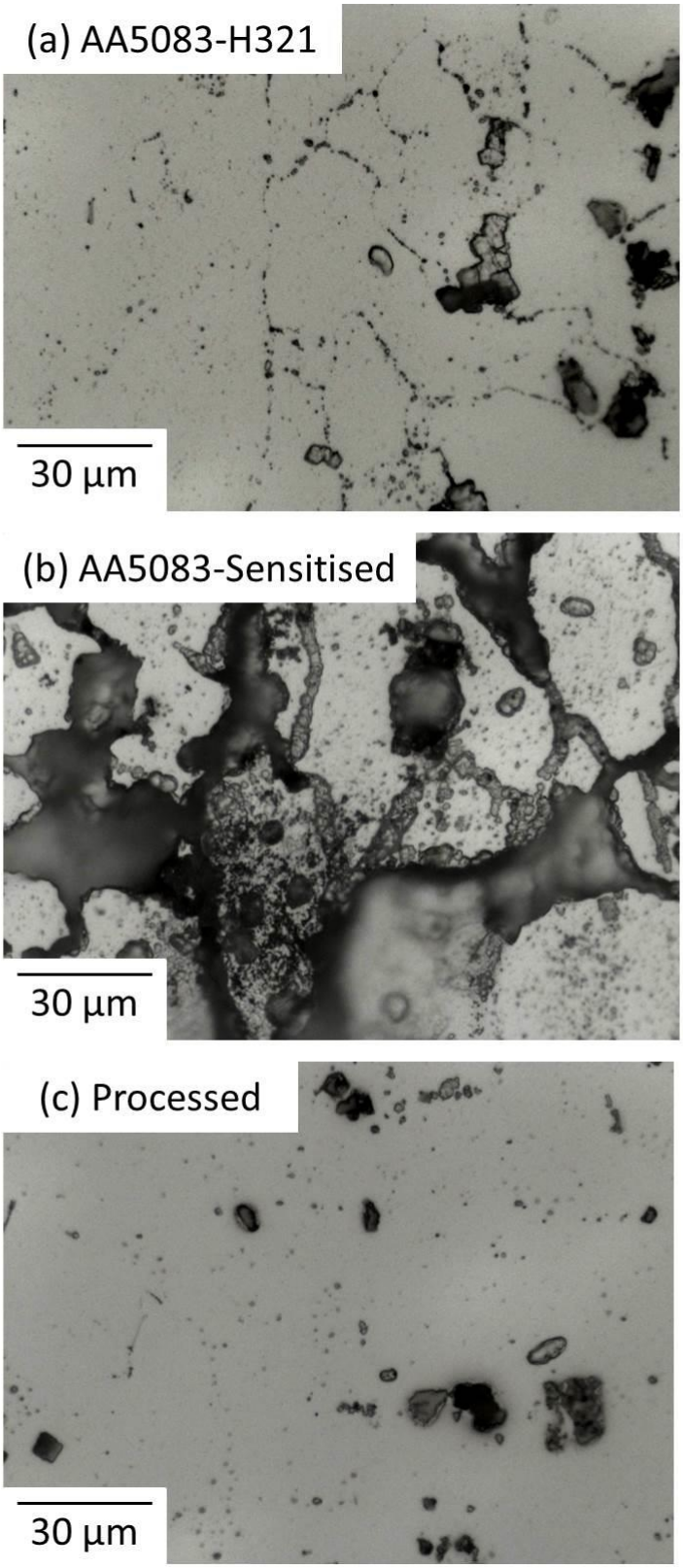

Figure 88 Optical micrographs of the surface of AA5083-H321, AA5083-sensitised and sensitised then processed samples after potentiostatic polarisation at -710 mV for 24 hours in 0.1 M NaCl, shown in Figure 87.

5.4. Discussion

5.4.1. Macrostructural changes brought about by Friction Surface Processing

Figure 63 demonstrates the ability of the FSP process to generate overlapping passes which can cover a large surface area of the plate. Inspection of the processed cross section after etching in Kellers reagent in Figure 64 reveals discontinuous regions of thermo-mechanically affected region exist at the top of the plate, as a result of the small submerged pin on the FSP tool. The top surface which displays the rotating tool pattern is also thermo-mechanically affected. While this region is heterogeneous and may display favourable corrosion properties as shown in full thickness processing in Chapter 4, it also has a very rough processed surface, the removal of which exposes a continuous coverage of HAZ.

The heat affected zone underneath the surface of the processed region forms a continuous layer across the plate, extending 3-4 mm below the surface, the formation of a HAZ being well documented in related processes [130]. The thinnest regions of the HAZ under the surface area in between two TMAZ regions and will have had the majority of its heat input from the tool shoulder rather than the submerged pin.

5.4.2. Microstructural changes brought about by sensitisation and Friction Surface Processing

5.4.2.1. Intermetallic particles

Following a sensitisation heat treatment of the base AA5083-H321sample, no change can be seen in the distribution or the particle size, Figure 65 (a) and (b) compared to (c) and (d). This is to be expected as the sensitisation was conducted at 100 °C for 2 weeks which is insufficient to dissolve these second phase particles.

In the HAZ region of the FSP pass, no difference can be seen in the size of the intermetallic particles compared to those in the sensitised plate. This region has only transiently been through elevated temperatures due to the FSP, which is again insufficient to cause large scale dissolution or precipitation, depending on the particle temperatures associated with those processes for each particle.

5.4.2.2. TEM observations

Inspection of the fine scale microstructure via TEM shows the grain boundaries of the AA5083-H321 plate to be free from any grain boundary precipitates, Figure 67, an observation which was true of 100+ other grain boundaries of the same condition and previous studies into this alloy [18, 39]. Sensitisation of the H321 plate led to the precipitation of β-phase onto the grain boundary as discrete particles, which have been marked in Figure 68. These precipitates are up to 500 nm in length and 200 nm in width.

Their morphology is dissimilar to that seen in previous studies [16, 18, 39], in that no repeating pattern of triangular precipitates has been formed. Searles et al. also observed this morphology as ageing time was increased from 182 to 262 hours in AA5083 which was sensitised at 150°C [73]. They reasoned that the continuous film of β-precipitates which had

formed at lower ageing times breaks up with sufficiently long ageing times. This result ties in with the observations in Chapter 4, where a shorter ageing time led to continuous precipitation.

After processing of the sensitised plate, TEM inspection of the HAZ region shows that the grain boundaries are once again free from observable precipitates, Figure 69, an observation which has no parallel in literature to date.

5.4.2.3. Phosphoric acid etching

The susceptibility of the alloy to IGC is shown most clearly when it is immersed in phosphoric acid to selectively etch out grain boundaries onto which β-phase has precipitated. The AA5083-H321 sample in Figure 70 (d) shows very little etch response, but the attack is discontinuous in nature and the sites are very spread out, indicating that there may have been pre-existing β-phase within the sample, likely to have been formed through tempering heat treatments in production and natural ageing, but which could not be identified easily under TEM. A sensitisation heat treatment of 100°C for 14 days led to the sample becoming very susceptible to corrosion, inferred from the high degree of grain boundary etching in Figure 70 (e). Here, the region etched out is both wide and continuous in nature, indicating that a much greater degree of β-phase was present and has been removed by etching. This result draws comparisons with the work of Oguocha et al. who observed a similar etch response when AA5083 was subjected to a heat treatment of 100 °C for 7 days [71].

The discontinuous nature of the precipitation observed under TEM does not match the continuous etch seen in Figure 70 (e). Despite clean sections of grain boundary occurring between precipitates, they would appear to be close enough together to allow the dissolution

to move between them. This method was proposed by Winsley [39], where breakdown of β-phase leads to the liberation of Mg^{2+} ions which result in a very aggressive localised solution which attacks the surrounding aluminium matrix. This attack continues along the grain boundary until the next precipitate is reached, thus allowing discontinuous precipitation to lead to continuous attack.

After processing the plate and inspecting the results of phosphoric acid etching in the HAZ of the FSP pass, very little attack resulting from the etch can be seen, Figure 70 (f). The attack is discontinuous to the point where the grain outline is no longer distinguishable as it was in the AA5083-H321 sample in Figure 70 (d), a result consistent with the lack of observable β-phase under TEM after processing.

5.4.3. Corrosion behaviour of Sensitised and Friction Surface Processed material

5.4.3.1. Immersion testing

Figure 71 (d) and Figure 72 (d) demonstrate the low degree of corrosion which the AA5083-H321 material undergoes when immersed in 1 M NaCl for 6 weeks. These observations are consistent with other studies into the corrosion behaviour of AA5083 [55]. After sensitisation, the same pattern of localised corrosion around intermetallic particles still exists, however there are several large sites of intergranular corrosion, highlighted in Figure 72 (b), Figure 72 (e), a finding consistent with other studies of Al-Mg alloys [71, 81, 188].

Confocal Laser Scanning Microscopy of the AA5083-H321 sample after immersion, Figure 74, shows there to be no intergranular attack. This behaviour is similar to that seen in AA5083-H116 exposed to 1 M NaCl for 1 week, which has also shown localised pitting

corrosion [39], while AA5456-H116 showed pits up to 6 μm in diameter after immersion in 3.5 % NaCl for 2 weeks [89].

Measurements obtained in this study show the sensitised sample to have suffered from a large area of IGC and grain fallout after 6 weeks of corrosion, Figure 75. This is far greater than the average volume of the corroded regions, 23.1 μm^3, reported in AA5456-H116 which had been sensitised for 100 hours at 150 °C and corroded for 2 weeks in a 3.5 % NaCl solution [89]. This is likely due to different sensitisation and corrosion times as well as the slightly different composition of the alloy.

In the HAZ of the sensitised then processed sample, the morphology of the corrosive attack, the etch response and TEM observations are all comparable to the AA5083-H321 material, indicating the removal of β-phase from grain boundaries returns the material to a state that is not susceptible to IGC.

5.4.3.2. Atmospheric corrosion

Atmospheric corrosion of both AA5083-H321 and sensitised material shows evidence of IGC. However that which occurs in the sensitised material covers a larger area, indicating a greater susceptibility, Figure 78 (d) and (e) and Figure 80 (a). No literature exists about the atmospheric corrosion of Al-Mg alloys; however grain boundary attack by this method of corrosion has been seen in the 2024 aluminium alloys [105, 189].

The occurrence of IGC in the AA5083-H321 sample under atmospheric corrosion but not under fully immersed corrosion may show the different types of corrosion that the testing conditions will promote. The droplet that was placed on the surface of the sample was of 1 M NaCl concentration, and would have then reached an equilibrium with regards to droplet

concentration and volume. As only single droplets were placed on the surface as opposed to the sample being fully immersed it is likely that the ability of oxygen to reach the surface of the sample at the thinner, outer edge of the droplet would be increased, thus increasing the rate of reduction reactions.

After 6 weeks of atmospheric corrosion, very little corrosion has taken place in the HAZ of the sensitised then processed sample Figure 78 (f). None of the 12 droplets on the HAZ region showed as much corrosion as any droplets that had been on the parent material under the same conditions, lending to the idea that the heat imparted to this region has removed the susceptible grain boundary phase to the point where corrosion behaviour has become better than the H321 temper.

5.4.3.3. Electrochemistry

It is evident from the results of potentiodynamic sweeps of the AA5083-H321, sensitised and processed samples that very little difference exists in the corrosion potential and breakdown potential of the various conditions, Figure 84.

Chang tested the intergranular susceptibility of AA5083 before and after applying a heat treatment of 500 °C for 1 hour [188]. The heat treatment was shown to significantly increase the intergranular corrosion susceptibility of the sample (tested by NAMLT), but most crucially lowered the corrosion potential from -842 to -992 $mV_{(SCE)}$ and the breakdown potential at 0.1 mA/cm^2 from -653 to -740 $mV_{(SCE)}$. This was attributed to the greater reactivity of the β-phase which is highly anodic to the alloy matrix. While the amount of β-phase on the grain boundaries was not quantified or observed, the significant change in

breakdown potential which occurs compared to the current study implies that it may be relatively large compared to the small, discontinuous precipitates observed here.

Chang also followed the sensitisation with further annealing at 345°C for 1 hour, which had the effect of returning the NAMLT values to those of the AA5083-H321 sample and returning the breakdown potential to within 6 $mV_{(SCE)}$ of the base sample [188]. These results concluded that the IGC susceptibility of the sample could be "eliminated by dissolution of the continuous precipitation layer along the grain boundaries", a finding consistent with both Summerson and Sprowls [190], and Dix [40].

Potentiostatic polarisation for 1 and 24 hours shows a dramatic increase in current density in the sensitised sample over the AA5083-H321 sample and sensitised then processed region, which show a passive current density, Figure 85 and Figure 87. A similar difference in polarisation behaviour has been seen in a 5083 alloy in the H116 temper and a sensitised condition [39].

The effect of the polarisation on the surface of the sample after 1 and 24 hours is shown in Figure 86 and Figure 88 where it is evident that the sensitised sample shows a much greater degree of attack than the AA5083-H321 sample.

5.5. Conclusions

1. Sensitisation of AA5083 for 336 hours at 100 °C leads to the formation of β-phase on grain boundaries, causing susceptibility to intergranular corrosion.

2. Friction surface processing of sensitised AA5083 leads to the formation of a heat-affected zone under the tool piece in which β-phase has been removed from the grain boundaries, leading to improved resistance to intergranular corrosion.

Chapter 6 – The effect of re-sensitisation of processed material on microstructure and corrosion behaviour of AA5083

Chapter 5 concluded that the heat imparted into the surface of the AA5083 plate which had undergone sensitisation was sufficient to re-dissolve the β-phase from the grain boundaries and leave the material un-susceptible to intergranular corrosion.

This technique would be applicable as an in-service repair mechanism to render the outer 2-4 mm immune to IGC while giving the outer surface a thin thermomechanical treatment which adds a layer of protection from further attack. If a component is then to be put back into service, the repair must withstand exposure to further sensitising conditions and corrosive environment.

To this end, a sensitised then FSP'd plate was re-sensitised using the same sensitising conditions of 14 days at 100 °C. This should give direct comparison of the microstructure and corrosion behaviour that arise from sensitising repaired material as opposed to sensitising the original H321 material.

6.1. Microstructural characterisation of re-sensitised plate

6.1.1. Observations of microstructure and intermetallic particles

Figure 89 shows an SEM micrograph from the cross section of the re-sensitised plate in the HAZ region that has undergone sensitisation for 14 days at 100°C, then processing and a second sensitisation heat treatment. These particles are larger and less homogenously distributed than those seen in the processed nugget region. Since this region has not undergone any mechanical deformation, the intermetallic particles are seen to be distributed in the same fashion as the parent material, and the HAZ of the processed region, Figure 89 (a) and (b).

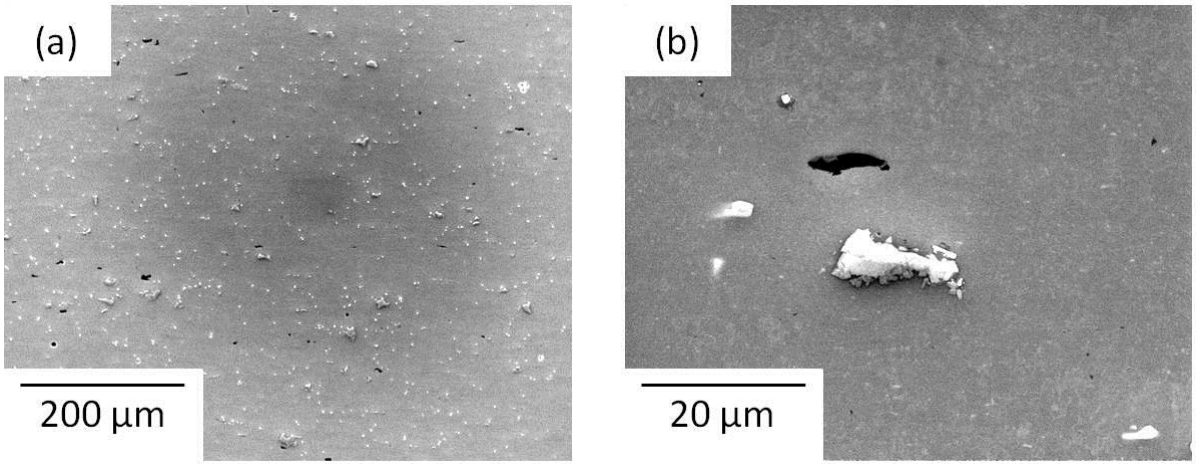

Figure 89 SEM micrographs taken from the HAZ of the processed sample after re-sensitisation for 2 weeks at 100°C showing (a) low magnification (b) high magnification.

6.1.2. TEM observations of grain boundaries

Figure 90 shows TEM micrographs taken from a section of the re-sensitised HAZ. The composite picture shows a grain boundary which starts at the surface in the bottom left corner, and extends 20 µm into the sample. Along this grain boundary, several sites of precipitates have been identified and highlighted, believed to be β-phase. These are between 500 nm to 1 µm in length and up to 500 nm in width, and are discontinuous in morphology, having a gap of 2 µm between them. One of these sites has been enlarged and is shown to lie on one side of the grain boundary, as did the other sites observed.

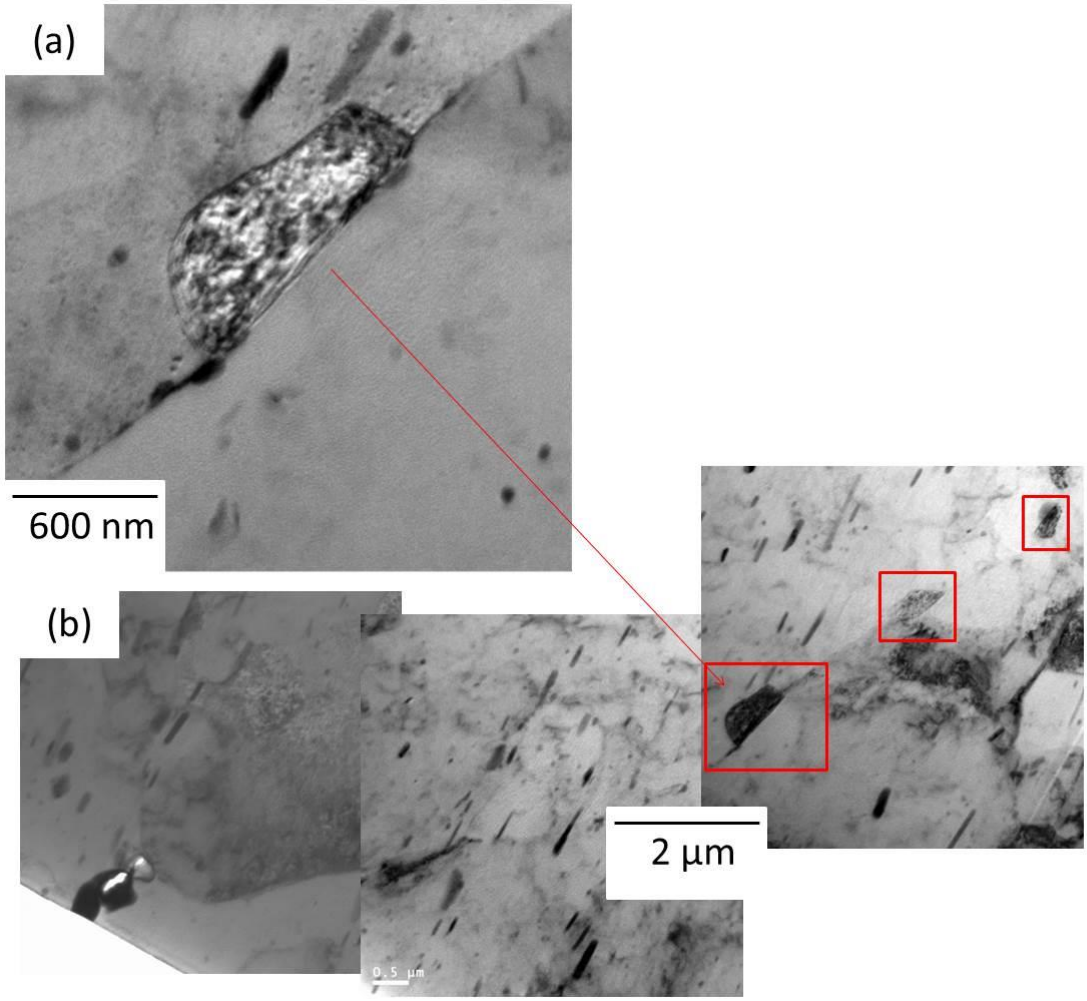

Figure 90 TEM micrographs taken from the HAZ of the processed sample after re-sensitisation for 2 weeks at 100°C showing where the occurrence of β-phase on grain boundaries is highlighted by arrows (a) high magnification (b) low magnification

6.1.3. Phosphoric acid etching to indicate degree of β-phase present on grain boundaries

Figure 91 shows SEM micrographs taken from the re-sensitised HAZ region after etching in phosphoric acid to reveal any grain boundaries which are susceptible to corrosive attack. This figure shows that the grain boundary network has been extensively etched out; however Figure 91 (b) shows this attack to be discontinuous in nature, which is slightly less severe than that seen in an equivalent etch on the once sensitised material seen in Figure 70 (e), Chapter 5, which showed a continuous attack under the same conditions.

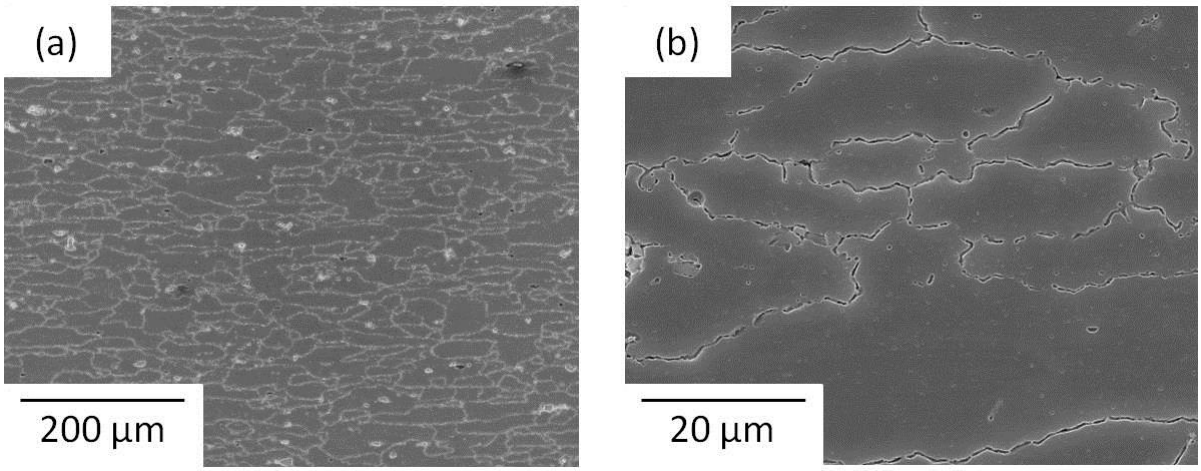

Figure 91 SEM micrographs taken from the HAZ of the processed sample after re-sensitisation for 2 weeks at 100°C, then etched in 10% phosphoric acid at 60°C for 30 seconds, showing (a) low magnification (b) high magnification

6.2. Corrosion testing

6.2.1. Immersion testing

Figure 92 (d) shows the extent of the corrosion product covering the re-sensitised sample after immersion in 1 M NaCl for 6 weeks. There are many large sites of corrosion product accumulation on the surface as well as heavy deposits over the majority of the surface, more than were seen on the previous three conditions (a) (b) and (c). Removal of the corrosion product shows the surface to have a large degree of attack around intermetallic particles, as is characteristic of all samples. However there are several large sites of IGC present, highlighted in Figure 93 (d). There are four sites of such attack in this sample, compared to the once sensitised sample which showed only one such site of heavy attack.

Figure 94 (d) shows this corrosion in greater detail, where the attack spreads to over 400 µm in width. While this is smaller in size and less severe than the grain fall-out observed in the once sensitised sample, there are 4 such sites observed in the re-sensitised conditions, indicating that the attack can initiate at multiple sites. This also shows a return to IGC susceptibility over the sensitised then processed sample (c).

The IGC nature of the corrosion is confirmed in Figure 95 (d) where the corroded, re-sensitised sample was etched in phosphoric acid to reveal the network of susceptible grain boundaries which have been brought about by the re-sensitisation. The network of grain boundaries match the IGC which has taken place, much like the corrosion in the once sensitised sample, Figure 95 (b).

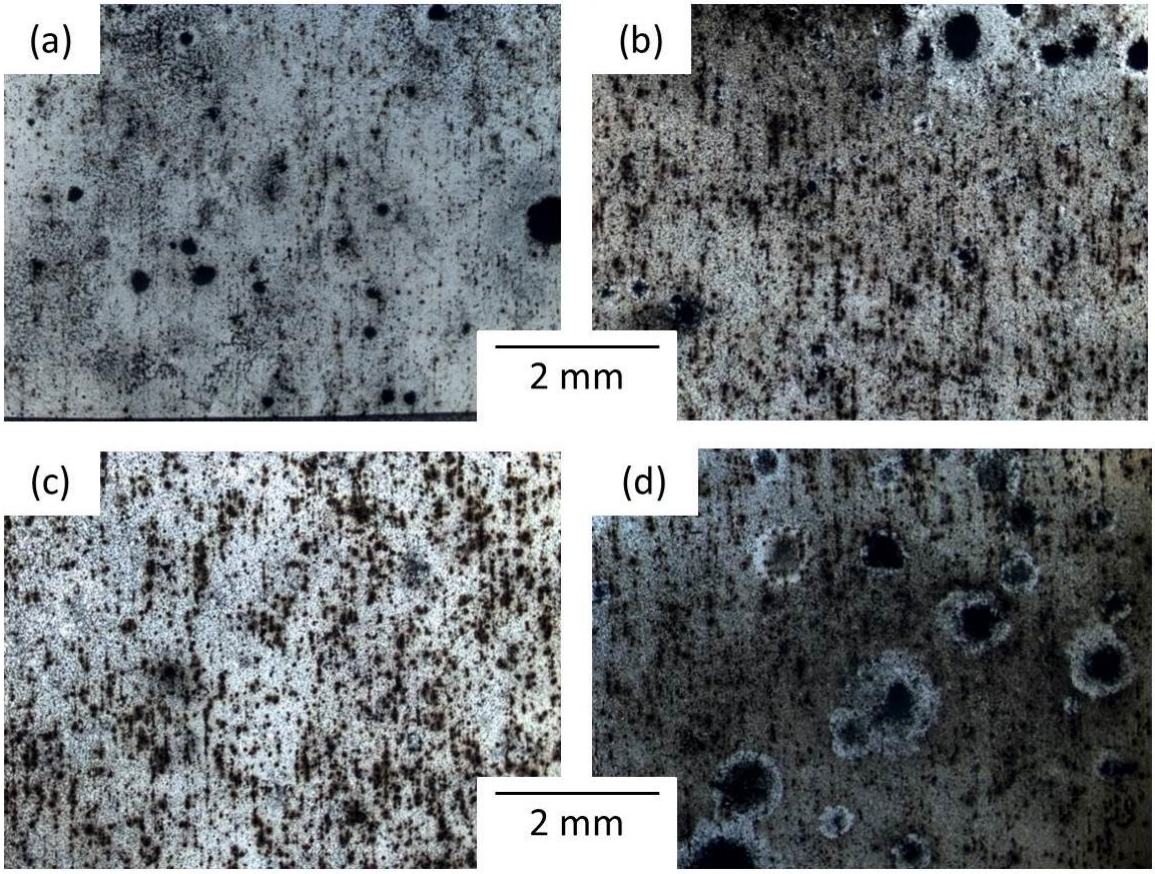

Figure 92 (a) (b) (c) and (d) Optical images of the surface of the AA5083-H321, AA5083-sensitised, sensitised then processed and sensitised, processed, re-sensitised samples respectively after immersion in 1M NaCl for 6 weeks.

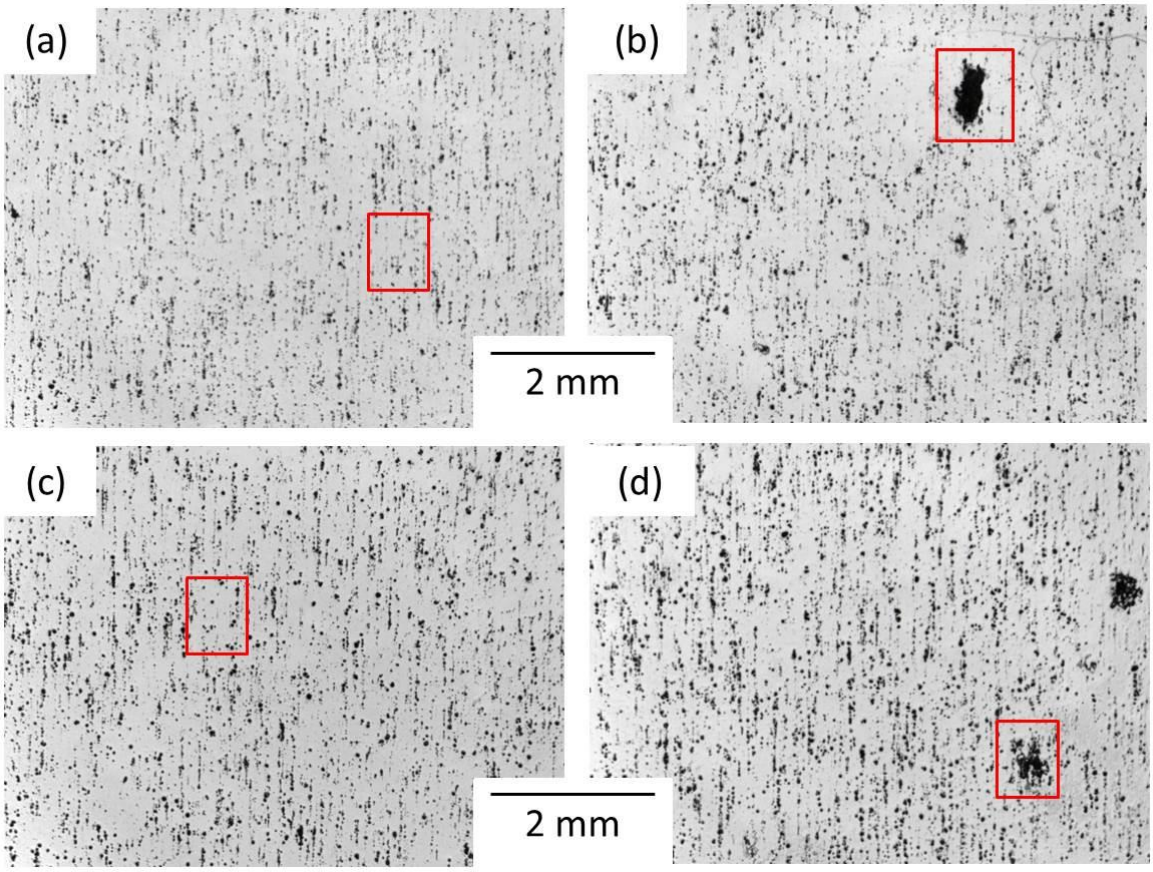

Figure 93 (a) (b) (c) and (d) Optical images of the surface of the AA5083-H321, AA5083-sensitised, sensitised then processed and sensitised, processed, re-sensitised samples respectively after immersion in 1M NaCl for 6 weeks and the corrosion product has been removed. The red boxes indicate the area magnified in Figure 94.

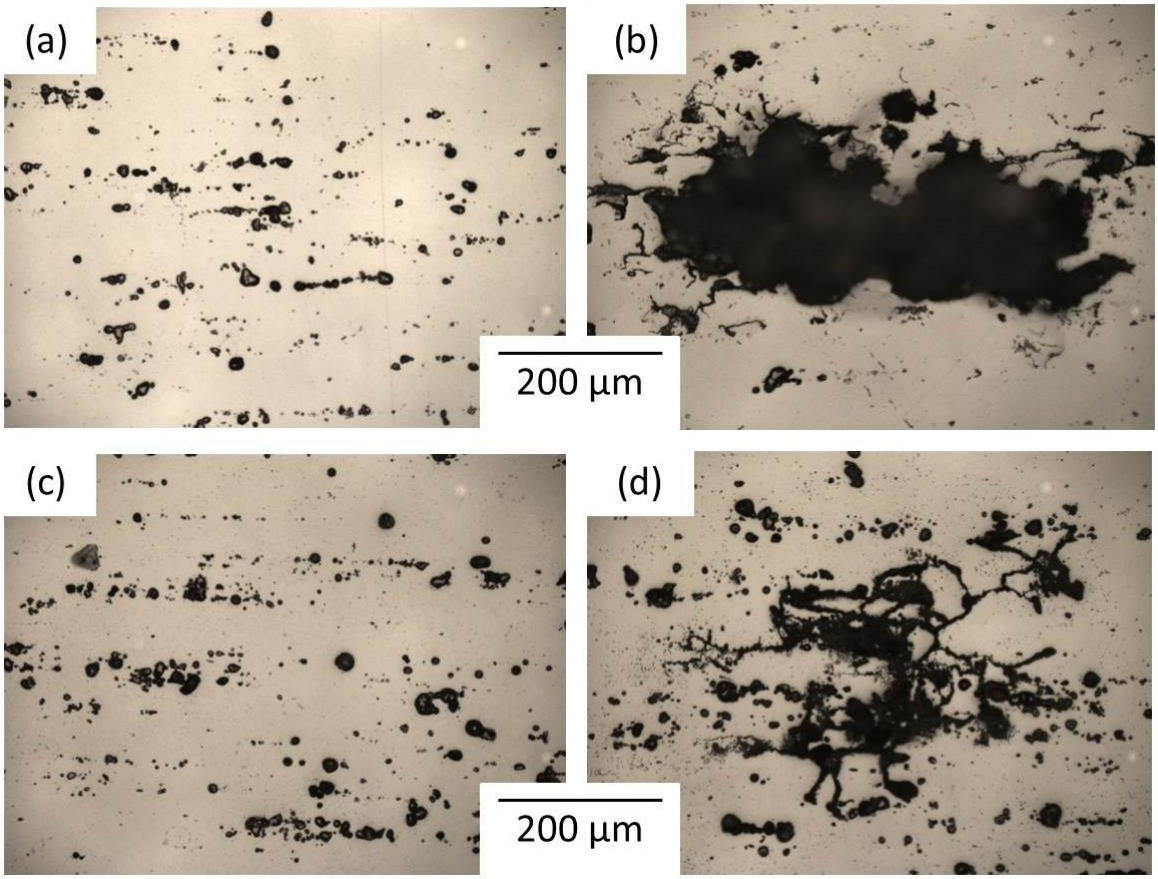

Figure 94 (a) (b) (c) and (d) Optical micrographs of the surface of the AA5083-H321, AA5083-sensitised, sensitised then processed and sensitised, processed, re-sensitised samples respectively after the corrosion product has been removed.

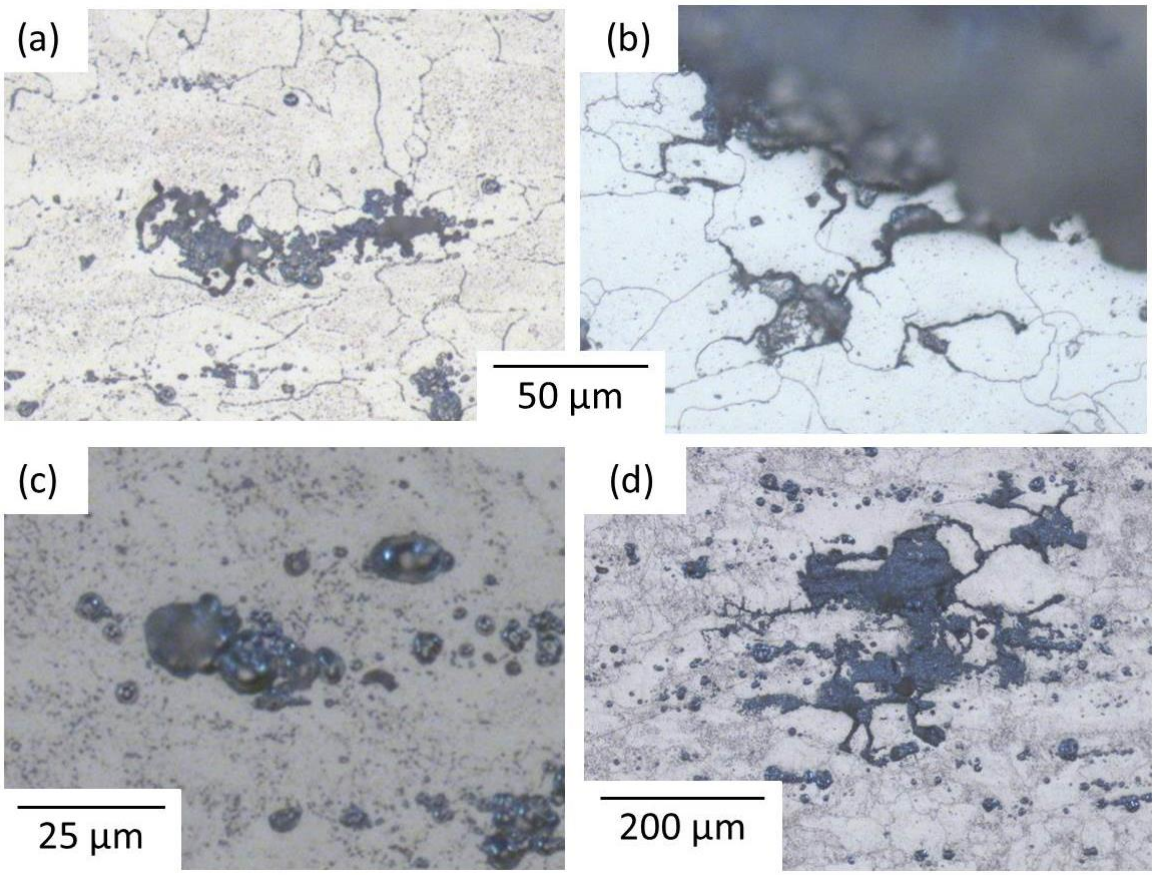

Figure 95 (a) (b) (c) and (d) Optical micrographs of the surface of the AA5083-H321, AA5083-sensitised, sensitised then processed and sensitised, processed, re-sensitised samples respectively after the corrosion product has been removed and the samples etched in phosphoric acid to show susceptible grain boundaries.

6.2.2. Confocal Laser Scanning Microscopy of immersion sample

Figure 96 (a) and (b) show an optical micrograph and image generated by CLSM of the IGC observed in the re-sensitised sample which was immersed in 1 M NaCl for 6 weeks. The model shows the depth of corrosion to reach 23 µm below the surface in the area where the micrograph indicates a large region of grain fall-out, while reaching a depth of about 10 µm in areas which have been subject to cathodic grooving. The model also shows the IGC to be very shallow compared to the depth of attack in the areas of grain fall-out.

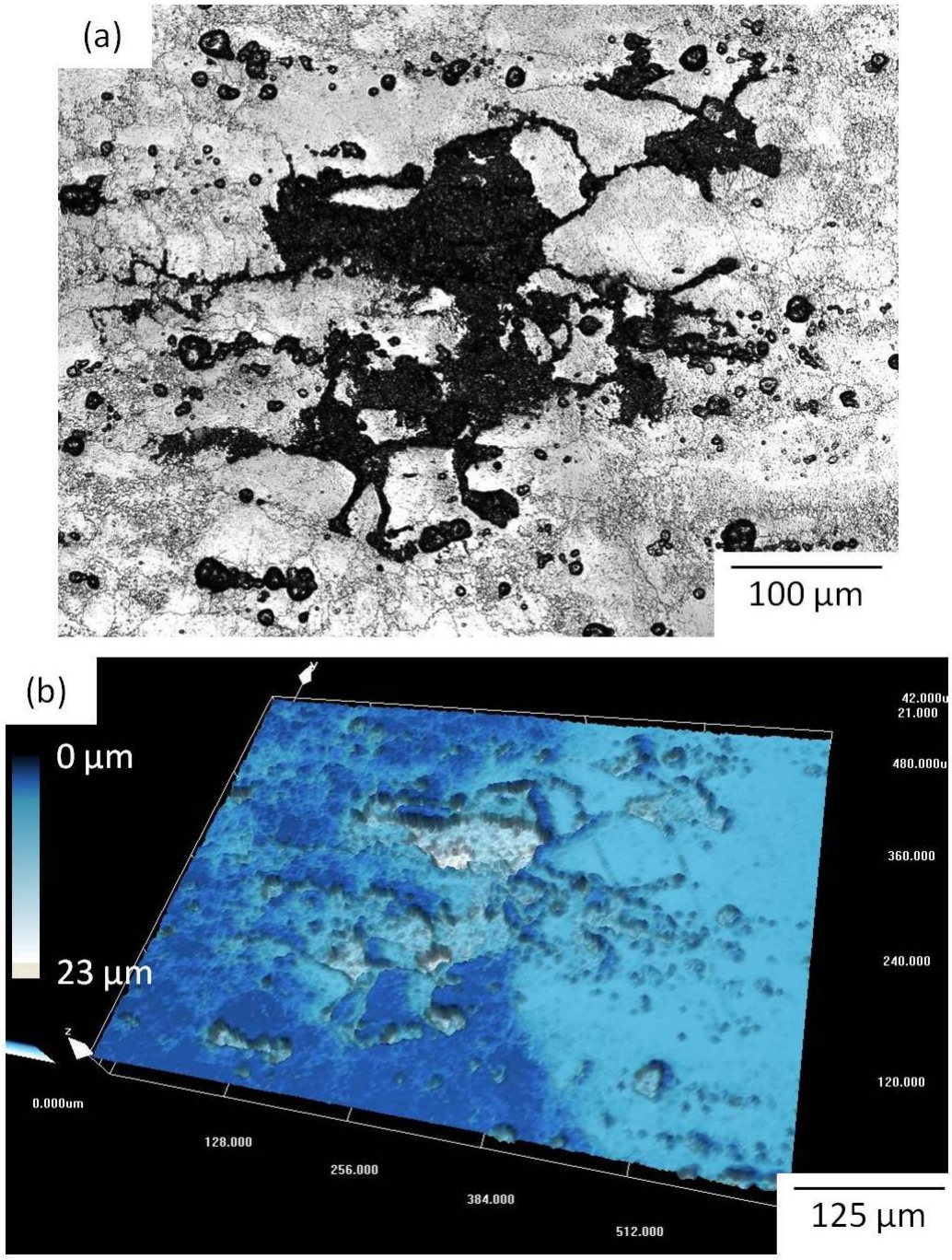

Figure 96 (a) Light microscopy image taken with the CLSM (b) 3D texture representation of same area, taken using data from CLSM, both from the re-sensitised sample which was corroded by immersion in 1 M NaCl for 6 weeks.

6.2.3. Atmospheric corrosion tests

Atmospheric corrosion testing was carried out on a sample of sensitised, processed then re-sensitised material at the same time as those samples tested in Chapter 5. Once again 12 droplets of NaCl were placed on samples of this material and allowed to corrode in an 85 % RH atmosphere for 6 weeks. All of the samples showed similar behaviour relative to each other and relative to the other conditions, and is outlined here with one representative droplet

Figure 97 (d) shows there to be several small sites of localised corrosion product which have built up under the droplet placed on the re-sensitised sample. The majority of the surface appears to be free from the large covering of corrosion, much like the processed sample (c) which however is present in the once sensitised sample (b). When the droplet is removed, it is apparent that extensive corrosion product is in fact present over the majority of the surface in addition to the large localised sites**,** Figure 98 (d).

Removal of the corrosion product shows there to be many sites of extensive corrosive attack, both in the centre of the droplet and at the perimeter, Figure 99 (d). The extent of the corrosion is worse than the once sensitised sample and much worse than the AA5083-H321 and processed samples, which displayed no such attack. SEM inspection reveals there to be a degree of grain fall-out as well as large scale IGC which covers a few large grain boundaries, Figure 100 (d). This corrosion is worse than that seen in the once sensitised sample (b), where the IGC had only spread across the surface but had not penetrated into the metal to cause grain fall-out. It is also evident that the grains which have been attacked have suffered a degree of exfoliation corrosion, where corrosion product built up under the surface have pushed the grains upwards slightly

After the sample was etched in phosphoric acid to reveal the susceptible grain boundaries, the IGC observed can be seen to be continuous with those exposed boundaries Figure 101 (d). While this observation is consistent with the IGC on susceptible grain boundaries in the once sensitised material Figure 101 (b), no observations can be made at this level as to why the corrosion appears to be more severe after the re-sensitisation. It is clear however that the IGC has returned with the susceptible boundaries after the processed sample showed no susceptibility and no corrosion Figure 101 (c).

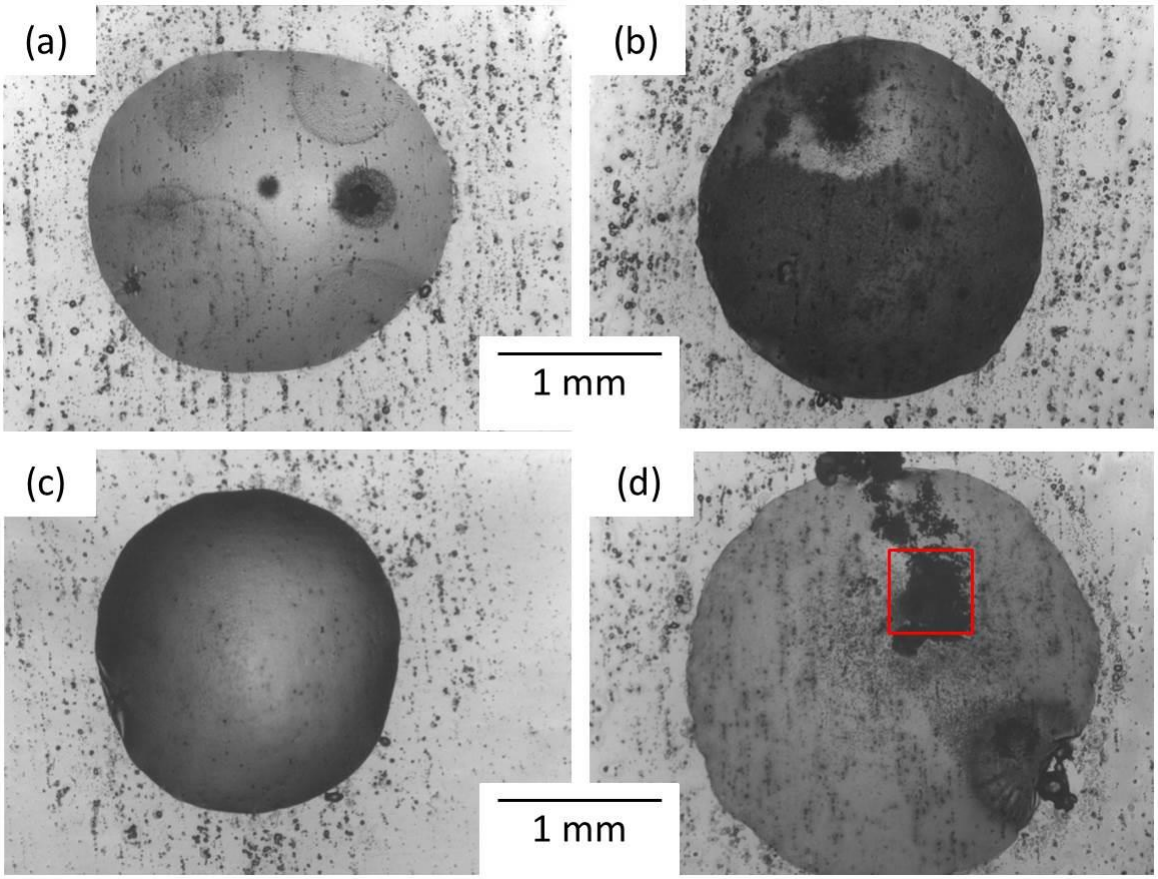

Figure 97 (a) (b) (c) and (d) Optical image of atmospheric droplets on the AA5083-H321, AA5083-sensitised, sensitised then processed and sensitised, processed, re-sensitised samples respectively after 6 weeks. (Initial droplet volume 0.5 µl of 1 M NaCl, deposition density of 1266 µg of Cl^- / cm^2, deposited on polished surface and left in 85% RH). (e) (f) (g) and (h) Optical image of the same droplet areas after being removed from 85% RH environment and allowed to dry out, leaving behind the NaCl crystals.

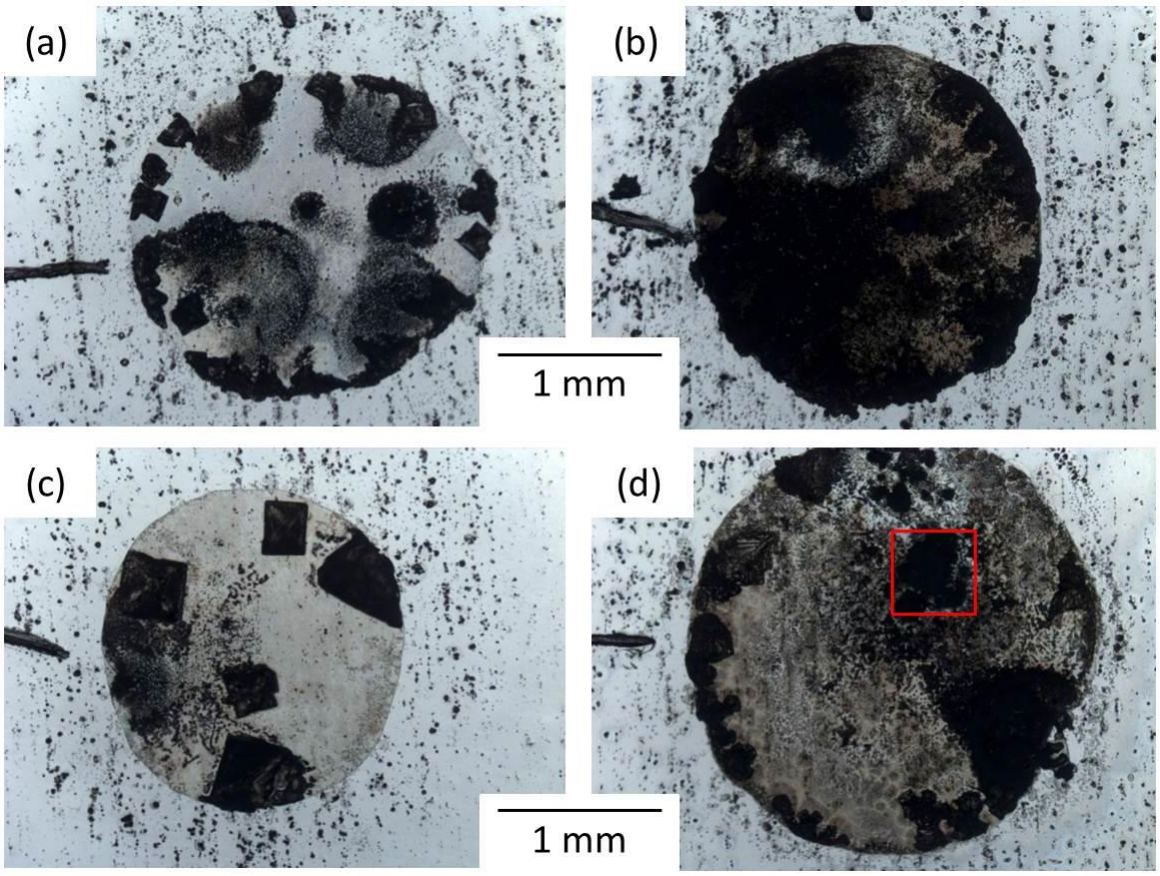

Figure 98 (a) (b) (c) and (d) Optical image of atmospheric droplets on the AA5083-H321, AA5083-sensitised, sensitised then processed and sensitised, processed, re-sensitised samples respectively after 6 weeks. (Initial droplet volume 0.5 µl of 1 M NaCl, deposition density of 1266 µg of Cl- / cm2, deposited on polished surface and left in 85% RH). Images after being removed from 85% RH environment and allowed to dry out, leaving behind the NaCl crystals.

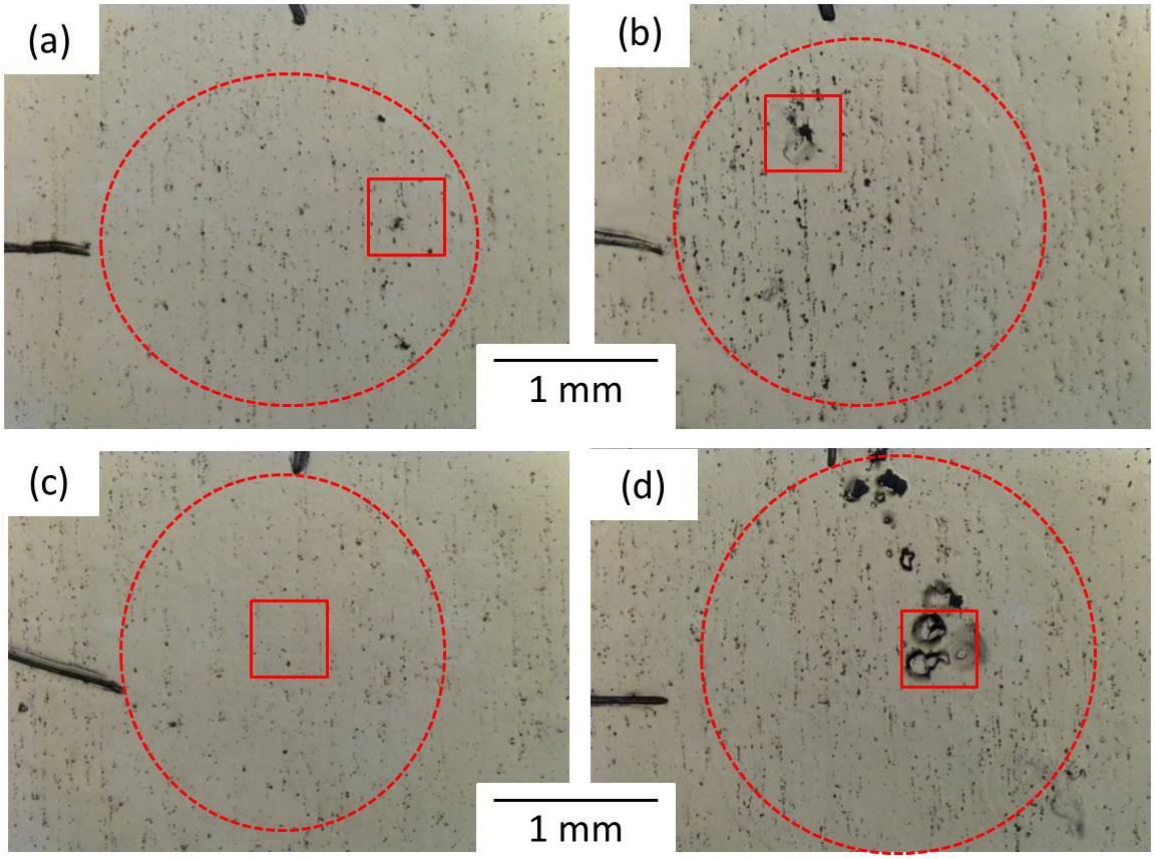

Figure 99 (a) (b) (c) and (d) Optical image of the AA5083-H321, AA5083-sensitised, sensitised then processed and sensitised, processed, re-sensitised sample droplet areas respectively after salt and corrosion product have been removed. The red boxes indicate the area magnified in Figure 100.

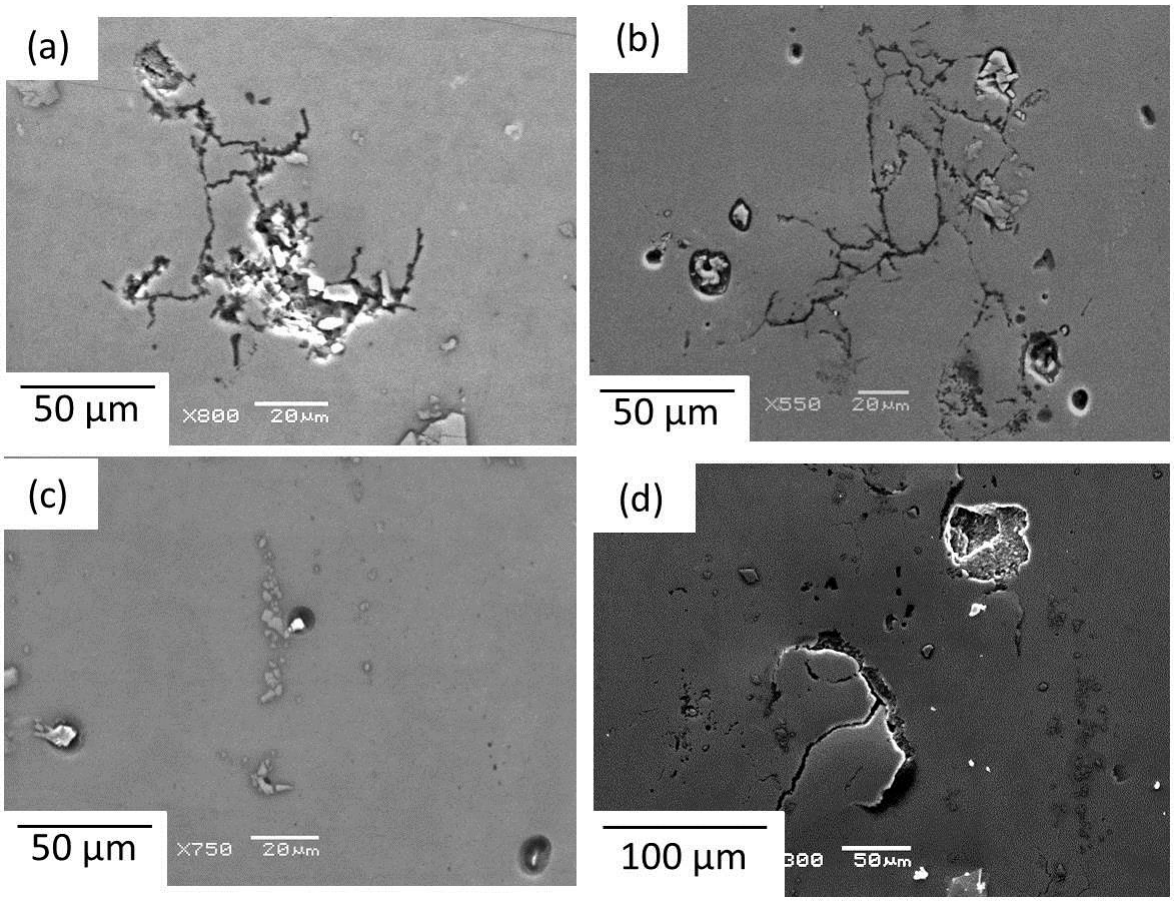

Figure 100 (a) (b) (c) and (d) SEM images of the main sites of corrosive attack in the AA5083-H321, AA5083-sensitised, sensitised then processed and sensitised, processed, re-sensitised sample droplets respectively after salt and corrosion product have been removed.

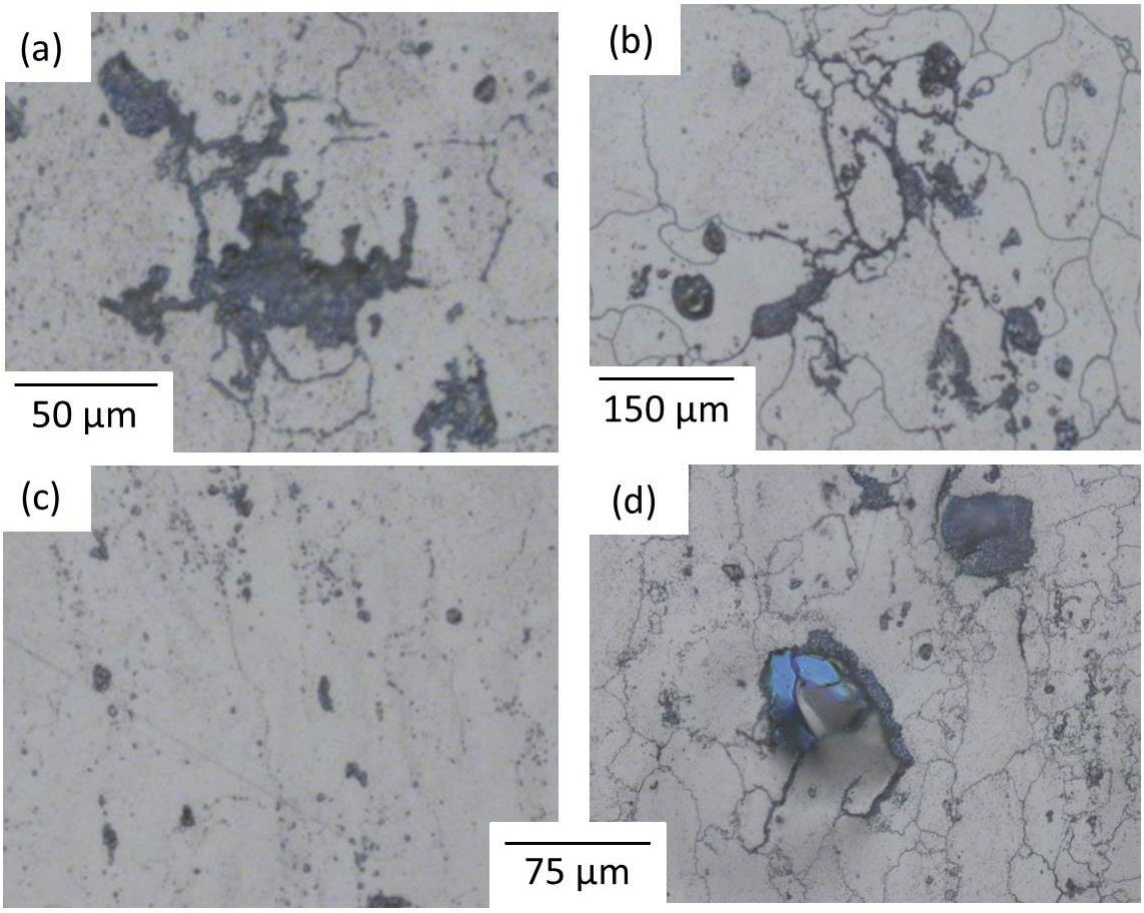

Figure 101 (a) (b) (c) and (d) Optical image of the main site of attack under the AA5083-H321, AA5083-sensitised, sensitised then processed and sensitised, processed, re-sensitised droplets respectively, after etching in phosphoric acid to show the susceptible grain boundaries.

6.2.4. Confocal Laser Scanning Microscopy of atmospheric corrosion sample

Figure 102 (a) and (b) show an optical micrograph and image generated by CLSM of the IGC observed in the re-sensitised sample onto which a droplet of NaCl was placed for 6 weeks. The 3D model shows the dark areas of IGC in the micrograph to be very deep areas of corrosion, where an occurrence of grain fall-out and deep IGC can be seen. The model shows this corrosion to extend 21 μm into the sample in both regions. The model also shows there to be very little cathodic grooving around the intermetallics present, indicating that anodic dissolution was centred on the grain boundaries identified.

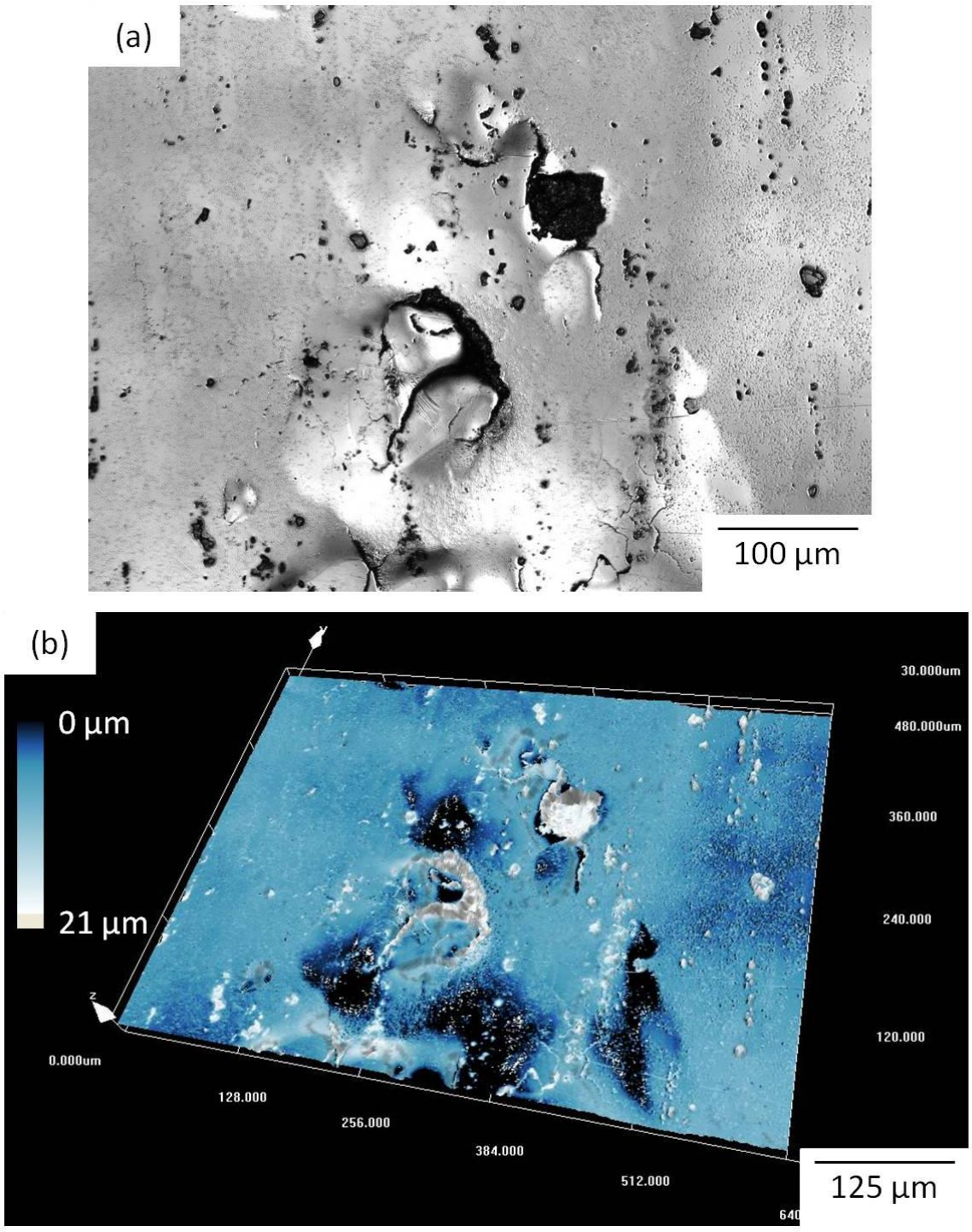

Figure 102 (a) Light microscopy image taken with the CLSM (b) 3D texture representation of same area, taken using data from CLSM, both from the re-sensitised sample which was corroded by an atmospheric droplet (Initial droplet volume 0.5 µl of 1 M NaCl, deposition density of 1266 µg of Cl^- / cm^2, deposited on polished surface and left in 85% RH) for 6 weeks.

6.3. Electrochemistry

Potentiodynamic sweeps were conducted on the re-sensitised sample using the same flat cell and potentiostat as before. The sweep has been plotted in Figure 103 against the AA5083-H321, sensitised and processed samples. It can be seen that the breakdown potential measured at 0.1 mA/cm^2 is much lower than those of the previous three conditions, at around -700 mV $_{(SCE)}$ as opposed to -680 mV $_{(SCE)}$.

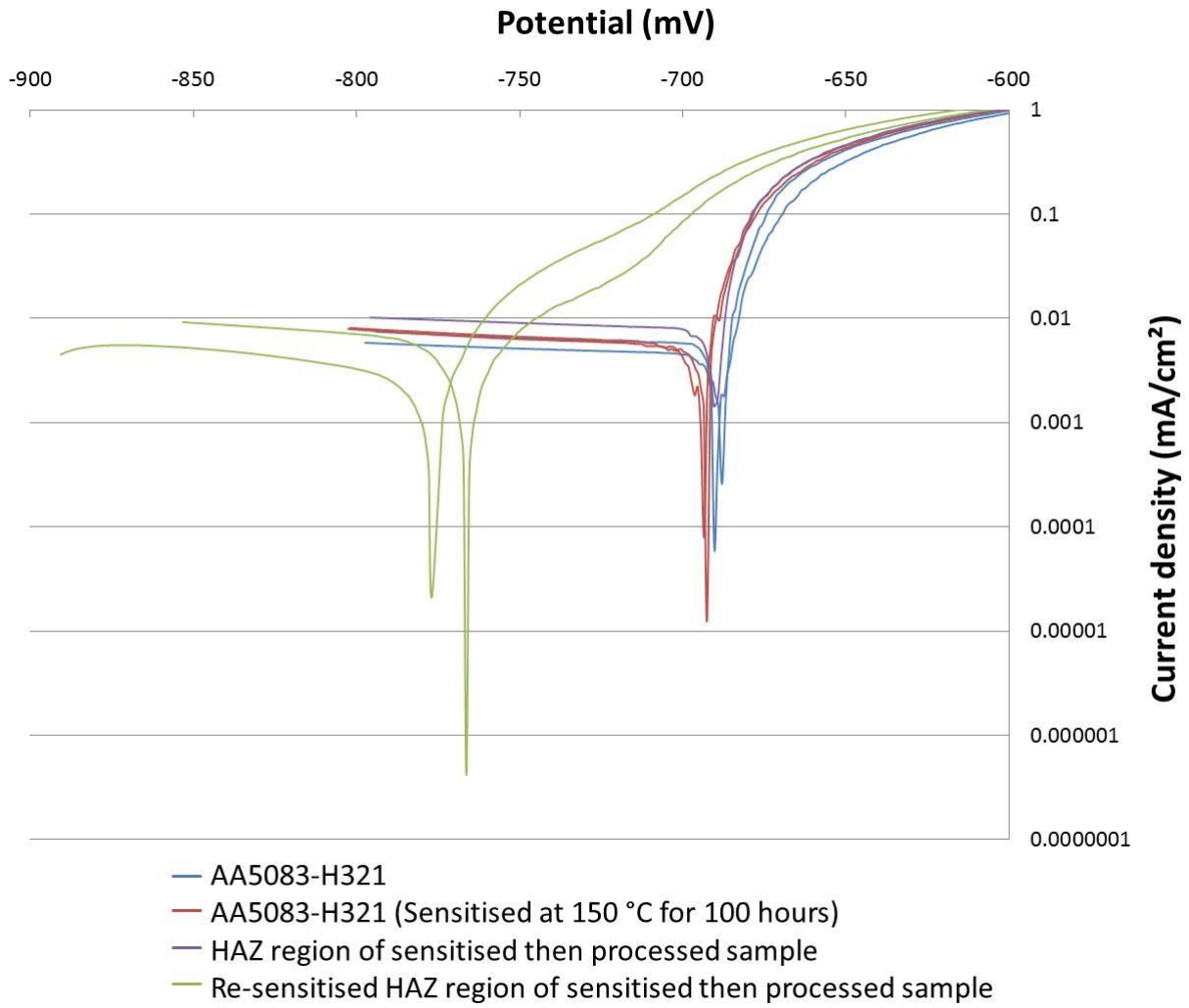

Figure 103 Potentiodynamic sweeps conducted on the AA5083-H321, AA5083-sensitised, sensitised then processed and sensitised, processed, re-sensitised samples in 0.1 M NaCl, acidified to pH 2.75, measured in a Electrochemical flat cell, Gill AC Potentiostat against a saturated calomel electrode.

When potentiostatic polarisation of -710 mV is applied to the re-sensitised sample, the measured current density over 1 hour is shown to reach 0.43 mA/cm^2 in the re-sensitised sample, Figure 104. This is more than an order of magnitude higher than even the once sensitised material which was measured at the same point to be 0.02 mA/cm^2. The surface of the sample after 1 hour of polarisation is shown in Figure 105, where the grain boundary structure has clearly been attacked, while there are many small sites of attack within the grain boundary itself.

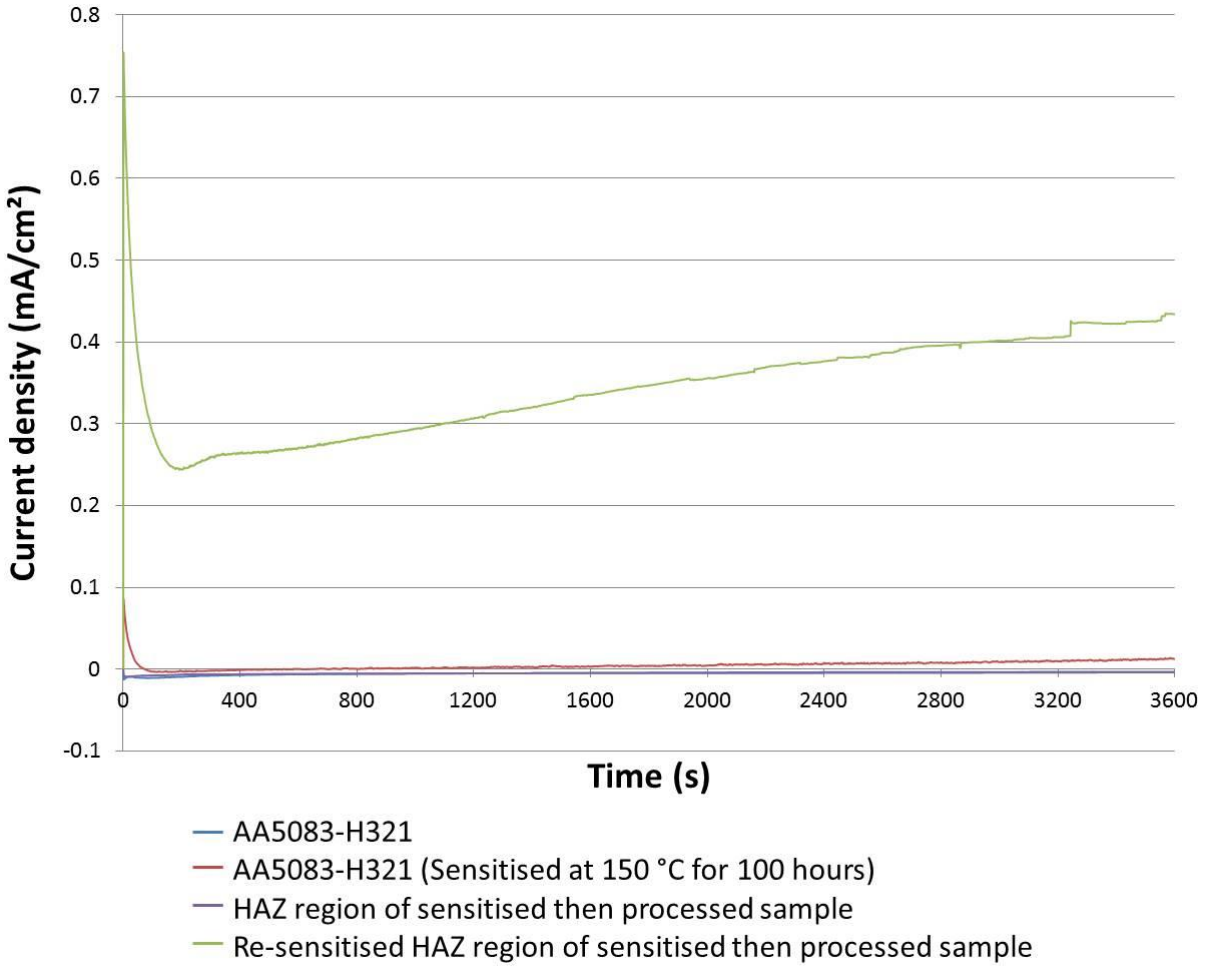

Figure 104 Potentiostatic hold at -710 mV for 1 hour conducted on the AA5083-H321, AA5083-sensitised, sensitised then processed and sensitised, processed, re-sensitised samples in 0.1 M NaCl, acidified to pH 2.75, measured in a Electrochemical flat cell, Gill AC Potentiostat against a saturated calomel electrode.

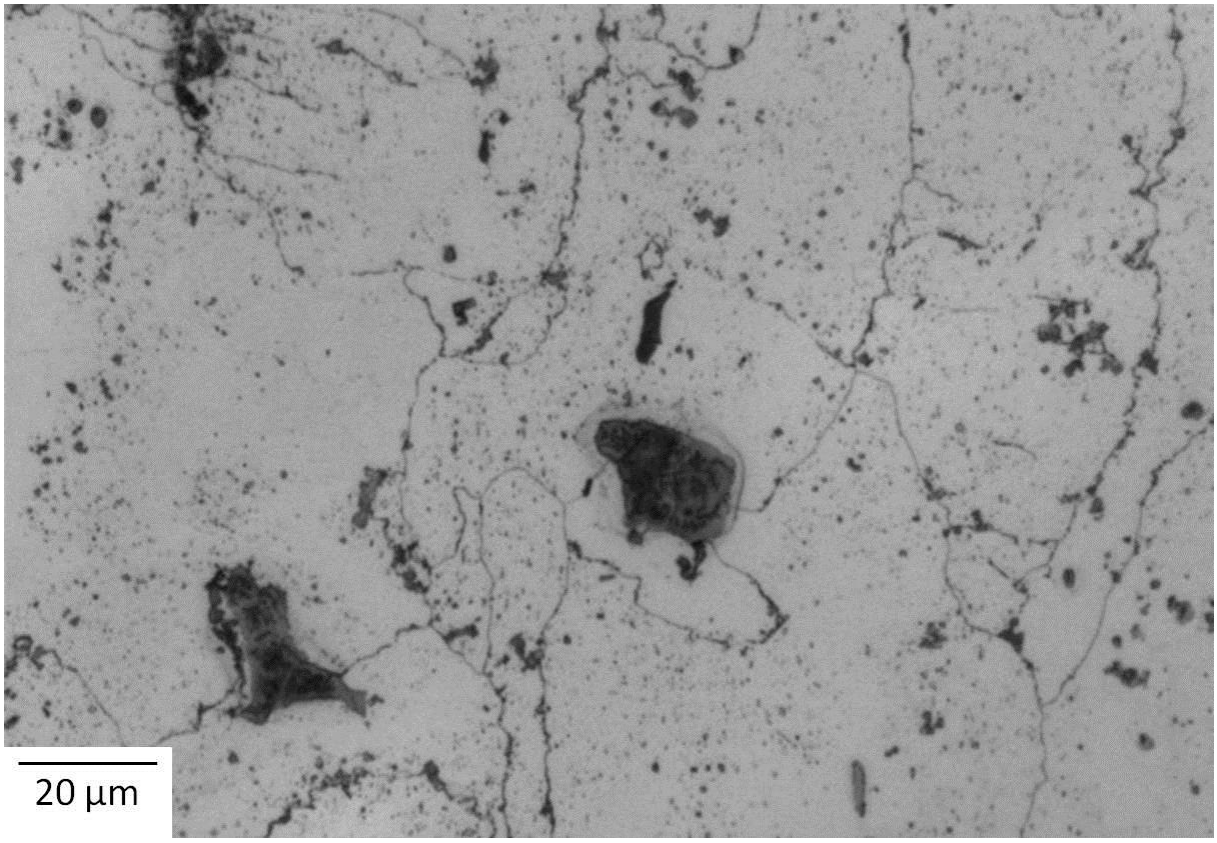

Figure 105 Optical micrograph of the surface of the re-sensitised sample after potentiostatic polarisation at -710 mV for 1 hour in 0.1 M NaCl.

Figure 106 shows the result of another potentiostatic polarisation at -710 mV, this time for 24 hours. Again, the current density shown in the re-sensitised material is much greater at 1.5 mA/cm^2 than any of the other conditions after 24 hours, and to a lesser extent the once sensitised sample, which reached a maximum of 0.3 mA/cm^2. The result of this 24 hour polarisation is shown in Figure 107, where it is clear to see that a great deal of corrosion has taken place. The intergranular nature of the attack is evident from the surface grain boundaries which are still in place, however the majority of the surface has suffered from extensive grain fall out at this applied potential.

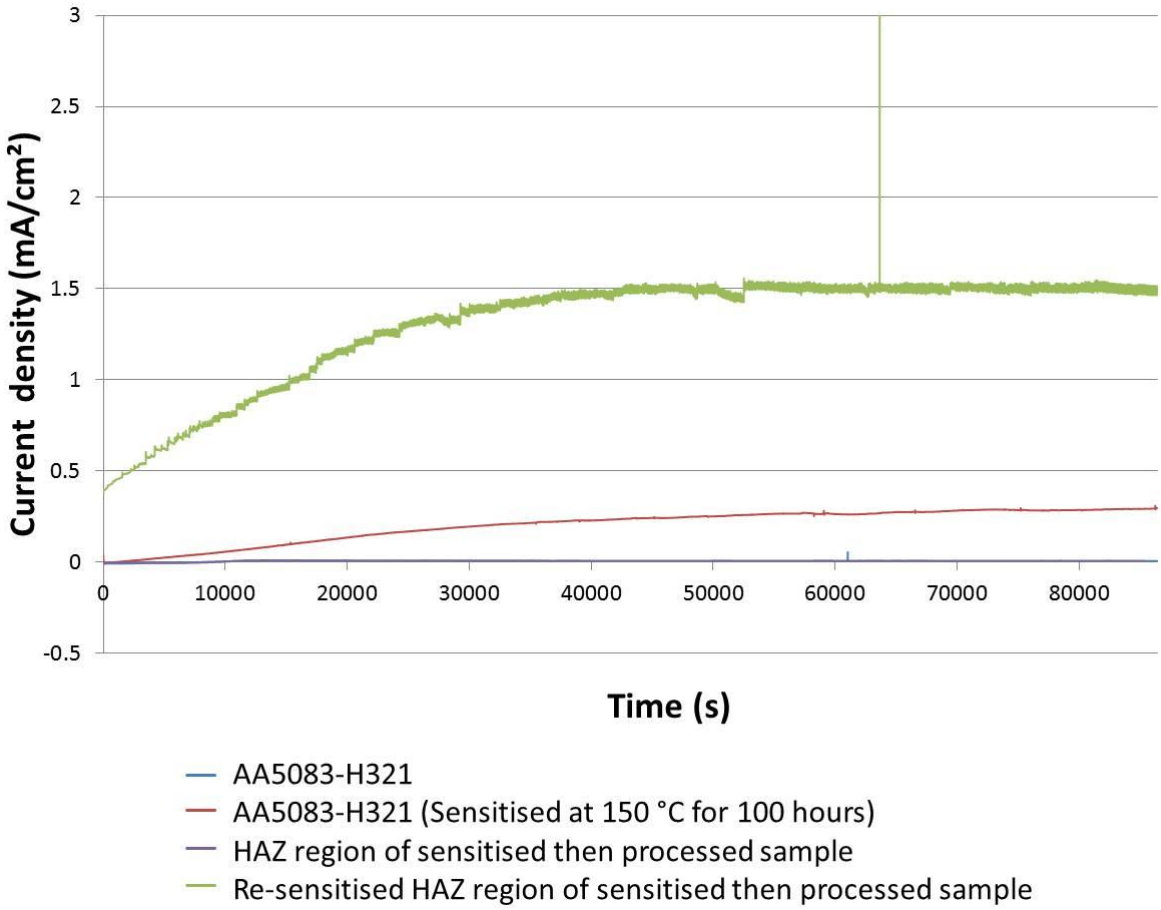

Figure 106 Potentiostatic hold at -710 mV for 24 hours conducted on the AA5083-H321, AA5083-sensitised, sensitised then processed and sensitised, processed, re-sensitised samples in 0.1 M NaCl, acidified to pH 2.75, measured in a Electrochemical flat cell, Gill AC Potentiostat against a saturated calomel electrode.

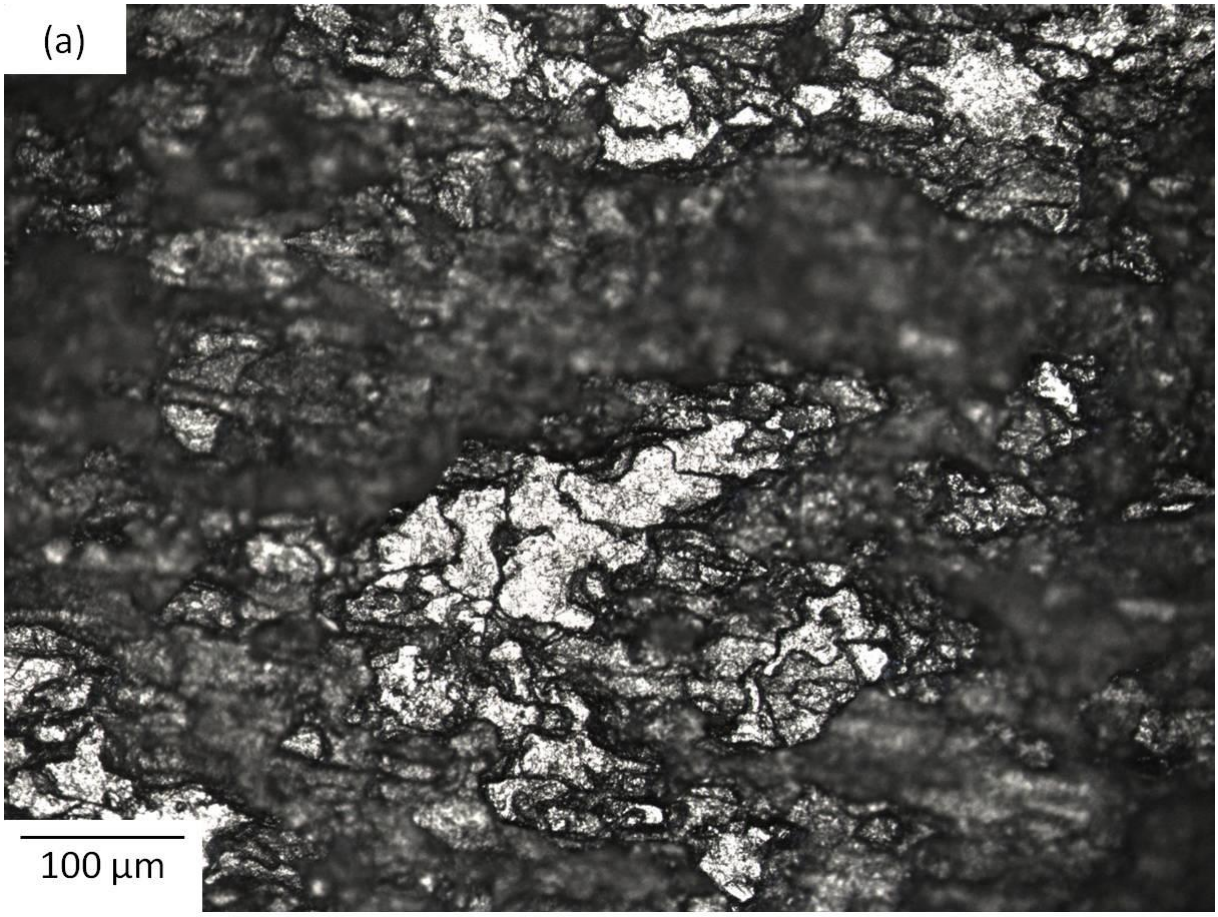

Figure 107 (a) Optical micrographs of the surface of the re-sensitised sample after potentiostatic polarisation at -710 mV for 24 hours in 0.1 M NaCl.

6.4. Discussion

6.4.1. Re-appearance of β-phase after re-sensitisation leading to a return of IGC under immersion and atmospheric corrosion

The re-sensitised sample has undergone three distinct processes which can be equated to three heat treatments; one heat treatment of 100°C for 14 days, then processing imparted a temperature of over 400 °C for several seconds, followed by a second heat treatment of 100°C for 14 days.

The β-phase precipitation in the re-sensitised sample has been visualised by TEM in Figure 90, where discontinuous precipitation is seen along the grain boundary, with precipitates up to 600 nm in width, much thicker than the discontinuous precipitation seen in the once sensitised material. These thicker, discontinuous precipitates are similar to those seen to grow during sensitisation at 200 °C for 24 hours [34, 35].

One explanation for the much thicker discontinuous precipitates may come from the thermal history of the sample up to this point. The first long sensitisation created discontinuous precipitates, rather than a continuous film created by shorter heat treatment times, a morphology seen previously by Searles et al [73]. When the FSP was applied, sufficient heat was imparted to the HAZ to put the β-phase precipitates back into solution, but they did not necessarily have the energy or time to re-distribute themselves away from the grain boundary. This created a magnesium segregation profile close to the grain boundary which has been frequently been reported before [11-14]. Hence when the second long sensitisation was applied, the magnesium was already discontinuously segregated at the grain boundary and would have required less time and energy to re-form β-phase precipitates, along with more magnesium which can segregate inwards during this time, forming thicker precipitates, Figure

90. The material has accumulated over 600 hours of sensitisation with a period in the middle where the magnesium was locally put back into solution.

When the re-sensitised sample is etched in phosphoric acid to reveal its susceptibility to intergranular corrosion, the resulting surface seen in Figure 91 shows a network of grain boundaries in the sample that have etched away, revealing the sample is very susceptible to IGC. Comparison of this image to the equivalent image from the once sensitised sample shows that the re-sensitised sample has a slightly discontinuous etch, whereas the once sensitised sample, when etched under the same conditions shows a continuous etch.

When the re-sensitised material is immersed in 1M NaCl for 6 weeks, the sample shows extensive coverage of cathodic grooving attack, while there are several instances of large sites of intergranular corrosion**,** Figure 93(d). One of these sites is shown magnified under an optical microscope in Figure 94 (d), and shows the intergranular corrosion after immersion is not as severe as that seen in the once sensitised condition, where grain fall-out was seen to occur, Figure 94 (b). Etching the corroded surface in phosphoric acid shows the IGC to have propagated along susceptible grain boundaries, Figure 95(d).

The 3D CLSM image of the corrosion under immersion shows corrosion to have reached a depth of 23 µm, with the damaged area 500 µm across, Figure 96 (b). This damage is not as severe as that caused to the sensitised sample after an equivalent immersion. No comparable confocal microscopy exists for the currently studied conditions, however sensitisation for 100 hours at 150 °C followed by 14 days immersion in 3.5 % NaCl showed IGC and grain fall-out down to a depth of 15 µm, while the corrosive attack spread out over an area of 100 µm [89].

Under a droplet exposed to atmospheric conditions, the sample exhibits intergranular corrosion again, Figure 99(d) and Figure 100 (d). Etching in phosphoric acid shows the IGC

to have occurred on susceptible grain boundaries, Figure 101 (d). These sites of IGC are smaller than those seen in the once sensitised material (100 µm as opposed to 300 µm); however there are many of them. The observation of grain fall-out after exposure to an atmospheric droplet is worse than the IGC seen in the once sensitised sample.

The 3D image of the corrosion caused by the atmospheric droplet shows the corrosion to have spread to an area of 200 µm, and down to a depth of 21 µm, Figure 102. While the corrosion did not cover as many grain boundaries as the once sensitised material, the corrosion did penetrate much deeper into the sample and has caused an area of grain fall out. This has the potential to be more damaging in terms of in service situations where IGSCC will take over, the deeper crack providing a region of more intense stress which can also harbour an aggressive solution.

6.4.2. Worsening electrochemical behaviour after re-sensitisation

Potentiodynamic sweeps conducted on the re-sensitised material show there to be a large difference in electrochemical response compared to the AA5083-H321, AA5083-sensitised and sensitised then processed regions. The breakdown potential measured at 0.1 mA/cm^2 in the re-sensitised sample is around -750 mV compared to -680 mV in the once sensitised region, shown in Figure 103. The breakdown potential of the re-sensitised material being 70 mV lower than that of the once sensitised material would imply that the re-sensitised material should corrode with greater ease; however this has proved not to be the case when subjected to immersed and atmospheric tests. The lower breakdown potential is likely to have been measured as much larger β-phase precipitates are present on the grain boundaries, Figure 90, each one shifting the breakdown potential in a more negative direction. The only comparison with current literature that can be drawn is between the processed and re-

sensitised materials which have equivalence to base and sensitised AA5083. It has been shown that sensitised material will show a lower breakdown potential due to the greater reactivity of the β-phase when present [188].

When the surface of the re-sensitised sample was subjected to a potentiostatic hold at -710mV, the difference in reactivity is the most obvious. After one hour of polarisation, the current density in the re-sensitised sample reached 0.43 mA/cm^2, whereas the once sensitised material recorded a current density of 0.02 mA/cm^2, Figure 104. After polarisation for 24 hours, the re-sensitised sample showed a current density of 1.5 mA/cm^2, whereas the once sensitised sample showed only 0.35 mA/cm^2, Figure 106. This large difference indicates that a far greater current can pass through the surface of the re-sensitised sample. There currently exists no such comparison in the electrochemical behaviour of sensitised and re-sensitised samples and no immediate indication as to the factors behind this result. The nearest comparison in literature comes from AA5083 in the H116 and sensitised conditions where the latter also showed a dramatic rise in current density [39].

Figure 105 and Figure 107 show the surfaces of the re-sensitised sample after 1 and 24 hours of polarisation, where a clear network of intergranular attack has taken place, leading to large amounts of grain fallout at the longer exposure time. The severity of the attack is worse than that seen in the once sensitised sample after one hour, seen in chapter 5.

When considered with the hypothesis of aggressive solutions resulting from β-phase dissolution corroding the gap between precipitates [39], the significantly worse electrochemistry results in the re-sensitised material may be explained. When the polarisation is applied, the dissolution of the precipitates is driven forward, causing much larger quantities of Mg^{2+} containing solution to be released. This was believed to decrease water activity,

impair repassivation, and increasing the rate at which the grain boundary is corroded towards the next precipitate. With greater anodic dissolution comes a greater electron flow and a greater resulting charge density.

6.5. Conclusions

- Following re-sensitisation of the HAZ region of the processed sample, β-phase is seen to have returned to the grain boundaries of the alloy, coupled with an increase in corrosive attack over the processed sample.
- Corrosion behaviour of the processed then sensitised material shows variation in the severity of attack depending on the exposure methods compared to the once sensitised material; however the electrochemical testing shows a far more susceptible material.

Chapter 7 – Synchrotron x-ray microtomography investigation into the occurrence of IGC under an atmospheric droplet

The occurrence of IGC under atmospheric droplets in sensitised and processed samples of AA5083 has been outlined in chapter 5 and 6, where susceptibility to IGC was seen to worsen with sensitisation, be removed after processing and return upon a second sensitisation heat treatment.

Through the use of x-ray microtomography, it is possible to obtain information as to the extent of corrosion into a sample over a course of time, without resorting to destructive techniques. The stages of corrosion growth can be visualised with respect to exposure time, while the volume of material corroded away can also be measured.

The TOMCAT tomography beamline at the Swiss Light Source (SLS) was used to generate the experimental tomographic data to be analysed at a later point.

1mm diameter sample pins turned down from various larger plates were subjected to atmospheric droplets of $MgCl_2$ and scanned at 0, 10, 20 and 34 hours after exposure. The initial scans were used to confirm that the sites observed after exposure were not present before the test started and could be used to chart the progression of corrosion over time. The full experimental details are outlined in Chapter 3.

7.1. The effect of different sensitisation heat treatments on IGC in AA5083

In the previous chapters, two different sensitisation heat treatments have been applied to AA5083-H321 plate in order to study the effect of β-phase precipitation on the corrosion behaviour, but were not studied concurrently as it was not thought necessary to ascertain the degree to which each brought about sensitisation, only that the change was achieved in each case.

The extent of corrosion produced by both heat treatments was studied by x-ray microtomography, where the depth to which corrosion has progressed is measured. Figure 108(a) shows a 3D model of one site of IGC in the AA5083-H321 temper plate. This particular site penetrated 28 µm into the sample in 34 hours, and an average depth of all IGC sites was found to be 30 µm, Table 7.

The IGC in the sample sensitised for 14 days at 100 °C was seen to progress an average of 38 µm into the sample, while the much greater incidence of IGC sites led to the total depth of all sites measured being 338 µm as opposed to only 60 µm in the AA5083-H321 sample. Figure 108 (b) shows a 3D model of one such site. By contrast, the sample sensitised for 100 hours at 150 °C showed a lower average depth of corrosion at 33 µm, while fewer sites meant that the sum of the depths was half that of the other sensitisation, at 160 µm. One IGC site from this condition is shown as a 3D model in Figure 108 (c). This site of attack shows mostly subsurface attack, with a narrow point of entry at the surface.

The data presented here shows the longer, 100 °C sensitisation has led to the deepest corrosion, while that of the 150 °C sensitisation was not as severe, but still worse than the AA5083-H321 material.

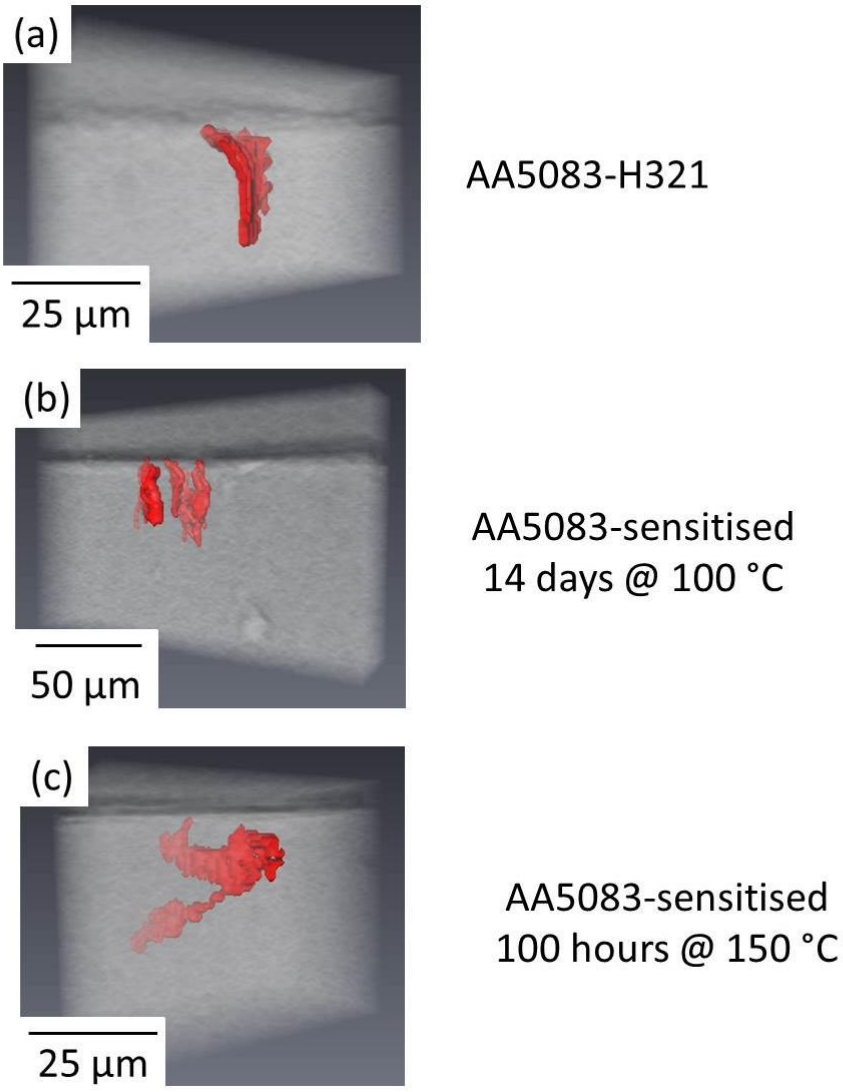

Figure 108 3D models of the IGC penetration in to the (a) AA5083-H321, (b) AA5083-sensitised 14 days at 100 °C and (c) AA5083-sensitised 100 hours at 150 °C.

Table 7 Average and total depths of IGC penetration in each sample

	AA5083-H321	AA5083-sensitised 14 days @ 100 °C	AA5083-sensitised 100 hours @ 150 °C
Average depth (µm)	30	39	33
Cumulative depth (µm)	60	338	164

7.2. The effectiveness of Friction Stir Processing on removing IGC susceptibility in sensitised AA5083

Figure 109 (a) shows a 3D reconstruction of one site of IGC from the sample sensitised for 14 days at 100 °C. This particular site penetrated 56 µm into the sample after 34 hours, while the average depth of all IGC sites in this sample was measured to be 38 µm, Table 8. The sum of IGC penetration depths in the table also shows there to have been 9 such sites of attack. By contrast, Figure 109 (b) shows a site of IGC in the sensitised then processed sample which had penetrated 26 µm into the sample over the same time period. Table 8 shows the average penetration depth to be only 25 µm compared to 38 µm in the sensitised sample, a clear reduction. This average was based on 4 such sites of IGC, another decrease in occurrence over the sensitised sample.

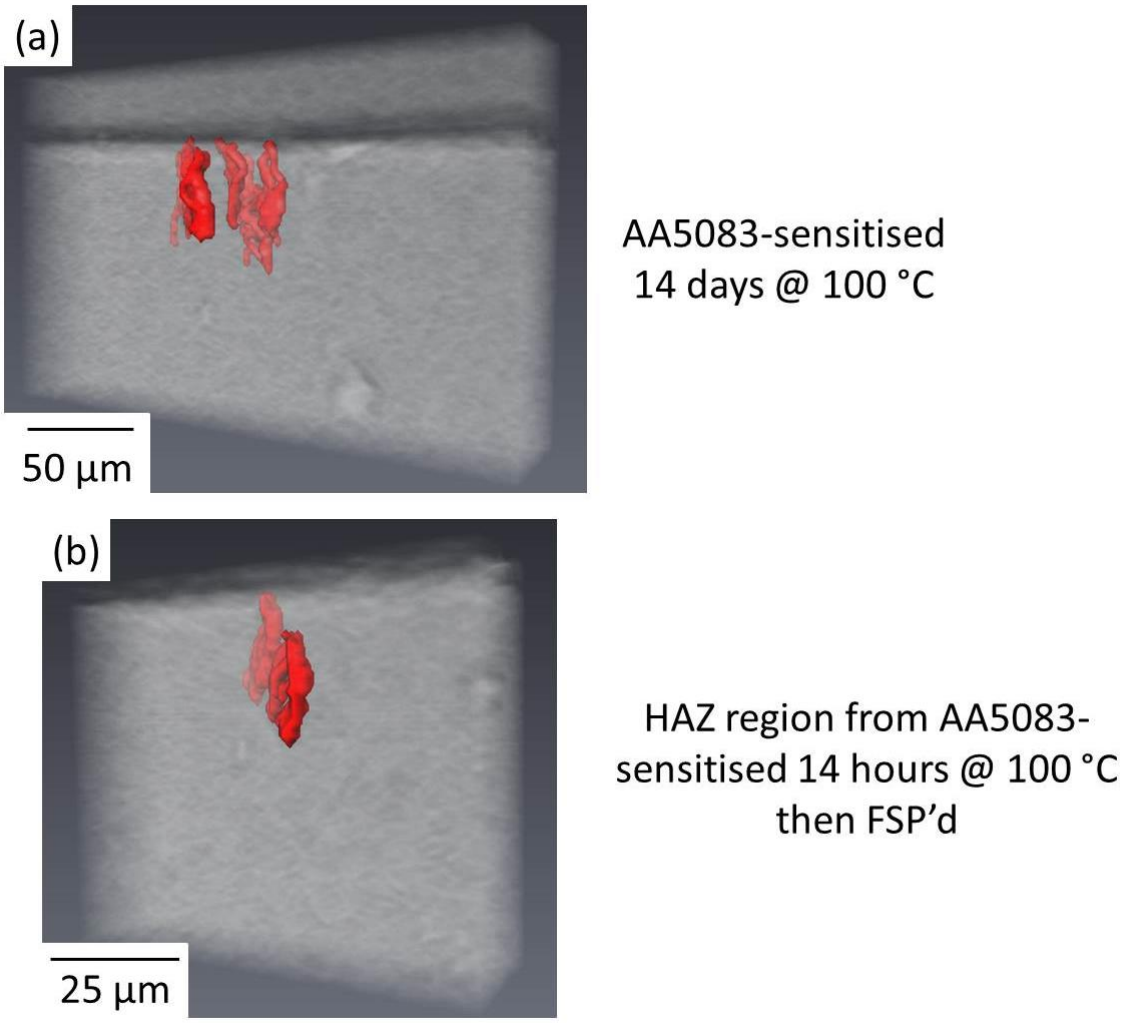

Figure 109 3D models of the IGC penetration in to the (a) AA5083-sensitised 14 days at 100 °C and (b) the HAZ from AA5083-sensitised 14 days at 100 °C then FSP'd.

Table 8 Average and total depths of IGC penetration in each sample

	AA5083-sensitised 14 days @ 100 °C	HAZ region from AA5083-sensitised 14 hours @ 100 °C then FSP'd
Average depth (µm)	38	25
Cumulative depth (µm)	338	100

7.3. IGC susceptibility of sensitised then processed AA5083 after a second sensitisation heat treatment

Figure 110 (a) and (b) shows 3D models of the IGC penetration into samples which had each experienced a different sensitisation treatment. The longer sensitisation treatment shows the deepest and more numerous sites of attack despite being at a lower temperature than the shorter sensitisation treatment. Table 8 showed this average and cumulative depth of attack to be much reduced in the sample which had undergone processing in order to mitigate the susceptibility to IGC, down to an average depth of 25 µm compared to 38 µm in the sensitised sample. Figure 110 (c) shows a 3D reconstruction of an IGC site in a sample which has undergone sensitisation, FSP, then another sensitisation treatment. Despite undergoing a re-sensitisation treatment, Table 9 shows the average depth of IGC sites to have remained as low as the processed sample, 24 µm. There has also been little measurable increase in the number of sites observed, increasing from 4 to 5 after re-sensitisation of the processed sample. This indicates that the FSP may reduce the degree to which the material can re-sensitise and hence suffers IGC. This differs to the findings of Chapter 6, however it is based on a limited selection of data and different exposure conditions.

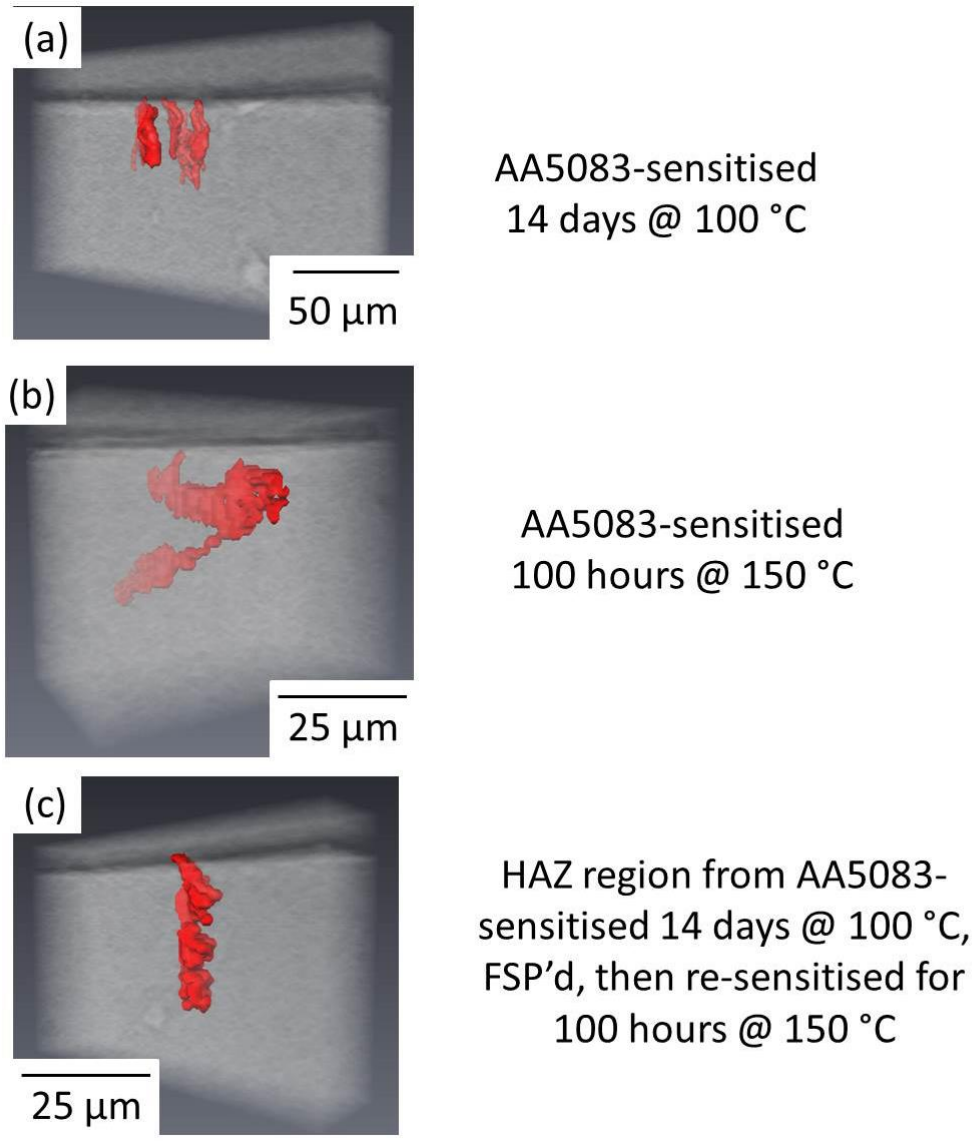

Figure 110 (a), (b), and (c) 3D models of the IGC penetration in to the (a) AA5083-sensitised 14 days at 100 °C, (b) AA5083-sensitised 100 hours at 150 °C and (c) HAZ from AA5083-sensitised 14 days at 100 °C, FSP'd, then re-sensitised for 100 hours at 150 °C.

Table 9 Average and total depths of IGC penetration in each sample

	AA5083-sensitised 14 days @ 100 °C	AA5083-sensitised 100 hours @ 150 °C	HAZ region from AA5083-sensitised 14 days @ 100 °C, FSP'd, then re-sensitised for 100 hours @ 150 °C
Average depth (µm)	38	33	24
Cumulative depth (µm)	338	164	121

7.4. Discussion

While the X-ray microtomography technique has been used successfully by others to visually reconstruct corrosive attack in a variety of materials, it should be noted that the current study had a limited scope of investigation regarding the efficacy of this method in identifying intergranular attack in AA5083 alloys under atmospheric corrosion conditions. As such it has been able to support the findings of the previous chapters in a general sense, in that sensitisation brings about more severe corrosion in AA5083, but this is seen to be reduced after FSP.

The data generated for this study has limitations in both the lack of repeat data from which to make statistically significant judgements, as well as the human element of deciding what does and does not constitute intergranular attack when viewed in the reconstructed slices. Given the low number of IGC sites observed (2-10) and the inherent error given the low spread of depths of attack between samples, these results should be viewed with caution as being experimentally validated and should only be indicative of trends, if present.

7.4.1. The effect of different sensitisation treatments on IGC occurrence

Comparison of the IGC present in the AA5083-H321 and the two samples which have received sensitisation show the corrosion to have proceeded much deeper in to the latter samples. Results from previous chapters indicate that the sensitisation will induce precipitation of β-phase onto the grain boundaries which has also shown to be more electrochemically active. The occurrence of IGC despite the lack of obvious β-phase on the grain boundaries was also seen in the atmospheric corrosion of AA5083-H321 material in

chapter 5. The worsening IGC behaviour in sensitised samples was also noted under atmospheric corrosion.

The deeper corrosion achieved in the sample sensitised for a longer time period can be explained in terms of the morphology of the β-phase present on the grain boundary. TEM micrographs in chapter 4 shows the precipitates to cover the grain boundary in a near continuous film after short term sensitisation while, micrographs in chapter 5 show the precipitates to be thicker and discontinuous after a longer sensitisation time. Application of the hypothesis that dissolution of the precipitates leads to a highly concentrated solution and a burst of dissolution along the grain boundary with the current observations may show that to be a more rapid method of IGC penetration rather than along a continuous, thin film.

7.4.2. The effectiveness of FSP in removing IGC susceptibility

Table 8 shows the average depth of IGC in the sample which received sensitisation then processing to be 25 μm, much less than the 38 μm average seen in the sensitised sample. This figure is also slightly better than the 30 μm average depth seen in the AA5083-H321 samples. An improvement in corrosion behaviour after processing compared to the base material has also been seen in immersion and atmospheric corrosion, and inspection of the sample surfaces after polarisation in Chapter 5. This is reasoned to be due to the heat generated in the HAZ by FSP completely re-dissolving any β-phase on the grain boundaries, while there may have been some in the AA5083-H321 material due to natural ageing. These results support the observation that FSP may be beneficial in returning the material to a non-susceptible state.

7.4.3. The susceptibility of FSP'd then re-sensitised material to IGC

Table 9 and Figure 110 (c) show the depth of IGC attack in the re-sensitised material to be no worse than that of the processed material and less severe than that in the two sensitised conditions. Two trains of thought exist as to the significance of this result. This may show that FSP reduces the ability of the material to re-sensitise, especially considering the knowledge that FSP can return the material to a point close to or better than the AA5083-H321 material in terms of IGC susceptibility.

Alternatively, it is thought that this result is due to the choice of using the shorter, yet higher temperature sensitisation heat treatment (100 hours at 150 °C) to re-sensitise the material, as at the time it was believed to be the more severe of the heat treatments. This has since been shown to be incorrect as it only brings about thin films of β-phase as opposed to the thick precipitates from longer heat treatments. The larger precipitates will create a high concentration of Mg^{2+} ions which serve to drive the corrosion onwards down the grain boundary faster than a slower release in the precipitate film.

Considering this, it appears logical that the re-sensitised material shows little difference from the AA5083-H321 material, whereas application of the longer heat treatment as the re-sensitiser may have yielded a greater IGC susceptibility.

7.5. Conclusions

- The longer time, lower temperature sensitisation increases the average depth of IGC penetration compared to the H321 sample, in addition to creating a greater number of attack sites.
- The shorter time, higher temperature sensitisation also increases the depth of IGC attack, but to a smaller degree compared to the H321 sample. There is also an increase in the number of sites of IGC.
- Processing reduces the depth to which IGC can penetrate compared to the H321 and sensitised samples.
- Re-sensitisation of the sensitised then processed sample has not significantly increased susceptibility to IGC over that of the processed sample, either by FSP positively protecting the sample, or the heat treatment not being sufficient to bring about a comparable change.

Chapter 8 – Summary and Conclusions

8.1. Summary

This thesis investigated the potential that Friction Stir Processing has to repair a ‘damaged’ microstructure which makes AA5083 susceptible to IGC, in addition to the degree to which the process can mitigate the future degradation in corrosion resistance by sensitisation.

AA5083 plate has found significant usage as the structural material for ship hulls; hence a process which can prevent further microstructural degradation and the corrosion that comes with it is seen as highly beneficial. Friction Stir Processing shows potential as a technique which can achieve such results in laboratory testing; however the following points should be considered for real-world application:

- Processing of an individual plate is currently possible because it easily fits onto a conventional FSW machine, and uses a very similar technique. If this process were to be applied to hull plate still attached to the superstructure of a vessel, consideration must be given to the forces applied through the FSP tool to the plate. In the current study, a z-axis force of 45,000 N was applied into the plate to maintain tool shoulder contact with the plate, while an un-quantified force was required to advance the tool. The feasibility of applying such forces through an in-service repair technique should be considered.
- The current study has shown the top surface of the plate to have a banded pattern left in the wake of the FSP tool. For experimental observations this was easily milled off to expose the HAZ underneath, however for naval applications, it is likely that this

surface roughness will be unacceptable, hence consideration must be given for subsequent removal to maintain the specified surface condition.

- Given the observation in Chapter 4 that the full thickness FSP was able to remove IGC susceptibility in the nugget region, this should be noted in conjunction with the findings of Chapter 6 that re-sensitisation of HAZ region can lead to further IGC susceptibility. The local mixing and recrystallisation observed in the nugget region are likely to have removed large amounts of magnesium from grain boundaries, hence it is not readily available for precipitation of the β-phase. This lends to the concept of a thin, continuous layer of recrystallised nugget region which may be less susceptible to re-sensitisation.

8.2. The relative influence of sensitisation and Friction Stir Processing in increasing and decreasing Intergranular Corrosion susceptibility in AA5083-H321

Sensitisation heat treatments of AA5083 alloys have been shown to precipitate a relatively reactive β-phase onto grain boundaries [32-39], and has been demonstrated in the current study by visualisation with TEM, Figure 48, and chemical analysis, Figure 49. Following Friction Stir Processing, the microstructure in the nugget region and HAZ was observed to be free from β-phase on grain boundaries, Figure 51, as was the case in the AA5083-H321 material.

In order to assess the corrosion behaviour of the AA5083 in the various stages of processing, corrosion testing was performed that subjected the material to both immersed and atmospheric corrosion, as might be expected below and above the waterline of a ship hull. These tests showed the AA5083-H321 material to suffer a small degree of IGC. However the sensitised

material suffered much more, which was reasoned to be due to the presence of the β-phase on grain boundaries. This was also ascertained through electrochemical testing, which is much more sensitive to microstructural variations which can influence corrosion behaviour

8.3. Using Surface FSP to impart heat into sensitised AA5083-H321 to remove β-phase from grain boundaries and decrease corrosion susceptibility

When it was observed that the HAZ outside of the nugget region in the full thickness processing route also showed improved corrosion behaviour over sensitised AA5083, focus shifted to an FSP technique which did not introduce grain recrystallisation to the full thickness of the plate, instead imparted heat into the top surface which was that which would be exposed to a marine environment.

TEM observations again showed the β-phase to have been removed from the sensitised microstructure after heat was imparted through surface FSP, Figure 69. Atmospheric and immersion corrosion testing showed improved corrosion behaviour after processing, which was backed up by potentiostatic polarisation experiments where the AA5083-H321 and FSP'd material showed a greatly improved behaviour over the sensitised condition.

These results show that locally imparting heat into the surface of AA5083 which was sensitised and was previously susceptible to IGC can return the material to a near-new condition which will not readily suffer more corrosion, hence expensive repair procedures which involve replacement of material can be avoided. This concept has been trialled using an apparatus which inputs heat into the hull plate without mechanical interaction, with the aim of locally reversing sensitisation [41].

8.4. The degree to which sensitised then FSP'd AA5083 can re-sensitise

Upon re-sensitisation of the processed material, the β-phase which had been removed by FSP was shown to return. This was associated with a return of IGC, indicating that the microstructural mechanisms which take place during sensitisation are not prevented by heat input from FSP.

The speed with which this corrosion susceptibility returns is not currently clear, as short term testing showed behaviour similar to a once-sensitised material, however electrochemical tests which drove dissolution events at the grain boundary showed a susceptibility of the re-sensitised material much greater than that in the original material, Figure 106. This indicates that A5083 which has been sensitised then had FSP applied may degrade towards corrosion susceptibility at a faster rate than had been seen at the beginning of life.

8.5. Thermal history as an indicator for precipitation morphology and corrosion behaviour

Altering the sensitisation parameters from 100 hours at 150 °C to 336 hours at 100 °C showed the β-phase to form larger and more discrete precipitates than the thin film of β-phase seen at lower length sensitisation, Figure 68. While direct comparison has not been drawn from the range of tests conducted, data from the microtomography experiments suggests that a longer heat treatment, even at a lower temperature, creates a microstructure which is more susceptible to IGC.

Re-sensitisation of the sensitised then processed material was shown to produce the largest and most discrete precipitates, Figure 90. Corrosion behaviour in a short time period could not be differentiated from the once sensitised material; however polarisation drove the behaviour

much more quickly and produced significant IGC. This material had effectively undergone two sensitisation heat treatments, with a short burst of heat in between to put the β-phase back into solution where it had precipitated.

These larger precipitates are hypothesised to be able to drive a burst dissolution-advancement model of grain boundary corrosion [39].

8.6. Conclusions

- A sensitisation heat treatment applied to AA5083-H321in the range 100 – 150 °C, leads to the precipitation of β-phase onto grain boundaries and triple points. This precipitation occurs as thinner and longer precipitates at shorter times ageing times, while longer heat treatments form larger, more discrete particles.
- The occurrence of β-phase on the grain boundaries has been shown to increase the IGC susceptibility of the material, owing to the relatively anodic nature of the grain boundary precipitate compared to the matrix.
- The longer sensitisation heat treatment has led to more rapid IGC penetration into the material, reasoned to be due to a more concentrated chemistry at the tip of attack which promotes further corrosion
- Full thickness FSP of the sensitised material removes the β-phase from the grain boundary in the nugget and HAZ regions, as does surface FSP in the HAZ just beneath the surface. This is achieved with a heat input above the solidus temperature of the β-phase. The removal of β-phase is associated with a return to relatively low susceptibility of the alloy to IGC.
- Upon re-sensitisation of the processed material, thick and discrete β-phase precipitates return to the grain boundaries. This morphology is the result of a long period of sensitisation, interrupted by dissolution of the β-phase particles which put magnesium back into solution local to the grain boundary. This allowed a faster rate of precipitation upon re-sensitisation.
- It is unclear whether the resulting corrosion behaviour is better or worse than after the original sensitisation treatment. However electrochemical testing suggests that this material will suffer IGC at a faster rate.

Chapter 9 – Future Work

The present work has provided information on the mechanisms by which β-phase is precipitated and IGC susceptibly is acquired, removed and re-acquired in AA5083 by sensitisation heat treatments and Friction Stir Processing. Future work should establish:

- Whether the re-sensitisation heat treatment after FSP will produce better or worse IGC resistance than an equivalent sensitisation of the base material. This will answer the question of the efficacy of the technique in mitigating further corrosion taking place, which has not been fully answered in the current work.
    - This concept could be extended to sensitising base material, and base material which has been Friction Stir Processed. Results of microstructural and corrosion testing should give insight as to the specific effects of the process without the influence of other variables.
    - This should also be extended to the recrystallised nugget region as it the effects of re-sensitisation have not been investigated in this area.
- If there is time dependence to the re-sensitisation and degradation of corrosion performance after FSP of sensitised material. This will inform potential life improvements that can be gained by application of this technique.
- If the FSP process used in the current study is the optimum for removal of β-phase and reducing susceptibility to IGC. Processing parameters can be adjusted in order to input more or less heat into the sample, for longer and shorter periods of time.
    - This data can form the basis of understanding the precise microstructural changes that are required for any technique to reverse sensitisation.

Chapter 10 - References

1. Polmear, I.J., *Light Alloys, From Traditional Alloys to Nanocrystals*. 4th Edition ed. 2006, Amsterdam: Elsevier.
2. Sanders, R.E., Baumann, S.F., and Stumpf, H.C., *Non-heat-treatable Aluminium alloys,* in *Aluminium Alloys: Their physical and mechanical properties*, E.A. Starke Jr. and T.H. Sanders Jr, Editors. 1986: University of Virginia, Charlottesville, Virginia. p. 1441-1484.
3. Schmidt, C.G. and Miller, A.K., *The effect of solutes on the strength and strain hardening behavior of alloys.* Acta Metallurgica, 1982. 30(3): p. 615-625.
4. *ASM Metals Handbook - Corrosion*. Vol. 13. 1992: ASM International.
5. Murray, J.L., *Al-Mg phase diagram*, T.B. Massalski, Editor. 1990, ASM International, Materials Park, OH. p. 169-171.
6. Anthony, T.R., *Solute segregation in vacancy gradients generated by sintering and temperature changes.* Acta Metallurgica, 1969. 17(5): p. 603-609.
7. Faulkner, R.G., *Segregation to boundaries and interfaces in solids.* International Materials Reviews, 1995. 41: p. 198-208.
8. Beck, A.F. and Sperry, P.R., in *Fundamental Aspects of Stress Corrosion Cracking*, R.W. Staehle and A.J. Forty, Editors. 1969, National Association of Corrosion Engineers: Houston, TX.
9. Sprowls, D.O. and Brown, R.H., in *Fundamental Aspects of Stress Corrosion Cracking*, R.W. Staehle and A.J. Forty, Editors. 1969, National Association of Corrosion Engineers: Houston, TX.
10. Perryman, E.C.W., *Some observations on the relationship between vacancies, recovery and precipitation in Al---Mg alloys.* Acta Metallurgica, 1955. 3(4): p. 412-413.
11. Brock, A.J. and Heine, M.A., *Formation of MgO Crystals in Anodic γ - Al2 O 3 Formed on Aluminum-3% Magnesium Alloy.* Journal of The Electrochemical Society, 1972. 119(8): p. 1124-1127.
12. Cundy, S.L., Metherell, A.J.F., Whelan, M.J., Unwin, P.N.T., and Nicholson, R.B., *Studies of Segregation and the Initial Stages of Precipitation at Grain Boundaries in an Aluminium 7 wt.% Magnesium Alloy with an Energy Analysis Electron Microscope.* Proceedings of the Royal Society of London. Series A. Mathematical and Physical Sciences, 1968. 307(1490): p. 267-281.
13. Doig, P. and Edington, J.W., *Stress Corrosion Susceptibility of As-Quenched Al-5·9 wt-% Zn-3·2 wt-% Mg Alloy.* British Corrosion Journal, 1974. 9(4): p. 220-222.
14. Jones, R.H., Baer, D.R., Danielson, M.J., and Vetrano, J.S., *Role of Mg in the stress corrosion cracking of an Al-Mg alloy.* Metallurgical and Materials Transactions a-Physical Metallurgy and Materials Science, 2001. 32(7): p. 1699-1711.
15. Scamans, G.M., Holroyd, N.J.H., and Tuck, C.D.S., *The Role of Magnesium Segregation In The Intergranular Stress-Corrosion Cracking Of Aluminium Alloys.* Corrosion Science, 1987. 27(4): p. 329-347.
16. Vetrano, J.S., *Influence of microstructure and thermal history on the corrosion susceptibility of AA5083.* Automotive Alloys, 1997.
17. Yukawa, H., Murata, Y., Morinaga, M., Takahashi, Y., and Yoshida, H., *Heterogeneous distributions of Magnesium atoms near the precipitate in Al-Mg based alloys.* Acta Metallurgica et Materialia, 1995. 43(2): p. 681-688.

18. Yuan, Y., *Localised Corrosion and Stress Corrosion Cracking of Aluminium-Magnesium Alloys*, in *Department of Metallurgy and Materials*. 2005, University of Birmingham: PhD Thesis. p. 207.
19. Bournane, M., Nedjar, M., and Sirenko, A.F., *Precipitation in solid solutions of Al-Mg.* Scripta Materialia, 1999. 40(3): p. 375-382.
20. Hamana, D., Bouchear, M., Betrouche, M., Derafa, A., and Rokhmanov, N.Y., *Comparative study of formation and transformation of transition phases in Al-12 wt.% Mg alloy.* Journal of Alloys and Compounds, 2001. 320(1): p. 93-102.
21. Nebti, S., Hamana, D., and Cizeron, G., *Calorimetric study of pre-precipitation and precipitation in Al-Mg alloy.* Acta Metallurgica et Materialia, 1995. 43(9): p. 3583-3588.
22. Russell, K.C. and Aaronson, H.I., *Sequences of precipitate nucleation.* Journal of Materials Science, 1975. 10(11): p. 1991-1999.
23. Starink, M.J. and Zahra, A.M., *Low-temperature decomposition of Al-Mg alloys: Guinier-Preston zones and L1(2) ordered precipitates.* Philosophical Magazine a-Physics of Condensed Matter Structure Defects and Mechanical Properties, 1997. 76(3): p. 701-714.
24. Starink, M.J. and Zahra, A.M., *β′ and β precipitation in an Al–Mg alloy studied by DSC and TEM.* Acta Materialia, 1998. 46(10): p. 3381-3397.
25. Itoh, G., Cottereau, B., and Motohiro, K., *Precipitation of the intermediate phase β′ in an Al-8%Mg alloy.* Materials Transactions, JIM, 1990. 31(12): p. 1041-1049.
26. Eikum, A. and Thomas, G., *Precipitation and dislocation nucleation in quench-aged Al-Mg alloys.* Acta Metallurgica, 1964. 12(5): p. 537-545.
27. Gao, J. and Quesnel, D.J., *Enhancement of the Stress Corrosion Sensitivity of AA5083 by Heat Treatment.* Metallurgical and Materials Transactions a-Physical Metallurgy and Materials Science, 2011. 42A(2): p. 356-364.
28. Kubota, M., Nie, J.F., and Muddle, B.C. in *6th Inter. Conf. on Al-alloys*. 1998. ICAA-6, Toyohashi, Japan.
29. Starink, M. and Zahra, A.M., *Precipitation kinetics of an Al-15% Alloy studied by microcalorimetry and TEM.* Mater. Sci. Forum, 1996: p. 217-222.
30. van Mourik, P., Maaswinkel, N., de Keijser, T., and Mittemeijer, E., *Precipitation in liquid-quenched Al-Mg alloys; a study using X-ray diffraction line shift and line broadening.* Journal of Materials Science, 1989. 24(10): p. 3779-3786.
31. Perryman, E.C.W. and Hadden, S.E., *Stress-Corrosion Of Aluminium-7-Percent Magnesium Alloy.* Journal of the Institute of Metals, 1950. 77(3): p. 207-&.
32. Goswami, R., Spanos, G., Pao, P.S., and Holtz, R.L., *Precipitation behavior of the [beta] phase in Al-5083.* Materials Science and Engineering: A, 2010. 527(4-5): p. 1089-1095.
33. Choi, D.-H., Ahn, B.-W., Quesnel, D.J., and Jung, S.-B., *Behavior of B phase (Al3Mg2) in AA 5083 during friction stir welding.* Intermetallics. 35(0): p. 120-127.
34. Bensaada, S., Bouziane, M.T., and Mohammedi, F., *Effect of the temperature on the mechanism of the precipitation in Al-8% mass.Mg alloy.* Materials Letters, 2011. 65(17-18): p. 2829-2832.
35. Carroll, M.C., Gouma, P.I., Mills, M.J., Daehn, G.S., and Dunbar, B.R., *Effects of Zn additions on the grain boundary precipitation and corrosion of Al-5083.* Scripta Materialia, 2000. 42(4): p. 335-340.
36. Wen, W., Zhao, Y.M., and Morris, J.G., *The effect of Mg precipitation on the mechanical properties of 5xxx aluminum alloys.* Materials Science and Engineering a-

Structural Materials Properties Microstructure and Processing, 2005. 392(1-2): p. 136-144.
37. Unwin, P.N.T. and Nicholson, R.B., *Nucleation And Initial Stages Of Growth Of Grain Boundary Precipitates In Al-Zn-Mg and Al-Mg Alloys.* Acta Metallurgica, 1969. 17(11): p. 1379.
38. Popović, M. and Romhanji, E., *Characterization of microstructural changes in an Al-6.wt.% Mg alloy by electrical resistivity measurements.* Materials Science and Engineering: A, 2008. 492(1-2): p. 460-467.
39. Winsley, R.J., *Corrosion Resistance of Heat Treated and Friction Stir Welded Alloy 5083-H116*, in *Department of Metallurgy and Materials*. 2008, University of Birmingham: PhD Thesis. p. 281.
40. Dix, E.H., Anderson, W.A., and Shumaker, M.B., Corrosion, 1959. 15: p. 19-26.
41. Kramer, L., Phillippi, M., Tack, W.T., and Wong, C., *Locally Reversing Sensitization in 5xxx Aluminum Plate.* Journal of Materials Engineering and Performance, 2012. 21(6): p. 1025-1029.
42. Pourbaix, M., *Atlas of Electrochemical Equilibria in Aqeous Solutions*. 1974: N A C E International
43. Hollingsworth, E.H. and Hunsicker, H.Y., *Corrosion of Aluminium and Aluminium Alloys*, in *ASM Handbook - Corrosion*, J.R. Davis, Editor. 1987, ASM International. p. 583-609.
44. Brown, R.H., Fink, W.L., and Hunter, M.S., *Measurement of Irreversible Potentials as Metalurgical Research Tools.* Trans. AIME, 1941. 143: p. 115.
45. Binger, W.W., Hollingsworth, E.H., and Sprowls, D.O., in *Aluminium, properties, physical metallurgy and phase diagrams*, K.R. Van Horn, Editor. 1967, American Society for Metals: Metals Park, Ohio. p. 226-235.
46. Birbilis, N. and Buchheit, R.G., *Electrochemical Characteristics of Intermetallic Phases in Aluminum Alloys.* Journal of The Electrochemical Society, 2005. 152(4): p. B140-B151.
47. Szklarska-Smialowska, Z., *Pitting corrosion of aluminum.* Corrosion Science, 1999. 41(9): p. 1743-1767.
48. Reboul, M.C., Warner, T.J., Mayet, H., and Baroux, B. *A ten-step mechanism for the pitting corrosion of aluminium*. in *Aluminium Alloys: Their physical and mechanical properties*. 1996. Grenoble, France.
49. Stehblow, H.-H., *Nucleation and Repassivation of Corrosion Pits for Pitting on Iron and Nickel.* Werkst. Korros, 1976. 27: p. 792.
50. Wong, K.P. and Alkire, R.C., *Local Chemistry and Growth of Single Corrosion Pits in Aluminum.* Journal of The Electrochemical Society, 1990. 137(10): p. 3010-3015.
51. Kaesche, H., *Localized Corrosion*, B. Staehle, et al., Editors. 1974, NACE: Houston, Texas. p. 516.
52. Frankel, G.S., *Pitting corrosion of metals - A review of the critical factors.* Journal of the Electrochemical Society, 1998. 145(6): p. 2186-2198.
53. Davis, G.D., Shaw, B.A., Rees, B.J., and Ferry, M., *Mechanisms of Passivity of Nonequilibrium Al-W Alloys.* Journal of The Electrochemical Society, 1993. 140(4): p. 951-959.
54. Rynders, R.M., Paik, C.H., Ke, R., and Alkire, R.C., *Use of In Situ Atomic Force Microscopy to Image Corrosion at Inclusions.* Journal of The Electrochemical Society, 1994. 141(6): p. 1439-1445.

55. Yasakau, K.A., Zheludkevich, M.L., Lamaka, S.V., and Ferreira, M.G.S., *Role of intermetallic phases in localized corrosion of AA5083.* Electrochimica Acta, 2007. 52(27): p. 7651-7659.
56. Aballe, A., Bethencourt, M., Botana, F.J., Marcos, M., and Sánchez-Amaya, J.M., *Influence of the degree of polishing of alloy AA 5083 on its behaviour against localised alkaline corrosion.* Corrosion Science, 2004. 46(8): p. 1909-1920.
57. Mizuno, K., Nylund, A., and Olefjord, I., *Surface reactions during pickling of an aluminium-magnesium-silicon alloy in phosphoric acid.* Corrosion Science, 2001. 43(2): p. 381-396.
58. Park, J.O., Paik, C.H., Huang, Y.H., and Alkire, R.C., *Influence of Fe-rich intermetallic inclusions on pit initiation on aluminum alloys in aerated NaCl.* Journal of The Electrochemical Society, 1999. 146(2): p. 517-523.
59. Aballe, A., Bethencourt, M., Botana, F.J., Cano, M.J., and Marcos, M., *Localized alkaline corrosion of alloy AA5083 in neutral 3.5% NaCl solution.* Corrosion Science, 2001. 43(9): p. 1657-1674.
60. Ambat, R., Davenport, A.J., Scamans, G.M., and Afseth, A., *Effect of iron-containing intermetallic particles on the corrosion behaviour of aluminium.* Corrosion Science, 2006. 48(11): p. 3455-3471.
61. Birbilis, N. and Buchheit, R.G., *Investigation and Discussion of Characteristics for Intermetallic Phases Common to Aluminum Alloys as a Function of Solution pH.* Journal of The Electrochemical Society, 2008. 155(3): p. C117-C126.
62. Eckermann, F., Suter, T., Uggowitzer, P.J., Afseth, A., and Schmutz, P., *The influence of MgSi particle reactivity and dissolution processes on corrosion in Al-Mg-Si alloys.* Electrochimica Acta, 2008. 54(2): p. 844-855.
63. Galvele, J.R. and de De Micheli, S.M., *Mechanism of intergranular corrosion of Al-Cu alloys.* Corrosion Science, 1970. 10(11): p. 795-807.
64. Ren, W.-d., Li, J.-f., Zheng, Z.-q., and Chen, W.-j., *Localized corrosion mechanism associated with precipitates containing Mg in Al alloys.* Transactions of Nonferrous Metals Society of China, 2007. 17(4): p. 727-732.
65. Baer, D.R., Windisch, C.F., Engelhard, M.H., Danielson, M.J., Jones, R.H., and Vetrano, J.S., *Influence of Mg on the corrosion of Al.* Journal of Vacuum Science & Technology a-Vacuum Surfaces and Films, 2000. 18(1): p. 131-136.
66. Chang, J.C. and Chuang, T.H., *Stress-corrosion cracking susceptibility of the superplastically formed 5083 aluminum alloy in 3.5 pct NaCl solution.* Metallurgical and Materials Transactions a-Physical Metallurgy and Materials Science, 1999. 30(12): p. 3191-3199.
67. Esposto, F.J., Zhang, C.S., Norton, P.R., and Timsit, R.S., *Segregation of Mg to the surface of an Al---Mg single crystal alloy and its influence on the initial oxidation at room temperature.* Surface Science, 1994. 302(1-2): p. 109-120.
68. Jones, R.H., Vetrano, J.S., and Windisch, C.F., *Stress corrosion cracking of Al-Mg and Mg-Al alloys.* Corrosion, 2004. 60(12): p. 1144-1154.
69. Lea, C. and Molinari, C., *Magnesium Diffusion, Surface Segregation And Oxidation in Al-Mg Alloys.* Journal of Materials Science, 1984. 19(7): p. 2336-2352.
70. Miller, W.S., Zhuang, L., Bottema, J., Wittebrood, A.J., De Smet, P., Haszler, A., and Vieregge, A., *Recent development in aluminium alloys for the automotive industry.* Materials Science and Engineering A, 2000. 280(1): p. 37-49.

71. Oguocha, I.N.A., Adigun, O.J., and Yannacopoulos, S., *Effect of sensitization heat treatment on properties of Al-Mg alloy AA5083-H116.* Journal of Materials Science, 2008. 43(12): p. 4208-4214.
72. Pickens, J.R., Gordon, J.R., and Green, J.A.S., *The Effect Of Loading Mode On The Stress-Corrosion Cracking Of Aluminium Alloy 5083.* Metallurgical Transactions a-Physical Metallurgy and Materials Science, 1983. 14(5): p. 925-930.
73. Searles, J.L., Gouma, P.I., and Buchheit, R.G., *Stress corrosion cracking of sensitized AA5083 (Al-4.5Mg-1.0Mn).* Aluminum Alloys 2002: Their Physical and Mechanical Properties Pts 1-3, 2002. 396-4: p. 1437-1442.
74. Speidel, M.O. and Hyatt, M.V., in *Advances in Corrosion Science and Technology*, M.G. Fontana and R.W. Staehle, Editors. 1972, Plenum: New York. p. 115.
75. Vetrano, J.S., Baer, D.R., and Jones, R.H., *Solute segregation and beta-phase precipitation at internal interfaces in AA5083.* Automotive Alloys Ii, 1998: p. 117-123.
76. Windisch, C.F., Baer, D.R., Engelhard, M.H., Danielson, M.J., and Jones, R.H., in *198th Meeting of the Electrochemical Society*. 2000: Phoenix, AZ.
77. Huang, T.-S. and Frankel, G.S., *Kinetics of sharp intergranular corrosion fissures in AA7178.* Corrosion Science, 2007. 49(2): p. 858-876.
78. Doig, P. and Edington, J.W., *Low-temperature diffusion in A1–7 wt. % Mg and A1–4 wt. % Cu alloys.* Philosophical Magazine, 1973. 28(5): p. 961-970.
79. Jain, S., Lim, M.L.C., Hudson, J.L., and Scully, J.R., *Spreading of intergranular corrosion on the surface of sensitized Al-4.4Mg alloys: A general finding.* Corrosion Science, 2012. 59(0): p. 136-147.
80. Mears, R.B., Brown, R.H., and Dix, E.H.J., *A Generalised Theory of Stress Corrosion of Alloys*. 1945, Jointly by ASTM and AIME.
81. Davenport, A.J., Yuan, Y., Ambat, R., Connolly, B.J., Strangwood, M., Afseth, A., and Scamans, G. *Intergranular corrosion and stress corrosion cracking of sensitised AA5182*. in *10th International Conference on Aluminium Alloys (ICAA-10)*. 2006. Vancouver, CANADA: Trans Tech Publications Ltd.
82. Kar, S., Rodchanarowan, A., and Free, M.L., *The effect of cyclic and constant thermal exposure on AA5083 and related alloy susceptibility to intergranular corrosion*, in *NACE International Corrosion* 2009.
83. Lin, S., Nie, Z., Huang, H., and Li, B., *Annealing behavior of a modified 5083 aluminum alloy*. Materials & Design, 2010. 31(3): p. 1607-1612.
84. Jones, R.H., in *ASM Handbook: Corrosion: Fundamentals, Testing and protection*. 2003, ASM International, Materials Park, OH. p. 345.
85. Burleigh, T.D., *The Postulated Mechanisms for Stress Corrosion Cracking of Aluminium Alloys.* Corrosion, 1991. 47(2): p. 89-98.
86. Speidel, M.O., *Stress-Corrosion Cracking Of Aluminium Alloys.* Metallurgical Transactions, 1975. A 6(4): p. 631-651.
87. Gao, J. and Quesnel, D.J., *The Effect of Sensitization On Stress Corrosion Cracking of AA5083*, in *Corrosion 2010*. 2010: San Antonio, TX.
88. Goswami, R., Spanos, G., Pao, P.S., and Holtz, R.L., *Microstructural Evolution and Stress Corrosion Cracking Behavior of Al-5083.* Metallurgical and Materials Transactions A, 2010: p. 1-8.
89. Gunson, J., *Effect of Sensitsation on the Corrosion Fatigue Properties of AA5456-H116*, in *Department of Metallurgy and Materials*. 2010, University of Birmingham: Birmingham.

90. Holtz, R.L., Pao, P.S., Bayles, R.A., Longazel, T.M., and Goswami, R., *Corrosion-Fatigue Behavior of Aluminum Alloy 5083-H131 Sensitized at 448 K (175 degrees C).* Metallurgical and Materials Transactions a-Physical Metallurgy and Materials Science, 2012. 43A(8): p. 2839-2849.
91. Popovic, M. and Romhanji, E., *Stress corrosion cracking susceptibility of Al-Mg alloy sheet with high Mg content.* Journal of Materials Processing Technology, 2002. 125: p. 275-280.
92. Braun, R. and Hack, T., *Effects of cold working and thermal exposure on the SCC behaviour of AA5182 alloy sheet.* Materials Science Forum, 1996. 217-222: p. 1635-1640.
93. Summerson, T.J. and Sprowls, D.O., in *Aluminium Alloys - Their physical and Mechanical Properties*, E.A. Starke Jr. and T.H. Sanders Jr, Editors. 1986, Cradley Heath. p. 1575.
94. Jones, R.H., Gertsman, V.Y., Vetrano, J.S., and Windisch, C.F., *Crack-particle interactions during intergranular stress corrosion of AA5083 as observed by cross-section transmission electron microscopy.* Scripta Materialia, 2004. 50(10): p. 1355-1359.
95. Scamans, G. and Rehal, A., *Electron metallography of the aluminium-water vapour reaction and its relevance to stress-corrosion susceptibility.* Journal of Materials Science, 1979. 14(10): p. 2459-2470.
96. Gruhl, W., Zeitschrift Fur Metallkunde, 1964. 75(11): p. 819-826.
97. Ohnishi, T. and Higashi, K., J. Jpn. Inst. Light Met., 1984. 34(11): p. 850-856.
98. Vargel, C., Jacques, M., and Schmidt, M.P., *Chapter C.2 - The Parameters of Atmospheric Corrosion*, in *Corrosion of Aluminium*. 2004, Elsevier: Amsterdam. p. 241-257.
99. Hernandez, F.J., Santana, J.J., Souto, R.M., Gonzalez, S., and Morales, J., *Characterization of the Atmospheric Corrosion of Aluminum in Archipelagic Subtropical Environments.* International Journal of Electrochemical Science, 2011. 6(12): p. 6567-6580.
100. Syed, S., *Influence of the environment on atmospheric corrosion of aluminium.* Corrosion Engineering Science and Technology, 2010. 45(4): p. 282-287.
101. Dan, Z., Muto, I., and Hara, N., *Effects of environmental factors on atmospheric corrosion of aluminium and its alloys under constant dew point conditions.* Corrosion Science, 2012. 57(0): p. 22-29.
102. Blücher, D.B., Svensson, J.E., and Johansson, L.G., *The influence of CO2, AlCl3;6H2O, MgCl2;6H2O, Na2SO4 and NaCl on the atmospheric corrosion of aluminum.* Corrosion Science, 2006. 48(7): p. 1848-1866.
103. Sun, S., Zheng, Q., Wen, J., and Li, D., *Atmospheric corrosion of aluminium in the northern Taklamakan Desert environment.* Materials and Corrosion-Werkstoffe Und Korrosion, 2010. 61(10): p. 852-859.
104. Chen, C., Breslin, C.B., and Mansfeld, F., *Scanning Kelvin probe analysis of the potential distribution under small drops of electrolyte.* Materials and Corrosion-Werkstoffe Und Korrosion, 1998. 49(8): p. 569-575.
105. King, P.C., Cole, I.S., Corrigan, P.A., Hughes, A.E., and Muster, T.H., *FIB/SEM study of AA2024 corrosion under a seawater drop: Part I.* Corrosion Science, 2011. 53(3): p. 1086-1096.

106. Tsuru, T., Tamiya, K.-I., and Nishikata, A., *Formation and growth of micro-droplets during the initial stage of atmospheric corrosion.* Electrochimica Acta, 2004. 49(17-18): p. 2709-2715.
107. Cheng, Y.L., Zhang, Z., Cao, F.H., Li, J.F., Zhang, J.Q., Wang, J.M., and Cao, C.N., *A study of the corrosion of aluminum alloy 2024-T3 under thin electrolyte layers.* Corrosion Science, 2004. 46(7): p. 1649-1667.
108. Li, J.F., Maier, B., and Frankel, G.S., *Corrosion of an Al-Mg-Si alloy under MgCl2 solution droplets.* Corrosion Science, 2011. 53(6): p. 2142-2151.
109. Tsutsumi, Y., Nishikata, A., and Tsuru, T., *Pitting corrosion mechanism of Type 304 stainless steel under a droplet of chloride solutions.* Corrosion Science, 2007. 49(3): p. 1394-1407.
110. Zhang, J.B., Wang, J., and Wang, Y.H., *Phenomenon of micro-droplets formation on metals during the deliquescence of salt particles in atmosphere.* Acta Physico-Chimica Sinica, 2005. 21(9): p. 993-996.
111. Mishra, R.S. and Ma, Z.Y., *Friction stir welding and processing.* Materials Science & Engineering R-Reports, 2005. 50(1-2): p. 1-78.
112. Rhodes, C.G., Mahoney, M.W., Bingel, W.H., Spurling, R.A., and Bampton, C.C., *Effects of friction stir welding on microstructure of 7075 aluminum.* Scripta Materialia, 1997. 36(1): p. 69-75.
113. Cui, S. and Chen, Z.W., *Effects of tool speeds and corresponding torque/energy on stir zone formation during friction stir welding/processing.* IOP Conference Series: Materials Science and Engineering, 2009. 4(1): p. 012019.
114. Rodrigues, D.M., Leitao, C., Louro, R., Gouveia, H., and Loureiro, A., *High speed friction stir welding of aluminium alloys.* Science and Technology of Welding and Joining, 2010. 15(8): p. 676-681.
115. Watanabe, T., Takayama, H., and Yanagisawa, A., *Joining of aluminum alloy to steel by friction stir welding.* Journal of Materials Processing Technology, 2006. 178(1-3): p. 342-349.
116. Peel, M., *Dissimilar friction stir welds in AA5083-AA6082. Part I: Process parameter effects on thermal history and weld properties.* Metallurgical and Materials Transactions A, 2006. 37(7): p. 2183.
117. Somasekharan, A.C. and Murr, L.E., *Microstructure in friction-stir welded dissimiliar magnesium alloys to 6061-T6 aluminum alloy.* Materials Characterization, 2004. 52(1): p. 49-64.
118. Li, Y., Murr, L.E., and McClure, J.C., *Flow visualization and residual microstructures associated with the friction-stir welding of 2024 aluminum to 6061 aluminum.* Materials Science and Engineering A, 1999. 271(1-2): p. 213-223.
119. Liu, G., Murr, L.E., Niou, C.S., McClure, J.C., and Vega, F.R., *Microstructural aspects of the friction-stir welding of 6061-T6 aluminum.* Scripta Materialia, 1997. 37(3): p. 355-361.
120. Charit, I. and Mishra, R.S., *Evaluation of microstructure and superplasticity in friction stir processed 5083 Al alloy.* Journal of Materials Research, 2004. 19(11): p. 3329-3342.
121. Prangnell, P.B. and Heason, C.P., *Grain structure formation during friction stir welding observed by the [`]stop action technique'.* Acta Materialia, 2005. 53(11): p. 3179-3192.
122. Benavides, S., Li, Y., Murr, L.E., Brown, D., and McClure, J.C., *Low-temperature friction-stir welding of 2024 aluminum.* Scripta Materialia, 1999. 41(8): p. 809-815.

123. Ma, Z.Y., Mishra, R.S., and Mahoney, M.W., *Superplastic deformation behaviour of friction stir processed 7075Al alloy.* Acta Materialia, 2002. 50(17): p. 4419-4430.
124. Mahoney, M., Rhodes, C., Flintoff, J., Bingel, W., and Spurling, R., *Properties of friction-stir-welded 7075 T651 aluminum.* Metallurgical and Materials Transactions A, 1998. 29(7): p. 1955-1964.
125. Murr, L., Liu, G., and McClure, J., *Dynamic recrystallization in friction-stir welding of aluminium alloy 1100.* Journal of Materials Science Letters, 1997. 16(22): p. 1801-1803.
126. Salem, H.G., Reynolds, A.P., and Lyons, J.S., *Microstructure and retention of superplasticity of friction stir welded superplastic 2095 sheet.* Scripta Materialia, 2002. 46(5): p. 337-342.
127. Sato, Y.S., Park, S.H.C., and Kokawa, H., *Microstructural factors governing hardness in friction-stir welds of solid-solution-hardened Al alloys.* Metallurgical and Materials Transactions a-Physical Metallurgy and Materials Science, 2001. 32(12): p. 3033-3042.
128. Tang, W., Guo, X., McClure, J.C., and Murr, L.E., *Heat input and temperature distribution in friction stir welding.* Journal of Materials Processing & Manufacturing Science, 1999. 7(2): p. 163-172.
129. Fonda, R.W. and Bingert, J.F., *Microstructural evolution in the heat-affected zone of a friction stir weld.* Metallurgical and Materials Transactions a-Physical Metallurgy and Materials Science, 2004. 35A(5): p. 1487-1499.
130. M. Mahoney, R.S. Mishra, T. Nelson, J. Flintoff, R. Islamgaliev, and Hovansky, Y., in *Friction Stir Welding and Processing*, K.V. Jata, et al., Editors. 2001, TMS: Warrendale, PA, USA. p. 183.
131. Jata, K.V. and Semiatin, S.L., *Continuous dynamic recrystallization during friction stir welding of high strength aluminum alloys.* Scripta Materialia, 2000. 43(8): p. 743-749.
132. Su, J.Q., Nelson, T.W., Mishra, R., and Mahoney, M., *Microstructural investigation of friction stir welded 7050-T651 aluminium.* Acta Materialia, 2003. 51(3): p. 713-729.
133. Lockwood, W.D., Tomaz, B., and Reynolds, A.P., *Mechanical response of friction stir welded AA2024: experiment and modeling.* Materials Science and Engineering: A, 2002. 323(1–2): p. 348-353.
134. Mishra, R.S., Mahoney, M.W., McFadden, S.X., Mara, N.A., and Mukherjee, A.K., *High strain rate superplasticity in a friction stir processed 7075 Al alloy.* Scripta Materialia, 1999. 42(2): p. 163-168.
135. Chang, C.I., Du, X.H., and Huang, J.C., *Achieving ultrafine grain size in Mg–Al–Zn alloy by friction stir processing.* Scripta Materialia, 2007. 57(3): p. 209-212.
136. Kwon, Y.J., Shigematsu, I., and Saito, N., *Mechanical properties of fine-grained aluminum alloy produced by friction stir process.* Scripta Materialia, 2003. 49(8): p. 785-789.
137. Morishige, T., Hirata, T., Tsujikawa, M., and Higashi, K., *Comprehensive analysis of minimum grain size in pure aluminum using friction stir processing.* Materials Letters, 2010. 64(17): p. 1905-1908.
138. Saito, N., Shigematsu, I., Komaya, T., Tamaki, T., Yamauchi, G., and Nakamura, M., *Grain refinement of 1050 aluminum alloy by friction stir processing.* Journal of Materials Science Letters, 2001. 20(20): p. 1913-1915.
139. Su, J.-Q., Nelson, T.W., and Sterling, C.J., *Friction stir processing of large-area bulk UFG aluminum alloys.* Scripta Materialia, 2005. 52(2): p. 135-140.

140. Gandra, J., Miranda, R.M., and Vilaca, P., *Effect of overlapping direction in multipass friction stir processing.* Materials Science and Engineering a-Structural Materials Properties Microstructure and Processing, 2011. 528(16-17): p. 5592-5599.
141. Camurlu, H.E. and Unal, N., *Friction stir processing and characterisation of A380 cast aluminium alloy.* International Journal of Cast Metals Research, 2011. 24(6): p. 357-362.
142. Fonda, R.W., Bingert, J.F., and Colligan, K.J., *Development of grain structure during friction stir welding.* Scripta Materialia, 2004. 51(3): p. 243-248.
143. Yadav, D. and Bauri, R., *Microstructural characterisation of friction stir processed aluminium.* Materials Science and Technology, 2011. 27(7): p. 1163-1169.
144. El-Danaf, E.A., El-Rayes, M.M., and Soliman, M.S., *Friction stir processing: An effective technique to refine grain structure and enhance ductility.* Materials & Design, 2010. 31(3): p. 1231-1236.
145. Ma, Z.Y., Sharma, S.R., and Mishra, R.S., *Effect of friction stir processing on the microstructure of cast A356 aluminum.* Materials Science and Engineering: A, 2006. 433(1-2): p. 269-278.
146. Kurt, A., Uygur, I., and Cete, E., *Surface modification of Aluminium by friction stir processing.* Journal of Materials Processing Technology, 2010. In Press, Accepted Manuscript.
147. Zahmatkesh, B. and Enayati, M.H., *A novel approach for development of surface nanocomposite by friction stir processing.* Materials Science and Engineering: A, 2010. 527(24-25): p. 6734-6740.
148. Ma, Z.Y., *Friction stir processing technology: A review.* Metallurgical and Materials Transactions a-Physical Metallurgy and Materials Science, 2008. 39A(3): p. 642-658.
149. Katsas, S., Nikolaou, J., and Papadimitriou, G., *Microstructural changes accompanying repair welding in 5xxx aluminium alloys and their effect on the mechanical properties.* Materials & Design, 2006. 27(10): p. 968-975.
150. Calcraft, R.C., Wahab, M.A., Viano, D.M., Schumann, G.O., Phillips, R.H., and Ahmed, N.U., *The development of the welding procedures and fatigue of butt-welded structures of aluminium-AA5383.* Journal of Materials Processing Technology, 1999. 92-93: p. 60-65.
151. Jin, H., Ko, C., Saimoto, S., and Threadgill, P.L., *Microstructure of friction stir welded joints in AA5182*, in *Aluminium Alloys: Their Physical and Mechanical Properties, Pts 1-3*, E.A. Starke, T.H. Sanders, and W.A. Cassada, Editors. 2000, Trans Tech Publications Ltd: Zurich-Uetikon. p. 1725-1730.
152. Hirata, T., Oguri, T., Hagino, H., Tanaka, T., Chung, S.W., Takigawa, Y., and Higashi, K., *Influence of friction stir welding parameters on grain size and formability in 5083 aluminum alloy.* Materials Science and Engineering a-Structural Materials Properties Microstructure and Processing, 2007. 456(1-2): p. 344-349.
153. Peel, M., Steuwer, A., Preuss, M., and Withers, P.J., *Microstructure, mechanical properties and residual stresses as a function of welding speed in aluminium AA5083 friction stir welds.* Acta Materialia, 2003. 51(16): p. 4791-4801.
154. Svensson, L.E., Karlsson, L., Larsson, H., Karlsson, B., Fazzini, M., and Karlsson, J., *Microstructure and mechanical properties of friction stir welded aluminium alloys with special reference to AA 5083 and AA 6082.* Science and Technology of Welding and Joining, 2000. 5(5): p. 285-296.

155. Cui, G.R., Ma, Z.Y., and Li, S.X., *The origin of non-uniform microstructure and its effects on the mechanical properties of a friction stir processed Al–Mg alloy.* Acta Materialia, 2009. 57(19): p. 5718-5729.
156. Gan, W., Okamoto, K., Hirano, S., Chung, K., Kim, C., and Wagoner, R.H., *Properties of friction-stir welded aluminum alloys 6111 and 5083.* Journal of Engineering Materials and Technology-Transactions of the Asme, 2008. 130(3): p. 15.
157. Kumar, R., Singh, K., and Pandey, S., *Process forces and heat input as function of process parameters in AA5083 friction stir welds.* Transactions of Nonferrous Metals Society of China, 2012. 22(2): p. 288-298.
158. Kwon, Y.-J., Shim, S.-B., and Park, D.-H., *Friction stir welding of 5052 aluminum alloy plates.* Transactions of Nonferrous Metals Society of China, 2009. 19, Supplement 1(0): p. s23-s27.
159. García-Bernal, M.A., Mishra, R.S., Verma, R., and Hernández-Silva, D., *Hot deformation behavior of friction-stir processed strip-cast 5083 aluminum alloys with different Mn contents.* Materials Science and Engineering: A, 2012. 534(0): p. 186-192.
160. Attallah, M.M., Davis, C.L., and Strangwood, M., *Microstructure-microhardness relationships in friction stir welded AA5251.* Journal of Materials Science, 2007. 42(17): p. 7299-7306.
161. Jin, H., Saimoto, S., Ball, M., and Threadgill, P.L., *Characterisation of microstructure and texture in friction stir welded joints of 5754 and 5182 aluminium alloy sheets.* Materials Science and Technology, 2001. 17: p. 1605-1614.
162. Attallah, M.M., *Microstructure-Property development in Friction Stir Welds of Aluminium-based alloys*, in *Department of Metallurgy and Materials*. 2007, University of Birmingham: PhD Thesis.
163. El-Danaf, E.A., El-Rayes, M.M., and Soliman, M.S., *Low temperature enhanced ductility of friction stir processed 5083 aluminum alloy.* Bulletin of Materials Science, 2011. 34(7): p. 1447-1453.
164. Morishige, T., Hirata, T., Uesugi, T., Takigawa, Y., Tsujikawa, M., and Higashi, K., *Effect of Mg content on the minimum grain size of Al-Mg alloys obtained by friction stir processing.* Scripta Materialia, 2011. 64(4): p. 355-358.
165. Conserva, M. and Leoni, M., *Effect of thermal and thermo-mechanical processing on the properties of Al-Mg alloys.* Metallurgical and Materials Transactions A, 1975. 6(1): p. 189-195.
166. Tan, L. and Allen, T.R., *Effect of thermomechanical treatment on the corrosion of AA5083.* Corrosion Science, 2010. 52(2): p. 548-554.
167. Prasad Rao, K., Janaki Ram, G.D., and Stucker, B.E., *Effect of friction stir processing on corrosion resistance of aluminum-copper alloy gas tungsten arc welds.* Materials & Design, 2010. 31(3): p. 1576-1580.
168. Surekha, K., Murty, B.S., and Prasad Rao, K., *Comparison of corrosion behaviour of friction stir processed and laser melted AA 2219 aluminium alloy.* Materials & Design, 2011. 32(8–9): p. 4502-4508.
169. Squillace, A., De Fenzo, A., Giorleo, G., and Bellucci, F., *A comparison between FSW and TIG welding techniques: modifications of microstructure and pitting corrosion resistance in AA 2024-T3 butt joints.* Journal of Materials Processing Technology, 2004. 152(1): p. 97-105.

170. Xu, W., Liu, J., and Zhu, H., *Pitting corrosion of friction stir welded aluminum alloy thick plate in alkaline chloride solution.* Electrochimica Acta, 2010. 55(8): p. 2918-2923.
171. Biallas, G., Braun, R., Donne, C.D., Staniek, G., and Kaysser, W.A., *Mechanical properties and corrosion behavior of friction stir welded 2024-T3*, in *Proceedings of the First International Symposium on Friction Stir Welding*. 1999, TWI Ltd.: CA, USA, .
172. Davenport, A.J., *Corrosion Of Friction Stir Welds In Aerospace Alloys.* Electrochemical Society proceedings - Corrosion and protection of light metals, 2004. 23.
173. Paglia, C.S. and Buchheit, R.G., *A look in the corrosion of aluminum alloy friction stir welds.* Scripta Materialia, 2008. 58(5): p. 383-387.
174. Benedictus-deVries, S., Bakker, A., Janssen, G.C.A.M., and de Wit, H., *Fatigue Crack Initiation Behavior of Welded AA5083 in a Seawater Environment.* Journal of Engineering Materials and Technology, 2004. 126(2): p. 199-203.
175. Katsas, S., Nikolaou, J., and Papadimitriou, G., *Corrosion resistance of repair welded naval aluminium alloys.* Materials & Design, 2007. 28(3): p. 831-836.
176. Frankel, G.S. and Xia, Z., *Localized corrosion and stress corrosion cracking resistance of friction stir welded aluminum alloy 5454.* Corrosion, 1999. 55(2): p. 139-150.
177. Zucchi, F., Trabanelli, G., and Grassi, V., *Pitting and stress corrosion cracking resistance of friction stir welded AA 5083.* Materials and Corrosion-Werkstoffe Und Korrosion, 2001. 52(11): p. 853-859.
178. Fonda, R.W., Pao, P.S., Jones, H.N., Feng, C.R., Connolly, B.J., and Davenport, A.J., *Microstructure, mechanical properties, and corrosion of friction stir welded Al 5456.* Materials Science and Engineering a-Structural Materials Properties Microstructure and Processing, 2009. 519(1-2): p. 1-8.
179. Surekha, K., Murty, B.S., and Prasad Rao, K., *Effect of processing parameters on the corrosion behaviour of friction stir processed AA 2219 aluminum alloy.* Solid State Sciences, 2009. 11(4): p. 907-917.
180. Surekha, K., Murty, B.S., and Rao, K.P., *Microstructural characterization and corrosion behavior of multipass friction stir processed AA2219 aluminium alloy.* Surface and Coatings Technology, 2008. 202(17): p. 4057-4068.
181. Marone, F. and Stampanoni, M., *Regridding reconstruction algorithm for real-time tomographic imaging.* Journal of Synchrotron Radiation. 19(6): p. 1029-1037.
182. *International Alloy Designations and Chemical Composition Limits for Wrought Aluminium and Wrought Aluminium Alloys*. The Aluminium Association. 1998.
183. Buczynski, J. and Kelly, R., *Electrochemical Characterization of the β-phase (Al3Mg2) in 5XXX Aluminum Alloys.* Meeting Abstracts, 2011. MA2011-02(21): p. 1673.
184. Yu, H. and Granger, D.A., *Macrosegregation in Aluminium alloy ingot cast by the semicontinuous Direct Chill (DC) method*, in *Aluminium Alloys: Their physical and mechanical properties*, E.A. Starke Jr. and T.H. Sanders Jr, Editors. 1986: University of Virginia, Charlottesville, Virginia. p. 17-30.
185. Gaber, A., *Precipitation Kinetics in Supersaturated Aluminium-Magnesium Alloys.* Aluminium Transactions, 1999. 1(1).

186. Rodrigues, D.M., Loureiro, A., Leitao, C., Leal, R.M., Chaparro, B.M., and Vilaca, P., *Influence of friction stir welding parameters on the microstructural and mechanical properties of AA 6016-T4 thin welds.* Materials & Design, 2009. 30(6): p. 1913-1921.
187. Sato, Y.S., Kokawa, H., Enomoto, M., and Jogan, S., *Microstructural evolution of 6063 aluminum during friction-stir welding.* Metallurgical and Materials Transactions a-Physical Metallurgy and Materials Science, 1999. 30(9): p. 2429-2437.
188. Chang, J.C. and Chuang, T.H., *The degradation of corrosion resistance for Al 5083 alloy after thermal and superplastic forming processes.* Journal of Materials Engineering and Performance, 2000. 9(3): p. 253-260.
189. Knight, S.P., Salagaras, M., and Trueman, A.R., *The study of intergranular corrosion in aircraft aluminium alloys using X-ray tomography.* Corrosion Science, 2011. 53(2): p. 727-734.
190. Summerson, T.J. and Sprowls, D.O., *Corrosion behaviour of Aluminium alloys*, in *Aluminium Alloys: Their physical and mechanical properties*, E.A. Starke Jr. and T.H. Sanders Jr, Editors. 1986: University of Virginia, Charlottesville, Virginia. p. 1575-1664.